Collapse of dipolar Bose-Einstein condensates for different trap geometries

Von der Fakultät Mathematik und Physik der Universität Stuttgart
zur Erlangung des akademischen Grades eines Doktors der
Naturwissenschaften (Dr. rer. nat.) genehmigte Abhandlung

DISSERTATION

vorgelegt von

Jonas Metz

aus Frankfurt am Main

Betreuer und Referent:	Prof. Dr. Tilman Pfau
Koreferent:	Prof. Dr. Bernhard Keimer
Prüfungsvorsitzender:	Prof. Dr. Günter Wunner

Tag der mündlichen Prüfung: 16. September 2010

5. Physikalisches Institut
Universität Stuttgart
2010

Abstract

We experimentally investigate how the collapse dynamics of a ^{52}Cr Bose-Einstein condensate depends on the external harmonic trap geometry. When the collapse is initiated by reducing the s-wave scattering length below its critical value, a complex dynamics is observed, involving a d-wave symmetric explosion. We find good agreement between our experiments and simulations of the Gross-Pitaevskii equation including 3-body losses. In order to probe the phase-coherence of collapsed condensates we induce the collapse in several condensates simultaneously and let them interfere.

Zusammenfassung und wissenschaftlicher Kontext

Gegenstand der Dissertation ist die experimentelle Untersuchung der Kollapsdynamik eines dipolaren Bose-Einstein Kondensates bestehend aus ^{52}Cr Atomen. Der Schwerpunkt liegt dabei auf der Beobachtung und Analyse der wechselwirkungsinduzierten Instabilität und der damit verbundenen zeitlichen und räumlichen Entwicklung des Kondensates. Ziel der Dissertation ist es zum allgemeinen Verständnis dipolarer Quantensysteme beizutragen.

Ausgangspunkt und Grundlage der durchgeführten Experimente ist ein *Bose-Einstein Kondensat* (BEK). Ein BEK ist ein Vielteilchensystem, das aus Sicht der Quantenforschung zwei Vorteile vereint: Während es einerseits ausreichend einfach ist, um es auf dem Quantenniveau zu verstehen, ist es andererseits hinreichend komplex, um viele bisher ungeklärte Quantenphänomene der Festkörperphysik zu enthalten. So ist etwa das wissenschaftliche Verständnis der mikroskopischen bzw. mesoskopischen Vorgänge, die der Superfluidität [1], Supraleitung [2] oder dem anormalen Elektronen-Transport in nieder-dimensionalen Systemen [3–6] zu Grunde liegen noch immer unbefriedigend; diese Phänomene werden durch starke Korrelationen und Quanteneffekte bestimmt, die den klassischen (nicht quantenmechanischen) Erfahrungen widersprechen. Um diese Quantenphänomene besser zu verstehen, ist es daher sinnvoll die Quantenwelt zunächst in einfacheren Modellsystemen zu erforschen, die keine Komplikationen (Unreinheiten, Korngrenzen, stochastische Störstellen etc.) aufweisen. Quantenentartete Gase (sowohl bosonische [7–14] als auch fermionische [15–18]) sind solche Modellsysteme. In ihnen lassen sich alle systemrelevanten Parameter (externes Potential, inter-atomare Wechselwirkung etc.) dynamisch und mit hoher Präzision einstellen, während sie nahezu keine Defekte aufweisen. Sie sind ideale Quantensimulatoren [19], um theoretisch vorhergesagte Phänomene zu überprüfen und neuartige Zustände der Quantenmaterie zu erzeugen. Zwar wurden sie bisher hauptsächlich dazu benutzt, Fragen der Festkörper- und Vielteilchenphysik zu beantworten [20], jedoch bieten sie fachübergreifende Einsatzmöglichkeiten, für sowohl die Atom- und Molekülphysik als auch die Hochenergie-Physik. Die Experimente ermöglichen nicht nur fundamentale Tests der Quantenmechanik, sondern liefern auch Impulse zur Weiterentwicklung der Materialwissenschaften.

Im Laufe der letzten 15 Jahre entstand eine Vielfalt von Bose-Einstein Kondensaten, die sich in ihren Eigenschaften erheblich voneinander unterscheiden. Der Charakter eines BEKs wird im wesentlichen durch drei Faktoren bestimmt:

(1.) der Dimension der Wellenfunktion,

(2.) der Art der inter-atomaren Wechselwirkung[1] sowie

[1] Während die ursprüngliche Idee eines Bose-Einstein Kondensates [21–24] ein Ensemble von nicht-wechselwirkenden Teilchen behandelt, benutzen wir eine moderne Definition [25], bei der die Teilchen miteinander wechselwirken. Ohne Wechselwirkung wäre ein BEK weder phasenkohärent noch superfluid und würde somit zwei seiner spannendsten Eigenschaften verlieren [26, ch. 1.2].

(3.) der Wechselwirkung des BEKs mit seiner Umgebung.

Um diese drei Faktoren zu veranschaulichen, definieren wir das „*Standardkondensat*“ folgendermaßen:

(1.1) Es wird durch eine *skalare* Wellenfunktion beschrieben — d.h. seine Teilchen besitzen keinen internen Freiheitsgrad.

(2.1) Die inter-atomare Wechselwirkung ist analog zur *Kontaktwechselwirkung* inelastischer Kugeln, siehe Abb. 1(a) — d.h. sie ist sowohl

  (a) *kurzreichweitig*, weil zwei Kugeln nur dann wechselwirken, wenn sie aneinander stoßen, als auch

  (b) *isotrop*, weil die Kugeln keine Vorzugsrichtung aufweisen.

(3.1) Das isotrope externe Fallenpotential ist entweder linear oder harmonisch (in Abb. 1 nicht dargestellt). Es entkoppelt das BEK vollständig von seiner Umgebung und enthält keine Störstellen.

Wird eine dieser Eigenschaften grundlegend verändert, so verändert sich auch der Charakter des BEKs. Beispiele hierfür sind (1.1) die Spinorkondensate [27, ch. 4], (2.1) Efimov Zustände [28–32] und (3.1) die Kopplung eines BEKs mit einem Photon [33, 34] oder nano-mechanischen Resonator [35, 36].

Die vorliegende Arbeit behandelt den Sonderfall eines *dipolaren* Bose-Einstein Kondensats (DBEKs). Im allgemeinen unterscheidet sich ein DBEK vom „Standardkondensat“ indem es die ersten beiden Eigenschaften, (1.1) und (2.1), durch folgende ersetzt:

(1.1)→(1.2) Es wird durch eine *vektorielle* Wellenfunktion beschrieben — d.h. die Teilchen besitzen einen internen Freiheitsgrad (magnetisches oder elektrisches Dipolmoment), so dass die räumliche Symmetrie, bei Fehlen eines externen (magnetischen oder elektrischen) Feldes, spontan gebrochen werden kann.

(2.1)→(2.2) Die inter-atomare *Dipol-Dipol Wechselwirkung* (DDWW) ist sowohl

  (a) *langreichweitig*, als auch

  (b) *anisotrop* — d.h. abhängig von der Ausrichtung der beiden Dipole, ist sie entweder anziehend oder abstoßend [37].

Die ersten BEK-Experimente mit beobachtbaren *dipolaren Effekten* (am MIT mit ^{23}Na und am NIST mit ^{87}Rb) analysierten den vektoriellen Charakter der Wellenfunktion [27, ch. 4]. Vor kurzem gelang es in Hannover [38, 39] und Berkeley [40–43] (jeweils mit ^{87}Rb), diese Experimente weiterzuführen. Im Gegensatz dazu verwenden die Experimente in Stuttgart [44–46] und Paris [47, 48] mit ^{52}Cr, Florenz [49] mit ^{39}K sowie in Houston [50] mit ^{6}Li ein Magnetfeld, um die Dipole vollständig zu polarisieren. Der vektorielle Charakter der Wellenfunktion geht durch die explizite Symmetriebrechung verloren. Diese Experimente konzentrieren sich darauf, die Anisotropie der dipolaren Wechselwirkung zu untersuchen [51, 52].

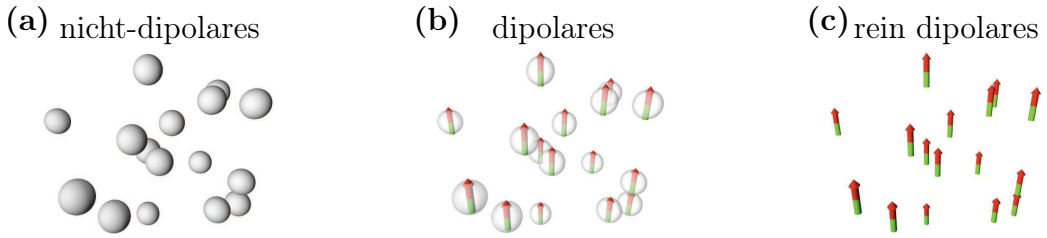

Abb. 1, Nicht-dipolares, dipolares, und rein dipolares BEK: Vernachlässigen wir, dass die Atome eines BEKs ununterscheidbar sind und das sich ihre 1-Teilchenwellenfunktionen überlappen, so kann ihre Wechselwirkung wie folgt dargestellt werden: Ein nicht-dipolares BEK (a) besteht aus inelastischen Kugeln. Ihre Kontaktwechselwirkung ist kurzreichweitig und isotrop. Im Gegensatz dazu besteht das rein dipolare Kondensat (c) aus Magneten (hier werden magnetische Dipole angenommen). Sie interagieren ausschließlich mittels der langreichweitigen und anisotropen Dipol-Dipol Wechselwirkung. Grafik (b) veranschaulicht ein dipolares BEK. Die Teilchen interagieren sowohl mittels der Kontakt- als auch der dipolaren Wechselwirkung.

Die vorliegende Arbeit geht von den genannten Experimenten zur Untersuchung der anisotropen Wechselwirkung aus und erweitert diese, indem sie die Dynamik von *instabilen* dipolaren Kondensaten erforscht. Zwar wurde die vielschichtige Dynamik instabiler Kondensate bereits in ^{7}Li [53–56] und ^{85}Rb Kondensaten [57–60] sowie in ^{40}K−^{87}Rb Mischungen [61, 62] beobachtet, jedoch weisen diese Systeme eine vernachlässigbare dipolare Wechselwirkung auf. Die Hinzunahme der dipolaren Wechselwirkung ist deshalb interessant, weil sie den Typus der Instabilität verändert: Abhängig von der Fallengeometrie stabilisiert oder destabilisiert die dipolare Wechselwirkung das BEK. Dies modifiziert nicht nur die zeitliche und räumliche Entwicklung des dipolaren Kondensates, sondern steigert auch beträchtlich die Anzahl der zu beobachtenden physikalischen Phänomene. Daher liegt der Schwerpunkt dieser Arbeit auf dem Verstehen der dipolaren Instabilität und der damit verbundenen Dynamik. Insbesondere wird die fließende Veränderung der Kollapsdynamik analysiert, wie sie im Übergang eines zigarrenförmigen (prolaten) zu einem kugelsymmetrischen DBEKs zu beobachten ist. Der Vergleich der experimentellen Daten mit den theoretischen Simulationen wird zeigen, wie die Grundgleichung dipolarer BEKe erweitert werden muss, um kollabierende Kondensate zu beschreiben.

Vor diesem Hintergrund besteht die Relevanz der Arbeit zum einen darin, ein experimentell bisher unerforschtes Feld zu erschließen. Die dabei beantworteten Fragen zur Abhängigkeit der Kollapsdynamik von der Geometrie der harmonischen Falle schaffen eine Vergleichs- und Verständnisgrundlage für weitere dipolare Kollaps-Experimente. Zum anderen dienen die Ergebnisse als Validierung der bestehenden Gross-Pitaevskii Molekularfeld Theorie [63] und tragen so zum generellen Verständnis dipolarer Kondensate bei. Die hier gewonnenen Einsichten helfen, die theoretisch vorhergesagten Eigenschaften dipolarer Quantengase — die Existenz eines Maxon-Roton Spektrums ähnlich dem superfluiden Heliums [64–68], strukturierte Wellenfunktion [69–72] deren Kollaps einen nicht-verschwindenden

Drehimpuls aufweisen [73], zwei-dimensionale anisotrope Solitonen [74], eine Vielzahl neuer Quantenphasen [75–78] etc. — auf ihre experimentelle Realisierbarkeit zu überprüfen und ggf. alternative Nachweismethoden zu entwickeln.

Schließlich wird die besondere Bedeutung der Forschung an DBEKen auch daran deutlich, dass, zeitlich parallel zu den hier vorgestellten Chrom-Experimenten, dipolare Alternativexperimente entwickelt werden. Zum einen gelang es 2006 (bzw. 2010) erstmalig atomares Erbium [79] (bzw. Dysprosium [80]) zu kühlen und in magnetischen Fallen zu fangen. Diese Atome weisen ein magnetisches Dipolmoment von $7\,\mu_\mathrm{B}$ (bzw. $10\,\mu_\mathrm{B}$) auf und könnten in Zukunft Chrom mit seinen $6\,\mu_\mathrm{B}$ als „dipolaren Riesen“ der atomaren Kondensate ablösen. Zum anderen bemühen sich verschiedene Arbeitsgruppen quantenentartete Gase mit elektrischen Dipolmomenten zu erzeugen. Viel versprechend erscheinen derzeit etwa hetero-nukleare Moleküle in ihrem jeweiligen rotations-vibrationalen Grundzustand (z.B. ^{40}K$-^{87}$Rb am NIST [81–85], ^{7}Li$-^{133}$Cs in Freiburg [86], oder ^{85}Rb$-^{133}$Cs in Yale [87]) und Grundzustandsatome mit schwach beigemischten Rydbergzuständen [88]. Während die hetero-nuklearen Moleküle ein elektrisches Dipolmoment von ca. einem Debye[2] aufweisen, besitzen Rydbergzustände einen zusätzlichen Faktor n^2, wobei die Hauptquantenzahl n leicht zwischen 30 und 40 liegen könnte. Diese Experimente würden erlauben den Bereich der stark korrelierten dipolarer Quantensysteme zu erforschen — mit selbst-organisierten Kristallen [89] und exotischen Quantenphasen [90, 91]. Im Gegensatz dazu dienen die hier gewonnen Erkenntnisse als Verständnisgrundlage für schwach-korrelierte DBEKe.

[2]Die „natürliche Einheit“ eines magnetischen Dipols ist das Bohr'sche Magneton $\mu_\mathrm{B} \stackrel{\mathrm{def}}{=} e\hbar/(2\,m_\mathrm{e})$ — das entspricht dem Dipolmoment eines Elektrons auf der ersten Bohr'schen Bahn (Bahndrehimpuls $\hbar$). Die „natürliche Stärke“ der magnetischen Dipol-Dipol Wechselwirkung (DDWW) ist somit $\mu_0{\mu_\mathrm{B}}^2$. Im Gegensatz dazu beträgt die „natürliche Einheit“ des elektrischen Dipols ein Debye $d = e\,a_\mathrm{B}$ — das entspricht dem Dipolmoment eines Elektron-Proton Paares, mit Abstand eines Bohr'schen Radius a_B. Die „natürliche Stärke“ der elektrischen DDWW beträgt somit d^2/ϵ_0. Deshalb ist die magnetische DDWW „natürlicherweise“ um den Faktor $[\mu_\mathrm{B}/(c_0\,d)]^2 \equiv [\alpha/2]^2$ kleiner als die elektrische, wobei $\alpha \approx 1/137$ die Feinstrukturkonstante und $c_0 \stackrel{\mathrm{def}}{=} 1/\sqrt{\mu_0\epsilon_0}$ die Lichtgeschwindigkeit im Vakuum bezeichnet.

List of publications

- Lahaye *et al.*: *"Strong dipolar effects in a quantum ferrofluid."* Nature **448**, 672 (2007).
- Koch *et al.*: *"Stabilization of a purely dipolar quantum gas against collapse."* Nature Physics **4**, 218 (2008).
- Lahaye *et al.*: *"d-Wave Collapse and Explosion of a Dipolar Bose-Einstein Condensate."* Physical Review Letters **101**, 80401 (2008).
- Metz *et al.*: *"Coherent collapses of dipolar Bose-Einstein condensates for different trap geometries."* New Journal of Physics **11**, 055032 (2009).

Contents

Abbreviations

Reference for abbreviations used in the text.

ac	alternating current (opposite to dc)
AOD	acusto-optical deflector
AOM	acusto-optical modulator
BEC	Bose-Einstein condensate (p. 19)
cw	continuous wave
DBEC	dipolar Bose-Einstein condensate
DDI	dipole-dipole interaction (p. 108)
FB	Feshbach (p. 47)
FT	Fourier transform (p. 105)
HF	high magnetic field
IGBT	insulated-gate bipolar transistor
MOSFET	metal-oxide-semiconductor field-effect transistor
MOT	magneto-optical trap (p. 39)
MT	magnetic trap
ODT	optical dipole trap (p. 39)
ODT1	horizontal optical dipole trap
ODT2	vertical optical dipole trap
OL	optical lattice (p. 39)
PDH	Pound-Drever-Hall (p. 44)
RF	radio frequency (p. 41)
TOF	time-of-flight (p. 35)
TF	Thomas-Fermi (p. 31)
ZS	Zeeman slower (p. 39)

Nomenclature of units and natural constants.

a_B	$5.3 \times 10^{-11}\,\mathrm{m}$	Bohr radius
k_B	$1.38 \times 10^{-23}\,\mathrm{J/K}$	Boltzmann constant
μ_0	$4\pi \times 10^{-7}\,\mathrm{Tm/A}$	permeability of free space
μ_B	$9.27 \times 10^{-23}\,\mathrm{J/T}$	Bohr magneton ($\mu_\mathrm{B}/h \approx 1.4\,\mathrm{MHz/G}$)
$\hbar$	$1.05 \times 10^{-34}\,\mathrm{Js}$	reduced Planck constant
E_h	$4.36 \times 10^{-18}\,\mathrm{J}$	Hartree energy
1 G	$10^{-4}\,\mathrm{T}$	conversion from Gauss to Tesla

Glossary of definitions.

characteristic dipolar length	a_{dd}	$\frac{\mu_0 \mu_{\mathrm{m}}^2 m}{12\pi\hbar^2} \sim 16\,\mathrm{a_B}$
(effective) s-wave scattering length[3]	a	
(effective) background scattering length[3]	a_{bg}	$\sim 100\,\mathrm{a_B}$
harmonic oscillator length	a_{ho}	$\sqrt{\hbar/(m\omega)}$
trap frequency in z-direction	$f_z \equiv \omega_z/(2\pi)$	
mean trap frequency	$\bar{\omega}/(2\pi)$	$(f_x f_y f_z)^{1/3}$
(effective) contact coupling strength[3]	g	$4\pi\hbar^2 a/m$
dipolar coupling strength	g_{dd}	$4\pi\hbar^2 a_{\mathrm{dd}}/m$
interaction coupling strength	g_α, g_{int}	
dipolar anisotropic function	$f_{\mathrm{dip}}(\kappa)$	see appendix A.5.5
scattering amplitude	$f_{\boldsymbol{k}}(\boldsymbol{r})$	see eq. (2.1b)
dipolar parameter	ϵ_{dd}	$\frac{g_{\mathrm{dd}}}{g} \equiv \frac{a_{\mathrm{dd}}}{a} \equiv \frac{\mu_0 \mu_{\mathrm{m}}^2 m}{12\pi\hbar^2 a}$
chemical potential	μ	
magnetic moment	$\boldsymbol{\mu}_{\mathrm{m}}$	$\mu_{\mathrm{B}} g_{\mathrm{J}} \boldsymbol{J}/\hbar$
Lande g-factor	g_{J}	
healing OR eff. interaction length	ξ	
2-body interaction range	r_0	$\sim 100\,\mathrm{a_B}$
cloud size	σ, ℓ	
Thomas-Fermi radius	R	
aspect ratio	κ	σ_ρ/σ_z
trap ratio	λ	ω_z/ω_ρ
(thermal) de-Broglie wavelength	λ_{th}	$\sqrt{2\pi\hbar^2/(m k_{\mathrm{B}} T)}$
spatial density	n	N/V
phase-space density	$\mathcal{D}$	$n\,\lambda_{\mathrm{th}}^3$
3-body loss coefficient	L_3	$\leq 2 \times 10^{-28}\,\mathrm{cm^6/s}$
2-body dipolar bare potential	$U_{\mathrm{dd}}(\boldsymbol{r})$	see eq. (A.15)
2-body dipolar pseudo-potential	$V_{\mathrm{dd}}(\boldsymbol{r})$	see eq. (A.15)
long-range part of $V_{\mathrm{dd}}(\boldsymbol{r})$	$V'_{\mathrm{dd}}(\boldsymbol{r})$	see section 2.2.2
2-body interaction pseudo-potential	$V_{\mathrm{int}}(\boldsymbol{r})$, $V_{\mathrm{int}}^{(2)}(\boldsymbol{r})$	(contact + dipolar)
long-range part of $V_{\mathrm{int}}(\boldsymbol{r})$	$V'_{\mathrm{int}}(\boldsymbol{r})$	
N-body dipolar mean-field potential	$\Phi_{\mathrm{dip}}(\boldsymbol{r})$, $\Phi_{\mathrm{dip}}^{(N)}(\boldsymbol{r})$	see appendix A.5.4
long-range part of $\Phi_{\mathrm{dip}}(\boldsymbol{r})$	$\Phi'_{\mathrm{dip}}(\boldsymbol{r})$	
N-body interaction mean-field potential	$\Phi_{\mathrm{int}}(\boldsymbol{r})$, $\Phi_{\mathrm{int}}^{(N)}(\boldsymbol{r})$	(contact + dipolar)
zero-point mean-field energy	E_{zero}	
dipolar mean-field energy	E_{dip}	
long-range part of E_{dip}	E'_{dip}	
interaction mean-field energy	E_{int}	(contact + dipolar)

"To study the abnormal is the best way of understanding the normal."
(William James)

1 Introduction and scientific background

The subject of this thesis is the experimental investigation of collapsed dipolar Bose-Einstein condensates consisting of neutral ^{52}Cr atoms. In particular, we observe and analyse the interaction induced instability and the associated temporal and spatial evolution of the condensate's density. The aim of this thesis is to contribute to the general understanding of dipolar quantum systems.

Starting point and basic principle of the performed experiments is a *Bose-Einstein condensate* (BEC). A BEC is a many-body system, which, from the prospect of quantum science, combines two advantages: On the one hand it is sufficiently simple to be understandable on a quantum level, while on the other hand it is sufficiently complex to accommodate many phenomena known from quantum matter in solid-state physics, which are not yet understood. For example, our knowledge of the microscopic or mesoscopic mechanisms which causes superfluidity [1], superconductivity [2], or anomalous transport of electrons in low-dimensional systems [3–6] is still very limited. This is mostly due to the fact that these properties are governed by strong correlations and quantum effects that are counter-intuitive to our classical experience. Therefore, in order to understand these phenomena it is reasonable to investigate the quantum world in simple model systems, which are free of complications (impurities, grain boundaries, random perturbations etc.). Quantum degenerate gases (bosonic [7–14] as well as fermionic [15–18]) are such model systems. They provide dynamically tunable handles to all system relevant parameters (external potential, inter-atomic interactions etc.), while being quasi-free of environmental defects. They are versatile quantum simulators [19] allowing to check proposed phenomena and to tailor novel states of quantum matter. Although they were so far mainly used to study long-lasting questions of condensed matter or many-body physics [20], their field of application is multi-disciplinary combining many modern research topics in such varied fields as atomic, molecular, solid-state, or high energy physics — reaching from tests of fundamental quantum mechanics to advances in material science.

During the last decade a diversity of BECs arose, with many distinguishable properties. The character of a BEC is essentially governed by three factors:
(1.) the dimension of the wavefunction,

[3]The short-range part of the dipole-dipole interaction is included, see eq. (A.15) (page 108).

(2.) the properties of the inter-atomic interactions[4], and

(3.) the interaction of the BEC with its environment.

In order to illustrate these three criteria, we define the "*standard condensate*" as follows:

(1.1) It is describable by a *scalar* wavefunction — i.e. the particles do not possess an internal degree of freedom.

(2.1) The inter-particle interaction is analogous to the *contact interaction* of hard-spheres, illustrated in fig. 1.1(a) — i.e. it is both

  (a) *short-range*, because two spheres interact only if they meet each other, and

  (b) *isotropic*, because a sphere does not feature a preferential direction.

(3.1) The isotropic external potential is either linear or harmonic (not shown in fig. 1.1). It entirely decouples the BEC from the environment and does not contain any defect.

If one of these properties is fundamentally altered, the BEC changes its character. Examples are (1.1) spinor condensates [27, ch. 4], (2.1) Efimov states [28–32] and (3.1) the coupling of a BEC to a photon [33, 34] or a nano-mechanical resonator [35, 36].

This thesis examines the special case of a *dipolar* Bose-Einstein condensate (DBEC). In general, a DBEC differs from the "standard condensate", as the two properties (1.1) and (2.1) get replaced by:

(1.1)→(1.2) It is describable by a *vectorial* wavefunction — i.e. the particles possess an internal degree of freedom (magnetic of electric dipole moment). Thus, if the spatial symmetry is not explicitly broken by an external (magnetic or electric) field, the dipoles might break it spontaneously.

(2.1)→(2.2) The particles interact not only *via* the contact interaction, but additionally through the *dipole-dipole interaction* (DDI), which is not only

  (a) *long-range*, but also

  (b) *anisotropic* — i.e. depending on the relative orientation of the two dipoles, it is either attractive or repulsive [37].

The first BECs-experiments with observable *dipolar effects* (performed at MIT using ^{23}Na and at NIST using ^{87}Rb) probed the vectorial character of the condensate's wavefunction [27, ch. 4]. Recently, these experiments have been extended in Hannover [38, 39] and Berkeley [40–43] (both using ^{87}Rb). In contrast, the experiments on ^{52}Cr in Stuttgart [44–46] and Paris [47, 48], on ^{39}K in Florence [49], and on ^{6}Li in Houston [50] use a magnetic field to fully polarise the dipoles. The vectorial character of the condensate's wavefunction is lost due to the explicit symmetry breaking. These experiments concentrate on the anisotropic character of the dipolar interaction [51, 52].

[4] Although the original idea of a Bose-Einstein condensate [21–24] examines an ensemble of non-interacting particles (the so-called *ideal gas model*), we use a modern definition of a Bose-Einstein condensate [25], where the particles interact with each other. Without interactions a BEC would neither be phase-coherent nor superfluid. Therefore, "[...] if the system truly were an ideal gas, there would be little left to study [...]" (Eric Cornell, [26, ch. 1.2]).

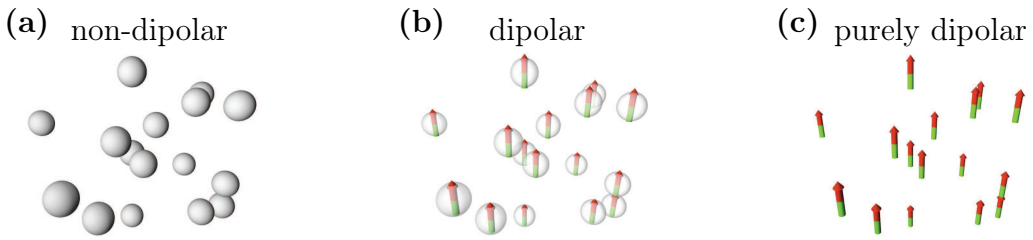

Fig. 1.1, Non-dipolar, dipolar, and purely dipolar BEC: Although the atoms in a BEC are indistinguishable and their wavefunctions are overlapping, the interactions can be illustrated as follows: A non-dipolar BEC (a) consist of hard spheres, which interact only when they bounce into each other. Therefore, the interaction is short-range and isotropic. In contrast, a purely dipolar condensate (c) consists of dipoles (here assumed to be magnetic), which interact solely *via* the long-range, anisotropic dipole-dipole interaction (DDI). Finally, a dipolar BEC (b) comprises both interactions, contact and DDIs. In general, the dipoles are non-polarised. Thus, the scalar wavefunction becomes a spinor [92].

This thesis is based on the studies of the anisotropic interaction and extends them by exploring the dynamics of *unstable* dipolar condensates. The complex dynamics of unstable condensates was already observed in ^{7}Li [53–56], ^{85}Rb [57–60] and in ^{40}K$-^{87}$Rb mixtures [61, 62]. However, these systems have negligible dipolar interactions. Incorporating dipolar interaction is desirable, because it alters the character of the instability: Depending on the external potential, the dipolar interactions either stabilise or destabilise the condensate. This modifies the temporal and spatial evolution of the condensate's density considerably. Therefore, the main objective of this thesis is to understand the occurrence of the instability and the associated dynamics. In particular, we analyse how the collapse dynamics depends on the trap geometry and examine its crossover from a cigar-shape (prolate) to a spherical trapping potential. In addition, we probe the phase-coherence of collapsed condensates. The comparison of the experimental and theoretical results will show, how the basic mean-field equations (Gross-Pitaevskii theory) for dipolar BECs have to be extended in order to describe collapsing condensates.

Within this background the relevance of this thesis is two-fold: On the one hand, it experimentally investigates the yet unexplored field of collapsing DBECs. It demonstrates how the collapse dynamics depends on the harmonic trap geometry and therefore provides the basis of understanding for other collapse experiments. On the other hand, the obtained results validate the existing Gross-Pitaevskii mean-field theory [63]. Thus, they contribute to the general understanding and deepen the scientific insight of dipolar quantum gases. This will help to experimentally realise the multitude of theoretical proposals for DBECs — the existence of a maxon-roton spectrum as in superfluid helium [64–68], structured wavefunctions [69–72] which lead to a collapse with non-vanishing angular momentum [73], two-dimensional anisotropic bright solitons [74], as well as many novel quantum-phases [75–78] etc.

Finally, the impact of working with dipolar quantum gases becomes apparent by noticing that, contemporaneous to the chromium experiments discussed in this thesis, alternatives are developed. Recently, erbium [79] and dysprosium atoms [80] were cooled and magnetically trapped. Their magnetic moments are $7\,\mu_\mathrm{B}$ and $10\,\mu_\mathrm{B}$, respectively, while chromium has a magnetic dipolar moment of "only" $6\,\mu_\mathrm{B}$. In addition, there are several groups trying to obtain a quantum degenerated gas of particles possessing electric dipole moments. Propitious candidates are hetero-nuclear molecules in their ro-vibrational ground-state (^{40}K$-^{87}$Rb at NIST [81–85], ^{7}Li$-^{133}$Cs in Freiburg [86], or ^{85}Rb$-^{133}$Cs at Yale [87]) or ground-state atoms with weakly admixed Rydberg states [88]. While the hetero-nuclear molecules would provide electric dipole moments of approximately one Debye[5], the dipole moment of atoms with weakly admixed Rydberg states has an additional factor of n^2, where the principal quantum number n could be easily 30 or 40. Therefore, they would allow to investigate the regime of strongly-correlated quantum systems, where dipolar interactions lead e.g. to self-organised crystals [89] and many new exotic quantum phases [90, 91]. In contrast, the results presented in this thesis belong to the regime of weakly-correlated dipolar quantum systems.

Outline

After a theoretical introduction to stationary DBECs in section 2, section 3 summarises how we experimentally generate the chromium condensate. Special emphasis is put onto the utilisation of a narrow Feshbach resonance in order to decrease the strength of the contact interactions. Section 4 is dedicated to the different types of instabilities found in dipolar condensates. It describes the phonon and roton instability, which are due to local density fluctuations. In addition, it compares our experimental observations to the predictions of the scaling instability model using a Gaussian wavefunction. The observed crossover dynamics from cigar-shape (prolate) to pancake-shape (oblate) collapsed DBECs are presented in section 5. Subsequently, in section 6, we analyse the phase-coherence of the collapsed cloud by inducing the collapse in several oblate condensates simultaneously and let them interfere. Finally, we summarise these findings in section 7 and give an outlook to further experiments.

[5]The "natural unit" of a magnetic dipole is the Bohr magneton $\mu_\mathrm{B} \stackrel{\mathrm{def}}{=} e\hbar/(2\,m_\mathrm{e})$, which is the dipole moment produced by an electron on the first Bohr orbit — its orbital angular momentum is $\hbar$. Therefore, the "natural strength" of magnetic DDIs is $\mu_0{\mu_\mathrm{B}}^2$. In contrast, the "natural unit" of an electric dipole is the Debye $d = e\,a_\mathrm{B}$, which is the dipole moment of an electron-proton pair separated by the Bohr radius a_B. Its "natural" DDI strength is d^2/ϵ_0. Hence, magnetic DDIs are "naturally" smaller than electric DDIs by the factor $[\mu_\mathrm{B}/(c_0\,d)]^2 \equiv [\alpha/2]^2$, where $\alpha \approx 1/137$ is the fine-structure constant and $c_0 \stackrel{\mathrm{def}}{=} 1/\sqrt{\mu_0\epsilon_0}$ is the speed of light in vacuum.

"Some say that the only thing that quantum theory has going for it, in fact, is that it is unquestionably correct." (Michio Kaku)

2 From perturbations to strong dipolar effects: Describing the ground-state of dipolar condensates

This section introduces the theory of dipolar condensates. Although we try to be as accurate as possible, its aim is not to derive the equations, but to make the performed experiments accessible to non-experts. Therefore, we emphasise the criteria needed for the theory to be valid and illustrate the physics by discussing simplifications.

The section is structured as follows: After a short introduction to Bose-Einstein condensates, we concentrate on inter-particle interactions. Summarising the scattering theory of two particle in the case of contact and dipole-dipole interactions, we develop the concept of pseudo-potentials. Then, using these 2-body results, the mean-field Gross-Pitaevskii equation is derived and its validity criteria are presented. Finally, we describe the Thomas-Fermi limit for dominant interactions and discuss the expansion dynamics if the condensate is released from the trap.

2.1 Bose-Einstein condensation: A purely statistical phase transition

Phase transitions happen in our every day lives. Popular examples are the melting of ice or the evaporation of liquids. Common to these, as well as to most other phase transitions, is that they are driven by the competition of different interactions: the system adjusts it short and long-range order to store energy in more favourable degrees of freedom (translation, vibration etc.). However, there are phase transitions which are purely statistical effects, happening although interactions are absent. Translating the quantisation of phase-space from photons [21, 22] to massive particles, Einstein was the first to realise [23, 24] that even non-interacting particles would occupy the same quantum state if they were only cold and dense enough.

A *Bose-Einstein condensate* is the phase, where a macroscopic fraction of the particles (atoms [7–11], molecules [93, 94], exciton-polaritons[6] [95] etc.) occupies the same ground-state (modern definition [25]). Therefore, in order to observe the phase transition take a system, where the number of energetically accessible states is approximately equal to

[6] A *polariton* is a half-light, half-matter quasi-particle. It arises if a photons couples strongly to "an excitation of the material", such that they are mixed. One possible "excitation of the material" is an *exciton*: It consists of a bound electron-hole pair in insulators or semiconductors. Thus, an *exciton-polariton* is a half-light, half-exciton quasi-particle.

the number of particles. Adding particles to such a system or lowering its temperature results in a degeneracy in phase-space[7]. Thus, the criteria for the condensation is that the phase-space density $\mathcal{D} \stackrel{\text{def}}{=} n\,\lambda_{\text{th}}^3$ becomes on the order of unity[8] [14, 63], where n is the spatial density and $\lambda_{\text{th}} \stackrel{\text{def}}{=} \sqrt{2\pi\hbar^2/(m k_{\text{B}} T)}$ is the thermal de-Broglie wavelength. Although Einstein used Bose's statistic, which takes the particles to be indistinguishable, note that the classical Boltzmann statistic, where the particles are assumed to be distinguishable, predicts condensation as well. However, since the indistinguishability reduces the number of distinct N-body states considerably[9], the transition occurs at the (classically counter-intuitive) critical temperature $T_c \sim N^{1/3}\,\hbar\omega/k_{\text{B}} \gg \hbar\omega/k_{\text{B}}$, where $\omega/(2\pi)$ is the trap frequency of the three-dimensional, spherical symmetric, harmonic confinement and $N \gg 1$ the number of particles [99].

For more than one decade, Einstein's prediction of condensing particles was thought as a purely academic model. Partly this was due to the lack of insight: Quantum theory was in its infancy, second-order phase transitions were misunderstood, and many-body theory was not developed, yet[10]. However, the main problem was to find a substance which does not liquefy or solidify during the cooling. An ideal gas at atmospheric pressure and room temperature has the spatial density $n = P/(k_{\text{B}} T) \simeq 10^{19}\,\text{cm}^{-3}$ and would condense at temperatures below[11] 4.2 K. The only element which is known to maintain weakly interacting at such temperatures is spin-polarised hydrogen [101–104]. Nevertheless, spin-polarised hydrogen is not the only condensate which is available today[12], it even was not the first. The trick is to cool the ensemble "fast enough" into a meta-stable gaseous state: not giving the atoms the time to relax to their absolute ground-state (which is a solid or liquid phase), but solely extracting the translational energy. Therefore, "fast enough" has to be understood with respect to the relaxation time.

In the experiments the only relevant relaxation processes are inelastic 3-body collisions, where two atoms form a molecule (first step towards a solid) and the third atom ensures

[7]The distinction between bosons and fermions was worked out by Pauli and Dirac in the end twenties. The proof that they have to obey different statistics was only given in 1940 [96].

[8]Approximating the momentum by $\bar{p}^2/(2\,m) \sim 3/2\,k_{\text{B}}\,T$, the condensation condition — that the number of states in phase-space $V\,\bar{p}^3/h^3$ is equal to the number of particles N — provides $\mathcal{D} \sim 1.4$. This differs from the exact result [97] only by a factor of 2.

[9]The indistinguishability of the Bose statistic [21, 22] reduces significantly the number of non-degenerate configurations compared to the Boltzmann statistic [12], [98, ch. 1.1.3], if the number of accessible micro-states is comparable to the number of particles. Hence, the Bose statistics increases the relative statistical weight of degenerate configurations: Assume N particles have to be distributed onto $M > N$ micro-states. In the case of distinguishable particles there are $M!/(M-N)!$ non-degenerate configurations, while for indistinguishable particles we additionally have to divide by $N!$, the number of particle permutations. Hence, if $M \sim N$, the Bose statistic weights the non-degenerate configuration, $\frac{M!}{N!(M-N)!} \sim 1$, equal to the fully degenerate configuration.

[10]A historical overview of the theoretical advances is given by Griffin [100], while experimental techniques and technologies are summarised in [26].

[11]Use $1 \sim \mathcal{D} \equiv n\,\lambda_{\text{th}}^3$ and $n = P/(k_{\text{B}}\,T)$, assuming that the pressure is kept constant. If the spatial density was kept constant, the ideal gas would condense at $T_c \approx 0.2\,\text{K}$.

[12]Condensed elements: ^{2}H [104], ^{4}He [105, 106], ^{7}Li [11], ^{23}Na [7], ^{39}K [107], ^{41}K [108], ^{40}Ca [109], ^{52}Cr [110] , ^{84}Sr [111, 112], ^{85}Rb [113], ^{87}Rb [8], ^{133}Cs [114], ^{170}Yb [115], ^{174}Yb [116], ^{176}Yb [117].

the energy and momentum conservation[13]. Hence, by using very dilute samples (densities on the order of $10^{14}\,\mathrm{cm}^{-3}$) 3-body collisions become unlikely[14], yielding lifetimes on the order of seconds. If the relaxation time to the absolute ground-state is large compared to the time needed to study the condensate, the atoms are said to be in a quasi-equilibrium state; being in thermal equilibrium (translational degree of freedom), although not in phase equilibrium (still a gas).

2.2 Describing binary interactions *via* pseudo-potentials

While interactions are most often negligible in a thermal gas, they become important for a condensate and even dominant[15] for $T \ll T_c$. Therefore, in order to describe condensates the ideal gas model (used to describe the thermal gas) should be replaced by some model including interactions. A dipolar condensate exhibits two kinds of 2-body interactions: the *short-range* contact and the *long-range* dipole-dipole interaction. Due to their different interaction ranges, they must be treated separately, which is done in the following sections.

2.2.1 2-body short-range interactions

This paragraph summarises the description of 2-body *short-range* interactions. Following closely the review given by Castin [99, ch. 3], the scattering theory for ultra-cold gases is developed and the concept of the so called *pseudo-potential* is introduced. Detailed discussions are given in [121, 122] and [119, ch. 5].

From section 2.1 we know that condensates are produced as extremely dilute samples in order to make 3-body collisions unlikely. Therefore, only 2-body interactions need to be considered, which simplifies the theory significantly: For two colliding particles the Schrödinger equation separates into a center-of-mass and a relative motion [123]. Transforming into the center-of-mass frame, only the latter is important. All parameters introduced below correspond to the relative motion, i.e. wavevector $\boldsymbol{k}$, position vector $\boldsymbol{r}$, wavefunction $\psi(\boldsymbol{r})$, and reduced mass m_{red}.

The description of the elastic scattering process of two particles considerably simplifies if the *asymptotic approximation* is used. It assumes that

1. the 2-body interaction is described by a *short-range* potential $U(\boldsymbol{r})$ [124]. A short-range potential has either a finite-range b (that is $U(\boldsymbol{r}) \neq 0$, only for $|\boldsymbol{r}| \leq b$) or

[13] We will encounter this relaxation process when discussing the dipolar collapse.

[14] The 3-body relaxation rate L_3 is defined by $\partial n/\partial t = -L_3 n^3$ for a homogeneous density [118, 119]. Typical values of L_3 range from few times $10^{-28}\,\mathrm{cm}^6/\mathrm{s}$ (for e.g. ^{23}Na or ^{52}Cr) to few times $10^{-30}\,\mathrm{cm}^6/\mathrm{s}$ (for e.g. ^{87}Rb). Again, the quantum statistic helps: It suppresses 3-body recombinations by a factor of 6 compared to the thermal Boltzmann statistic, see [118, 120] and [119, ch. 13.2].

[15] A simple argument is given in the Thomas-Fermi limit of a purely contact interacting condensate [119, ch. 6.2]. Here, the interaction energy per particle scales like $E_{\mathrm{tot}}/N \propto N^{2/5}$, which becomes large for macroscopic ground-state occupation numbers N.

an asymptotic power-law scaling $1/r^n$, where $n > 3$. Note that the dipole-dipole potential is *long-range*, because it scales like $1/r^3$.

2. the point of interest $\boldsymbol{r}$ must be in the far-field, satisfying $|\boldsymbol{r}| \gg r_0$ and $|\boldsymbol{r}| \gg kr_0^2$, where r_0 is the *characteristic range of the potential*[16]. While $r_0 = b$ for a potential with a finite-range b, the power-law potential $U(\boldsymbol{r}) = C_n/r^n$ provides $r_0 \stackrel{\text{def}}{=} (2\, m_{\text{red}}\, C_n/\hbar^2)^{1/(n-2)}$. It is on the order of the size of the last bound-state[17], which is typically[18] $r_0 \sim 100\, \text{a}_\text{B}$.

These two criteria ensure that most atoms are non-interacting at every instant in time, if the gaseous ensemble is sufficiently diluted — the mean particle distance $d_{\text{mean}} \sim n^{-1/3}$, where n is the spatial density, must be much larger than r_0. Assuming additionally that the internal states of the atoms are maintained throughout the scattering process — only a single scattering channel is considered — the stationary Schrödinger equation of the relative motion with eigenenergy $E = \hbar^2\boldsymbol{k}^2/(2m_{\text{red}})$, where $\boldsymbol{k}$ is the relative wavevector and m_{red} is the reduced mass, yields the outgoing far-field solution

$$\psi_{\boldsymbol{k}}(\boldsymbol{r}) \approx \psi_0(\boldsymbol{r}) + \frac{\text{e}^{ikr}}{r} f_{\boldsymbol{k}}(\boldsymbol{r}) \tag{2.1a}$$

with the ingoing wavefunction $\psi_0(\boldsymbol{r})$, the *scattering amplitude*

$$f_{\boldsymbol{k}}(\boldsymbol{r}) \stackrel{\text{def}}{=} -\frac{m_{\text{red}}}{2\pi\hbar^2} \int d^3r'\, \text{e}^{-ik\,\boldsymbol{e}_r\,\cdot\,\boldsymbol{r}'}\, U(\boldsymbol{r}')\, \psi(\boldsymbol{r}') \tag{2.1b}$$

the *bare 2-body interaction potential*[19] $U(\boldsymbol{r})$, and the unit vector $\boldsymbol{e}_r \stackrel{\text{def}}{=} \boldsymbol{r}/r$. In principle eq. (2.1) is solvable iteratively, however, the bare potential $U(\boldsymbol{r})$ is extremely complicated; it incorporates the van der Waals interactions as well as the complete atomic structure. Therefore, the rest of this section explains the concept of a pseudo-potential $V(\boldsymbol{r})$ for 2-body short-range interactions, which is an effective interaction potential. Being much simpler than the bare 2-body potential $U(\boldsymbol{r})$, it provides an easy expression for the scattering amplitude (2.1b).

In order to obtain the validity criteria for describing the inter-particle interactions *via* a pseudo-potential we will discuss the physics of the cooling process in some details. Thus, we consider the "low energy collisions" of two atoms with relative wavevector $k \sim 1/\lambda_{\text{th}}$. Starting with a thermal cloud at a few Kelvin, the thermal wavelength λ_{th} is on the order

[16] These conditions are reminiscent of the Fraunhofer diffraction criteria from linear optics [125].

[17] In the vicinity of a Feshbach resonance the characteristic range becomes macroscopic. A so called "halo-state" is present.

[18] For ^{52}Cr the C_6-coefficient was measured [126, 127] to be $(733 \pm 70)\, \text{E}_\text{h}\text{a}_\text{B}^6$, where E_h is the Hartree energy and a_B is the Bohr radius. Approximately the same result for r_0 is obtained, if the C_6-coefficient for ^{6}Li, ^{23}Na, ^{40}K, ^{87}Rb, or ^{133}Cs is used instead [128].

[19] We use "bare potential" as a synonym of the position dependent potential, containing *all* details of the 2-body interactions. This expression stems from quantum field theory, where it is also called non-renormalised potential.

of the Bohr radius and therefore smaller than the characteristic range r_0 of the 2-body potential. However, during the cooling process the temperature of the atoms decreases by several orders of magnitude. The condensate's temperature is typically $T_{\mathrm{BEC}} \leq 1\,\mu\mathrm{K}$, which corresponds to a de-Broglie wavelength on the micro-meter scale. Hence, during the cooling process the atoms resolve less and less details of the 2-body interaction potential. Details being smaller than $1/k$ are "coarse grained" — they are integrated and contribute only as their average to the effective 2-body potential [119, ch. 5]. If $k\,r_0 \ll 1$, all details are gone.

In addition, all partial waves, but the s-wave, freeze out during the cooling process. Since each partial wave with orbital angular momentum $L \neq 0$ has a centrifugal barrier, which lies typically at an inter-particle distance $R_L \gtrsim r_0$, it can only probe the short wavelength details of the 2-body interaction potential, if its energy is sufficient to overcome the barrier. Therefore, during the cooling of the cloud the partial waves are successively reflected from the centrifugal barrier; their contributions vanish [129, 130] — assuming that shape-resonances[20] are absent. The d-wave[21] typically vanishes at a temperature $T_{L=2} \approx \hbar^2 L(L+1)/(2mr_0^2 k_{\mathrm{B}}) \sim 1\,\mathrm{mK}$. Below $T_{L=2}$ the ensemble is said to be in the *ultra-low temperature regime*, only the s-wave scattering contributes to the scattering amplitude (2.1b). Hence, the outgoing wavefunction (2.1a) becomes spherically symmetric, even if the 2-body potential is not!

Mathematically, the term $\mathrm{e}^{-ik\,\boldsymbol{e}_r\,\cdot\,\boldsymbol{r}'}$ in eq. (2.1b) becomes unity and the scattering amplitude $f_{\boldsymbol{k}}(\boldsymbol{r})$ no longer depends on the scattering direction. Hence, in the far-field, at ultra-low temperatures and in the absence of a shape-resonance eq. (2.1a) is given by

$$\psi_{\boldsymbol{k}}(\boldsymbol{r}) \approx \frac{1}{\sqrt{V}} \left(\mathrm{e}^{i\boldsymbol{k}\,\cdot\,\boldsymbol{r}} - \frac{a}{r}\,\mathrm{e}^{ikr} \right) \tag{2.2}$$

where the ingoing wave is assumed to be a plane wave and the scattering amplitude is replaced by (minus) the *s-wave scattering length*, $\lim_{k\to 0} f_{\boldsymbol{k}}(\boldsymbol{r}) = -a$, to emphasise the *isotropy* of the scattering amplitude. In general, the scattering length a differs from the characteristic interaction range r_0.

Although the details of the bare interaction potential determine the scattering length a, their knowledge became irrelevant to describe interactions. This has three important consequences:

1. It simplifies the experimental effort: Instead of probing the bare 2-body potential at different inter-particle distances, it is sufficient to measure only the scattering length a. Choosing a model potential (often called pseudo-potential) which yields the measured scattering length, is enough to include interactions in our theory.

[20] If the potential supports a shape-resonance, the tunneling through the centrifugal barrier is non-negligible and higher partial waves must be considered [122].

[21] For two indistinguishable bosons the scattering cross-sections for all partial waves with odd angular momentum vanish, because the 2-body wavefunction is symmetric with respect to the exchange of particles [119, ch. 5.2].

2. Monte-Carlo simulations are possible: Since the condensate is only in a quasi-equilibrium state, Monte-Carlo simulations using the bare 2-body potential would not result in a description of the condensate, but of the true ground-state, which is either a liquid or a solid. Therefore, using a pseudo-potential without bound-states, makes exact numerical methods applicable.

3. The first-order Born approximation is valid, yielding a simple mean-field description: If the pseudo-potentials does not support a bound-state, the first-order Born approximation converges for all collision energies [131] and therefore yields a simple mean-field model[22]. In contrast, the bare potential poses a characteristic interaction range of $r_0 \sim 100\,\mathrm{a_B}$ and a depth of $U_{\min} \sim 10^3$ Kelvin, supporting many bound-states[23].

Due to all these complications the pseudo-potential approach is desirable — it can be understood as a low-energy, low-density renormalisation scheme. The simplest *pseudo-potential* describing 2-body short-range interactions is[24]

$$V_{\text{contact}}(\boldsymbol{r}) \stackrel{\text{def}}{=} g\,\delta(\boldsymbol{r}) \tag{2.3a}$$

with the so called *contact coupling strength*

$$g \stackrel{\text{def}}{=} \frac{4\pi\hbar^2}{m}\,a \tag{2.3b}$$

for indistinguishable particles of mass m. Calculating eq. (2.1b), where the bare 2-body potential is replaced by eq. (2.3), yields the exact result

$$\psi_{\boldsymbol{k}}(\boldsymbol{r}) = \frac{1}{\sqrt{V}}\left(\mathrm{e}^{i\boldsymbol{k}\,\cdot\,\boldsymbol{r}} - \frac{a}{1+ika}\frac{\mathrm{e}^{ikr}}{r}\right) \tag{2.3c}$$

for the outgoing, scattered wavefunction. Therefore, eq. (2.2) is valid only if $|k\cdot a| \ll 1$. In the opposite limit, so called *unitarity limit*, $|k\cdot a| \gg 1$, the scattering length in eq. (2.2) has to be replaced by $1/k^2$.

Summarising this paragraph, we found a very satisfying result: Fulfilling the asymptotic approximation, being at ultra-low temperatures and far from shape-resonances, the 2-body short-range interactions are described by a Dirac δ-distribution (2.3).

---

[22] Note that the pseudo-potential supports a single bound-state in the vicinity of a Feshbach resonance — in the region of positive scattering length [99, ch. 3.2.3].

[23] Bound-states are usually present if they are not inhibited by the zero-point energy (arising from Heisenberg's uncertainty principle). The zero-point energy prohibits bound-states if $E_{\text{zero}} \gg U_{\min}$, where $E_{\text{zero}} \sim \hbar^2/(2m_{\text{red}}\,r_0^2)$ for a confinement within a domain of radius r_0.

[24] Choosing the 2-body interaction operator such that its action is given by $\langle \boldsymbol{r}_1, \boldsymbol{r}_2|\hat{\mathrm{V}}_{\text{contact}}|\psi\rangle \stackrel{\text{def}}{=} g\,\delta(\boldsymbol{r})\left[\frac{\partial}{\partial r}\Big(r\,\psi(\boldsymbol{r})\Big)\right]_{\boldsymbol{r}=0}$, "repairs" $1/r$-divergences in the wavefunction [132, ch. 13.8]. As before, $\boldsymbol{r} \stackrel{\text{def}}{=} \boldsymbol{r}_2 - \boldsymbol{r}_1$ is the relative position vector and $\psi(\boldsymbol{r})$ is the relative 2-body wavefunction.

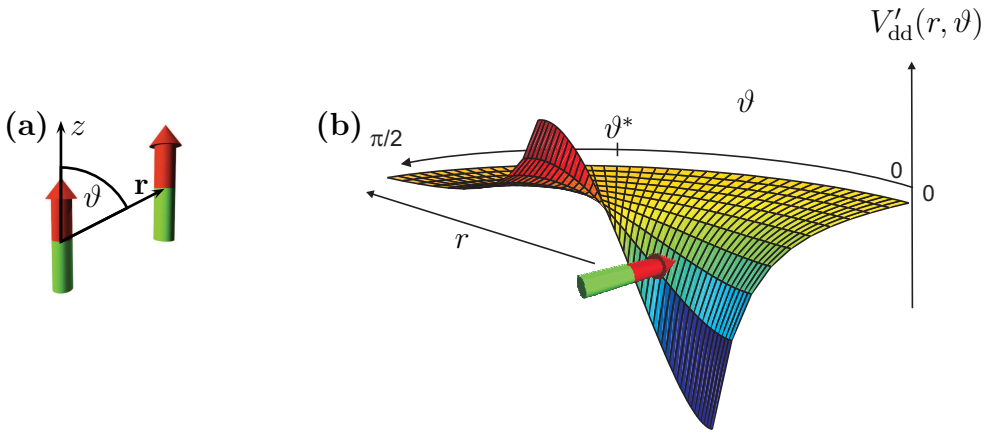

Fig. 2.1, Dipole-dipole interactions: The long-range part of the DDI depends on the relative distance r and the relative orientation ϑ of the polarised dipoles. Assigning the parameters as shown in (a), the dipolar interactions changes its sign at the *magic angle* $\vartheta^* \approx 55^\circ$: Being attractive ($V'_{\rm dd} < 0$) in the head-to-tail and repulsive ($V'_{\rm dd} > 0$) in the side-by-side configuration (b). (Taken from [136])

2.2.2 Dipole-dipole interactions

While the bare short-range potential of two atoms includes all kinds of interactions and therefore is extremely complicated, the bare dipole-dipole interaction (DDI) potential is given by a simple formula, see eq. (2.4) below. However, at ultra-low collision energies the scattering amplitude for short-range interactions turned out to be describable by a single, scalar parameter yielding the strength of the interaction. This is not the case for DDIs. Its scattering amplitude (2.1b) includes (in principle) all partial waves irrespectively of the collision energy — an ultra-low temperature regime for dipolar interaction does not exists. Therefore, the DDIs become much more complicated than the short-range interactions. Nevertheless, a simple approximation can be obtained. Details are given in [133–135].

The *bare magnetic dipole-dipole interaction potential* is given by[25] (appendix A.5.1)

$$U_{\rm dd}(\boldsymbol{r}) = \frac{\mu_0\,\mu_{\rm m}^2}{4\pi}\,\frac{1-3\,\cos^2\vartheta}{r^3} - \frac{2}{3}\,\mu_0\,\mu_{\rm m}^2\,\delta(\boldsymbol{r}) \tag{2.4}$$

if the point-like magnetic dipole moments[26] $\boldsymbol{\mu}_{\rm m} \stackrel{\rm def}{=} \mu_{\rm B} g_{\rm J}\,\boldsymbol{J}/\hbar$ are permanent[27] and polarised by a static external magnetic field[28], where ϑ is the angle between the polarisation direction

[25]Notation: $\mu_0 \stackrel{\rm def}{=} 4\pi \times 10^{-7}\,\mathrm{T\,m/A}$ is the permeability of free space.

[26]Notation: $\mu_{\rm B} \stackrel{\rm def}{=} e\hbar/(2m_e) \approx h\,1.4\,\mathrm{MHz/G}$ is the Bohr magneton and $g_{\rm J}$ is the Lande g-factor, where J is the total angular momentum. Note that ^{52}Cr does not have a nuclear spin.

[27]Induced dipole interactions, which are commonly known as van der Waals interactions, scale like $1/r^6$ (or $1/r^7$, if the retardation effect is included [137]). Hence, they are short-range and therefore subject of the previous section. Förster resonances for quasi-degenerate 2-body states are discussed in [138–140].

[28]The DDI energy (at the mean inter-particle distance) becomes equal to the Zeeman energy for magnetic fields on the order of 10 μG. Therefore, even the earth magnetic field, which is on the order of 0.5 G,

(in the following always chosen to be the z-axis) and the relative position $\boldsymbol{r}$ of the dipoles, see fig. 2.1(a). The *characteristic dipolar length* is

$$a_{\mathrm{dd}} \stackrel{\mathrm{def}}{=} \frac{\mu_0\,\mu_{\mathrm{m}}^2\,m}{12\pi\,\hbar^2} \tag{2.5a}$$

which defines the *dipolar coupling strength*

$$g_{\mathrm{dd}} \stackrel{\mathrm{def}}{=} \frac{4\pi\hbar^2}{m}\,a_{\mathrm{dd}} = \frac{\mu_0\,\mu_{\mathrm{m}}^2}{3} \tag{2.5b}$$

The numerical factor in eq. (2.5a) will become clear later — it is defined such that a three-dimensional, homogeneous dipolar condensate becomes unstable against local density fluctuations, if the ratio between the dipolar and contact coupling strengths

$$\epsilon_{\mathrm{dd}} \stackrel{\mathrm{def}}{=} \frac{g_{\mathrm{dd}}}{g} = \frac{a_{\mathrm{dd}}}{a} = \frac{\mu_0\,\mu_{\mathrm{m}}^2\,m}{12\pi\,\hbar^2\,a} \tag{2.5c}$$

exceeds unity, see section 4.1.1.

In order to describe dipolar interactions in a condensate we need to construct a dipole-dipole pseudo-potential such that its first-order Born approximation yields the *complete* scattering amplitude. This is a formidable task, accommodating plenty of difficulties. The origin of these difficulties is that all partial waves contribute to the scattering process[29], resulting e.g. in a logarithmically diverging scattering amplitude (2.1b) if the sample is non-polarised [124]. Such a scattering process is not describable by a pseudo-potential in general. Fortunately, if the sample is polarised, the scattering amplitude is finite [141] and it was shown in [133, 134] that the *dipole-dipole pseudo-potential* $V_{\mathrm{dd}}(\boldsymbol{r})$ is well approximated by the bare potential $U_{\mathrm{dd}}(\boldsymbol{r})$. Using eq. (2.4) in the first-order Born approximation yields the complete scattering amplitude within a few percent[30].

The "renormalised" DDI pseudo-potential, eq. (2.4), consists therefore of two terms: A short-range and a long-range term. Indicating with a prime that the short-range term is absorbed in the effective scattering length (discussed in the previous section), we denote the long-range term by $V'_{\mathrm{dd}}(\boldsymbol{r})$. However, one has to remember that the effective scattering length depends on the dipole-dipole interactions $a(\boldsymbol{\mu}_{\mathrm{m}})$. Although this dependency is usually weak it might become large in the vicinity of shape-resonances. In the following we will omit this dependency, the general case is discussed in [135].

---

is sufficient to fully polarise the sample. Hence, the wavefunction becomes a spinor only at ultra-low external magnetic fields [92]. Time-averaged potentials, resulting from a magnetic field rotating with frequency $f_{\mathrm{B}} \gg f_{\mathrm{trap}}$, where f_{trap} is the trap frequency, are discussed in [52, ch. 2.2].

[29] For short-range potentials $V(\boldsymbol{r}) \propto r^{-n}$ (where $n > 3$) the phase-shifts of all partial waves with angular momentum $L \neq 0$ vanish in the ultra-low temperature limit as $\lim_{k\to 0}\delta_L \propto k^{2L-1}$, while for bosonic dipole-dipole interactions $\lim_{k\to 0}\delta_L \propto k$ for *all* even and non-zero L, see [51, ch. 2.1].

[30] The multi-channel calculations were made for ^{7}Li, ^{39}K, ^{41}K, ^{85}Rb, and ^{87}Rb, but not for ^{52}Cr.

Since the subject of this thesis are many-body dipolar interactions (rather than 2-body, dipole-dipole interaction), we postpone the discussion about dipolar properties. Nevertheless, in order to contrast it with the pseudo-potential for 2-body short-range interactions we like to point out its most important characteristic: its anisotropy. Being partly attractive and partly repulsive, see fig. 2.1(b), the interaction between two dipoles depends on their relative orientation. In the following we will encounter this dependency regularly. Note that the long-range nature of the DDI is a prerequisite to obtain anisotropic pseudo-potentials.

2.3 Mean-field description of dipolar condensates

While the previous paragraphs discuss the 2-body interactions, we will concentrate on many-body interactions now. The simplest many-body model is the so called *mean-field model*. By neglecting all correlations, it maps the N-body problem onto a single particle problem[31]. The single test particle interacts with all the other particles in the condensate. Hence, the effective potential of the test particle is an average of the many 2-body interaction potentials over different distances. However, care has to be taken on how to include the interactions into this model. Fortunately, the pseudo-potential for the contact and DDI interactions were constructed such, that their first-order Born approximation coincide with the complete scattering amplitude. Therefore, the interactions are automatically included correctly.

2.3.1 Validity criteria of the N-body mean-field description

The goal of this section is to provide the validity conditions for the mean-field approximation to be a good description of the condensate. Details can be found e.g. in [99, ch. 3.2.2 & 3.3].

For a purely contact interacting condensate the criteria are phenomenologically obvious:

1. Large atom number $N \gg 1$: The basic idea of the mean-field potential is to average over *many* 2-body interaction potentials.
2. Low collision energy, $k|a| \ll 1$, and far from any shape-resonance: This ensures eq. (2.2), which is only valid for ultra-low temperatures.
3. Weak contact interactions $n^{1/3}|a| \ll 1$: Here "weak" should be understood in the sense of 2-particle correlations. Since the underlying idea of the mean-field model is to remove the corpuscular nature of 2-body collisions and replace it by a continuous potential, 2-body correlations are not included. Therefore, they must be negligible[32].

[31] Without correlations all particles are equivalent, and it is sufficient to describe a single test particle.

[32] The interactions might be "strong" in the sense that they dominate the quantum pressure term and strongly affect the physical properties of the system (see section 2.3.4).

The condensate should be describable by a single, macroscopic wavefunction[33]. The given criterion is deduced from the argument that weak interactions should leave the incident wavefunction almost unchanged. Equation (2.3c) satisfies this request if $|a|/r \ll 1$. On average, the inter-particle distance r is given by $n^{-1/3}$, where n is the spatial density, which leads to the stated condition. Therefore, it is a reformulation of the asymptotic approximation (see page 21), however, now for many particles.

How to incorporate long-range interaction into these criteria is to my knowledge an open question. For the case of dipolar interactions, I believe that the two last conditions should be extended by adding

4. Low collision energy with respect to DDIs and weak coupling of the partial waves: Relying on the numerical findings [133, 134], I am tempted to attribute $k\, a_{\mathrm{dd}} \ll 1$ to this condition. However, there is no analytic argument, why the dipole-dipole pseudo-potential is well approximated by eq. (2.4).

5. Weak dipolar interactions[34] $n^{1/3}\, a_{\mathrm{dd}} \ll 1$: The line of argument is analogous to the third condition. The wavefunction of a pair of dipoles is strongly influenced by the DDI for inter-particle distances $r \lesssim a_{\mathrm{dd}}$. However, this deformation is negligible [144, 145], because the dipoles are on average separated by $n^{-1/3} \gg a_{\mathrm{dd}}$.

Despite the challenge to find precise criteria for the dipolar mean-field model to be valid, it was shown that the mean-field model does accurately describe dipolar condensates if the above criteria are satisfied. This was done in [146, 147] by comparing it to numerically exact Monte-Carlo simulations. In addition, the authors showed that the dependency of the scattering length on the dipolar interaction strength, $a(\boldsymbol{\mu}_{\mathrm{m}})$, is negligible in the case of ^{52}Cr. It has to be taken into account, only if the characteristic dipolar length a_{dd} exceeds the characteristic range of the short-range potential r_0.

In the experiments presented in this thesis the condensate's temperature is on the order of 500 nK, the spatial density $n \leq 10^{15}\,\mathrm{cm}^{-3}$, the scattering length $|a| \leq 100\,\mathrm{a_B}$, and the dipolar characteristic length $a_{\mathrm{dd}} \approx 16\,\mathrm{a_B}$. This yields $k|a| \sim 0.05$, $n^{1/3}|a| \sim 0.05$, and $n^{1/3}\, a_{\mathrm{dd}} \sim 0.01$. Hence, the mean-field criteria are well satisfied.

2.3.2 Time dependent Gross-Pitaevskii equation

The aim of the previous sections was to prepare the basis for the mean-field description of dipolar condensates. We will now combine these parts and present the Gross-Pitaevskii equation (GPE). The GPE is a generalised Schrödinger equation in the sense that it

[33] In contrast, superfluid helium is strongly interacting [100, 142]: The depletion of the condensate is approximately 90%.

[34] This term is non-uniquely defined: Comparing the energy scales, the authors in [143] define "weak dipolar interaction" by $n\mu_{\mathrm{B}}\mu_{\mathrm{m}}^2/(4\pi) \ll \mu$, where μ is the chemical potential.

incorporates 2-body interactions using a mean-field approximation[35]. While we obtain the GPE starting with a quantum field theoretical model, alternative approaches are given e.g. in [119, 151].

In quantum field theory the "equation of motion" is given by the *Heisenberg equation* [152–154]

$$i\hbar\frac{\partial}{\partial t}\hat{\Psi}(\boldsymbol{r}) = [\hat{\Psi}(\boldsymbol{r}), \hat{\mathrm{H}}] \tag{2.6a}$$

for the field operator $\hat{\Psi}(\boldsymbol{r})$, where $\hat{\mathrm{H}}$ is the Hamilton operator. Whereas eq. (2.6a) is most general, we now specify it to the case of interest: The effective Hamilton operator describing a dipolar condensate confined in a harmonic trap, consisting of N particles[36], which interact solely *via* binary interactions, is given by [134, 155]

$$\hat{\mathrm{H}} = \int d^3r\, \hat{\Psi}^\dagger(\boldsymbol{r}) \left[\frac{\hat{\boldsymbol{p}}^2}{2\,m} + \frac{m}{2}\,(\boldsymbol{\omega}\cdot\hat{\boldsymbol{r}})^2 + \frac{1}{2}\,\hat{\Phi}^{(N)}_{\mathrm{int}}(\boldsymbol{r})\right]\hat{\Psi}(\boldsymbol{r}) \tag{2.6b}$$

with the canonical momentum[37] $\hat{\boldsymbol{p}}$, and the *N-particle interaction operator*

$$\hat{\Phi}^{(N)}_{\mathrm{int}}(\boldsymbol{r}) \stackrel{\mathrm{def}}{=} \int d^3r'\, \hat{\Psi}^\dagger(\boldsymbol{r}')\, V^{(2)}_{\mathrm{int}}(\boldsymbol{r}-\boldsymbol{r}')\, \hat{\Psi}(\boldsymbol{r}') \tag{2.6c}$$

where

$$V^{(2)}_{\mathrm{int}}(\boldsymbol{r}) \stackrel{\mathrm{def}}{=} \frac{4\pi\hbar^2}{m}\,a\,\delta(\boldsymbol{r}) + \frac{\mu_0\,\mu_{\mathrm{m}}^2}{4\pi}\,\frac{1-3\cos^2\vartheta}{r^3} \tag{2.6d}$$

is the 2-body contact and dipole-dipole pseudo-potential[38] for polarised magnetic dipoles. The field operator is normalised to the number of particles, $\int d^3r\,\langle\hat{\Psi}^\dagger(\boldsymbol{r})\,\hat{\Psi}(\boldsymbol{r})\rangle = N$, where $\langle.\rangle$ denotes the expectation value.

Next, the quantum correlations are neglected: Assuming that the number of particles in the condensate N is large, the correspondence principle suggests to describe the BEC by a classical, mesoscopic field $\Psi(\boldsymbol{r})$. This was first realised by Bogoliubov, who argued that the BEC density is not altered if a single particle is added or removed from the

[35] Formally, a Schrödinger equation must be linear in the wavefunction. Hence, the GPE is a generalisation, which explains peculiar phenomena, e.g. bifurcation [148, 149] or solitary solutions [74], which are not describable using the Schrödinger equation. An early review is given in [150].

[36] In quantum field theory the particle number is not fixed, but should be understood in the sense of a grand canonical ensemble: The condensate is coupled to a particle bath.

[37] Formally, the effect of the magnetic field must be included. This would be done by using the *kinetic momentum* $m\,d\hat{\mathbf{r}}/dt \stackrel{\mathrm{def}}{=} \hat{\mathbf{\Pi}} \stackrel{\mathrm{def}}{=} \hat{\boldsymbol{p}} - e\hat{\mathbf{A}}/c$ instead of $\hat{\boldsymbol{p}}$, where $\hat{\mathbf{A}}$ is the vector potential. In addition, the Pauli term $\hat{\mathrm{H}}_{\mathrm{pauli}} = \hat{\boldsymbol{\mu}}_{\mathrm{spin}}\cdot\boldsymbol{B}$ as well as the fine structure coupling $\hat{\mathrm{H}}_{\boldsymbol{LS}} = \frac{1}{2}\boldsymbol{\mu}_{\mathrm{spin}}\cdot\boldsymbol{B}_{\boldsymbol{LS}}$ — where $\boldsymbol{B}_{\boldsymbol{LS}} = \frac{\mu_0}{4\pi}\,\frac{Z\,e}{m r^3}\boldsymbol{L}$ and the 1/2 is the so called Thomas factor — need be added. However, we skip these complications and add a Zeeman energy at the end of the calculations. The crossover from the Zeeman to the Paschen-Back regime takes place at $B \sim 150\,\mathrm{T}$, far beyond our applied magnetic fields.

[38] The factor 1/2 in front of the interaction potential (2.6b) accounts for the double counting, due to $\boldsymbol{r} \rightleftarrows \boldsymbol{r}'$ using eq. (2.6c). The short-range part of the dipolar interactions is absorbed in the effective scattering length a.

condensate[36]. Using the perturbation ansatz

$$\hat{\Psi}(\boldsymbol{r}) = \Psi(\boldsymbol{r})\,\hat{\mathbb{1}} + \delta\hat{\Psi}(\boldsymbol{r}) \tag{2.6e}$$

with the *condensate's wavefunction*[39] $\Psi(\boldsymbol{r}) \stackrel{\text{def}}{=} \langle\hat{\Psi}^\dagger(\boldsymbol{r})\,\hat{\Psi}(\boldsymbol{r})\rangle^{1/2}$, and neglecting the fluctuations[40] $\delta\hat{\Psi}(\boldsymbol{r})$ completely, we obtain the *time dependent Gross-Pitaevskii equation* of a pure, dipolar condensate without spin degree of freedom[41]

$$i\hbar\frac{\partial}{\partial t}\Psi(\boldsymbol{r}) = \left(-\frac{\hbar^2}{2m}\boldsymbol{\nabla}^2 + V_{\text{trap}}(\boldsymbol{r}) + \Phi_{\text{int}}^{(N)}(\boldsymbol{r})\right)\Psi(\boldsymbol{r}) \tag{2.7a}$$

with the N-particle *mean-field interaction potential*[42]

$$\Phi_{\text{int}}^{(N)}(\boldsymbol{r}) \stackrel{\text{def}}{=} \int d^3r'\; V_{\text{int}}^{(2)}(\boldsymbol{r}-\boldsymbol{r}')\,|\Psi(\boldsymbol{r}')|^2 \tag{2.7b}$$

If particle losses due to 3-body collisions were added, this equation would "explain" all the experiments presented in this thesis. However, eq. (2.7a) is not very illustrative. Therefore, we will simplify it further in the next paragraphs.

2.3.3 Stationary Gross-Pitaevskii equation and energy functional

Before studying the dynamics of a collapsing dipolar condensate in section 5, we first have to understand how a condensate becomes unstable. To this end, we have to investigate the physics of stable, stationary dipolar condensates. Deriving the time independent GPE and discussing its energy contributions is done in the following section.

In order to obtain the stationary GPE we separate the time dependence of the wavefunction, $\Psi(\boldsymbol{r},t) = \psi(\boldsymbol{r})\,\mathrm{e}^{-i\bar{E}t/\hbar}$. Here $\psi(\boldsymbol{r}) \stackrel{\text{def}}{=} \Psi(\boldsymbol{r},t=0)$, and $\bar{E}$ is the mean energy per particle[43], which is identified with the chemical potential [158] $\mu \stackrel{\text{def}}{=} (\partial E_{\text{tot}}/\partial N)_{\text{S,V}} \approx E_{\text{tot}}/N$. Plugging this ansatz into the time dependent GPE (2.7a) yields the *stationary Gross-Pitaevskii*

[39] Here we choose the phase of the condensate's wavefunction and therefore spontaneously break the gauge symmetry [156], [157, ch. 1].

[40] Even at vanishing temperature the interactions lead to a *depletion* of the condensate [119]. This depletion is on the order of $\sqrt{n\,a^3}$ (for a purely contact interacting BEC) and therefore small for weak interactions (compare validity criteria of the mean-field theory in section 2.3.1).

[41] A polarised dipolar condensate is considered. As the directions of all spins are fixed by a strong external field, a single scalar wavefunction is sufficient to describe the condensate. Spinor (non-polarised) condensates are reviewed in [27, 92]. Rescaling the GPE as in [149] is very useful for numerical simulation, because it eliminates some free parameters.

[42] A mathematical introduction to dipole-dipole interactions and its mean-field potential is given in appendix A.5.

[43] The macroscopic wavefunction ψ is a 1-particle wavefunction in the sense that it describes a single test particle in the mean-field potential (see section 2.3). Therefore, we need to take the energy per particle.

equation [119]

$$\mu\psi(\boldsymbol{r}) = \left(-\frac{\hbar^2}{2m}\boldsymbol{\nabla}^2 + V_{\text{trap}}(\boldsymbol{r}) + \Phi_{\text{int}}^{(N)}(\boldsymbol{r})\right)\psi(\boldsymbol{r}) \tag{2.8}$$

The energy of the condensate's wavefunction $\psi(\boldsymbol{r}) \overset{\text{def}}{=} \langle \boldsymbol{r}\,|\psi\rangle$ is given by

$$\begin{aligned} E &\overset{\text{def}}{=} \langle\psi|\hat{\mathrm{H}}|\psi\rangle \\ &\overset{(2.6\text{b})}{=} \int d^3r \left[+\frac{\hbar^2}{2m}\left|\boldsymbol{\nabla}\,\psi(\boldsymbol{r})\right|^2 + \left(V_{\text{trap}}(\boldsymbol{r}) + \frac{\Phi_{\text{int}}^{(N)}(\boldsymbol{r})}{2}\right)\,|\psi(\boldsymbol{r})|^2\right] \end{aligned} \tag{2.9}$$

and called the *Gross-Pitaevskii energy functional* [119, 151]. The three different terms correspond to the kinetic[44], potential, and interaction energy.

Equation (2.9) will turn out to be very useful, because it provides an intuitive understanding of dipolar condensates. Although, in principle a dipolar condensate can be understood either in terms of its 2-body forces or its mean-field interaction energy, the "intuitive usage" of the former does not agree with the observed many-body phenomena of dipolar BECs. Only if we take into account that the relative positions of the atoms are not fixed, but that they are free to move, the intuition is "restored". However, since this constitutes an additional step, most of our understanding about dipolar condensates is based on energy arguments deduced from eq. (2.9). Hence, we will encounter the energy picture throughout the thesis — explaining why dipolar condensates are observed to elongate along the external field direction or why the collapse is initiated by a contraction in radial direction. Although the terms "attractive" and "repulsive" refer to forces, we will use them in the energy picture as synonyms for "energetically favourable" and "unfavourable" configuration, respectively.

2.3.4 Thomas-Fermi limit: dominant interactions

The solution $\psi(\boldsymbol{r})$ of the GPE (2.8) describes the stationary state of a dipolar condensate. However, due to the non-locality of the kinetic term and the non-local, non-linear interaction term, it is only numerically solvable. Thus, analytic expressions for limiting cases are valuable not only to check the numerics, but also to obtain intuitive insights. Two such limiting cases are simple to calculate: (*i*) the non-interacting gas, where the interactions are neglected and (*ii*) the so called Thomas-Fermi limit, neglecting the kinetic term. Both cases are extensively discussed in the literature (for the purely contact interacting gas [119, 157], and for the dipolar case see [159–161]), so we will concentrate on the most important aspects for the experiments. Furthermore, we assume a cylindrical symmetric trap, where the symmetry axis coincides with the polarisation axis of the dipoles, because the analytic formulae are simple only in this configuration.

[44] For a pure condensate this is equal to the quantum pressure, see section 2.3.5.

First, let us estimate at which point the interactions become dominant. Starting with a non-interacting condensate, the condensate's wavefunction is a Gaussian [152, ch. 2.3]. If weak interactions are added, the wavefunction is only perturbed by the interactions, but practically maintains its shape. The corresponding energies are (see appendix A.6.2)[45]

$$\frac{E_{\text{zero}}}{N\,\hbar\bar{\omega}} = \frac{a_{\text{ho}}^2}{4}\left(\frac{1}{\sigma_z^2} + \frac{2}{\sigma_\rho^2}\right) \tag{2.10a}$$

$$\frac{E_{\text{int}}}{N\,\hbar\bar{\omega}} = \frac{N}{\sqrt{2\pi}}\left(\frac{a_{\text{ho}}}{\sigma_\rho}\right)^2 \frac{a - a_{\text{dd}}\, f_{\text{dip}}(\kappa)}{\sigma_z} \tag{2.10b}$$

where σ_z and σ_ρ are the axial and radial sizes of the condensate (with respect to the polarisation axis), and $a_{\text{ho}} \stackrel{\text{def}}{=} \sqrt{\hbar/(m\bar{\omega})}$ is the *harmonic oscillator length* with mean trap energy $\hbar\bar{\omega} \stackrel{\text{def}}{=} \hbar(\omega_x\omega_y\omega_z)^{1/3}$. The *dipolar anisotropic function* $f_{\text{dip}}(\kappa)$ depends on the *aspect ratio*[46] $\kappa \stackrel{\text{def}}{=} \sigma_\rho/\sigma_z$. It is presented in fig. 2.2 and derived in appendix A.5.5.

In order to estimate at which point the interaction energy dominates the kinetic energy, we define the so called *Thomas-Fermi parameter* $\chi_{\text{TF}} \stackrel{\text{def}}{=} E_{\text{int}}/E_{\text{zero}}$ as their ratio, see eq. (2.10). Since the sign as well as the magnitude of the dipolar contribution depends on the aspect ratio κ, we need to distinguish three cases[47]

1. **Spherical symmetric density distribution** ($\sigma \stackrel{\text{def}}{=} \sigma_z = \sigma_\rho$)
   For a spherical symmetric density distribution the dipolar mean-field energy vanishes (see fig. 2.2). Thus, the Thomas-Fermi parameter for a purely contact interacting gas, $\chi_{\text{TF}} \sim N\,a/\sigma$, is recovered.

2. **Cigar-shape density distribution** ($\sigma_z \gg \sigma_\rho$)
   The dipolar anisotropic function becomes 1 and $\chi_{\text{TF}} \sim N\,(a - a_{\text{dd}})/\sigma_z$.

3. **Pancake-shape density distribution** ($\sigma_z \ll \sigma_\rho$)
   Here, the dipolar anisotropic function becomes -2 and the Thomas-Fermi parameter $\chi_{\text{TF}} \sim N\,\kappa^{-2}\,(a + 2a_{\text{dd}})/\sigma_z$.

If the Thomas-Fermi parameter is much larger than unity, the interaction energy dominates the zero-point energy. The assumption that the interaction is just a perturbation is obviously not valid any more, but rather the kinetic term should be skipped in eq. (2.8). Doing so is called the *Thomas-Fermi* (TF) *approximation*.

Deep in the three-dimensional Thomas-Fermi regime ($\chi_{\text{TF}} \gg 1$ and $\mu \gg \hbar\omega$) the dipolar mean-field interaction potential $\Phi_{\text{dip}}^{(N)}(\boldsymbol{r})$ can be calculated analytically [159]. It is a

[45] Recall: Dipolar characteristic length $a_{\text{dd}} \equiv \mu_0\mu_{\text{m}}^2\, m/(12\pi\hbar^2)$, see page 26.

[46] The parameter κ is defined as the ratio of the radial to the axial size of the condensate, with respect to the polarisation axis of the dipoles. Depending on the context, the size is either the $1/e$-radius of the Gaussian wavefunction or the Thomas-Fermi radius (see text). We distinguish between *aspect ratio*, which is the ratio of the cloud sizes, and the *trap ratio*, which is the ratio of the trap frequencies.

[47] The Thomas-Fermi parameter is not uniquely defined, see e.g. [160] for the definition in low-dimensional systems.

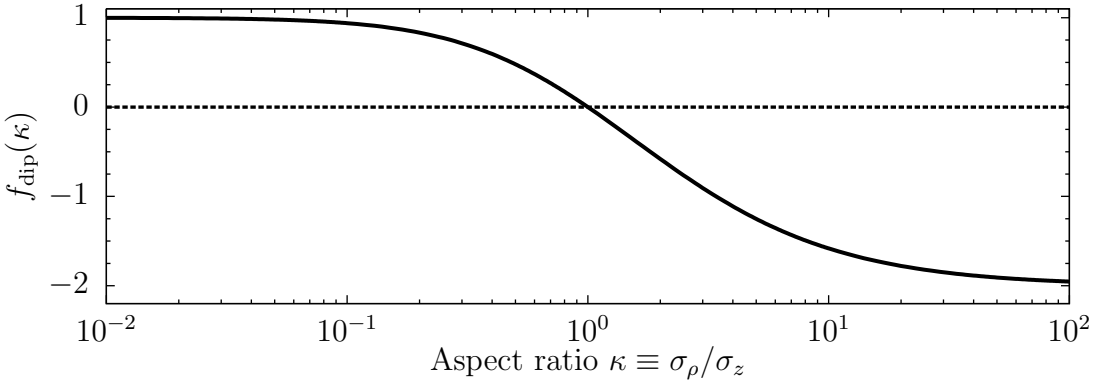

Fig. 2.2, Dipolar anisotropic function: $f_{\rm dip}(\kappa)$ is a monotonic decreasing function with $f_{\rm dip}(0) = 1$, crossing zero at $\kappa = 1$ (the dipolar mean-field interaction energy vanishes for isotropic density distributions), and asymptotically approaching $f_{\rm dip}(\infty) = -2$.

parabolic potential, see appendix A.5.6. Furthermore, in this regime the spatial density distribution is an inverted parabola [159, 161, 162]

$$n(\boldsymbol{r}) = n_0 \left[1 - \left(\frac{\rho}{R_\rho}\right)^2 - \left(\frac{z}{R_z}\right)^2\right] \tag{2.11}$$

inside the condensate, $(\rho/R_\rho)^2 + (z/R_z)^2 \leq 1$, and zero otherwise[48]. The peak density $n_0 \stackrel{\rm def}{=} 15\,N/(8\pi\,R_z\,R_\rho^2)$ is given by the atom number divided by the volume of the ellipsoid. For a spherically symmetric density distribution ($\kappa = 1$) the long-range part of the *Thomas-Fermi dipolar interaction potential* is given by[49] [159, 162, 163]

$$\Phi_{\rm dip}^{\prime\,({\rm TF})}(\boldsymbol{r}) = N\,\frac{\mu_0\mu_{\rm m}^2}{4\pi}\,\frac{1 - 3\,\cos^2\vartheta}{r^3}\,\frac{r^5}{R^5} \tag{2.12}$$

inside the condensate[50], $r \leq R$, where $R \stackrel{\rm def}{=} R_\rho = R_z$, and ϑ is the angle between $\boldsymbol{r}$ and the polarisation direction of the dipoles. Note that, just like the dipole-dipole potential $V_{\rm dd}'(\boldsymbol{r})$, eq. (2.12) is d-wave symmetric!

As in the purely contact interacting case, analytic expressions are obtainable for the different energy contributions — trapping potential and interaction energy (see section 4.2) — as well as for the chemical potential $\mu = n_0\,[g - g_{\rm dd}\,f_{\rm dip}(\kappa)] = (7/2)E_{\rm int}/N$.

[48]The physical density does not vanish abruptly, but smoothly on the scale set by the healing length, see eq. (2.14b) below.
[49]Use eq. (A.28a), page 108.
[50]The Thomas-Fermi dipolar potential outside of the condensate is give in [159, 163].

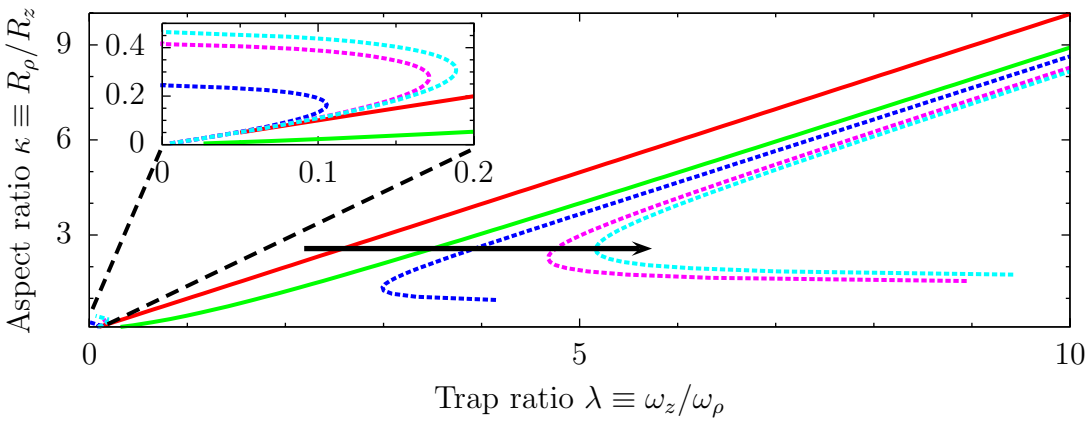

Fig. 2.3, Aspect ratio in the Thomas-Fermi regime: Decreasing the scattering length in a chromium condensate enhances the dipolar interactions effects. This is shown by plotting the real solution of eq. (2.13) for different scattering lengths (the arrow crosses the curves $\epsilon_{\rm dd} = 0, 1, 2, 10$, and 10^3 subsequently). While for $\epsilon_{\rm dd} \leq 1$ the condensate only elongates along the polarisation axis ($\lambda \geq \kappa$), the function $\kappa(\lambda)$ becomes multi-valued for $\epsilon_{\rm dd} > 1$, indicating the instability. The inset highlights the "small λ region".

However, the dipolar Thomas-Fermi radii R_ρ, R_z are coupled[51] by[52] [134, 159, 162]

$$\lambda = +\kappa \left(\frac{1 + 2\,\epsilon_{\rm dd} - \frac{3\,\epsilon_{\rm dd}\, f_{\rm dip}(\kappa)}{1-\kappa^2}}{1 - \epsilon_{\rm dd} + \frac{\kappa^2}{2}\,\frac{3\,\epsilon_{\rm dd}\, f_{\rm dip}(\kappa)}{1-\kappa^2}} \right)^{1/2} \tag{2.13}$$

where $\lambda \stackrel{\rm def}{=} \omega_z/\omega_\rho$ is the *trap ratio* — analytic expressions for the radii are given in [159]. Although eq. (2.13) is not simple, it demonstrates two important properties of dipolar condensates, see fig. 2.3. First, for $\epsilon_{\rm dd} > 1$ the function $\kappa(\lambda)$ develops an imaginary part (not shown) and becomes multi-valued. Both facts indicate the instability of the condensate. Second, while the aspect ratio κ of a purely contact interacting condensate ($\epsilon_{\rm dd} = 0$) is equal to the trap ratio λ, a dipolar condensate elongates along the polarisation direction, $\lambda \geq \kappa$. It becomes spherical ($\kappa = 1$) for[53] $\lambda = [(5 + 4\,\epsilon_{\rm dd})/(5 - 2\,\epsilon_{\rm dd})]^{1/2}$, which is real only if $\epsilon_{\rm dd} < 5/2$.

In order to estimate the relevance of the Thomas-Fermi regime for the experiment let us put some typical numbers: The standard chromium BEC is produced in a crossed optical dipole trap with mean trap frequency $\bar\omega/(2\pi) \approx 500\,$Hz, contains approximately 50 000 atoms, and has a (background) scattering length of $a \approx 100\,a_{\rm B}$. As $a \gg a_{\rm dd} \approx 16\,a_{\rm B}$, we use the Thomas-Fermi parameters for a spherical cloud, obtaining $\chi_{\rm TF} \sim N|a|/a_{\rm ho} \approx 400$.

[51] The coupling is due to the fact that the chemical potential is constant inside the condensate, see eq. (2.8).

[52] Recall: The dimensionless dipolar parameter $\epsilon_{\rm dd}$ is the ratio of the dipolar and contact interaction coupling strengths. It is given by $\epsilon_{\rm dd} \equiv a_{\rm dd}/a \equiv \mu_0\mu_{\rm m}^2 m/(12\pi\hbar^2 a)$, see page 26. If zero-point effects were neglected, a Gaussian wavefunction would satisfy eq. (2.13), too.

[53] Take the limit $\lim_{\kappa\to 1} f_{\rm dip}(\kappa)/(1-\kappa^2) = 2/5$ in eq. (2.13).

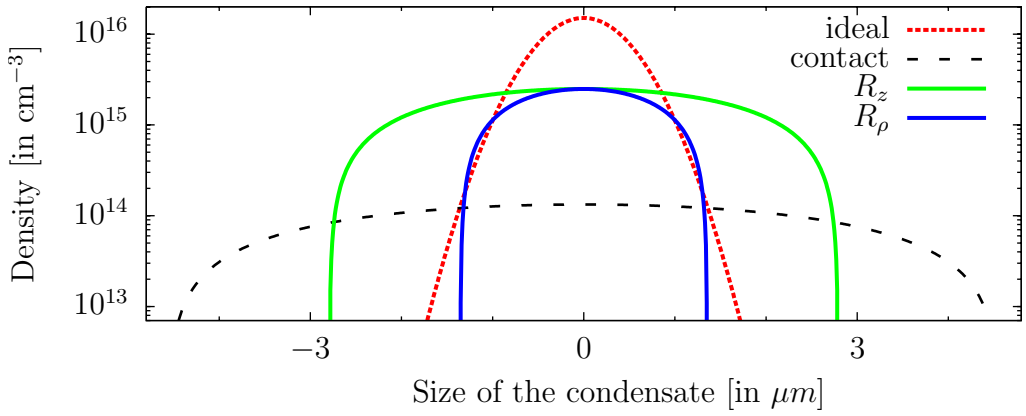

Fig. 2.4, Density profiles with and without interactions: The radial R_ρ and axial R_z Thomas-Fermi radii differ by approximately a factor of two for a chromium condensate consisting of $N = 20\,000$ atoms in a spherical harmonic trap with $\omega/(2\pi) = 500$ Hz and a scattering length of $a = a_{\rm dd} \approx 16\,a_{\rm B}$. The Thomas-Fermi density distribution for a purely contact interacting BEC (with $a = 100\,a_{\rm B}$) and the Gaussian distribution for an ideal gas are shown for comparison. Note that the reduction of the scattering length from $a = 100\,a_{\rm B}$ to $a_{\rm dd}$ reduces the volume of the condensate such that the peak density increases by a factor of ~ 10.

Thus, the Thomas-Fermi model describes the condensate very well. However, in order to induce the collapse the scattering length is reduced. Close to the instability point the atom number is on the order of 20 000 and the scattering length is $|a| \leq 10\,a_{\rm B}$, resulting in $\chi_{\rm TF} \leq 20$. Therefore, the Thomas-Fermi approximation breaks down [160] and the full GPE (2.7a) should be used instead.

Figure 2.4 shows the Thomas-Fermi density profile, eq. (2.11), for $\epsilon_{\rm dd} = 1$. The repulsive interactions between the atoms widens and flattens the density distribution compared to the non-interacting gas. However, the axial diameter is still only $\sim 5.5\,\mu$m, which is on the order of the spatial resolution of the experimental imaging system[54]. Therefore, it is necessary to expand the condensate first and then taking the image. Hence, the expansion process must be understood in order to extract information about the in-trap condensate from the expanded cloud. This is the subject of the following section.

2.3.5 Expansion dynamics

Releasing the condensate from the trap initiates the expansion dynamics. During the expansion, the interaction energy transforms into kinetic energy. Therefore, neglecting the kinetic energy completely (as in the Thomas-Fermi approximation) is certainly not wise. The trick is to separate the two kinetic contributions: The negligible in-trap zero-point

[54] In our experimental set-up the imaging system is a $1:1.12$ map of the atoms onto a CCD camera (PCO: "pixelfly qe"), which has a pixel area of $6.45 \times 6.45\,\mu$m^2.

energy and the velocity obtained during the expansion. In the following, we consider a condensate in the Thomas-Fermi regime, initially confined in a harmonic trap, from which it is released at time $t = 0\,\mathrm{s}$. A comprehensive discussion for purely contact interacting condensates is given in [99, 164], the dipolar case is explained in [161, 162].

The separation of the two contributions is done by expressing the condensate's wavefunction as an amplitude and a phase, $\psi(\boldsymbol{r}) = \sqrt{n(\boldsymbol{r})}\,\mathrm{e}^{iS(\boldsymbol{r})}$. Identifying the density variation $\boldsymbol{\nabla} n(\boldsymbol{r})$ with the zero-point energy (also called *quantum pressure*) and the phase variation $\boldsymbol{\nabla} S(\boldsymbol{r})$ with the velocity obtained during the expansion results in the hydrodynamic equations, see appendix A.5.8. If the characteristic length related to the quantum pressure,

$$\ell_{\mathrm{zero}} \stackrel{\mathrm{def}}{=} \left[(\boldsymbol{\nabla}^2\sqrt{n})/\sqrt{n}\right]^{1/2} \tag{2.14a}$$

which becomes $\ell_{\mathrm{zero}} \sim R$ in the Thomas-Fermi regime, is much larger than the *healing length* (characteristic length related to the interactions)

$$\xi \stackrel{\mathrm{def}}{=} \hbar/\sqrt{2\,m\mu} \tag{2.14b}$$

the quantum pressure can be neglected and the *classical hydrodynamic equations*

$$\boldsymbol{F}(\boldsymbol{r}) = m\frac{\partial^2}{\partial t^2}\boldsymbol{r} = -\boldsymbol{\nabla}\left(V_{\mathrm{trap}}(\boldsymbol{r}) + \Phi_{\mathrm{int}}^{(N)}(\boldsymbol{r})\right) \tag{2.15}$$

are obtained. Formally, they resemble a collisionless classical gas. While for a purely contact interacting condensate (in the TF regime) the acceleration is linear [99, 164] (both, the trap potential as well as the interaction potential, $g\,n(\boldsymbol{r})$, depend quadratically on $\boldsymbol{r}$, see eq. (2.11)), the expansion dynamics for a dipolar condensate is much more complicated. It is described by the scaling solution [161] (see appendix A.5.9 for misprints in the publication)

$$b_j(t) \stackrel{\mathrm{def}}{=} R_j(t)/R_j(0) \tag{2.16a}$$

$$\frac{d^2}{dt^2}b_j(t) = \frac{1}{b_x(t)\,b_y(t)\,b_z(t)}\,\frac{\omega_j^2(0)}{b_j(t)}\left(1 + \epsilon_{\mathrm{dd}}\,\mathcal{A}[\kappa, f_{\mathrm{dip}}, \frac{\partial\, f_{\mathrm{dip}}}{\partial\kappa}]\right) \tag{2.16b}$$

with the initial trap frequencies $\omega_j(0)/(2\pi)$, where $j = x, y, z$. The dipolar contribution $\epsilon_{\mathrm{dd}}\,\mathcal{A}[\kappa, f_{\mathrm{dip}}, \partial f_{\mathrm{dip}}/\partial\kappa]$ depends on the dipolar anisotropic function $f_{\mathrm{dip}}(\kappa)$ as well as its derivative $\partial f_{\mathrm{dip}}/\partial\kappa$. Therefore, the expansion becomes non-linear[55].

The non-linear expansion was used already in [44], where the authors observed the first evidence of "weak" ($\epsilon_{\mathrm{dd}} \approx 0.16$) dipolar effects in condensates. However, the dipolar expansion is not important to understand their findings, because they basically measured the change of the in-trap density distribution due to dipolar interactions. Therefore, the results remain qualitatively valid if the expansion would be linear. Only in [165], when

[55] Internal link to the program 'TOF-DipolarExpansion02.nb'.

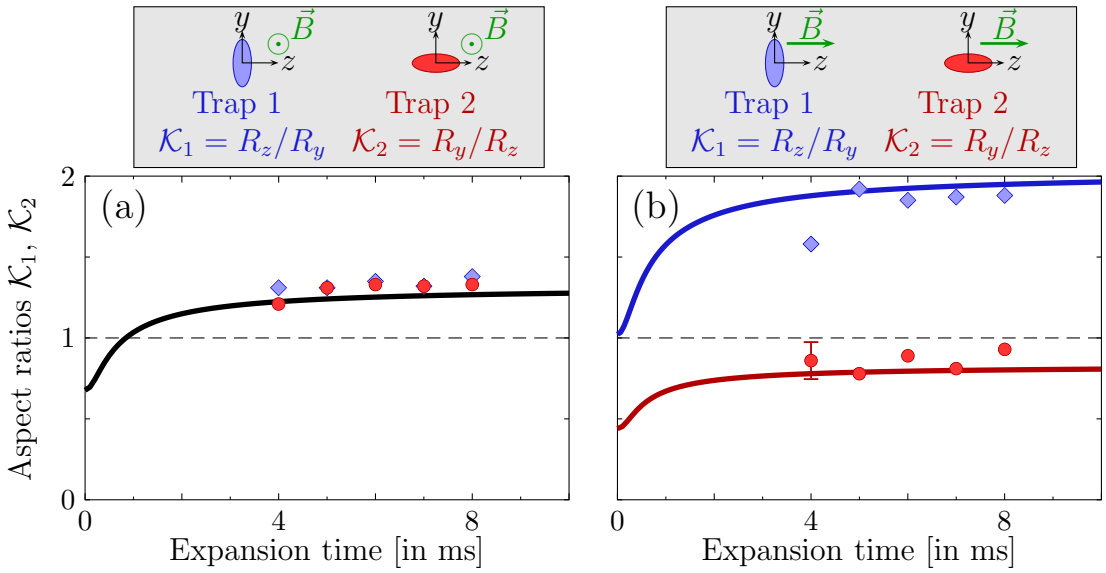

Fig. 2.5, Dipolar expansion dynamics: Measured aspect ratio for two traps (red and blue data points) with interchanged y and z trap frequencies (see sketches above graphs). The solid lines are the solutions of the hydrodynamic eqs. (2.16), with $\epsilon_{\mathrm{dd}} = 0.16$, $\boldsymbol{B} \parallel x$ in (a) and $\epsilon_{\mathrm{dd}} = 0.75$, $\boldsymbol{B} \parallel z$ in (b). The error bar in panel (b) shows the typical uncertainty over several runs. While in (a) both configurations yield the same aspect ratio, the aspect ratio in (b) differ, because the dipolar interactions break the spatial symmetry. Notably, $\mathcal{K}_2$ remains smaller than unity for all times. Hence, the dipoles inhibit the inversion of ellipticity. The trap frequencies of trap 1 are $(f_x, f_y, f_z) \approx (660, 370, 540)$ Hz. Both aspect ratios $\mathcal{K}_{1,2}$ are defined as the ratio of the short to the long condensate radius. (For details see [165].)

we observed the first "strong" dipolar effects in quantum degenerate gases, the dipolar expansion became essential: By reducing the scattering length, the contact interactions become almost equal to the dipolar interactions ($\epsilon_{\mathrm{dd}} \approx 0.75$). Therefore, the dipolar contribution to the expansion dynamics is enhanced such that the condensate does not invert its ellipticity during the free expansion, see fig. 2.5.

In the context of the dipolar collapse the described hydrodynamic expansion is only of secondary importance. If the scattering length becomes close to zero or later even negative, the total interaction energy (contact + dipolar) is not necessarily much larger than the quantum pressure. Hence, the assumption $\ell_{\mathrm{zero}} \ll \xi$ is not satisfied, the condensate is not in the Thomas-Fermi regime and the full GPE should be used instead. Nevertheless, it has a technical relevance for this thesis: In the experiment we need to calibrate the magnetic field which determines the scattering length. This is done by expanding the cloud at different magnetic field strengths, where the condensate is well within the Thomas-Fermi regime, and by fitting a calculated hydrodynamic expansion curve to the measured axial and radial radii. For details see section 3.3.2

"In the end we retain from our studies only that which we practically apply." (Johann Wolfgang von Goethe)

3 Generating a chromium condensate

This section describes the experimental set-up and sequence used to produce a ^{52}Cr condensate. Since the chromium-BEC project started more than a decade ago, many people contributed to and reported about the current set-up. Therefore, we mainly summarise their work [127, 136, 166–172]. An overview about techniques used to produce alkali condensate is given in [14, 173].

3.1 Experimental sequence

The experimental set-up consists of two joined vacuum chambers: the oven and the main chamber. In the oven chamber a high temperature effusion cell[56] produces the chromium vapor[57]. It operates at $T_{\text{oven}} \approx 1450°\text{C}$, which provides a pressure of approximately 10^{-9} mbar. At this pressure the lifetime of stored atoms would be less than a second, due to collisions with the background gases. In order to obtain lifetimes of several minutes the pressure must be reduced by approximately two orders of magnitude. This is achieved by a spin-flip *Zeeman slower* (ZS) [166, 174, 175], which acts as a differential pumping stage connecting the oven and the main chamber. In addition, the ZS decelerates and pre-cools[58] the atoms. This is necessary, because the maximum of the Boltzmann velocity distribution[59] is approximately 900 m/s, whereas the deepest atom traps are provided by the so called *magneto-optical trap* (MOT) [166, 173], possessing depths of a few Kelvin (corresponding to velocities of $10\,\text{m/s} - 40\,\text{m/s}$).

The level scheme[60] of ^{52}Cr is sketched in fig. 3.1. Using the differential Zeeman shift of the states $|^7\text{S}_3, m_\text{J} = +3\rangle$ and $|^7\text{P}_4, m_\text{J} = +4\rangle$ the ZS adapts the resonant absorption line

[56] CreaTec

[57] Distributor from 99.99+% chromium: "Goodfellow".

[58] *Deceleration* refers to the decrease of the velocity, while *cooling* emphasises the increase in phase-space density [176].

[59] Consider a beam of atoms, which escapes from the oven in z-direction. Their velocity distribution [173, ch. 5.2] is given by $f(v_z) = \frac{v_z^3}{2\,v_\text{th}^4} \exp\big(-\frac{v_z^2}{2\,v_\text{th}^2}\big)$, where $v_\text{th} \stackrel{\text{def}}{=} \sqrt{k_\text{B}T/m}$. Its average velocity is $v_\text{ave} \stackrel{\text{def}}{=} \langle v_z \rangle = \sqrt{9\pi/8}\,v_\text{th}$, the root mean square velocity $v_\text{rms} = 2\,v_\text{th}$, and the most probable velocity is given by $v_\text{mp} = \sqrt{3}\,v_\text{th}$ and stated in the text.

[60] We use the NIST nomenclature for the LS coupling: A *state* specifies all quantum numbers $|n\,\beta\,{}^{2S+1}L_\text{J}, m_\text{J}\rangle$. To emphasise this fact, we sometimes call it a Zeeman sub-state. A *level* $|n\,\beta\,{}^{2S+1}L_\text{J}\rangle$ refers to all states disregarding the magnetic quantum number m_J, and a *term* $|n\,\beta\,{}^{2S+1}L\rangle$ does not specify the quantum number of the total angular momentum J. Usually, we omit the main quantum number n and the spectroscopic shorthand notation β for low and high terms. The group of transitions are denoted *line component*, *line*, and *multiplet*, respectively.

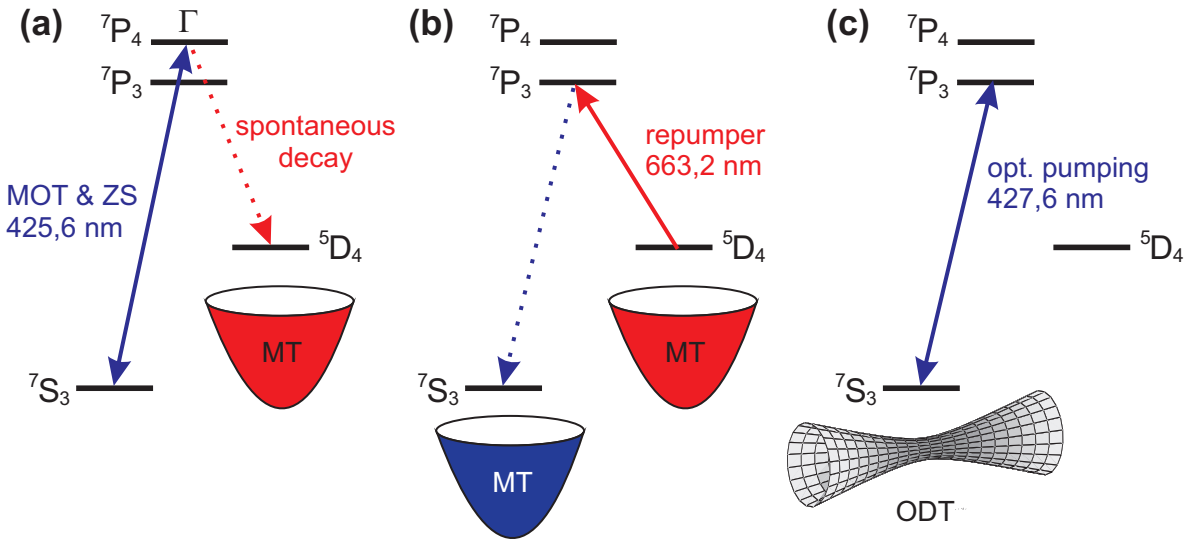

Fig. 3.1, Level scheme and experimental sequence: (a) The Zeeman slower (ZS) and the magneto-optical trap (MOT) operate between the ground-level[62] $^7S_3$ and the excited-level $^7P_4$, which has a linewidth of $\Gamma/(2\pi) \approx 5$ MHz. The atoms spontaneously decay with a probability of $1 : 250\,000$ into the $^5D_4$ level, where they are magnetically stored due to their large magnetic moments. (b) Only after the MOT light is switched-off, the meta-stable $^5D_4$ atoms are repumped to the $^7P_3$ level, from where they spontaneously decay. (c) Since dipolar relaxations become severe during the RF-cooling, the atoms are transferred into an optical dipole trap (ODT) and are optically pumped *via* the $^7S_3 \rightarrow {}^7P_3$ transitions to the lowest Zeeman sub-state.

component to compensate the decreasing Doppler shift due to the photon kicks [173]. Thereby, it decelerates all atoms having an initial longitudinal velocities $v \leq v_{\max} \approx 580\,\mathrm{m/s}$ to a final velocity $\sim 30\,\mathrm{m/s}$. The transversal velocity component of the atoms is hardly effected by the ZS[61]. Therefore, we first spatially filtered the transversal velocity component by apertures and subsequently cooled it by a *two-dimensional molasses* [173] at the entrance of the ZS [177, ch. A.1]. Collimating the atom beam, the two-dimensional molasses increases the loading rate of the MOT [178, 179] by approximately a factor of two.

The decelerated atoms reach the main chamber, where they are captured by the MOT[63] [182]. In order to obtain a large capture volume[64] the magnetic field gradients during

[61] Formally, the re-emission of the photons has to be described by a two-dimensional random walk.

[62] Note that ^{52}Cr does not satisfy Hund's law [180, 181]: Since the electronic $4s$-orbital has a non-vanishing overlap with the nucleus, it is energetically lower than the $3d$-orbital. Nevertheless, the ground-state of ^{52}Cr has the configuration [Ar] $4s^1\,3d^5$, which support a magnetic moment of $6\,\mu_B$, and not [Ar] $4s^2\,3d^4$.

[63] For reasons discussed below, we use a two-dimensional MOT plus a one-dimensional optical molasses, instead of a three-dimensional MOT.

[64] The MOT-light ($\lambda_{\mathrm{MOT}} \simeq 425\,\mathrm{nm}$) is red-detuned by $\delta_{\mathrm{MOT}}/(2\pi) \approx -2\,\gamma$ with respect to an atom at rest, where $\gamma \stackrel{\mathrm{def}}{=} \Gamma/(2\pi) \approx 5\,\mathrm{MHz}$ is the natural linewidth of the $^7P_4$ level. Its radial capture radius is

the MOT phase are weak. Therefore, for alkali atoms the magnetic force $\mu_\mathrm{m} \boldsymbol{b}'$ is not sufficient to compensate the gravitational force $m\,\boldsymbol{g}$. Atoms in states which are decoupled from the MOT light would be lost if they were not continuously repumped into the MOT circle. For chromium the situation is somehow inverted: Probably due to excited-state collisions, the number of atoms circulating in the MOT transition is limited to only $N_\mathrm{MOT} \sim 10^7$. This would not be sufficient to produce a condensate. However, due to the large magnetic moment of chromium, $6\,\mu_\mathrm{B}$, even a shallow magnetic field gradient is enough to magnetically trap the atoms. Therefore, we continuously load meta-stable $^5\mathrm{D}_4$ atoms into a cloverleaf *magnetic trap* (MT) [14, ch. 2.3.2]. Most of these meta-stable atoms are already cooled to the Doppler temperature $\hbar\,\Gamma/(2\,k_\mathrm{B}) \approx 120\,\mu\mathrm{K}$, because of the branching ratio of 250 000 : 1 between the electric dipole transition $^7\mathrm{P}_4 \to {}^7\mathrm{S}_3$ and the magnetic dipole transition $^7\mathrm{P}_4 \to {}^5\mathrm{D}_4$. In addition, we enlarge the magnetic trap volume and thus increases the number of trapped atom by using a two-dimensional MOT plus a one-dimensional optical molasses [183, 184], instead of a three-dimensional MOT. Decoupled from the MOT-light, approximately $2 \cdot 10^8$ atoms accumulate in the magnetically trapped $^5\mathrm{D}_4$ level, which is sufficient to produce a condensate.

After switching off the MOT-light, the *repump laser* ($\lambda \simeq 663\,\mathrm{nm}$) transfers the atoms from the meta-stable $^5\mathrm{D}_4$ level into the $^7\mathrm{P}_3$ level. From here most atoms spontaneously decay into the ground-level $^7\mathrm{S}_3$. However, this is not a good starting point for efficient evaporative cooling yet, because the elastic scattering rate is given by $\Gamma_\mathrm{el} \stackrel{\mathrm{def}}{=} n\,\sigma_\mathrm{at}\,v$, with the spatial density $n \propto \bar{\omega}_\mathrm{trap}^2$ (where $\bar{\omega}_\mathrm{trap}/(2\pi)$ is the mean frequency of the harmonic trap), the inter-atomic scattering cross-section σ_at, and the atom velocity v. Hence, Γ_el scales with $\bar{\omega}_\mathrm{trap}^2$ for a given temperature [26, ch. 2.10] and therefore the re-thermalisation time is long in soft trapping potentials. Thus, we first stiffen the magnetic potential by "adiabatically" compressing[65] the cloud. Subsequently, an axial[66] *Doppler shot* cools the sample to a temperature $T \sim 240\,\mu\mathrm{K}$ and a phase-space density $\mathcal{D} \sim 10^{-7}$. Beside its simplicity this cooling scheme is applicable to dense samples [185].

While for most alkali atoms these starting conditions would be sufficient to produce condensates by *radio-frequency cooling* (RF-cooling), this is not the case for chromium: The working principle of RF-cooling [119, 186–188] is to remove selectively only the hottest atoms from the trap. The remaining atoms re-thermalise at a lower temperature due to elastic collisions, while simultaneously their spatial density increases — because the effective trapping volume decreases. In the case of chromium the increase of the spatial density has a severe effect, because *dipolar relaxations* [170, 189, 190] are only negligible

given by $R_\rho = \hbar\,\delta_\mathrm{MOT}/(\Delta\mu\,b'_\rho) \approx 7.3\,\mathrm{mm}$, where $b'_\rho \approx 9.7\,\mathrm{G/cm}$ is the radial magnetic field gradient, and $\Delta\mu$ is the difference of the magnetic moments of the $^7\mathrm{S}_3$ and $^7\mathrm{P}_4$ levels.

[65] Violating the adiabaticity criterion $d\omega_\mathrm{trap}/dt \ll \omega_\mathrm{trap}^2$ does not have severe consequences, see e.g. [14, ch. 2.3].

[66] The atomic velocity components perpendicular to the propagation direction of the laser beam are cooled by re-absorbing spontaneously emitted photons [185].

for sufficiently low densities[67]. Removing preferably the coldest atoms — from the center of the trap, where the density has its maximum — dipolar relaxations are a heating process, which counteracts the RF-cooling.

The relaxation mechanism is the dipole-dipole interaction (DDI), which does not conserve the magnetic quantum number m_J of an atom (see appendix A.5.3). Since the atoms are initially in an excited Zeeman sub-state, m_J, they relax to energetically lower Zeeman sub-states, $m_{J'} < m_J$, to minimise their Zeeman energy[68], $\mu_B\, g_J\, m_J\, B$. While relaxations into the positive $m_{J'}$-states heat the sample, the atoms are lost from the magnetic trap if they reach a state with $m_{J'} \leq 0$. Compared to alkali atoms dipolar relaxations are strongly enhanced in chromium samples, because in its simplest form it scales with S^3, where S is the spin quantum number of a single atom [189].

In order to overcome the dipolar relaxations we only pre-cool the ensemble to a temperature of $T_{RF} \approx 40\,\mu$K using the RF-cooling technique[69], while simultaneously transferring them into a far-detuned *optical dipole trap* (ODT) — details are given in section 3.2.4 below. An ODT uses the ac-Stark shift to trap the atoms (see appendix A.1). Its trap depth is almost equal for all Zeeman sub-states. Therefore, the atoms can be stored in the ground-state $|^7S_3, m_J = -3\rangle$, where dipolar relaxations would cool[70] the sample. Using a prolate magnetic trap and a laser beam which propagates in horizontal direction — in the following called ODT1 — maximises the overlap between both traps and thus the transfer efficiency becomes 40%.

After switching off the magnetic trap, the atoms are optically pumped *via* the $^7P_3$ level into the ground-state. Then, the intensity of a second optical dipole trap — propagating in vertical direction, and called ODT2 — is increased, forming a dimple in ODT1. The dimple not only adiabatically changes the trap geometry and thereby increases the *local* phase-space density [176, 192, 193], but also provides high elastic scattering rates, which allows very efficient evaporative cooling [194].

The standard ^{52}Cr BEC is achieved by decreasing the intensity of ODT1 [110, 167]. However, in order to obtain a BEC with strong or even dominant dipolar effects we need to utilise a *Feshbach resonance* (FR) — introduced in section 3.3 below. Unfortunately, the FRs in chromium are narrow compared to most alkali atoms [128], which complicates the control of the scattering length. Furthermore, as only the 14$^{\text{th}}$ FR has a width, which is larger than 1 G, we need to cross the thirteen others. Hence, we need to avoid large

[67] Using the relaxation rate coefficient $\beta_{dr} = (2.5 \pm 0.5) \times 10^{-11}$ cm^3/s (measured at 27 G in [189]), the lifetime of a ^{52}Cr condensate would be less than 1 ms (assuming $n \sim 10^{14}$ cm^{-3}).

[68] The ground-state $|^7S_3, m_J = -3\rangle$ is a "strong magnetic field seeker", which is not trapable (in three-dimensions) with static magnetic fields [191].

[69] In order to minimise the heating rate it is very important to fine-tune the magnetic offset field to a value of ~ 35 mG during the RF-ramps [167, ch. 4.7.2].

[70] Although *demagnetization cooling* [46] was shown to be perfectly suited for chromium, it is not used at the moment, because it demands a ultra-high control of the magnetic field. However, it is planed to be implemented in an upcoming set-up, where a deeper ODT will be used. Allowing to stop the RF ramps earlier, the deep ODT relaxes the requirement on the magnetic field control.

densities during the crossings, because it would be accompanied by strong atomic losses and heating[71]. Therefore, instead of first producing the condensate and subsequently crossing the FRs, we split the forced evaporation into two parts: First, we pre-cool the ensemble in the crossed ODTs at a low magnetic field ($B \sim 10\,\mathrm{G}$), where the evaporative cooling is especially efficient, then we switch on the magnetic field to $B_{\mathrm{evap}} \approx 600\,\mathrm{G}$ crossing all the FRs, and finally we condense in high magnetic field [172].

A condensate at B_{evap} containing $N \approx 50\,000$ atoms is the starting point for all experiments presented in this thesis. After generating the BEC, we change the trapping potential by adjusting the powers in both ODTs and (if needed) by adding a one-dimensional *optical lattice* (OL) — a standing wave produced by two laser beams crossing under a "small" angle (see section 3.2.5 below). Finally, we decrease the contact interactions by ramping the magnetic field to a value B_{f} close to the FR [136]. We hold the atoms at B_{f} in the trap for a variable time, before releasing them [44, 165] and taking an absorption image after a time-of-flight. Although imaging the atoms at high magnetic fields B_{f} is in principle possible, it reduces the quality of the pictures, because the direction of B_{f} is perpendicular to the imaging axis, see [172, ch. C.3]. Therefore, after 4 ms of free expansion, we replace B_{f} by a field along the imaging axis, $B_{\mathrm{image}} \approx 11\,\mathrm{G}$, and take the absorption image on the $|^7\mathrm{S}_3, m_{\mathrm{J}} = -3\rangle \rightarrow |^7\mathrm{P}_4, m_{\mathrm{J}} = -4\rangle$ line component.

3.2 Laser systems

As discussed in the previous paragraph, several lasers are needed to obtain a chromium condensate. Since the system is continuously developed and extended, the following section is a status report of the current system. Its aim is not to provide an introduction but a technical overview. A comprehensive and detailed discussion of the optical set-up is given in [167].

3.2.1 Magneto-optical trap and Zeeman slower (425 nm)

The blue-violet 425 nm light for the MOT and the ZS constitutes the heart of the experiment. It is generated in three steps: (*i*) a diode-pumped solid state laser[72] produces approximately 15.5 W of green ($\lambda \simeq 532\,\mathrm{nm}$) light. This is used to (*ii*) pump a titanium-sapphire laser[73], which produces typically 2.8 W of infrared ($\lambda_{\mathrm{Ti:Sa}} \simeq 851\,\mathrm{nm}$) light. Then, the infrared light is (*iii*) coupled into a home build monolithic bow-tie cavity [171], where a Brewster cut lithium triborat (LBO) crystal generates $\sim 800\,\mathrm{mW}$ of the frequency doubled 425 nm light. The length of the bow-tie cavity is feedback controlled *via* a Hänsch-Couillaud lock [195], which does not need any frequency modulation.

[71] The rate of 3-body losses scales with a^4, if the scattering length a is "large" [20]. At a FR the scattering length diverges.

[72] Coherent, Verdi V18. Reliable replacement for an argon-ion laser (Coherent, Sabre R 25 TSM).

[73] Coherent, MBR110.

Tab. 3.1, Optimised light power for the experiment: The current set-up is compared to the "old" set-up, when the two-dimensional molasses cooling in front of the ZS was not implemented. The powers for the ZS, MOT, and molasses are the frequency shifted values, measured behind the AOMs.

	"old" power	current power[77]	AOM configuration
bow-tie cavity	600 mW	800 mW	no AOM (lock point)
ZS	150 mW	200 mW	no AOM (lock point)
MOT	130 mW	140 mW	double-pass
2d-molasses	0 mW	180 mW	single-pass

The absolute frequency of the Ti:Sa-light is locked by using the polarisation spectroscopy[74] technique [197, 198] in a chromium hollow cathode lamb[75] [199]. Since the 425 nm power level is very important to obtain stable atom numbers after the magnetic trap and because most of the light is consumed by the ZS (see tab. 3.1), the spectroscopy is locked to the ZS frequency, which is 200 MHz detuned with respect to an atom at rest. However, since the optimal frequency for the two-dimensional molasses (in front of the ZS) is approximately equal to the frequency of the MOT, it might be desirable to set the lock point between the frequency of the two and to shift the ZS frequency in a single pass AOM configuration in the future[76].

3.2.2 Repump laser (663 nm)

In former experiments two repump laser were used: one for the $^5D_4 \rightarrow ^7P_3$ transition ($\lambda \simeq 663\,\text{nm}$) and one for the $^5D_3 \rightarrow {}^7P_3$ line ($\lambda \simeq 654\,\text{nm}$). However, we currently only use the 663 nm laser. It is a home built external cavity diode laser producing $\sim 10\,\text{mW}$. The laser wavelength is stabilised *via* the external grating, which is locked onto an etalon[78] using the Pound-Drever-Hall (PDH) technique [201–203].

[74] We significantly improved the day-to-day stability by generating a low-noise spectroscopy error signal. In order to minimise the effect of pick-up noise we use a light balanced detection circuit and amplifying the signal *before* sending it to the lock-in amplifier [196, ch. 3].

[75] In contrast to alkali atoms the vapor pressure of chromium is negligible at room temperature. Therefore, we produce the chromium vapor by sputtering.

[76] The alignment of the ZS beam is less sensitive than the alignment of the MOT beams. Therefore, a single pass AOM configuration might be practicable. The 10 mW for the axial Doppler cooling, which is frequency shifted by $\sim +4.5\,\Gamma/(2\pi)$ with respect to the MOT frequency, could be generated by a double pass AOM configuration, which is fed by the frequency shifted ZS beam. Since the beam profile of the two-dimensional molasses is not too important, one could even use the zero-th order of the ZS-AOM in this configuration.

[77] Status: 04.2010.

[78] The etalon has a free spectral range of $c/(2\,\ell) \approx 75\,\text{MHz}$ and a thermal drift $\sim 2\,\text{MHz/h}$. Due to its bad finesse, it will be replaced in the near future by a Fabry-Perot similar to the one described in [200].

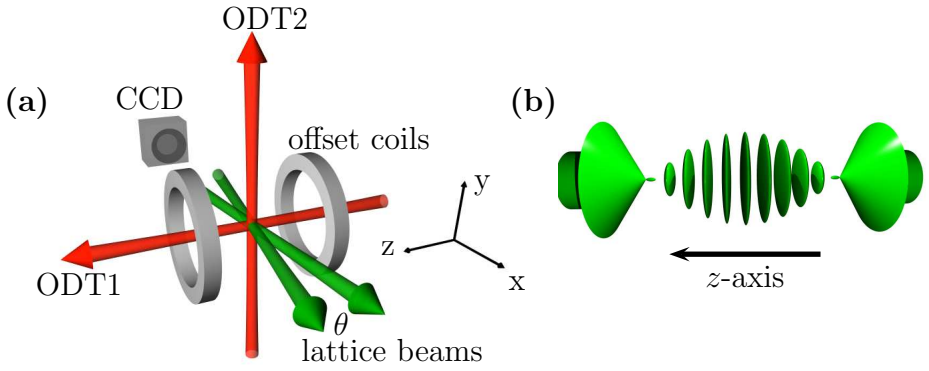

Fig. 3.2, Sketch of the experimental set-up: (a) The coordinate system is defined by the imaging axis (x-direction), the propagation direction of ODT2 (y-direction), and the offset coils (z-direction). While for the experiments presented in this thesis ODT1 propagated along the z-direction, in the current set-up it is shifted and tilted, propagating in the (x, z)-plane. The two green laser beams comprise an angle of $\theta_{\text{lat}} \approx 8.2°$. Their counter-propagating components form the one-dimensional optical lattice in z-direction with lattice spacing $d_{\text{lat}} = (7.4 \pm 0.2)\,\mu$m, which is shown in (b).

3.2.3 Optical pumping (427 nm)

In order to optically pump the atoms from the $|^7\text{S}_3, m_\text{J} = +3\rangle$ state *via* the $^7\text{P}_3$ level into the ground-state $|^7\text{S}_3, m_\text{J} = -3\rangle$ we start with $\sim 70\,$mW of infrared light ($\lambda \simeq 855\,$nm) produced by a home build external cavity diode laser[79]. Its wavelength is (grating) stabilised onto the same etalon as the repump laser *via* a PDH lock. The infrared light is fed into a home build bow-tie cavity [204], which's length is stabilised by a second PDH lock. By frequency doubling the seeded power, a potassium-niobate ($KNbO_3$) crystal produces approximately 10 mW of blue-violet light ($\lambda \simeq 427\,$nm).

3.2.4 Crossed optical dipole trap (1076 nm)

Since the ground-state $|^7\text{S}_3, m_\text{J} = -3\rangle$ is not trapable with static magnetic fields [191], but dipolar relaxations prevent us to obtain condensates in other Zeeman sub-states, we use an optical dipole trap (ODT) to produce the chromium BEC. The working principle of the ODT can be illustrated classically using the *Lorentz model* [198, ch. 2.6.2]: In this model each atomic transition is described as an eigenfrequency of a harmonic oscillator, the laser frequency as the driving force of the oscillations, and the spontaneous decay as damping process. The results do not differ from the quantum mechanical model of dressed eigenstates [173, 205]. While appendix A.1 summarises useful formulae and definitions,

[79] Toptica laser diode: "LD-0850-0100-1, SDL-5411-G1".

here we want to point that for a far-detuned laser beam[80] the *rotating wave approximation* [173, ch. 1.2] is not applicable. Of course, it is still true that the depth of the optical potential decreases with increasing detuning and so does the spontaneous scattering rate, however, in order to obtain the correct depth and scattering rates a numerical calculation including *all* atomic levels should be performed[81].

Figure 3.2 sketches the experimental set-up, which is used to generate the condensate. The two Gaussian laser beams ODT1 and ODT2 are produced by the same source: a continuous ytterbium fiber laser[82]. Its wavelength is $\lambda_{\mathrm{ODT}} \simeq 1076\,\mathrm{nm}$ and its linewidth (FWHM) $\Delta\lambda_{\mathrm{ODT}} \simeq 2.3\,\mathrm{nm}$. Both beams are linearly polarised, they cross under an angle of 90° such that their relative polarisation is perpendicular to each other. Their $1/e^2$-waists (of the intensities) at the position of the atoms are[83] $w_{\mathrm{ODT1}} \approx 30\,\mu\mathrm{m}$ and $w_{\mathrm{ODT2}} \approx 50\,\mu\mathrm{m}$, respectively. While ODT1 has a maximal power of 16 W and propagates in the horizontal direction[84] (taken to be the z-axis), ODT2 has a maximal power of 9 W and propagates in the vertical direction (taken to be the y-axis). Although not feedback controlled, the pointing stability of each beam is $\sim 1\,\mu\mathrm{m}$. This was achieved by using quartz lenses [136, ch. 3.2.3] as well as a two-frequency AOM drivers, which compensate the thermal lensing effect in the AOMs related to the change of RF-power [172, ch. A], [207].

3.2.5 One-dimensional optical lattice (1064 nm)

To obtain oblate (pancake-shape) traps we use a one-dimensional optical lattice [136, 208]. The optical lattice (OL) is produced by superimposing two laser beams of wavelengths $\lambda_{\mathrm{OL}} \simeq 1064\,\mathrm{nm}$ under an angle of $\theta_{\mathrm{lat}} \approx 8.2°$. This results in a measured lattice spacing of $d_{\mathrm{lat}} = \lambda_{\mathrm{OL}}/[2\,\sin(\theta_{\mathrm{lat}}/2)] = (7.4 \pm 0.2)\,\mu\mathrm{m}$, see section 6.1. In order to ensure phase-coherence the two beams are generated by the same continuous ytterbium fiber laser[85]. The linewidth (FWHM) of $\Delta f \leq 70\,\mathrm{kHz}$ provides a coherence length of $c/\Delta f \geq 4\,\mathrm{km}$. Both beams are linearly polarised, their polarisation axes being parallel (along the y-axis). Their $1/e^2$ waists (of the intensities) are $w_{\mathrm{OL}} = (110 \pm 5)\,\mu\mathrm{m}$ and the maximal power per beam is about 5 W. Using these parameters, the optical potential can be easily calculated numerically[86].

[80] Suppose all atoms are in the state $|\boldsymbol{\alpha}\rangle$. A laser is far-detuned, if it does not "connect" the state $|\boldsymbol{\alpha}\rangle$ to any other state $|\boldsymbol{\alpha}'\rangle$. More technical, if $|\omega_{\mathrm{laser}} - \omega_{\boldsymbol{\alpha},\boldsymbol{\alpha}'}| \approx |\omega_{\mathrm{laser}} + \omega_{\boldsymbol{\alpha},\boldsymbol{\alpha}'}|$ for all $\boldsymbol{\alpha}'$, where $\omega_{\boldsymbol{\alpha},\boldsymbol{\alpha}'}/(2\pi)$ is the atomic transition frequency $|\boldsymbol{\alpha}\rangle \to |\boldsymbol{\alpha}'\rangle$.

[81] Internal link to the program 'StarkShift.nb'.

[82] IPG: "VLR-100-LP".

[83] These waists where measured by detecting the laser power behind a razor plate on a translation stage. Alternatively, one could use the atoms as in [206].

[84] In the experiments presented in this thesis, the ODT1 beam was still propagating in z-direction. However, in the current set-up it is shifted and titled, because of a dark spot on the entrance window of the chamber. The current set-up is shown in fig. A.7 (page 126).

[85] IPG: "YLR-20-1064-LP-SF".

[86] Internal link to the program 'OpticalPotentialDepth.tgz', calculating the optical potential for the crossed ODT plus optical lattice.

3.3 Feshbach resonances

In section 2.2.1 we argued that the details of the bare 2-body interaction potentials are unimportant to describe the scattering process of two colliding ultra-cold atoms. All what matters is the scattering length, which is obtained by "averaging over the short wavelength details" of the bare potential. However, changing the details may result in a tremendous change of the scattering length and this is what happens in the vicinity of a Feshbach resonance. In the following we present a simple model to understand Feshbach resonances in chromium condensates. A detailed analysis is given in [20, 126–128, 209, 210].

3.3.1 Underlying idea of Feshbach resonances

Consider the elastic collision of two atoms. Again, by separating the center-of-mass and the relative motion of the atoms and by transforming into the center-of-mass frame, the scattering process is described by the motion of a single particle in a 2-body interaction pseudo-potential. In the simplest model the pseudo-potential is taken to be the *spherical square well potential*, defined as $V(r) = -\kappa^2 \left[1 - \Theta(r - b)\right]$, where κ^2 is the potential depth, and b is the potential range, with the Heaviside function $\Theta(r)$. The single particle describes the relative wavefunction of the two atoms. Changing the potential depth κ^2, results is a different kinetic energy inside the well. Therefore, the interaction time (the time the particle spends inside the potential well) depends on κ^2. As the scattering process is assumed to be elastic, the potential does not change the energy of the outgoing wavefunction — as in section 2.2 we are only interested in the asymptotic behaviour ($r \gg b$) of the wavefunction. Therefore, the change in the interaction time converts only in a phase shift δ, which is related to the scattering length a, see e.g. [123].

Changing the potential depth continuously, results in a resonance of the scattering length, whenever the potential supports a new bound-state. From a semi-classical picture this is reasonable: If the energy of a bound-state matches the kinetic energy of the incident particle, the particle transforms all its kinetic energy into potential energy. It stops inside the potential, the interaction time becomes infinite. However, if the energy of the bound-state slightly mismatches the kinetic energy, the "velocity" of the particle inside the potential strongly depends on the sign of the mismatch: If $E_{\text{bound}} < E_{\text{kin}}$ the velocity is small, while for $E_{\text{bound}} > E_{\text{kin}}$ it would be huge, because the bound-state is out of reach. Thus, the interaction time of the particle is influenced by the last bound-state inside the potential well. Therefore, small changes in the potential may tremendously change the scattering length. "All" we need to do is either changing the kinetic energy of the colliding atoms, or tune the details of the bare 2-body interaction potential such that the pseudo-potential changes dramatically.

In the case of ultra-cold atoms the kinetic energies of the particles are fixed to almost zero while the shape of the interaction potential is not changed easily. However, atoms are not point-like particles, but exhibit an internal structure. Therefore, instead of a single 2-body

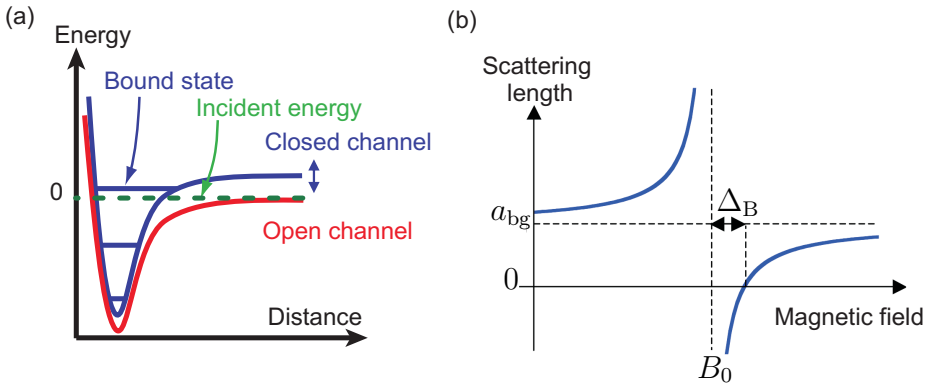

Fig. 3.3, Feshbach resonance: (a) The coupling between two molecular potentials allows to tune the scattering length. Whenever a bound-state matches the kinetic energy of the colliding atoms, a Feshbach resonance appears in the scattering length. (b) Behaviour of the scattering length in the vicinity of a magnetic Feshbach resonance, with width Δ_B and position B_0.

potential, they furnish a manifold of 2-body molecular potentials. The different molecular potentials are coupled and hence atoms approaching each other along one potential may be influenced by the other potentials. This is where the concept of Feshbach resonances in ultra-cold atom samples is founded.

Consider the two molecular potentials shown fig. 3.3(a). Starting the scattering process with two asymptotically free atoms — each of them in its internal 1-body ground-state[87] $|a\rangle$ and $|b\rangle$ — the 2-body internal molecular state is given by $|a,b\rangle$. The molecular potential associated with this state is called *open scattering channel* $V_{\text{open}}(r)$. It asymptotically approaches zero, $V_{\text{open}}(\infty) = 0$, see fig. 3.3(a). The second molecular potential, associated with a different internal 2-body structure $|c,d\rangle$, is called *closed scattering channel* $V_{\text{closed}}(r)$, because it is asymptotically forbidden, $V_{\text{closed}}(\infty) > E_{\text{kin}}$. The coupling between the two channels is due to some interactions, which mixes the states $|a,b\rangle$, $|c,d\rangle$. While in the case of alkali atoms this interaction is mainly "exchange energy", it is the DDI in the case of ^{52}Cr, see appendix A.5.3. Therefore, while the two atoms always start their scattering process in the open channel (red curve), the coupling admixes states which evolve in the closed channel (blue curve). By changing the energy *difference* between the two channels, the closed channel is lifted or lowered, which results in tuning its bound-states into resonance. The tuning is most often done *via* the relative Zeeman energy $\Delta\mu\, B$ of the two molecular potentials, where $\Delta\mu \stackrel{\text{def}}{=} \mu_{|c,d\rangle} - \mu_{|a,b\rangle}$ is the difference of the magnetic moments associated with the potentials[88].

[87] The atoms do not have to be distinguishable. Here our aim is to obtain a very simple description.
[88] An optical Feshbach resonance was used e.g. in [211].

In the vicinity of an isolated, magnetic Feshbach resonance the scattering length has the simple form [20, 128, 209, 210]

$$a(B) = a_{\mathrm{bg}} \left(1 - \frac{\Delta_{\mathrm{B}}}{B - B_0}\right) \tag{3.1}$$

where a_{bg} is the background scattering length, B_0 is the "position" of the resonance, and Δ_{B} is its width (see fig. 3.3b). "Broad" Feshbach resonances are found, if the coupling between the molecular potentials is "strong" and if the difference of their magnetic moments $\Delta\mu$ is "small". A "small" background scattering length a_{bg} is desirable, if one is interested in fine-tuning $a(B)$ around the zero-crossing. In the performed experiments we utilised a Feshbach resonance at the position $B_0 \approx 589.1\,\mathrm{G}$, which poses a width of $\Delta_{\mathrm{B}} \approx 1.4\,\mathrm{G}$. The background scattering of ^{52}Cr is $a_{\mathrm{bg}} \approx 100\,\mathrm{a_B}$.

3.3.2 Calibrating the scattering length

In the experiment we calibrate the scattering length by calibrating the current in the offset coils. Using the atoms as a probe, this is done in three steps (see as well [136, ch. 4.4.2]):

1. The condensate is freely expanded for $\sim 8\,\mathrm{ms}$ at different magnetic fields, before an absorption image is taken. From the absorption image we deduce the axial $R_z(B)$ and radial $R_\rho(B)$ Thomas-Fermi radii as well as the condensate's atom number N. Each magnetic field data point is typically averaged five times.

2. We calculate the Thomas-Fermi radii after the expansion for different scattering length $R_\rho(a)$ and $R_z(a)$ using the dipolar hydrodynamic[89] eq. (2.16) and (A.42).

3. Comparing both data sets yields the scattering length as a function of magnetic field $a(B)$, see fig. 3.4.

In principle the procedure is straight forward. The only constrain one needs to satisfy is that all data points are within the Thomas-Fermi regime. Otherwise the hydrodynamic equations becomes invalid (see section 2.3.5) and the solution of the full GPE must be used instead. Well within the Thomas-Fermi regime the contact interactions dominate the expansion dynamics. Therefore, we will start the discussion by considering a purely contact interacting condensate.

After a sufficient long expansion times ($t \gg 1/f_{\mathrm{max}}$, where f_{max} is the largest trap frequency) the atoms are not interacting any more and the initial interaction energy (per particle) $\mu \propto (N\,a)^{2/5}$ is completely transformed into kinetic energy $m\,(v^*)^2/2$. The cloud expands like an ideal gas $R(t) = R_0^* + v^*\,t$, where R_0^* is a constant (*not* the in-trap radius) and v^* is the asymptotic expansion velocity in the center-of-mass frame.

[89] Internal link to the program 'TOF-DipolarExpansion.nb'.

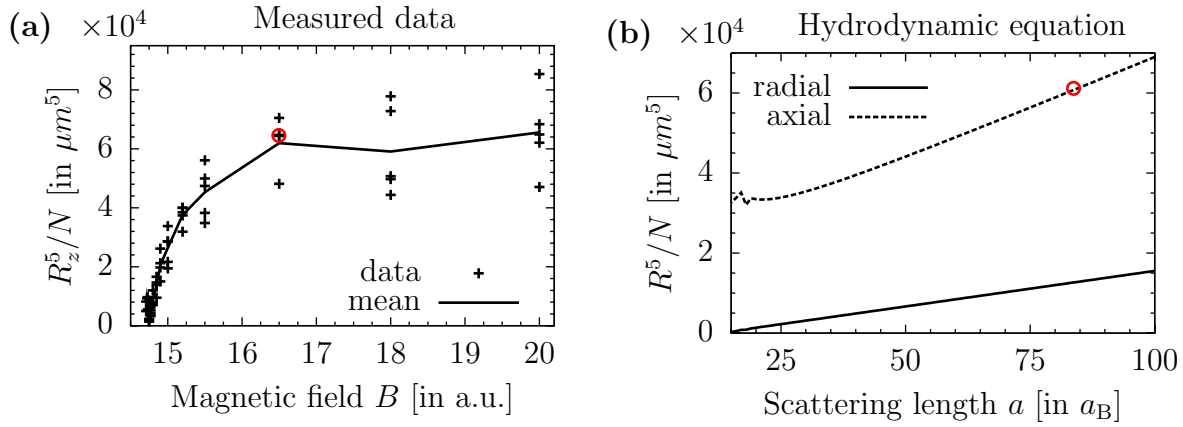

Fig. 3.4, Calibration of the scattering length: (a) In the experiment neither the absolute position of the Feshbach resonance B_0, nor the magnetic step size between the data points are known accurately. The dependency $a(B)$ is obtained by comparing each measured Thomas-Fermi radius R (shown in a) to a simulated hydrodynamic expansion (shown in b) — this maps the circled data point in (a) onto that in (b). The shown data is for $N = 30\,000$ and a trap with frequencies $(f_x, f_y, f_z) \approx (650, 380, 520)$ Hz where $\boldsymbol{B} \parallel \boldsymbol{e}_z$.

Due to the conservation of energy, the asymptotic velocity is proportional to $\mu^{1/2}$, thus $R(t) \propto (N\,a)^{1/5}\,t$. The dipolar contribution to the expansion should be visible as a derivation of this behaviour.

This motivated us to take $r_j(a) \stackrel{\text{def}}{=} R_j^5(a)/N$, where $j = y, z$, as the relevant parameters. Figure 3.4(b) presents the simulated axial and radial $r(a)$ functions after an expansion of 8 ms. It shows that taking the axial Thomas-Fermi for the calibration has two advantages compared to the radial radius[90]: (*i*) its absolute size is larger (if a "oblate" $\kappa_{y,z}$ column density is used) — therefore the finite resolution of the CCD camera[91] has less influence — and (*ii*) its slope is steeper, which allows to distinguish small differences in a and therefore yields a higher precision. However, it is less linear[92]. Therefore, we cross-checked the calibration by evaluating both radii, the radial and the axial. While for the axial radius each measured data point must be compared to the simulation, the linearity of the radial Thomas-Fermi radius allows to approximate $r_y(a) \approx m\,a + b$, which yields the simple expression $a(B) \approx \left(R_y^5/N - b\right)/m$ to calculate the scattering length from the measurement. Both methods provide the same result, within the error bars.

[90] Two remarks: First, the arguments get inverted if a prolate trap is used. Second, if the shot-to-shot fluctuations in the atom number N are severe, the aspect ration $\kappa \equiv R_y/R_z$ should be taken instead [45].

[91] The radial Thomas-Fermi radius varies from $\sim 70\,\mu$m at $a = 100\,a_B$ to $\sim 50\,\mu$m at $a = 30\,a_B$. This must be compared to the $6.45 \times 6.45\,\mu\text{m}^2$ pixel size of the CCD camera.

[92] This is due to the fact that the maximal dipole-dipole attraction is twice as strong as its repulsion. The minimum at $a \sim 18\,a_B$ in fig. 3.4(b) indicates the crossover from the purely contact ($\epsilon_{dd} \ll 1$) to purely dipolar ($\epsilon_{dd} \gg 1$) expansion dynamics, which finally results in the break down of the model due to the dipolar instability, see section 4.

As the calibration of the scattering length depends on the absolute size of the expanded condensate, the magnification factor of the imaging system must be accurately measured. This was done by diffracting the atoms from a standing light field [212–215]: Just after releasing an ultra-cold cloud from the trap, a laser[93] with wavelength $\lambda_{\text{puls}} \simeq 532\,\text{nm}$ illuminates them for $t_{\text{puls}} \sim 5\,\mu\text{s}$. The laser beam is retro-reflected such that an atom obtains the momentum $2\,h/\lambda_{\text{puls}}$ if it absorbs a single photon from the laser beam propagating in one direction and re-emits it into the laser beam which propagates in the opposite direction. This provides an accurate measurement of the resolution of the imaging system, because the relative position of the atoms is not disturbed by magnetic field gradients, but only by curvatures. Fitting the distance between the diffraction peaks after 7 ms of free expansion, we found an magnification factor of 1.12 for the imaging system [177, ch. 3.5]. All experimental Thomas-Fermi radii are rescaled by this factor. Note that the imaging of the cloud should be done in high magnetic field ($B \sim 600\,\text{G}$), because magnetic field curvatures during the switch-off might disturb the size of the cloud[94].

3.3.3 Experimental tasks: Working with a Feshbach resonance

Using a Feshbach resonance induces several experimental challenges. These are:

1. **atom losses:** Crossing or holding the condensate in the vicinity of a Feshbach resonance (on either side) is accompanied by strong atom losses. For "large" scattering lengths ($a \gg r_0$) the losses scale with a^4 and increase with increasing spatial density[95] [216, 217]. Therefore, in order to obtain large condensates at $B \sim 600\,\text{G}$ we need to cross the 14 Feshbach resonances sufficiently fast with a low spatial density. The switch-on of the magnetic Feshbach field is done[96] in less than 6 ms, crossing the broadest resonance with a slope $\dot{B} \simeq 130\,\text{G/ms}$, and a density of $n \approx 10^{13}\,\text{cm}^{-3}$. The atom losses for a condensate in the vicinity of the Feshbach resonance at $B_0 \approx 589\,\text{G}$ are shown in fig. 3.5. A simple estimate of the 3-body loss coefficient provides $L_3 \lesssim 2 \cdot 10^{-28}\,\text{cm}^6/\text{s}$ for $a \leq a_{\text{bg}}$.

[93] This laser is *only* used for this measurement. It has a $1/e^2$ waist (of the intensity) $w_{\text{puls}} \approx 110\,\mu\text{m}$, a maximal power $P_{\text{puls}} \approx 5\,\text{W}$, and it is retro-reflected. Do not confuse it with the one-dimensional 1064 nm optical lattice used to shape the trap. For details see [177].

[94] The absorption image shown in fig. 5.1 (page 72) shows a change in the size of the collapsed cloud. However, we never checked if a non-collapse cloud, which satisfies the Thomas-Fermi conditions, exhibits the same effect.

[95] A naive estimate provides $n\,a^3$: In order to get 3-body losses all three particles need to be within a sphere of radius R, where R is the 2-body interaction range. The (uncorrelated) probability that this happens is given by $n\,4\pi\,R^3/3$. Taking R to be on the order of the scattering length a results in the scaling $n\,a^3$.

[96] The coil configuration is given in tab. A.1 (page 104). Alternatively, one could use Helmholtz coils with a "small" radius and only a few windings to achieve a faster switching, while using coils with a "large" radius and many windings to obtain a stable offset-field. However, these are not available in the current set-up.

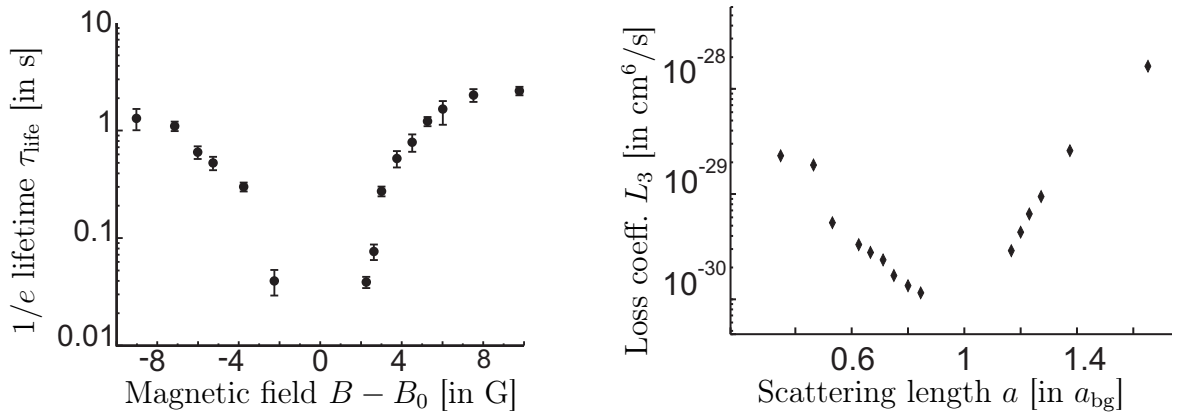

Fig. 3.5, Lifetime of the condensate and 3-body losses: The $1/e$ lifetime of the condensate around the Feshbach resonance is estimated by fitting an exponential $N(t) = N_0\,\mathrm{e}^{-t/\tau_{\rm life}}$. Using this estimate the 3-body relaxation coefficient is *approximated* by $1/\tau_{\rm life} \sim -L_3\,n^2$. A sophisticated measurement of L_3 is given in [118]. (Taken from [136])

2. **curvature compensation:** Any imperfection in the arrangement of the magnetic field coils results in magnetic field gradients b'_z, b'_ρ and curvatures b''_z, b''_ρ. Whereas the gradients are only on the order of the 1.2 G/cm and therefore are negligible across the condensate[97], the curvatures must be carefully compensated. Otherwise "hot" atoms which are evaporated from the crossed ODT are trapped by the resulting magnetic trap.

   The compensation is done by the pinch coils, which have curvatures approximately 25 times larger than those of the offset coils, at the same current. Note that the radial and axial curvatures produced by a cylindrical coil are coupled [172, ch. C2], which provides the relation $f_z^2 = -2\,f_\rho^2$ for the trap frequencies. Therefore, the curvatures produced by the offset coils can not be exactly compensated by the pinch coils. The atoms are either trapped in radial or in axial direction. For an efficient evaporative cooling process we choose anti-trapping in radial (two-dimensions) and trapping in axial direction. Axially as well as radially the trapping frequency is less than 10 Hz. The final optimisation was done by maximising the number of atoms in the condensate. For more details see [172].

3. **eddy currents:** The experiments are performed in a stainless steel chamber with coils outside of the vacuum system and the entrance windows flanged using copper gaskets. Therefore, changing the magnetic field induces eddy currents in the gaskets. We measured the $1/e$ lifetime of the eddy currents to be $\tau_{\rm B} = (0.57 \pm 0.05)$ ms using Zeeman spectroscopy. Therefore, even if the magnetic field produced by the offset

[97] The gradients mainly result in a shift of the trap equilibrium position. This shift is approximately equal to the gravitational sag ($mg/\mu_{\rm m} \approx 1.5$ G/cm) and therefore they are negligible in sufficiently strong trapping potentials.

coils $B_0(t)$ were changed abruptly, the atoms would experience a smooth change, according to $B(t) = B_0(t) - \tau_B \dot{B}(t)$.

4. **current noise:** As the current noise in the offset coils translates into an uncertainty of the scattering length, we need to control it as accurate as possible. This is done by controlling the resistance of an MOSFET[98] *via* a PI-loop[99]. Using high-stable power supplies[100] and a high-precision current transducer[101] the (peak-to-peak) noise-to-signal ratio[102] was measured to be $\Delta I/I = 4.5 \times 10^{-5}$, for details see [136, ch. 4.2]. However, the PI contains a second integration stage, which is currently not used. In principle it should increase the gain at low frequencies and thereby improve the current stabilisation further[103].

5. **high-field imaging:** In order to optimise the evaporation ramps an imaging system was build to probe the atoms with linear polarised light at a 600 G magnetic offset field. However, because both, the propagation direction as well as the polarisation axis of the probe beam, are perpendicular to the magnetic field, the probe light needs to be decomposed *point-wise* into $\sigma^{\pm}$ light [172, ch. 4.4]. The atomic column density (integrated over the x-axis, which is defined to be the line-of-sight) is given by

$$n(y,z) = -\frac{1}{\sigma_{\text{res}}} \ln\left(2\,\frac{I_{\text{out}}(y,z)}{I_{\text{in}}(y,z)} - 1\right) \tag{3.2}$$

where[104] $\sigma_{\text{res}} \stackrel{\text{def}}{=} 3\,\lambda^2/(2\pi)$ is the resonant absorption cross-section for σ^- light [173], and I_{in} and I_{out} are the in- and out-going intensities [167, ch. 3.1]. Note that this is equivalent to $n(y,z) = -\frac{2}{\sigma_{\text{res}}} \ln\left(\frac{I_{\text{out}}(y,z)}{I_{\text{in}}(y,z)}\right)$ only in the limit of low optical density. Thus, only in this limit the total cross-section is given by $\sigma_{\text{res}}/2$.

Conclusion:
Applying the techniques discussed in this section, we obtain a ^{52}Cr condensate composed of 50 000 atoms at 600 G. By using the Feshbach resonance at 589.1 G, we are able to reduce the usual contact interactions such that the anisotropic dipolar interactions become dominant. This allows us not only to observe strong dipolar effects, e.g. the elongation of the condensate along the magnetic field direction or the suppression of the inversion of the ellipticity during free expansion, but also to induce a dipolar instability. The dipolar instability is the subject of the following section.

[98] Care has to be taken by choosing the correct MOSFET (metal-oxide-semiconductor field-effect transistor). We currently use two "DYNEX: DIM400BSS12-A000" in parallel. However, this configuration will be replaced by a single "DIM1200DM12-E000" in the future.

[99] Designed by Marco Fattori and Werner Braun: "ELAB 30/05 b" (changed 18.11.2008).

[100] Agilent: "6682A".

[101] Danfysik: "Ultrastab 860 R".

[102] Due to eddy currents in the copper gaskets of the experimental chamber, only the current noise in the frequency range 1 Hz to 10 kHz is important. The measurement was done as in [136, ch. B], but using high-quality resistors and a low-noise voltage source in the PI-loop. These minor changes improved the current stability by a factor of 1.4.

[103] However, one has to carefully choose its operational amplifier.

[104] The Clebsch-Gordan is unity for the $|^7\text{S}_3, m_\text{J} = -3\rangle \rightarrow |^7\text{P}_4, m_\text{J} = -4\rangle$ transition.

"If I can't picture it, I can't understand it." (Albert Einstein)

4 Instabilities of dipolar condensates

Now we focus on the main subject of this thesis: unstable dipolar condensates. Unstable and collapsing condensates were first observed in ^{7}Li [56] and ^{85}Rb [57]. Having negligible dipolar interactions, these instabilities were fully explained by considering contact interactions only. However, inducing the instability in a condensate with non-negligible dipolar interactions changes the discussion considerably. Therefore, the main objective of this section is to understand the occurrence of an *instability* in a *dipolar* condensate. The collapse dynamics is discussed in section 5 together with the experimental measurements[105].

4.1 Instability due to local density fluctuations

The instability reveals itself by generating unphysical solutions indicating the breakdown of the model used to describe the condensate. For example, the eigenenergy of the ground-state becomes negative or complex valued, or the condensate's size becomes non-positive, manifesting an tremendous increase of the density[106]. Fortunately, the eigenenergy of the ground-state is an easily calculated quantity. Therefore, we will use it to consider first the case of three and two-dimensional homogeneous condensates, before discussing the experimentally most relevant configuration of a confined dipolar condensate.

4.1.1 Three-dimensional homogeneous dipolar condensates

A *homogeneous condensate* is an infinitely extended BEC with constant density. In the following it is assumed to be dipolar and pure[107]. The purely contact interacting case is summarised in [218].

Since the energy contribution from the dipolar interactions vanishes for any spherical symmetric density distribution (see appendix A.5.7), the stability criterion for a truly homogeneous condensate is the same as in the purely contact interacting case: the

[105] While *instability* refers to the threshold between the stable and the unstable region in the stability diagram, the term *collapse* refers to the dynamics of the condensate if this threshold is crossed. The collapse will be defined more precisely in section 5.

[106] The break down of the mathematical model is not enough to conclude that the condensate becomes unstable. Additionally, we have to identify a physical mechanism, which is responsible for the instability: E.g., in the case of the phonon-instability 3-body collisions result in the production of molecules.

[107] The thermal cloud is neglected, all atoms are assumed to be part of the condensate.

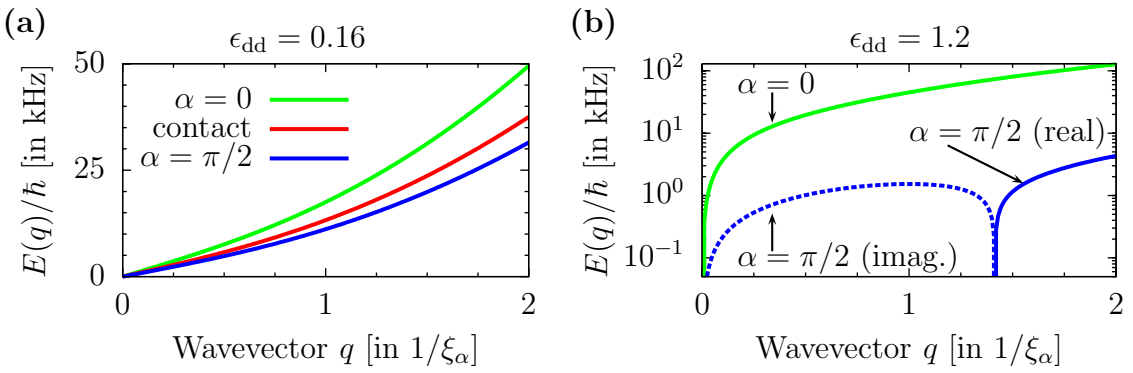

Fig. 4.1, Bogoliubov excitation spectrum: (a) The anisotropy of the dipolar interactions stiffens the excitation spectrum (4.1) for phonons travelling parallel ($\alpha = 0$) to the polarised dipoles $\boldsymbol{\mu}_\mathrm{m}$ compared to a purely contact interacting BEC. In contrast, phonons travelling perpendicular ($\alpha = \pi/2$) to $\boldsymbol{\mu}_\mathrm{m}$ are softened. (b) If the contact interactions were reduced such that ϵ_dd exceeds unity[109], the soft mode becomes imaginary for "small" phonon wavevectors $|\boldsymbol{q}|$ indicating the dipolar instability. The healing length is given by $\xi_\alpha \equiv \hbar/\sqrt{2\,m\,n_0\,|g_\alpha|}$. The calculation assumes a ^{52}Cr condensate with $n_0 = 10^{14}\,\mathrm{cm}^{-3}$.

scattering length must be positive[108] (repulsive contact interactions). However, allowing local density perturbations, the dipolar contribution do no longer vanish and must be taken into account. Assuming that travelling plane waves with wavevector $\boldsymbol{q}$ perturb the system, the *Bogoliubov excitation spectrum* (see appendix A.5.8)

$$E(\boldsymbol{q}) = \sqrt{E_\mathrm{free}(\boldsymbol{q})\Big[E_\mathrm{free}(\boldsymbol{q}) + 2\,n_0\,\tilde{V}_\mathrm{int}(\boldsymbol{q})\Big]} \tag{4.1}$$

is obtained, where $E_\mathrm{free}(\boldsymbol{q}) \stackrel{\mathrm{def}}{=} (\hbar\boldsymbol{q})^2/(2m)$ is the free particle dispersion relation, n_0 the non-perturbed equilibrium value of the spatial density, and $\tilde{V}_\mathrm{int}(\boldsymbol{q})$ is the Fourier transform of the 2-body interaction potential. The *effective coupling strength* including dipolar interactions is defined by $g_\alpha \stackrel{\mathrm{def}}{=} \tilde{V}_\mathrm{int}(\boldsymbol{q}) = g + g_\mathrm{dd}\,(3\cos^2\alpha - 1)$, where α is the angle between the fully polarised magnetic moments $\boldsymbol{\mu}_\mathrm{m}$ and the wavevector $\boldsymbol{q}$. The Bogoliubov spectrum (4.1) can either be understood as a collective excitation of many interacting atoms, or as the production of non-interacting quasi-particles (see appendix A.5.8). Since the quasi-momentum $\boldsymbol{q}$ vanishes linearly for zero excitation energy, these quasi-particles are called *phonons* [180, 219]. Due to the conservation of angular momentum, they have to obey Bose-Einstein statistic[110]. The crossover from a linear (collective) into a quadratic

[108] This condition can be deduced from thermodynamics [157, ch. 4.1]: For the homogeneous case, the quantum pressure vanishes and the total energy E is equal to the interaction energy $N\,n_0\,g/2$. Hence, the pressure is given by $P \stackrel{\mathrm{def}}{=} -\partial E/\partial V = n_0^2\,g/2$, yielding the compressibility $\kappa_\mathrm{comp} \stackrel{\mathrm{def}}{=} -\frac{1}{V}\frac{\partial V}{\partial P} = 1/(n_0^2\,g)$, which must be positive in order to obtain a stable system.

[109] Recall: ϵ_dd is the ratio between the dipolar and the contact coupling strength, see page 26.

[110] The excitation spectrum of a bosonic system has to obey Bose-Einstein statistic [220, ch. 66].

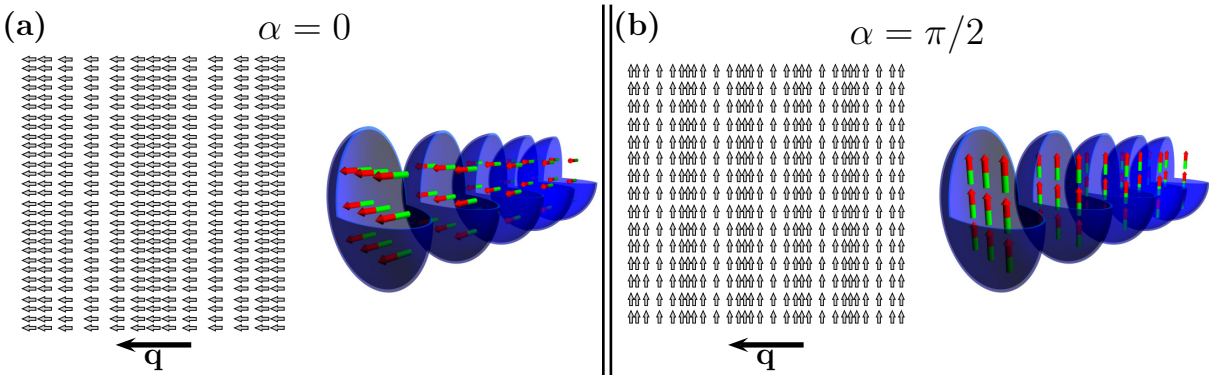

Fig. 4.2, Illustrating the phonon instability: A density wave generates stacks of condensates. In the extreme case it effectively reduces the dimensionality of the interactions by one. Depending on the direction of the density wave, either the repulsive or the attractive part of the DDIs is effected. (a) Phonons travelling parallel to the dipoles reduce the attractive part by producing pancake-shape BECs. In contrast, radial phonons (b) reduce the repulsive part of dipolar interactions. The total energy decreases, an instability even at positive scattering length is possible. The left and the right picture illustrate the two and three-dimensional case, respectively.

(single free particle like) excitation occurs at $q_\alpha \sim 1/\xi_\alpha$, where $\xi_\alpha \stackrel{\text{def}}{=} \hbar/\sqrt{2\,m\,n_0\,|g_\alpha|}$ is the healing length associated with g_α.

Figure 4.1(a) presents the excitation spectrum for phonons produced in a homogeneous chromium condensate ($\epsilon_{\text{dd}} \approx 0.16$) and compares it to the purely contact interacting case ($\epsilon_{\text{dd}} = 0$). For repulsive contact interactions ($g > 0$), it can be illustrated as follows: Place the atoms on an equally spaced two-dimensional grid and fix their relative positions by springs. Due to the anisotropy of the dipolar interactions, the spring constant between axial and radial neighbours are not chosen equal, but according to the effective coupling g_α. Hence, it is stiffer between two axial neighbours[111]. For the chromium background scattering length ($\epsilon_{\text{dd}} \approx 0.16$) this simple picture illustrates why density waves (phonons) travelling parallel ($\alpha = 0$) to the polarised dipoles have a stiffer excitation spectrum than density waves travelling perpendicular ($\alpha = \pi/2$) to the polarisation direction [180, ch. 4.1].

For density waves propagating parallel ($\alpha = 0$) to the polarised dipoles $\boldsymbol{\mu}_{\text{m}}$ the spring model works for all positive scattering lengths $\epsilon_{\text{dd}} > 0$. However, it breaks down for density waves propagating perpendicular ($\alpha = \pi/2$) to $\boldsymbol{\mu}_{\text{m}}$ if the contact interactions were decreased such that the dipolar interactions become dominant ($\epsilon_{\text{dd}} > 1$). Here, the radial spring constants would become negative resulting in an imaginary energy for excitations

[111] As mentioned in section 2.3.3, the mean-field dipolar interaction becomes "counter-intuitive" in the 2-body forces-picture. By choosing the spring constant according to g_α, we remain in the energy-picture.

with wavevectors

$$q < q_{\text{unstable}} \stackrel{\text{def}}{=} \sqrt{16\,\pi\,n_0\,(a_{\text{dd}} - a)} \tag{4.2}$$

as shown in fig. 4.1(b). This can be understood in the following way: Modulating the atomic density radially, these phonons generate stacks of prolate condensates, see fig. 4.2(b), where the dipoles interact foremost attractively. Therefore, the dipolar interactions decrease the total energy and eventually induce an instability. In contrast, for density waves propagating parallel to the dipoles ($\alpha = 0$) the condensate remains stable, because the dipoles interact mainly repulsively. We will encounter the radial character of the instability throughout this thesis.

Although homogeneous condensates are unphysical due to their infinite extension, they do provide valuable information for experiments. Despite their simplicity — which makes them numerically simple and sometimes even analytically solvable systems — they describe trapped condensates if the change in density is small within the wavelength of the excitation (e.g., for a condensate with Thomas-Fermi radius R the condition reads $R \gg 1/q$). If this is fulfilled, the single harmonically confined condensate can be treated as a collection of homogeneous condensates, with each of them having its own local density [221]. Coming back to the stability criterion (4.2), we may reverse this argument: Since homogeneous condensates describe *only* the short wavelengths properties of a trapped condensate, the condensate is stable if[112] $q_{\text{unstable}} \leq q_{\text{min}} \stackrel{\text{def}}{=} \pi/R_\rho$.

4.1.2 Two-dimensional homogeneous dipolar condensates

In the following section we will confine the dipolar condensate in one direction. Although this configuration is considerably more complicated than the three-dimensional homogeneous case, it still permits to work with analytic expressions. However, studying dipolar condensates in reduced dimensions allows to discuss one of the most thrilling aspects of dipolar condensates: its maxon-roton excitation spectrum [64]. Thus, the discussion provides a deeper understanding of dipolar condensates confined in three-dimensions.

Assuming a strong confinement in only one direction, the excitation spectrum transverse to this direction remains continuous. From the discussion in the previous section we know that the excitation spectrum is most interesting in the direction perpendicular to the dipole axis ($\alpha = \pi/2$). Therefore, we consider the configuration where the dipoles are polarised parallel to the confinement direction[113], with $\boldsymbol{\mu}_{\text{m}} \parallel z$ and the trap frequency $\omega_z/(2\pi) > 0$. For a sufficiently strong confinement, $\hbar\omega_z \gg \mu$, the two-dimensional transverse excitation

[112] Loosely speaking, the condensate is stable if the wavelength associated with the instability is to large to fit into the BEC.

[113] The case where the dipoles are oriented in the plane of strong confinement is discussed in [222].

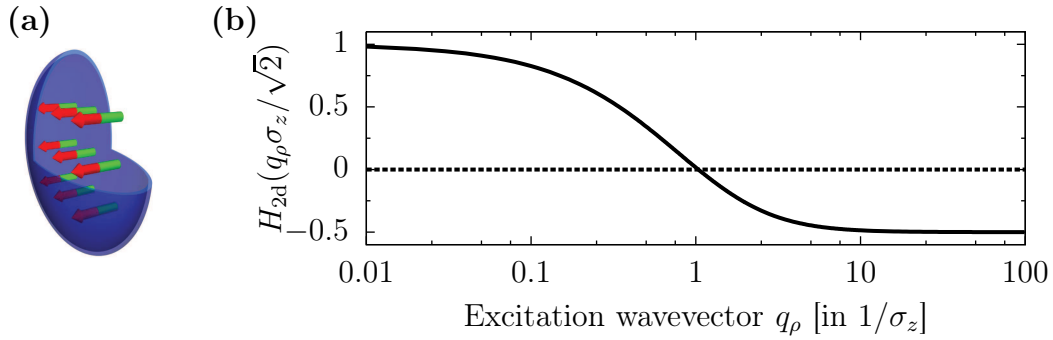

Fig. 4.3, Momentum dependency of dipolar interactions: The sketch in (a) illustrates the configuration of the dipolar condensate. Its effective coupling strength $g_{\rm int}^{(2d)}(q_\rho\sigma_z/\sqrt{2})$ depends on the momentum, as shown in (b). The positive contribution for "small" transverse wavevectors $|\boldsymbol{q}_\rho|$ is responsible for the stabilisation against phonons.

spectrum reads[114] [65, 66]

$$E(\boldsymbol{q}_\rho) = \sqrt{E_{\rm free}(\boldsymbol{q}_\rho)\,\left[E_{\rm free}(\boldsymbol{q}_\rho) + 2\,n_{2d}\,\tilde{V}_{\rm int}^{(2d)}(\boldsymbol{q}_\rho)\right]} \tag{4.3a}$$

with the Fourier transform of the two-dimensional 2-body interaction potential[115]

$$\tilde{V}_{\rm int}^{(2d)}(\boldsymbol{k}_\rho) \stackrel{\rm def}{=} \int_{-\infty}^{\infty} dk_z\,|\tilde{n}(k_z)|^2\,\tilde{V}_{\rm int}(\boldsymbol{k}) \tag{4.3b}$$

$$= \frac{1}{\sqrt{2\pi}\sigma_z}\,\left[g + 2\,g_{\rm dd}\,H_{2d}(\sqrt{2}\pi\boldsymbol{k}_\rho\,\sigma_z)\right] \tag{4.3c}$$

where $\boldsymbol{q}_\rho \equiv \boldsymbol{k}_\rho/(2\pi)$ is the transverse wavevector, $n_{2d} \stackrel{\rm def}{=} \sqrt{2\pi}\sigma_z\,n_{3d}$ the two-dimensional homogeneous density, $\sigma_z = \sqrt{\hbar/(m\omega_z)}$ is the width of the Gaussian wavefunction in z-direction, and $H_{2d}(\chi) \stackrel{\rm def}{=} 1 - 3/2\,\sqrt{\pi}\,|\chi|\,\exp(\chi^2)\,{\rm erfc}(\chi)$ with the complementary error function ${\rm erfc}(\chi)$. In order to discuss the stability of the condensate and to emphasise the similarity to the previous section, we define the *two-dimensional effective coupling strength* $g_{\rm int}^{(2d)}(\chi) \stackrel{\rm def}{=} \frac{g+2\,g_{\rm dd}H_{2d}(\chi)}{\sqrt{2\pi}\sigma_z}$. The chemical potential is given by $\mu_{2d} = n_{2d}\,g_{\rm int}^{(2d)}(0)$.

The major difference between the two-dimensional excitation spectrum (4.3a) and the three-dimensional one, eq. (4.1), is the momentum dependency of the effective coupling strength through $H_{2d}(\chi)$, see fig. 4.3: It is a strictly monotonic decreasing function, starting at unity, crossing zero at $\chi/\sqrt{2} \approx 1$ and asymptotically approaching $-1/2$. Therefore, the

[114] The system freezes in the z-direction into the ground-state of the harmonic oscillator, $\phi_0(z) \equiv \exp\left[-z^2/(2\sigma_z^2)\right]/(\pi^{1/4}\sqrt{\sigma_z})$. Therefore, the wavefunction factorises, $\Psi(\boldsymbol{r}) = \psi(\boldsymbol{\rho})\phi_0(z)$.

[115] For deriving the formula use Parseval's theorem as in section A.5.4, consider a Gaussian wavefunction in the direction z of strong confinement, and integrate over the z-direction using $\int_{-\infty}^{\infty} dk_z\,(-1 + \frac{3\,k_z^2}{k_\rho^2+k_z^2})\exp[-(\sigma_z\,k_z)^2/2] = \sigma_z/\sqrt{2\pi}\,H_{2d}(k_\rho\,\sigma_z/\sqrt{2})$.

phononic stability condition is given by

$$\lim_{q_\rho \to 0} g_{\mathrm{int}}^{(2\mathrm{d})}(q_\rho) = \frac{g + 2\, g_{\mathrm{dd}}}{\sqrt{2\pi}\sigma_z} \geq 0 \tag{4.4}$$

If condition (4.4) fails, the chemical potential becomes negative, indicating that a ground-state does not exist and that the model breaks down. However, since $H_{2\mathrm{d}}(q_\rho)$ decreases with increasing q_ρ, eq. (4.4) is only a necessary condition to ensure a stable condensate. Additionally, the *rotonic stability condition*

$$\lim_{q_\rho \to \infty} g_{\mathrm{int}}^{(2\mathrm{d})}(q_\rho) = \frac{g - g_{\mathrm{dd}}}{\sqrt{2\pi}\sigma_z} > 0 \tag{4.5}$$

must be satisfied to prevent an instability at finite transverse wavevector and sufficient large densities $n_{2\mathrm{d}}$. Note that although the system would become unstable if condition (4.5) was not fulfilled, the chemical potential would remain positive. This suggests that a new ground-state exists, which probably exhibits a periodic density modulation.

From these considerations it is obvious that the role of the dipolar interactions depends on the sign and magnitude of the scattering length. Therefore, three cases must be distinguished[116]:

1. **Purely dipolar interactions** ($g = 0$)
   Condition (4.4) is always fulfilled, and the system is stable against phonons. However, for sufficient large densities the *dipoles drive* the condensate into a roton instability.

2. **Repulsive contact interactions** ($g > 0$)
   Again condition (4.4) is always satisfied, and a phonon instability does not occur. However, if the dipolar coupling strength exceeds the contact coupling strength ($g_{\mathrm{dd}} > g$), the *dipoles drive* the condensate into a roton instability for sufficient large densities. In contrast, if the contact interactions dominate ($g_{\mathrm{dd}} < g$), the condensate is stable against phonons as well as rotons.

3. **Attractive contact interactions** ($g < 0$)
   For sufficient attractive contact interactions ($|g| > 2\, g_{\mathrm{dd}}$) the condensate is unstable against phonons for *any* density. However, for small enough contact interactions the *dipoles stabilise* the phonon instability. Only for sufficient large densities the condensate becomes unstable against rotons. Depending on the wavevector of the most unstable mode, the instability is either driven by the contact interactions alone or by both, the contact as well as dipolar interactions.

[116] Here, we assume a positive dipolar coupling constant g_{dd}, because rotating magnetic fields are unrealistic in our current set-up.

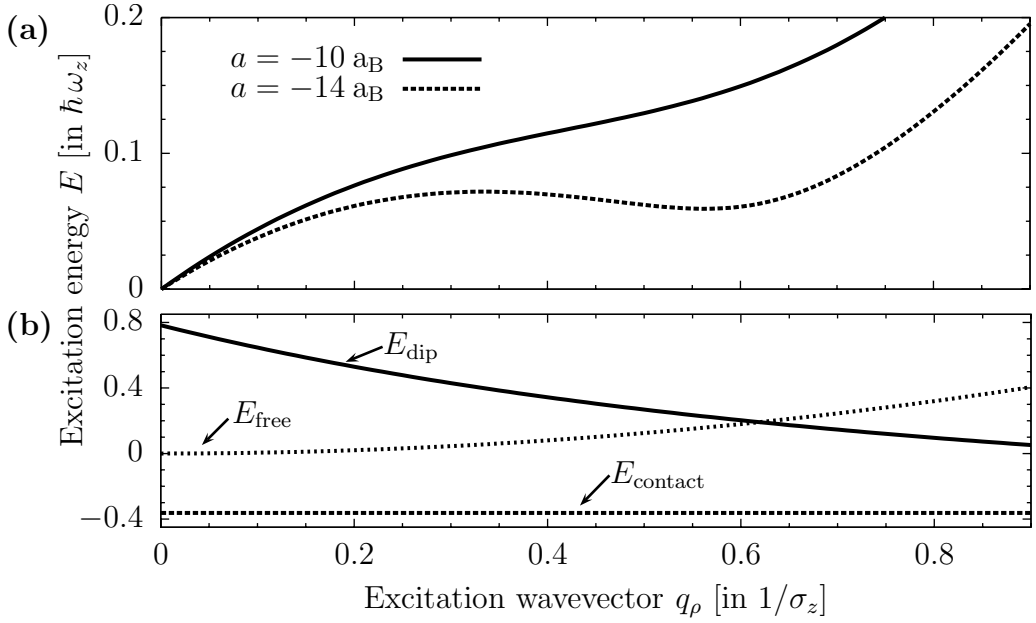

Fig. 4.4, Roton excitation spectrum: While (a) presents the total excitation energy (4.3a) for a single condensate for two different negative scattering lengths, (b) shows the dipolar, contact, and free-particle contributions for $a = -14\,a_B$. In both graphs the density is given by $n_{3d} = 10^{15}\,\mathrm{cm}^{-3}$ and the confinement by $\omega_z = 2\pi \cdot 10\,\mathrm{kHz}$. Note that the dipolar contribution is still positive at the roton minimum — the role of the dipoles is to stabilise the "short" wavelength excitation, but not to destabilise the system at the roton minimum.

4.1.3 Rotonic excitations

The origin of the roton instability lies in the momentum dependency of the inter-particle interactions and is an unique feature of *long-range* interactions in low-dimensional systems[117]. Although the anisotropy of the dipolar interaction enhances this effect, it is not necessary to obtain a roton spectrum. This was shown in [228], where an isotropic, but long-range interaction potential was used.

For the case of chromium the experimentally most promising configuration to observe rotonic effects is the case of attractive contact interactions ($g < 0$). The different contributions to the excitation spectrum (4.3a) are presented in fig. 4.4. However, even in this "simple case" the necessary densities are experimentally very demanding[118]. Thus, it is unlikely to observe a roton *instability*[119] with a chromium BEC and very challenging to

[117] In contrast, the maxon-roton spectrum in superfluid ^{4}He is a consequence of its proximity to a solid phase: Density fluctuations with a wavelength $\lambda \sim 1/k_{lat}$, where k_{lat} is the *reciprocal lattice vector* of solid helium, are enhanced [157, 218, 223–227].

[118] With decreasing density the roton minimum moves to smaller transversal momenta q_ρ and to smaller scattering length a. This can be easily seen from eq. (4.3a) if we rescale $\boldsymbol{q}_\rho \to \sqrt{n_{2d}}\,\boldsymbol{q}'_\rho$.

[119] A roton instability would occur if the excitation energy associated with the local minimum at momentum $q_\rho \sim 0.6/\sigma_z$ became negative.

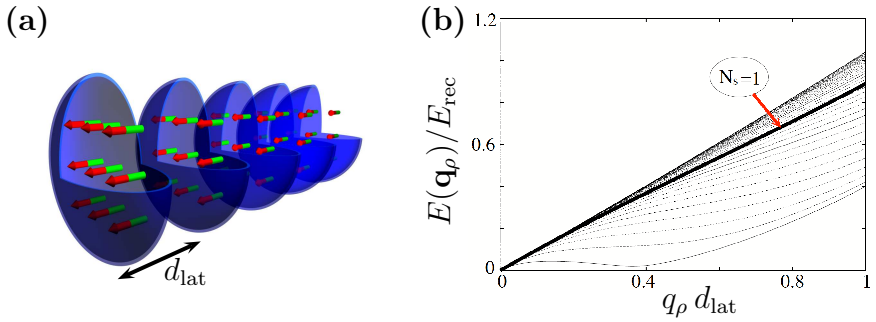

Fig. 4.5, Roton softening in a stack of condensates: Using the configuration sketched in (a), the inter-site dipolar coupling hybridises the maxon-roton spectrum. This is shown in (b) for $N_s = 40$ lattice sites, lattice spacing $d_{\mathrm{lat}} = 530\,\mathrm{nm}$, spatial peak density $n_0 = 10^{14}\,\mathrm{cm}^{-3}$, scattering length $a = -19\,a_{\mathrm{B}}$, and recoil energy $E_{\mathrm{rec}} = \hbar^2/(m d_{\mathrm{lat}}^2)$. While some eigenmodes possess a stiffer excitation spectrum than in the single condensate case ($N_{\mathrm{s}} = 1$), some become softer and develop a roton minimum. (Taken from [233])

measurement the roton signature in Faraday patterns [229] or the angular collapse [73]. Although Bragg spectroscopy is in principle possible [221, 230–232], the limited optical access of the current experimental set-up rules it out.

Therefore, the following configuration is more realistic [233, 234]: Instead of a single condensate, consider a stack of oblate condensates confined on different sites of a one-dimensional optical lattice with lattice spacing d_{lat}, see fig. 4.5. The optical lattice is assumed to be sufficiently deep such that tunneling is strongly suppressed. The otherwise isolated condensates are only coupled by the long-range dipolar interactions. While this configuration maintains the on-site repulsion, the inter-layer interaction of the sites j and j' is strongly attractive for a characteristic wavevector $k_{j,j'} \sim 1/(|j - j'|\, d_{\mathrm{lat}})$. The hybridisation of different modes leads to a softening of the roton mode. Effectively, the function $H_{2\mathrm{d}}(q_\rho)$ is replaced by a function $H_{2\mathrm{d}}^{(N_{\mathrm{lat}})}(q_\rho)$, which decreases faster with increasing number of sites N_{lat}.

Surely, the roton instability is a very interesting effect, which could be present in dipolar condensates. However, its relevance to the experiments presented in this thesis are not completely clear and still under debate.

4.2 Instability due to scaling deformations

Although the discussion of homogeneous dipolar condensates illustrates the instability, it does not provide a reliable description for the experimental results. Thus, we like to take the next step towards a quantitative description of a dipolar condensate in this section by considering the energy functional and ask: How does the trap geometry affect the stability? From the picture presented in the previous section, we expect condensates to be

more stable in pancake-shape (oblate) than in cigar-shape (prolate) external potentials. A more detailed discussion of the purely contact interacting case is given in [119, ch. 6.2], [157, ch. 11.6], and [59, 235, 236]. Our results for the dipolar case are published in [237] and discussed in [136, 144, 145, 238]. In appendix A.6.2 we generalise the calculations from a single BEC and include the inter-site dipolar interactions for a stack of pancake-shape condensates.

In order to get a simple quantitative model for the instability the mean-field energy (2.9) for different cylindrically symmetric, harmonic confinements is calculated. However, since we do not know the Gross-Pitaevskii solution $\psi(\boldsymbol{r})$, we use an educated guess: While in the non-interacting case the wavefunction is given by the Gaussian

$$\psi(\boldsymbol{r}) \stackrel{\text{def}}{=} \frac{\sqrt{N}}{\pi^{3/4}\,\sigma_\rho\,\sigma_z^{1/2}} \exp\left(-\frac{\rho^2}{2\,\sigma_\rho^2} - \frac{z^2}{2\,\sigma_z^2}\right) \tag{4.6}$$

the Thomas-Fermi density profile is a parabola, see eq. (2.11). Not only do these density distributions allow to check the limiting cases of negligible and dominant interactions, but the energy can be calculated analytically. The different energy contributions (quantum pressure, potential trap energy, contact interaction energy, and dipolar interaction energy) are given by (per atom in units of $\hbar\bar{\omega}$) [161, 237, 239][120]

	Gaussian	Thomas-Fermi
$\frac{E_{\text{zero}}}{N\hbar\bar{\omega}}$	$\frac{a_{\text{ho}}^2}{4}\left(\frac{2}{\ell_\rho^2} + \frac{1}{\ell_z^2}\right)$	0
$\frac{E_{\text{trap}}}{N\hbar\bar{\omega}}$	$\frac{2\,\ell_\rho^2+\lambda^2\,\ell_z^2}{4\,a_{\text{ho}}^2\,\lambda^{2/3}}$	$\frac{2\,\ell_\rho^2+\lambda^2\,\ell_z^2}{14\,a_{\text{ho}}^2\,\lambda^{2/3}}$
$\frac{E_{\text{contact}}}{N\hbar\bar{\omega}}$	$\frac{N}{\sqrt{2\pi}}\left(\frac{a_{\text{ho}}}{\ell_\rho}\right)^2 \frac{a}{\ell_z}$	$\frac{15\,N}{7}\left(\frac{a_{\text{ho}}}{\ell_\rho}\right)^2 \frac{a}{\ell_z}$
$\frac{E_{\text{dip}}}{N\hbar\bar{\omega}}$	$-\frac{N}{\sqrt{2\pi}}\left(\frac{a_{\text{ho}}}{\ell_\rho}\right)^2 \frac{a_{\text{dd}}\,f_{\text{dip}}(\kappa)}{\ell_z}$	$-\frac{15\,N}{7}\left(\frac{a_{\text{ho}}}{\ell_\rho}\right)^2 \frac{a_{\text{dd}}\,f_{\text{dip}}(\kappa)}{\ell_z}$

(4.7)

where $\bar{\omega} \stackrel{\text{def}}{=} (\omega_\rho^2\,\omega_z)^{1/3}$ is the mean angular trap frequency. In these formulae the only free parameters are the condensate sizes ℓ_ρ and ℓ_z. Surprisingly, the Gaussian and the parabola density distribution exhibit the same energy scaling, if the sizes are used as variational parameters to minimise the total energy. Only the numerical weights differ. To simplify the following discussion, the contact and the dipolar interactions are combined by defining an *effective interaction length* $\mathcal{L}(\kappa) \stackrel{\text{def}}{=} a - a_{\text{dd}}\,f_{\text{dip}}(\kappa)$.

The simplest case is obtained by taking the limit $N \to \infty$. Since the zero-point and the potential trap energy (per atom) do not depend on N, they are negligible and the Gaussian, as well as the Thomas-Fermi energy reduces to $E_{\text{tot}} \propto \mathcal{L}(\kappa)$. Hence, the instability occurs

[120] Recall: trap ratio $\lambda \equiv \omega_z/\omega_\rho$, harmonic oscillator length $a_{\text{ho}} \equiv \sqrt{\hbar/(m\,\bar{\omega})}$, and aspect ratio $\kappa \equiv \ell_\rho/\ell_z$ with cloud size $\ell = \sigma, R$ for the Gaussian and Thomas-Fermi profile, respectively. The anisotropic dipolar function $f_{\text{dip}}(\kappa)$ is discussed in appendix A.5.5.

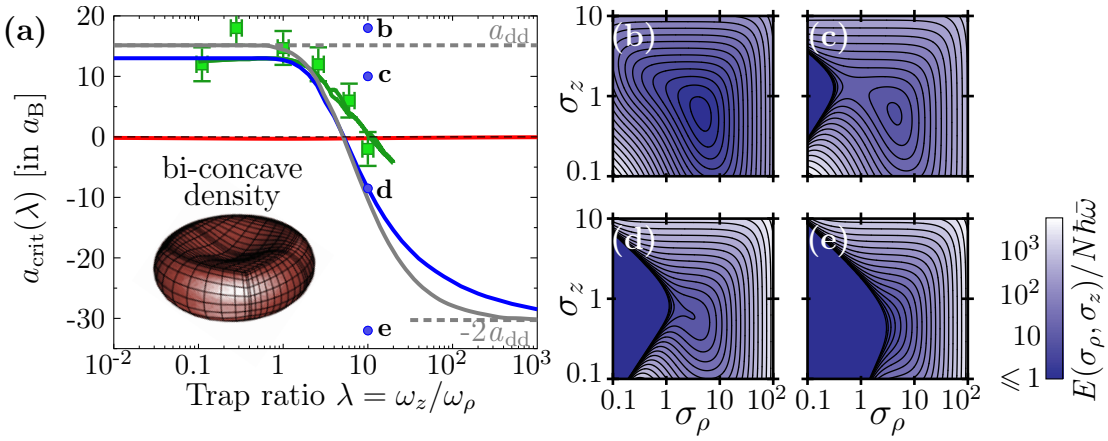

Fig. 4.6, Stability diagram for a single dipolar condensate: (a) Shown is the critical scattering length for different cylindrically symmetric trap geometries [237]. The mean trap frequency is $\bar{\omega}/(2\pi) = 700\,\text{Hz}$, and the atom number $N = 20\,000$. While the Gaussian ansatz without dipolar interactions (red) is almost constant, we find good agreement with the measured data points, if dipolar interactions are included (blue). The Gaussian stability curve for $N \to \infty$ is shown in grey. Interestingly, the GPE solution (which is shown as green solid curve and taken from [73]) exhibits a bi-concave density distributions of the ground-state (shape of a red blood cell). The iso-energy landscapes $E(\ell_\rho, \ell_z)$ shown in (b-e) are for $\lambda = 10$ and $a = (18, 10, -8.5, -32)\,a_{\rm B}$. (Discussed in the text)

at $\mathcal{L}(\kappa) = 0$, corresponding to a *critical scattering length* $a_{\rm crit}(\kappa) \stackrel{\rm def}{=} a_{\rm dd}\, f_{\rm dip}(\kappa)$. For the Thomas-Fermi energy this remains valid for all N, because the potential trap energy scales like ℓ^2 and therefore is always negligible for sufficient small ℓ, whereas the interaction energy increases with decreasing ℓ. Therefore, the instability found for a Thomas-Fermi distribution is equal to the critical scattering length $a_{\rm crit}(\kappa)$ found with a Gaussian density distribution for $N \to \infty$ (see fig. 4.7), if the coupling of the radii *via* eq. (2.13) is omitted[121]. Doing so, we consider only Gaussian density distributions in the following.

Studying the scaling of the Gaussian energy (4.7), it is obvious that only the interaction energies are responsible for the instability, because both the quantum-pressure and the potential trap energy are positive. Therefore, if $\mathcal{L}(\kappa) > 0$ the condensate is stable. Plotting the corresponding iso-energy landscape 4.6(b) shows that a single global minimum exists.

A necessary condition for the instability is $\mathcal{L}(\kappa) < 0$. Investigating the ℓ_ρ-scaling of the energies, one easily finds that a *global minimum* appears at $\ell_\rho = 0$ if the instability criterion

$$\frac{N\,\mathcal{L}(\kappa)}{\ell_z} < -\sqrt{\pi/2} \tag{4.8}$$

[121] Including the coupling of the radii the condensate becomes more stable in oblate traps, while it becomes less stable in prolate traps.

is fulfilled. However, for sufficient weak interactions ($\mathcal{L}_{\rm crit}(\kappa) < \mathcal{L}(\kappa) < 0$) a local minimum still exists[122] at finite ℓ_ρ and it is separated from the global minimum by a barrier, as shown in fig. 4.6(c). Therefore, assuming that the condensate is not excited (e.g. due to non-adiabatic changes of the trap frequencies), the condensate remains in this local minimum for all experimental relevant time scales. It is said to be *meta-stable*. Only if the barrier vanishes and with it the local minimum, the condensate becomes *unstable*, as shown in fig. 4.6(d). The disappearance of the local minimum is used to define the critical interaction length[123] $\mathcal{L}_{\rm crit}(\kappa)$, which yields the critical scattering length $a_{\rm crit}(\kappa) \stackrel{\rm def}{=} \mathcal{L}_{\rm crit}(\kappa) + a_{\rm dd}\, f_{\rm dip}(\kappa)$.

Using the same kind of argument for the axial direction, one finds that the quantum pressure always stabilises the condensate for $\ell_z \to 0$ but that a minimum at finite ℓ_z and negative energy might exist if

$$\frac{N\,\mathcal{L}(\kappa)}{\ell_z} < -\sqrt{\pi/2}\,\frac{\kappa^2}{2}\,\left[1 + \left(\lambda^{1/3}\,\frac{\ell_z}{a_{\rm ho}}\right)^4\right] \tag{4.9}$$

is fulfilled[124]. It is not related to an instability, but to the formation of a soliton [65]. This condition is only relevant for $\kappa < \sqrt{2}$.

It follows from the above discussion that in cigar-shape traps the instability is induced by dipolar interactions, while it is driven by the contact interactions in pancake-shape traps. Due to the different role of the dipolar interactions the stability diagram is divided into two regions: the region of the *dipolar instability* ($a_{\rm crit} > 0$) and of *dipolar stabilisation* ($a_{\rm crit} < 0$). Figure 4.6(a) compares the critical scattering length $a_{\rm crit}(\kappa)$ obtained from the Gaussian energy to experimental data for different trap geometries. It shows that the simple Gaussian model agrees well with the measured data [237] and that the full numerical solution $\psi(\boldsymbol{r})$ of the Gross-Pitaevskii equation improves the description of the measurements further. All data points lie within the region of the dipolar instability, except $\lambda \simeq 10$. This last trap configuration constitutes the first purely dipolar condensate. The error bars are mainly due to uncertainties in the trap frequencies, which enter *via* the calibration of the scattering length (section 3.3.2).

We would like to close this paragraph with a remark about the applicability of the Gaussian model, its predicting power and the conclusion one may draw. Figure 4.7 presents the critical scattering length found with the Gaussian density for different atom numbers N. It shows that the critical scattering length becomes zero at $\lambda_0 \approx 5.17$. Therefore, it exists a critical trap ratio λ_0 for which the aspect ratio is oblate ($\kappa \geq 1$) for all *purely* dipolar condensates — independent of the dipolar interactions strength. The dipolar contribution is repulsive in these traps, thus, the condensate is stable. This conclusion is drawn in

[122] For the Thomas-Fermi density profile local minima do exist as well. This is due to eq. (2.13), which couples both Thomas-Fermi radii. Examples are given in [240].

[123] At the critical scattering length the local minimum becomes a saddle point $\partial E_{\rm tot}/\partial \ell_\rho = 0 = \partial E_{\rm tot}/\partial \ell_z$ and $(\partial^2 E_{\rm tot}/\partial \ell_\rho^2)\,(\partial^2 E_{\rm tot}/\partial \ell_z^2) = (\partial^2 E_{\rm tot}/\partial \ell_\rho \partial \ell_z)^2$. This is discussed in [144, 145, 238].

[124] Note that the Thomas-Fermi wavefunction supports axial contraction to a "point-like state".

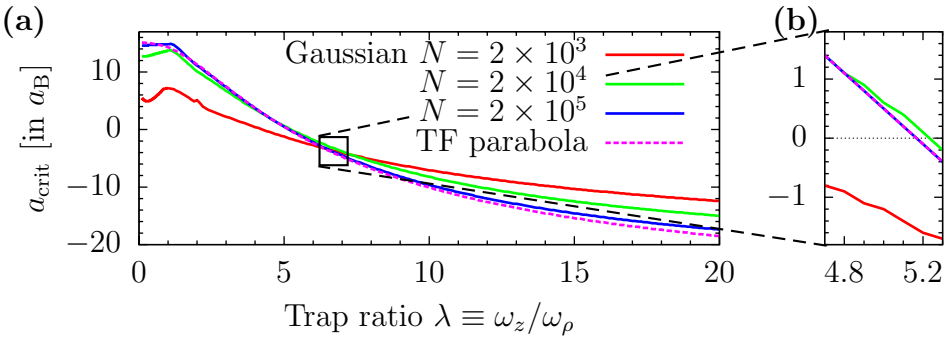

Fig. 4.7, Universal stability diagram: For increasing atom numbers N, the critical scattering length $a_{\rm crit}(\lambda)$ for the Gaussian wavefunction (4.6) approaches the one found with the Thomas-Fermi parabola ($N = \infty$). The mean trap frequency is $\bar{\omega}/(2\pi) = 700\,\text{Hz}$. In (b) the region at $\lambda_{\rm crit} \approx 5.17$ is accentuated, where the $a_{\rm crit}$ becomes negative.

several articles [134, 144, 159]. However, one should be aware that the Gaussian model is a severe simplification and therefore its predictive power is limited.

That the predicted "absolute stability" for purely dipolar condensates confined in oblate traps with$\lambda \geq \lambda_0$ is not physical and only a peculiarity of the Gaussian model was shown in [70, 134, 240], where more sophisticated numerical calculations were used[125]. The authors conclude that the Gaussian model is a good description of the full GPE for a wide parameter range. However, the agreement between both models is excellent only for cigar-shape traps. This can be understood as follows: In cigar-shape traps both energy contributions (from the trap and the interactions) favour the elongation of the condensate along the polarisation direction. Hence, it is "natural" that the peak density is located in the center of the trap, which is consistent with the Gaussian density profile. In contrast, in pancake-shape traps the contribution of the dipolar interactions competes with the potential energy of the trap. Therefore, a structured density distribution whose peak density is located at the periphery of the condensate ($\ell_\rho \neq 0$) is possible [67, 70, 71], see fig. 4.6(a). However, the Gaussian trial wavefunction is incapable of describing this density distribution[126]. Therefore, in oblate traps different mechanisms are *expected* to be responsible for the instability. The most prominent mechanism is the softening of a roton mode, which is driven by local density fluctuations. It was suggested in [243] that the difference between the measured critical scattering length and the Gaussian $a_{\rm crit}(\kappa)$ (blue solid line in fig. 4.6(a)) indicates the onset of the "rotonisation". However, such indirect

[125] A simple argument, showing the limits of the Gaussian model, is the following: Since the aspect ratio κ approaches the trap ratio λ with increasing atom number, the Gaussian model predicts that for $\lambda > \lambda_0$ the condensate becomes more stable with increasing N, see fig. 4.7. However, this contradicts our expectations that by increasing the non-linearity in the GPE, the condensate should become less stable. This is also reflected in the Bogoliubov spectrum of a *homogeneous* condensate, eq. (4.1), where the condensate becomes less stable if either the atom number or the dipolar interaction strength increases.

[126] The bi-concave wavefunction, which solves the full GPE, is well approximated by a sum of Gaussian wavefunctions with different widths and statistical weigths [241, 242].

evidences should be taken as motivation to directly measure the roton[127]. In the following we will not refer to the roton instability, although we will present the collapse dynamics of a condensate with trap ratio $\lambda \simeq 10$.

[127]Note that our Gaussian ansatz assumes a cylindrical symmetric density distribution. However, in the region around $\kappa \simeq 1$ this is not the case.

"Suicide may also be regarded as an experiment — a question which man puts to Nature, trying to force her to answer."
(Arthur Schopenhauer)

5 Collapse of dipolar condensates

The subject of this section is the controlled collapse of dipolar condensates in different harmonic trapping potentials. While we obtained the threshold between a stable and an unstable dipolar condensate in the previous section, we will now present its time evolution, if this threshold is passed. After describing the experimental procedure used to induce the collapse, we compare the experimental data with three-dimensional simulations of the Gross-Pitaevskii equation (GPE) including 3-body losses. Since the anisotropy of the dipolar interactions breaks the spatial symmetry, four different trap geometries are studied: a prolate trap, two non-cylindrical traps with interchanged trap frequencies ($f_y \leftrightarrow f_z$), and an oblate trap. Parts of this section are published in [244, 245] in a close collaboration with Ueda's theory group in Tokyo.

5.1 Phenomenological description of the collapse

The collapse of a purely contact interacting condensate was first experimentally observed in ^{7}Li [9–11, 56] and ^{85}Rb [57, 59, 113]. It is a complex phenomenon exhibiting many surprising effects such as anisotropic atom bursts, radial jets, or the formation of remnant soliton trains [246, 247]. Nevertheless, these extensive studies resulted in a consistent and simple explanation [248, 249], whose basic principle is similar to the dipolar case. Therefore, we start by summarising the collapse for purely contact interacting condensates.

Suppose the collapse is initiated in a spherical harmonic trap by abruptly changing the scattering length from repulsive to attractive interactions. When the scattering length becomes sufficiently negative[128], the quantum pressure (arising from the Heisenberg's uncertainty principle) does no longer counter balance the inter-particle attractions. The cloud starts to shrink. Thereby, the density increases, and thus enhances the attraction. However, the contraction accelerates non-uniformly over the cloud — it is largest in the region close to the trap center, where the density has its maximum. This non-uniform acceleration is important, because it allows for a *local* collapse.

The local collapse can be understood as follows: Initially, just after the abrupt change of the scattering length, the spatial density is well approximated by a Gaussian distribution. However, the non-uniform acceleration slowly generates a narrow density peak on top of it [249]. Although it might take several trap periods to develop this non Gaussian density

[128] In the context of the section 4.2 (scaling instability model) the local minimum has to disappear.

distribution (depending on how deep the scattering length was ramped down into the unstable region), eventually this central peak rapidly grows. Within a fraction of the trap period it increases by orders of magnitude — the condensate collapses.

Up to this point the standard time dependent GPE (2.7a) is sufficient to describe the dynamics. However, due to the tremendously increasing density, the 3-body collision rate becomes non-negligible. A 3-body collision allows for the production of a dimer, where the third contributing atom is needed to fulfill energy and momentum conservation. The binding energy which is absorbed by the atom and the molecule in form of kinetic energy is sufficient for both to escape from the trap[129]. Hence, instead of reaching a fully contracted, point-like state, more and more atoms are lost so that finally the quantum pressure dominates over the remaining interaction energy.

Then, the dynamics inverts. The atoms from the central region accelerate outwards to the *new* equilibrium state. Since the 3-body losses have changed the total energy, this new equilibrium state differs from the initial one. Therefore, the outwards accelerating atoms (stemming from the central peak) are observed as *bursts*. With the atoms removed from the central region, subsequent collapses and bursts are possible. Furthermore, since the atom bursts belong to the condensate, they are expected to be coherent. Therefore, if two local collapses are simultaneously induced in a prolate trap, their bursts produce radial interference fringes. These interferences are the so called *jets*, observed in [57].

A collapsing dipolar condensate is expected to constitute the same three-fold action as just described for the case of a purely contact interacting BEC — (*i*) a "slow" contraction initiating the collapse, followed by (*ii*) the *collapse*[130]: a "fast" contraction of the condensate, which is accompanied by atom losses, and which results in (*iii*) an explosion. However, the details of its dynamics are expected to be quite different: While in the case of purely contact interacting condensates it is surprising that the atom bursts are not isotropic, one would expect to find something anisotropic in the dipolar case. Furthermore, we know from the discussion in section 4 that the cloud's aspect ratio κ determines the dipolar energy contribution. Therefore, depending on κ, the dipolar interactions either induce or stabilise the condensate against the collapse. Hence, one expects that the dynamics of the collapse strongly depend on the trap geometry.

Time scale of the collapse

For purely contact interacting condensates the time scale which governs the "usual dynamics" of a non-collapsing cloud is set by the largest trap frequency. In contrast,

[129] A sample is in the collisionless (hydrodynamic) regime if the mean free path between two collisions is much larger (smaller) than the size of the condensate [250]. Assuming a homogeneous condensate with spatial density $n = 10^{15}\,\mathrm{cm}^{-3}$ and scattering length $a \approx a_{\mathrm{dd}}$, the mean free path is given by $1/(\sqrt{2}\,n\,\sigma_{\mathrm{at}}) \approx 40\,\mu\mathrm{m}$, where $\sigma_{\mathrm{at}} \equiv 8\pi a^2$ is the atom-atom scattering cross-section.

[130] Some authors use different definitions of the collapse. However, for us it is a *fast* and *non-reversible* process.

for dipolar condensates this time scale is given by the largest *radial* trap frequency[131] $\tau_x \stackrel{\text{def}}{=} 2\pi/\omega_x$, because the collapse is induced in radial direction (see section 4.2).

5.2 Collapse of dipolar condensates for different harmonic trap geometries

It follows from the above discussion that a Gaussian wavefunction would certainly not be sufficient to describe the rich dynamics of a collapsing dipolar condensate. It is even not *a priori* clear, whether the three-dimensional time dependent GPE (2.7a) provides a good description. The collapse could induce many-body quantum correlations, which are not included in the mean-field description of the GPE. However, we will find excellent agreement between the experiment and the simulations using the *generalised Gross-Pitaevskii equation*

$$i\hbar\frac{\partial}{\partial t}\Psi(\boldsymbol{r}) = \left(-\frac{\hbar^2}{2m}\boldsymbol{\nabla}^2 + V_{\text{trap}}(\boldsymbol{r}) + \Phi_{\text{int}}^{(N)}(\boldsymbol{r}) - \frac{i\hbar}{2}L_3\left|\Psi(\boldsymbol{r})\right|^4\right)\Psi(\boldsymbol{r}) \tag{5.1}$$

where the non-hermitian term $-\frac{i\hbar}{2}L_3\left|\Psi(\boldsymbol{r})\right|^4$ describes 3-body losses. The *3-body loss coefficient* L_3 was estimated[132] to be $L_3 \lesssim 2\cdot 10^{-28}\,\text{cm}^6/\text{s}$ by measuring the $1/e$ lifetime of the condensate in the vicinity of the Feshbach resonance, see fig. 3.5. The codes for the fully numerical three-dimensional simulations of the GPE (5.1) have been developed recently and are now available in several groups (e.g., Ueda *et al.* in Tokyo [244], Wunner *et al.* in Stuttgart [71], or Bohn *et al.* in Boulder [251]).

5.2.1 Experimental sequence to induce the collapse

In order to produce a BEC dominated by dipolar interactions we use the experimental procedure described in section 3 and sketched in fig. 5.1: We condense approximately 50 000 atoms in a far detuned crossed optical dipole trap at $B \approx 600\,\text{G}$ corresponding to a scattering length $a_{\text{evap}} \approx 85\,a_{\text{B}}$. The magnetic field is directed along the z-direction and fully polarises the atoms. Then, we shape the external confining potential to obtain the desired ratio of the trapping frequencies $\lambda \equiv \omega_z/\omega_y$ by adjusting the power in each beam — only for pancake-shape traps ($\lambda > 1$) we superimpose an additional one-dimensional optical lattice along the z-direction. Afterwards, we first adiabatically ramp the current in the offset coils linearly in 8 ms to a scattering length a_{i} close to the point where the collapse occurs, and wait for 1 ms for eddy currents to faint out (see section 3.3.3). Subsequently, we decrease the current linearly within 1 ms to a value corresponding to the scattering a_{f}, which lies below the critical scattering length $a_{\text{crit}}(\lambda)$ for the given trapping potential, see

[131] In the following, this will always be the x-direction (imaging axis), due to the configuration of the laser beams.

[132] A sophisticated measurement of L_3 as in [118] was not performed.

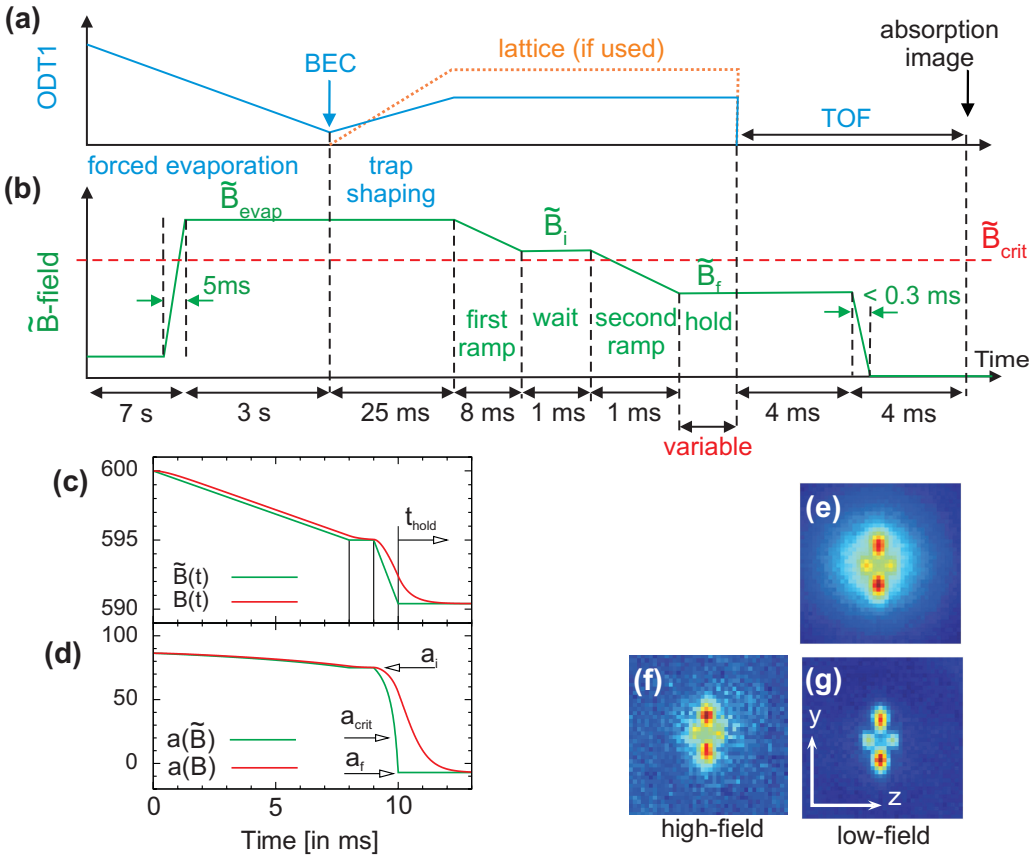

Fig. 5.1, Experimental sequence and image processing: A sketch of the laser and magnetic field ramps used to measure the collapse is shown in (a) and (b). While (c) highlights the magnetic fields produced by the offset coils without $\tilde{B}(t)$ and with $B(t)$ eddy currents, the corresponding scattering lengths[133] are shown in (d). One example of a single absorption image is presented in (e). By fitting a Gaussian distribution to the wings of the image — excluding the central region — the thermal background is removed and (g) is obtained. While (g) was taken at $B_x \approx 11$ G after switching-off the Feshbach field, (f) shows the image for the same experimental parameters taken at $B_z \approx 600$ G. Comparing (f) and (g) shows, that the switch-off does not disturb the shape of the expanding condensate. (Details to (e-g) are given in section 5.2.3)

section 4.2. We hold the atoms in the trap for a variable time t_{hold} at a_{f} before releasing them and taking an absorption image after 8 ms of expansion.

In order to get the maximal light absorption cross-section (see section 3.3.3) we split the time-of-flight into two parts: a first part, lasting 4 ms, at the magnetic field corresponding to a_{f} (in order not to disturb the dynamics) and a second part, lasting again 4 ms, where the large magnetic field along z is replaced by a field of 11 G along the x-direction. However, because the PI-loop[99] — which controls the current in the offset coils (producing

[133]Internal link to the program 'EddyCurrents.nb'.

the Feshbach field) — is much slower than the push-pull [252] — used to switch-off the current in the pinch coils (producing the curvature compensation) — their relative switch-off timing becomes important. Pre-triggering the PI-loop by 0.2 ms, we checked that the total magnetic field switches-off faster than 0.3 ms and that it does not disturb the shape of the expanding cloud, compare fig. 5.1(f, g). However, the switch off slightly magnifies the size of the condensate. Therefore, it should not be used for calibrating the scattering length (section 3.3.2).

The measured column density consists of two parts: (*i*) a broad isotropic thermal cloud, which is well fitted by a Gaussian distribution, and (*ii*) a dense, highly anisotropic central structure, which is interpreted as the remnant BEC[134], fig. 5.1(e). Since the size of the thermal cloud as well as its atom number does not depend on the holding time $t_{\rm hold}$ (within the shot-to-shot fluctuations), it is believed not to contribute to the physics of the collapse, but only be a spectator. Furthermore, we will find excellent agreement between the experiments and the simulations of the GPE for $T = 0$ K. Therefore, we will subtract the thermal cloud from the images and adjust the color scale of each picture separately to maximise the contrast.

In the upcoming section we will study the dependence of the dipolar collapse *dynamics* on the trap geometry. In order to simplify its understanding we like to go ahead and put the experiments already now into their context. In addition, we will point out their shortcomings and how we overcome them. As mentioned in section 4.2 the important parameter for the instability of a dipolar condensate is the effective interaction length $\mathcal{L}(\kappa) \equiv a - a_{\rm dd} f_{\rm dip}(\kappa)$. Thus, we will focus on the aspect ratio $\kappa \equiv \sigma_\rho/\sigma_z$ and not on the trap ratio $\lambda \equiv \omega_z/\omega_\rho$; only in the extreme cases of prolate ($\lambda \ll 1$) and oblate traps ($\lambda \gg 1$) their distinction becomes obsolete. Up to this point we always considered the total energy, which describes the onset of the dipolar collapse. In contrast, its dynamics is governed by the dipolar force. Only because both are closely related, we expect to find the strongest dependency of the dynamics on the trap geometry in the crossover region from a spherical trap ($\lambda = 1$) — where only the dipolar interactions break the spatial symmetry — to a spherical aspect ratio ($\kappa = 1$, corresponding to $\lambda \approx 5.2$, if a Gaussian density distribution is assumed, see section 4.2) — where fluctuations would seed the dipolar dynamics. Therefore, the "perfect experiments" would measure the following:

1. the collapse in a prolate trap ($\lambda \ll 1$),
2. the collapse at several points in the "prolate crossover regime", from $\lambda = 1$ to $\kappa = 1$,
3. the collapse in the "oblate crossover regime", say from $\kappa = 1$ to $\kappa \simeq 5$,
4. and finally the collapse in an oblate trap ($\lambda \gg 1$).

However, these experiments are at the edge of what is technological possible. Furthermore, these "perfect experiments" have to put in contrast to the current experimental set-up.

[134] We do not distinguish between a remnant BEC and a coherent matter-wave.

The two most limiting factors are: the eddy currents and the configuration of the crossed ODT. On the one hand, the eddy currents are on the same order of magnitude as the time scale set by the inverse of the trapping frequencies as well as the lifetime of the atoms[135]. Therefore, they prohibit "abrupt" changes of the scattering length and give rise to non-negligible atom losses during the preparation sequence preceding the collapse. On the other hand, the crossed ODT does not allow cylindrical symmetric trapping potentials, if all three trap frequencies are on the same order of magnitude[136]. Therefore, we will study the crossover of the dynamics from a condensate with mostly attractive dipolar interactions (analog to a prolate cloud) to a condensate with almost equally strong attractive and repulsive dipolar interactions (analog to the spherical cloud) using asymmetric traps, with three distinct trap frequencies. Although the three-dimensional dynamics significantly complicates the understanding of our measurements, their interpretation is still possible by comparing them to numerical simulations. Hence, the experimental challenge is to fine-tune all parameters of the quantum system in order to obtain a good agreement with the simulations.

5.2.2 Collapse of prolate dipolar condensates

Figure 5.2 presents the dynamics of a dipolar condensate in a prolate trap with trap frequencies $(f_x, f_y, f_z) = (1350 \pm 40, 1340 \pm 30, 140 \pm 25)\,\mathrm{Hz}$, which corresponds to a trap ratio of $\lambda \simeq 0.12$. The initial scattering length $a_\mathrm{i} = (35 \pm 2)\,\mathrm{a_B}$ is ramped to $a_\mathrm{f} = (8 \pm 3)\,\mathrm{a_B}$, which lies below the critical scattering length $a_\mathrm{crit} \approx 12\,\mathrm{a_B}$ (obtained from the full GPE solution). However, on the time scale of the fastest radial trap period $\tau_x \approx 0.76\,\mathrm{ms}$ the condensate only starts to split. This is explicitly shown in fig. 5.2(c): The atom number does not drop "abruptly" to its final value, but changes linearly on the time scale τ_x. Therefore, this time evolution does not fulfill the above definition of a collapse.

Nevertheless, we call this dynamics a "moderate collapse" for two reasons, solely based on the simulations: (*i*) the spatial peak density increases during the first 0.1 ms, only subsequently does the condensate split, and (*ii*) if the final scattering length a_f is reduced further, only the "speed" of the collapse changes, but the shape of the density distribution (which drives the dynamics) is maintained. Therefore, apart from rescaling the time axis, the collapse is insensitive to the final scattering length a_f. However, note that the splitting of the condensate is *not* a direct evidence of the collapse. If the final scattering length is ramped only to $a_\mathrm{f} = 17\,\mathrm{a_B} > a_\mathrm{crit}(\lambda)$ the cloud splits as well. We checked experimentally

[135] Note that the time scale τ_dd for DDIs is of the order of 10 ns and therefore not limiting us.

[136] Whereas ODT1 propagates along the z-direction, ODT2 propagates along the y-direction. Therefore, neglecting the longitudinal contribution of each laser beam, the trap frequencies f_x and f_y always differ. While the difference is small for prolate traps, it is large if all three trap frequencies are on the same order of magnitude. The measurements, where we additionally used one of the "lattice beams", were never completed.

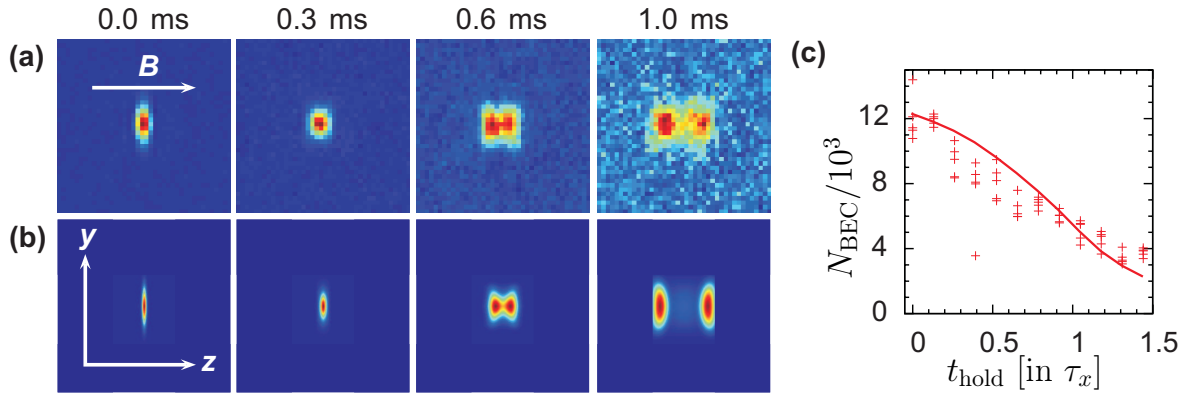

Fig. 5.2, Collapse of a prolate dipolar condensate: Comparison of the experimental absorption images (a) with the simulations (b) for different in-trap holding times t_{hold}, which are given above each image. The trap frequencies are $(f_x, f_y, f_z) = (1350 \pm 40, 1340 \pm 30, 140 \pm 25)$ Hz, the final scattering length is $a_{\mathrm{f}} = (8 \pm 3)\, a_{\mathrm{B}}$. Each image shows the averaged column density of five pictures taken after 8 ms of expansion. The field of view is $250 \times 250\, \mu\mathrm{m}^2$. The remnant condensate atom number is shown in (c) as a function of the holding time in units of the fastest radial trap period $\tau_x \equiv 1/f_x \simeq 0.76$ ms. The solid line is the result of the numerical simulation without any adjustable parameter.

that the splitting is not due to excitations during the magnetic field ramps: When we decrease the speed of the ramps by a factor of three[137] we still obtain equivalent dynamics. Therefore, we attribute the splitting to the dipolar interactions in the three-dimensional[138] cigar-shape cloud[139].

5.2.3 Collapse of dipolar condensates in asymmetric traps: Crossover from prolate to round column density

This section presents the crossover in the collapse dynamics from a condensate with mainly attractive dipolar interactions to a condensate with almost equally strong attractive as repulsive dipolar interactions. However, this is not straight forward, because the set-up does not allow for cylindrically symmetric trapping potentials, and thus we have to use asymmetric traps with three distinct trap frequencies instead. The question is, how to reduce the coupled parameter space (f_x, f_y, f_z) in order to observe a crossover which is similar to those along the $(f_x = f_y = \mathrm{const})$-line?

[137] Note that even this "slow" ramp does not fulfill the adiabaticity criterion $\dot{a}/a \ll f_{\mathrm{min}}$, but only provides $\max\{|\dot{a}/a|\} \approx 700$ Hz. (Internal link to the program 'EddyCurrents.nb'.)

[138] The condensate is not in the quasi one-dimensional regime ($k_{\mathrm{B}}T, \mu \ll \hbar\omega_\rho$), because $\hbar\omega_\rho/k_{\mathrm{B}} \approx 60$ nK and its temperature is $T \geq 100$ nK.

[139] The aspect ratio $\kappa \equiv \ell_\rho/\ell_z$ exceeds unity for $t_{\mathrm{hold}} = 0$ ms, although a condensate with strong dipolar interactions does not invert its ellipticity during the time-of-flight.

It turned out that this technical complication is "resolved" by fixing the trap frequency parallel to the imaging axis[140] (x-direction). Imposing this artificial constraint simplifies the interpretation of our measurements, because it defines a single line in parameter space along which we observe the crossover behaviour[141]. Furthermore, by choosing $f_x > f_y$ we ensure that the collapse is always initiated in x-direction.

In the following we will present two data sets with interchanged trap frequencies, $f_y \leftrightarrow f_z$. Since the trap is not cylindrical symmetric in the crossover region, neither a prolate nor spherical cloud does exist. However, regarding the desired attractive and repulsive forces, these terms are replaced by a cloud with a *prolate*[142] *column density* ($\kappa_{y,z} \stackrel{\text{def}}{=} \sigma_y/\sigma_z < 1$) and a cloud with a *round column density* ($\kappa_{y,z} = 1$) with respect to the line-of-sight.

Trap 1: Prolate column density

Figure 5.3 shows the collapse in a trap with trapping frequencies $(f_x, f_y, f_z) = (650 \pm 30, 520 \pm 20, 400 \pm 20)$ Hz, corresponding to $\tau_x \approx 1.5$ ms. In the experiment we start with $N_{\text{BEC}} = 13\,500 \pm 1\,500$ atoms before ramping the scattering length non-adiabatically from $a_{\text{i}} = (35 \pm 2)\,\text{a}_\text{B}$ to $a_{\text{f}} = (8 \pm 3)\,\text{a}_\text{B}$, which lies $4\,\text{a}_\text{B}$ below the critical scattering length obtained by solving the full GPE. However, the simulations agree better, if $a_{\text{f}}^{(\text{sim})} = 2\,\text{a}_\text{B}$ is used instead. This discrepancy is most probably due to slow drifts in the magnetic fields and/or the alignment of the crossed ODT. Since the experimental calibration of the scattering length rely on data not taken at the same day as the measurements shown in fig. 5.3, the experimental scattering lengths contain an additional systematic error (not included in the stated errors). Therefore, we compare the experimental data to simulations performed for $a_{\text{f}} = 2\,\text{a}_\text{B}$.

The presented absorption images indicate a highly anisotropic dynamics, which consist of three different stages: First, for $t_{\text{hold}} = 0$ ms, the condensate is strongly elongated along the magnetic field direction, demonstrating dominant dipolar interactions [165]. Second, we observe an inversion of ellipticity after $t_{\text{hold}} \approx 0.3$ ms corresponding to $0.2\,\tau_{\text{x}}$. This is a consequence of the radial implosion and subsequent explosion, because a stable cigar-shape condensate with sufficient strong dipolar interactions does not invert its ellipticity during the free expansion (see section 2.3.5). Note that if the 3-body atom losses were absent only the implosion would occur, but not the explosion. Third, we observe a splitting of the condensate in axial direction, similar to fig. 5.2. For longer holding times the splitting becomes more pronounced. However, the dynamics is completed after

[140] The fixed trap frequency f_x is not large enough to be in the quasi two-dimensional regime. Thus, the constraint does not freeze the dynamics in x-direction. The dynamics of the condensate remains three-dimensional.

[141] As we are using a crossed ODT, only two trap frequencies can be chosen independently. Therefore, the constraint $f_x = \text{const}$ defines a single line in the three-dimensional parameter space (f_x, f_y, f_z).

[142] Notation: We refer to a prolate (oblate) column density, when the major (minor) axis of the elliptical x-integrated column density is parallel to the magnetic field direction. As the shape of the condensate will change with the holding time t_{hold}, the prolate (oblate) column density refers only to the time $t_{\text{hold}} = 0$ s, when the collapse is initiated.

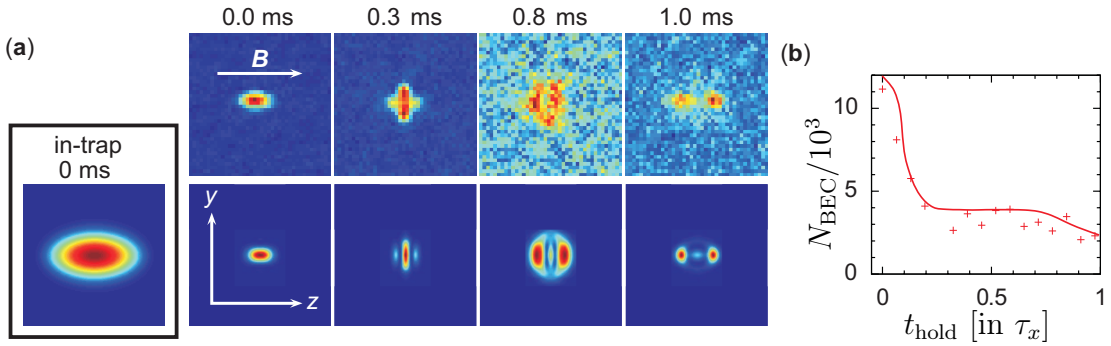

Fig. 5.3, Collapse of a cloud with prolate column density: The simulated in-trap column density for $t_{\mathrm{hold}} = 0$ ms is shown in (a) together with absorption images of condensates after 8 ms of free expansion. The condensates are kept for a variable time t_{hold} (indicated above each image) in a trap with frequencies $(f_x, f_y, f_z) = (650 \pm 30, 520 \pm 20, 400 \pm 20)$ Hz. While the upper graphs present measured single absorption images, the lower graphs are obtained by numerically solving eq. (5.1). The field of view is $250 \times 250\,\mu\mathrm{m}^2$ for all expanded clouds and $6.9 \times 6.9\,\mu\mathrm{m}^2$ for the in-trap image. While the measured final scattering lengths is $a_{\mathrm{f}} = (8 \pm 3)\,\mathrm{a_B}$ the simulations use $a_{\mathrm{f}}^{(\mathrm{sim})} = 2\,\mathrm{a_B}$ (see text). The measured (crosses) and simulated (solid curve) atom number is shown in (c) as a function of the holding time t_{hold} in units of $\tau_x \equiv 1/f_x$.

$t_{\mathrm{hold}} = 0.8$ ms $\approx 0.5\,\tau_{\mathrm{x}}$. Therefore, this evolution satisfies our definition of a collapse, with its rich dynamics on a time scale shorter than the fastest radial trap period.

That the dynamics is completed after $t_{\mathrm{hold}} \approx 0.5\,\tau_{\mathrm{x}}$ is explicitly shown in fig. 5.3(b): The atom number of the remnant condensate $N_{\mathrm{BEC}}(t)$ drops from 12 000 to 4 000 within this time scale. Although the simulations exhibit atom losses for $t_{\mathrm{hold}} \geq 0.8$ ms, which are produced in the two dense "blobs" of the remnant condensate, these atom losses are weak and do neither induce a second collapse, nor change the expected dynamics.

Trap 2: Round column density

In order to initiate the collapse in a condensate with a round $\kappa_{y,z}$ column density we use a trap with frequencies $(f_x, f_y, f_z) = (660 \pm 40, 380 \pm 20, 530 \pm 25)$ Hz and ramp non-adiabatically from $a_{\mathrm{i}} \approx 30\,\mathrm{a_B}$ to $a_{\mathrm{f}} \approx 5\,\mathrm{a_B}$. The fixed trap frequency f_x provides again the time scale for the collapse, $\tau_x \approx 1.5$ ms. The final scattering length a_{f} is well below the critical scattering length $a_{\mathrm{crit}} = (15 \pm 3)\,\mathrm{a_B}$ calculated from the full GPE.

Figure 5.4 compares the measured dynamics to simulations of the generalised GPE (5.1) with no adjustable parameter. Since the dipolar interactions break the spatial symmetry, the interchange of the trap frequencies $f_y \leftrightarrow f_z$ does not correspond to the a rotation of the absorption image by 90°, but results in a new dynamics. Therefore, the absorption images differ significantly from those of the previous collapse. Nevertheless, the crossover in the collapse dynamics from a condensate with mainly attractive dipolar interactions

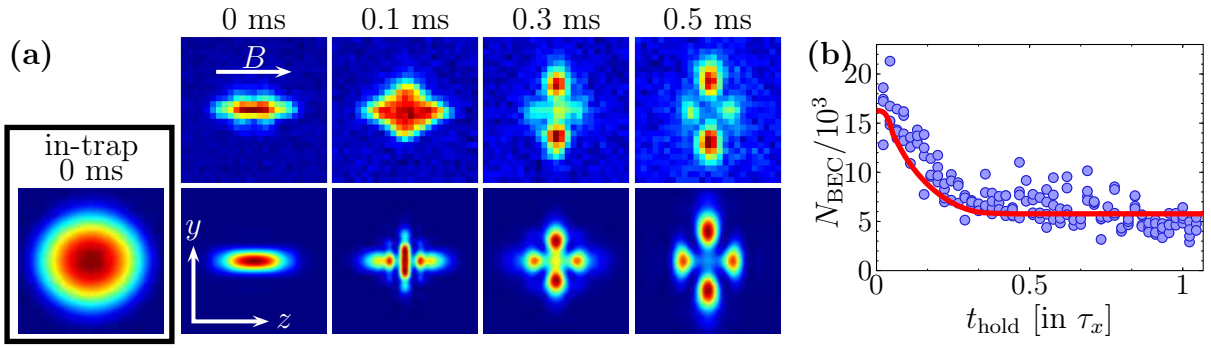

Fig. 5.4, *d*-wave collapse of a BEC with round column density: (a) Comparison of the measured (upper row) and simulated (lower row) dynamics for different holding times $t_{\rm hold}$ of a condensate confined in a $(f_x, f_y, f_z) = (660 \pm 40, 380 \pm 20, 530 \pm 25)$ Hz trap. Each picture is an average of five absorption images after 8 ms of expansion. The field of view is $130 \times 130\ \mu$m^2 for all expanded clouds and $5 \times 5\ \mu$m^2 for the $t_{\rm hold} = 0$ ms in-trap column density. (b) Measured (blue circles) and simulated (red solid curve) condensate atom number during the collapse in units of $\tau_x \equiv 1/f_x$.

to a condensate providing strong attractive as well as repulsive dipolar interactions is clearly visible: Again, the radial contraction is inverted into a radial explosion. However, this time the axial attraction is weaker. Thus, the condensate almost maintains its axial size. It generates an anisotropic structure, whose x-integrated column density obtains a cloverleaf-like shape[143] for "long" $t_{\rm hold}$. While this pattern was only vaguely sketched in the simulated $t_{\rm hold} = 0.3$ ms image in fig. 5.3(a), the round column density amplifies it. It becomes prominent. Figure 5.4(b) shows that the dynamics is completed after $t_{\rm hold} \simeq 0.4\,\tau_{\rm x}$. Therefore, for longer holding times we merely observed the reflection of the remnant condensate from the trapping potential — due to the different trap frequencies the refocusing of the cloud is imperfect, see fig. 5.5.

The simulations reveal that the three-dimensional density distribution $n(\boldsymbol{r}) \equiv |\psi(\boldsymbol{r})|^2$, whose projection provides the cloverleaf-like pattern, resembles the shape of a donut[144] plus a dumbbell. Therefore, the collapse of the round in-trap column density exhibits the d-wave symmetry $Y_{2,0}(\vartheta)$ of the dipole-dipole interaction potential[145] $V_{\rm dd}(\boldsymbol{r})$, see appendix A.5.1 (page 108). The d-wave pattern can be understood by the fact that the collapse happens during the free expansion for all images shown in fig. 5.4(a), except for $t_{\rm hold} = 0.5$ ms: Since the trap is already switched off when the collapse occurs, it does not

[143] The presented pictures are raw absorption images. However, a Savitzky-Golay filter (internal link to the program 'SavGol2D.m') was useful at first place. It helped to identify the pattern.

[144] The donut radius depends on the azimuthal angle φ, due to the non-cylindrical trap symmetry, see fig. 5.6.

[145] In section 2.3.4 (page 31) we have shown that the dipolar mean-field potential $\Phi'_{\rm dip}(\boldsymbol{r})$ preserves the d-wave symmetry of the dipole-dipole interaction potential $V'_{\rm dd}(\boldsymbol{r})$ for a spherical symmetric density distribution in the Thomas-Fermi limit. Here, the condensate has only a round $\kappa_{y,z}$ column density and it is not in the Thomas-Fermi regime. The experimental observation suggests that $\Phi'_{\rm dip}(\boldsymbol{r})$ remains d-wave symmetric, nevertheless.

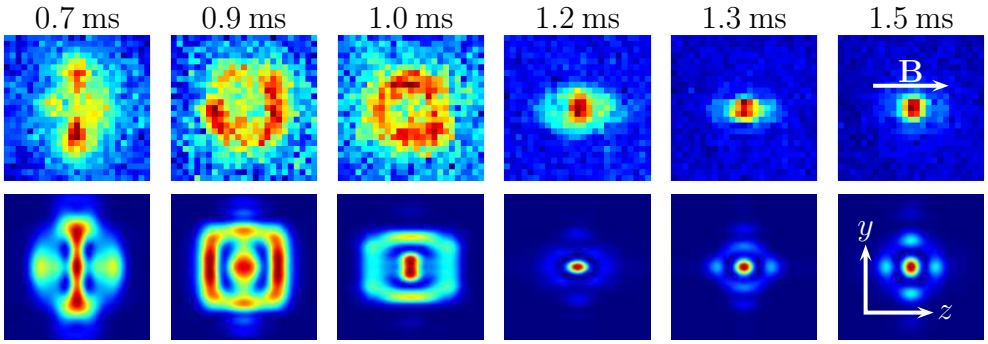

Fig. 5.5, Refocusing of the collapsed condensate: The experimental data (upper row) and simulation (lower row) are for the same parameters as in fig. 5.4, but for longer holding times t_{hold}. The cloverleaf-like pattern refocuses due to the presence of the trapping potential.

disturb the explosion dynamics of the remnant condensate. It only influences the initial potential landscape ($V_{\mathrm{trap}} + \Phi_{\mathrm{int}}$) in which the collapse is initiated. Therefore, the round column density reflects the anisotropy of the dipolar mean-field interaction potential.

Furthermore, the simulations do not only provide the density $n(\boldsymbol{r})$, but the complete wavefunction $\psi(\boldsymbol{r}) = \sqrt{n(\boldsymbol{r})}\,\mathrm{e}^{iS(\boldsymbol{r})}$ including the phase $S(\boldsymbol{r})$. They predict the generation of two *vortex rings* with opposite charges ± 1. Vortices are quantised topological defects, which are closely connected to the concept of superfluidity. They appear, because a superfluid has a well defined macroscopic phase (see section 6). Therefore, it does not accommodate any angular momentum, unless the superfluid density vanishes at the center of the rotational flow [253–255].

Figure 5.6(a) shows an simulated in-trap iso-density surface for $t_{\mathrm{hold}} = 0.8\,\mathrm{ms}$, which exhibits the two vortex rings (indicated in red). They are produced by the collapse, which generates an anisotropic flow of density. This is shown in fig. 5.6(b), which presents the velocity field $\boldsymbol{v}(\boldsymbol{r}) \stackrel{\mathrm{def}}{=} \frac{\hbar}{m}\boldsymbol{\nabla} S(\boldsymbol{r})$ of the condensate in the $x = 0$ plane. Although the radial explosion occurred already, and therefore the flow of the spatial density points radially outward, the axial spatial density still flows inwards. Hence, the collapse produces a circulation of the density, which gives rise to the four non-superfluid spots.

The existence of the vortex rings is specific to the dipolar collapse. Although the bursts break the spatial symmetry, the collapse and explosion of purely contact interacting condensates is mainly isotropic and does not give rise to vortex rings [256]. However, we did not observe vortex rings in the experiment, but only measured density distributions, which are consistent with their presence.

Unfortunately, neither did we observe the crossover from a cloud having a round column density to a cloud having an oblate column density ($\kappa_{y,z} > 1$), because the gravitational force does not allow to decrease the power of the ODT1 further without loosing the

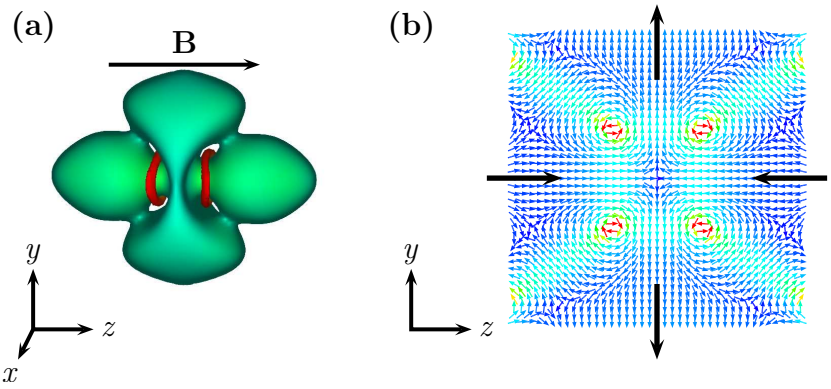

Fig. 5.6, Vortex rings: Having access to both, the amplitude and the phase of the condensate's wavefunction, the simulations predict topological defects located on a ring. While (a) presents the three-dimensional in-trap iso-density surface for $t_{\mathrm{hold}} = 0.8\,\mathrm{ms}$ (the vortex rings are indicated in red), the corresponding velocity field of the density $\boldsymbol{v}(\boldsymbol{r}) \equiv \hbar/m\,\boldsymbol{\nabla} S(\boldsymbol{r})$ in the $x = 0$ plane is shown in (b). The field of view is $2.5 \times 2.5\,\mu\mathrm{m}^2$, the color scale represents the modulus of the velocity field (blue is slower, red is faster). The black arrows emphasise the "quadrupole mode".

atoms[146]. Therefore, the following section discusses only the dipolar collapse of an oblate condensate. However, before doing so, we like to comment on the debate of local vs. global collapse.

Local vs. global collapse

In [257] a definition of the character of the collapse is given: "global and local collapse depending, respectively, upon whether [the modulus of] the (imaginary) healing length [...] is of the same order as, or much smaller than the size of the BEC." The authors analyse our measurements [237, 244, 258] of the dipolar collapse and conclude that "the system appears to undergo a global collapse *via* a quadrupole mode." However, the authors in [73, 243] obtain exactly the opposite conclusion: Referring to the same measurements, they compare the instability diagram obtained from the Gaussian model and for the full GPE (section 4.2). Attributing their deviation to the *onset* of a rotonic structure, they write "the data supports the idea of a local collapse."

The origin of this apparent contradiction is that the authors define the term "collapse" differently[147] — neither definition agrees with the definition we put forward in section 5.1. In order to resolve the contradiction we present the simulated in-trap images in fig. 5.7. It shows that the "slow" radial contraction incorporates the hole cloud, while the "fast" contraction and the subsequent explosion happen only in a small region in the center of

[146] In order to measure both crossovers in the current set-up one would have to increase the power in both beams (ODT1 and ODT2) and to re-measure the collapse for the prolate and round column density.

[147] They agrees on the physics (the dynamics of an unstable dipolar condensate), but they attribute different meanings to the word "collapse".

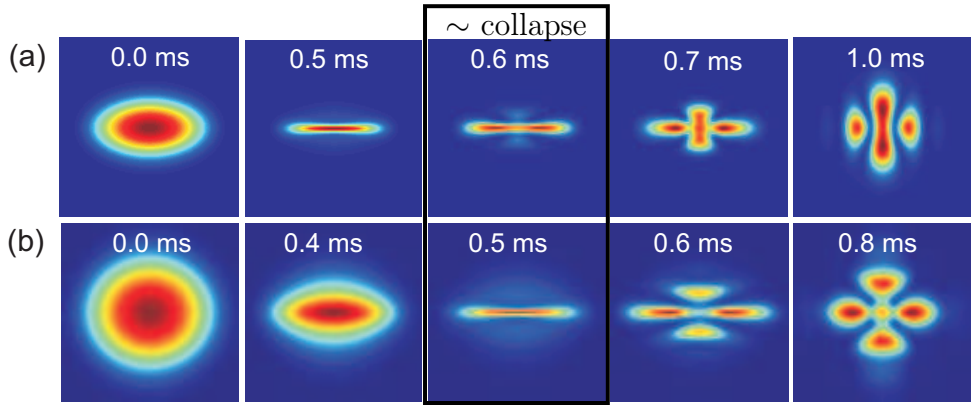

Fig. 5.7, Local dipolar collapses: The images in (a) and (b) show the simulated in-trap absorption images for the cloud with a prolate and almost round $\kappa_{y,z}$ column density (same parameters as in fig. 5.3 and 5.4). As the radial contraction and subsequent explosion occur only in the central region of the condensates, these are both local collapses.

the condensate. Therefore, the collapse is global, if it includes the "slow" contraction. In contrast, it is local if it includes only the "fast" contraction — definition of the term "collapse" in this thesis. However, note that the condensate's wavefunction (prior to the collapse) does not exhibit a bi-concave density distribution.

5.2.4 Collapse of oblate dipolar condensates

The pancake-shape BEC is generated by first producing a condensate in the crossed ODT and subsequently superimposing a one-dimensional optical lattice, with lattice spacing $d_{\mathrm{lat}} = (7.4 \pm 0.2)\,\mu$m in the z-direction (see section 3.2.5). Depending on the non-stabilised relative phase of the two laser beams forming the optical lattice, it is in principle possible that the condensate splits into two. However, we have never observed interference fringes in the experiments, even for expansion times t_{tof} long enough such that the fringe spacing $\Lambda \equiv h t_{\mathrm{tof}}/(m d_{\mathrm{lat}})$ exceeded our resolution limit. The trap frequencies of the oblate condensate are given by $(f_x, f_y, f_z) = (400 \pm 30, 400 \pm 30, 3400 \pm 130)$ Hz. While we used the technique of parametric heating [259, 260] to obtain the trap frequency in z-direction, all other trap frequencies stated in this thesis were measured by "kicking" the condensate out of its equilibrium position and observing its center-of-mass oscillation [136, ch. 5.2.2].

Figure 5.8(a) compares the measured and simulated absorption images for different holding times. As before, both agree well. For all shown t_{hold} the collapse happens during the free expansion such that the remnant condensate is not disturbed by the presence of the trap. In addition, fig. 5.8(b) and (c) show three-dimensional iso-density surfaces $n(\rho, z)$ for different optical densities and $t_{\mathrm{hold}} = 0.4$ ms. They are recovered from the two-dimensional

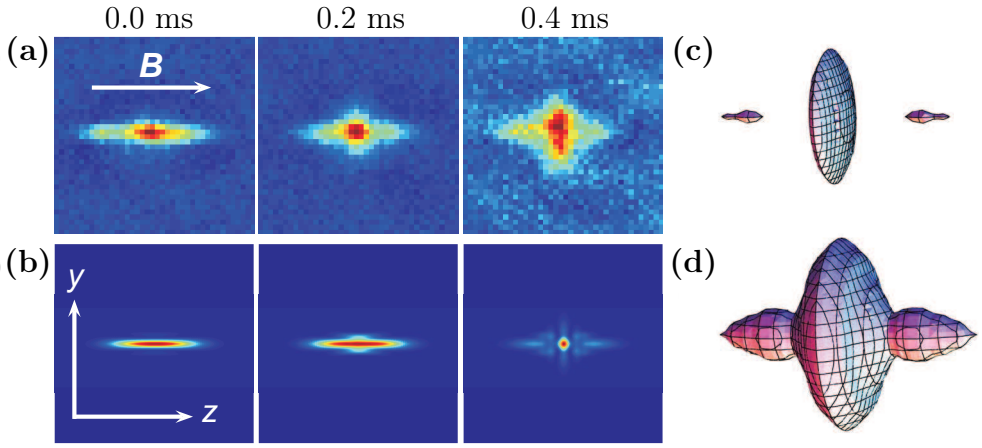

Fig. 5.8, Collapse of an oblate dipolar condensate: (a) The collapse dynamics for different holding times t_{hold} in a pancake-shape trap, which corresponds to trap-frequencies $(f_x, f_y, f_z) = (400 \pm 30, 400 \pm 30, 3400 \pm 130)$ Hz, trap ratio $\lambda \approx 8.5$ and radial period $\tau_x \simeq 2.5$ ms. The upper row present the average of five absorption images after 8 ms of free expansion. The final ramp starts at $a_{\mathrm{i}} = (30 \pm 2)\, a_{\mathrm{B}}$ and stops at $a_{\mathrm{f}} = (-13 \pm 2)\, a_{\mathrm{B}}$. The simulations provide $a_{\mathrm{crit}} = (-1.5 \pm 0.5)\, a_{\mathrm{B}}$. The field of view is $250 \times 250\ \mu$m. Iso-density surfaces for "high" (b) and "low" (c) densities of the $t_{\mathrm{hold}} = 0.4$ ms image obtained from the Abel transformation.

density distribution $n_{\mathrm{abs}}(y, z)$ of the measured absorption image by using the *inverse Abel transformation* (see appendix A.4)

$$n(\rho, z) = \frac{1}{2\pi} \int_0^\infty dk\ k \cdot J_0(k \cdot \rho) \int_{-\infty}^\infty dy\ n_{\mathrm{abs}}(y, z)\ \exp\left(-ik \cdot y\right) \tag{5.2}$$

where $J_0(x)$ is the Bessel function of the first kind. As in the case of the cloud with a round in-trap column density, the remnant condensate exhibits the d-wave symmetry $Y_{2,0}(\vartheta)$. Although the released kinetic energy is obtainable from the three-dimensional density distribution $n(\rho, z)$ in principle, we could not reliably extract it from the images of the collapsed condensates, because the Abel transformation is very sensitive to noise.

Summary

This section presented the dynamics of collapsing dipolar condensates in different trap geometries. Independent of the confining potential the collapse was initiated by ramping the scattering length across the stability threshold $a_{\mathrm{crit}}(\lambda)$. This resulted in a radial contraction followed by a radial explosion — except for the prolate trap, where the condensate merely splitted axially. The anisotropy of the dipolar interactions became particularly prominent in the case where all three trap frequencies were similar. All experiments were well reproduced by three-dimensional simulations of the Gross-Pitaevskii equation including 3-body losses.

"A physicist is just an atom's way of looking at itself." (Niels Bohr)

6 Phase-coherence of collapsed matter-waves

Analysing the collapse of dipolar condensates in different harmonic trapping potentials in the previous section, we showed that the collapsed cloud exhibits two parts: one part, which is well described by a thermal Gaussian distribution, and a second part, which we interpreted, because of its high optical density, as a remnant condensate. In order to confirm this interpretation we will check the phase-coherence of the collapsed cloud in the case of an array of pancake-shape traps[148].

The present section is structured as follows: First, we give a short introduction to the physics of interfering condensates. After discussing a one-dimensional model containing two isolated point-like condensates, we extend the description to the interference of multiple isolated BECs. Finally, we present the coherence experiments performed with the collapsed dipolar condensates.

6.1 Simple model of two interfering condensates

The phase-coherence (also called first-order coherence) is one of the most fascinating aspect of BECs. Giving rise to long-range order and therefore to a macroscopic wavefunction, it lies at the heart of superfluidity [20, appendix]. However, it was not clear *a priori* if this description of a condensate — having a macroscopic wavefunction — is correct. As the atom number is fixed, the condensate's wavefunction should be describable by a Fock number state $|N\rangle$ as well. Therefore, the question, whether or not two isolated condensates generate interference patterns similar to those of lasers [261, 262], was only settled after their first observation[149] [264, 265].

Following the discussions in [119, 156, 266, 267], we use a one-dimensional model to describe the interference of two isolated condensates. Neglecting the extension of the condensates, the many-body wavefunction of the combined system is given by the sum of the individual condensate's wavefunctions

$$\psi(z,t) = \sqrt{n_1}\,\mathrm{e}^{iS_1(z,t)}\,\mathrm{e}^{i\alpha_1} + \sqrt{n_2}\,\mathrm{e}^{iS_2(z,t)}\,\mathrm{e}^{i\alpha_2} \tag{6.1a}$$

[148] According to the definition (section 2.1), the atoms need to be in the ground-state of an external potential to generate a BEC. Therefore, a freely expanding cloud is formally not a condensate. However, since we are only interested in the coherence of the collapsed cloud, we will not distinguish between a "coherent matter-wave" and a "condensate".

[149] The analogous question for superfluids is, if two weakly coupled superfluids would result in an observable dc Josephson effect [263].

where n_j is the spatial density of the j^{th} condensate ($j = 1, 2$), $S_j(z,t)$ is its macroscopic phase, and α_j is an arbitrary but fixed global phase. Releasing both condensates from the trap at $t = 0\,\text{s}$, the optical density of an absorption image is proportional to

$$|\psi(z,t)|^2 \propto 1 + 2\frac{\sqrt{n_1\, n_2}}{n_1 + n_2} \cos\Big[\Delta S(z,t) + \Delta\alpha\Big] \tag{6.1b}$$

While $\Delta\alpha \stackrel{\text{def}}{=} \alpha_1 - \alpha_2$ is arbitrary and varies for each experimental realisation, the phase difference $\Delta S \stackrel{\text{def}}{=} S_1 - S_2$ is fixed and determines the spacing $\Lambda \stackrel{\text{def}}{=} \frac{2\pi}{\Delta S}\, z$ of the interference fringes.

In order to estimate the spacing of the interference fringes Λ we assume a sufficient long expansion time ($t = t_{\text{tof}} \gg 1/f_z$, where f_z is the trap frequency) such that the in-trap extension of the condensate as well as the inter-particle interaction is negligible. In this limit the velocity of each condensate is constant[150]. It depends linearly on the position $z/t_{\text{tof}} = v_j \equiv \hbar/m\, \nabla_z S_j(z, t_{\text{tof}})$, and we obtain a Gaussian wavefunction[151] with $S_j(z, t_{\text{tof}}) = mz^2/(2\hbar t_{\text{tof}})$. Being initially located at $z_{1,2} = \pm d_{\text{lat}}/2$, the phase difference of the condensates is $\Delta S = \frac{m}{2\hbar t_{\text{tof}}}\Big[(z + d_{\text{lat}}/2)^2 - (z - d_{\text{lat}}/2)^2\Big]$. Therefore, the *spacing of the interference fringes* $\Lambda = ht_{\text{tof}}/(md_{\text{lat}})$ increases with the time-of-flight.

We estimate the lattice spacing to be $d_{\text{lat}} = (7.4 \pm 0.2)\,\mu\text{m}$ by measuring the fringe spacing Λ for different t_{tof} ranging from 12 ms to 22 ms, see [136, ch. 5.2.2]. Although the model assumes negligible interactions, we expanded the condensates at the background scattering length $a \approx 100\,\text{a}_\text{B}$. This was done for two reasons: First, a large scattering length minimises dipolar effects — while the contact interaction is isotropic, dominant dipolar interactions would modify the initial momentum distribution and thus complicate the dynamics. Second, the time-of-flights are too short to be well within the asymptotic regime[152]. Therefore, we utilise the transformation of interaction energy into kinetic energy to compensate this shortcoming.

The relation between the lattice spacing d_{lat} and the fringe spacing Λ is a general property of the free expansion. The time-of-flight transforms each in-trap length scale x to a length scale $X \simeq ht_{\text{tof}}/(mx)$ after the expansion [156, 268, 269]. The only two requirements are that (*i*) the inter-particle interaction is "negligible", and that (ii) the image is taken in the asymptotic regime, where the in-trap density distribution can be treated as point-like. As we have just seen, the former condition is not very strict.

[150] In the experimental set-up the gravitation is perpendicular to the z-direction. If they were parallel, one would need to transform into the center-of-mass frame.

[151] This was expected, because we neglected interactions. Expressing the time evolution of the wavefunction in its Fourier representation, $\psi(z,t) = \int d\!k\, \text{e}^{-i2\pi kz}\, \tilde{\psi}(k,t) = \int d\!k\, \text{e}^{-i2\pi kz}\, \text{e}^{-iE(\boldsymbol{k})t/\hbar}\, \tilde{\psi}(k,0)$, and using that (*i*) the wavefunction of an ideal gas in an harmonic trap is a Gaussian, $\psi(z,0) = g(z,0)$, (*ii*) the Fourier transform of a Gaussian is a Gaussian, and (*iii*) the dispersion of a free particle is quadratic in the wavevector, $E(\boldsymbol{k}) = (\hbar\boldsymbol{k})^2/(2m)$ such that $\text{e}^{-iE(\boldsymbol{k})t/\hbar}$ becomes a Gaussian as well, we conclude that the time evolution does not change the Gaussian shape of the density $|g(z,t)|^2$, but only its size.

[152] The wavefunction of an ideal gas would spread over approximately three neighbouring lattice sites within the given 22 ms of free expansion.

6.2 Interference of many non-collapsed condensates

In the experiment we superimpose the two beams of the optical lattice *before* finishing the evaporation to reach quantum degeneracy. Therefore, we obtain (depending on the relative phase of the two laser beams with respect to the atoms) between three to five condensates located on adjacent sites. These condensates have a random relative phase, because we start with a thermal cloud and the single particle tunneling rate is vanishingly small — for a deep lattice ($U_0 \gg E_\mathrm{R}$) the *single particle tunneling rate* is given by [208]

$$\frac{J}{h} \approx \frac{4}{\sqrt{\pi}} \frac{E_\mathrm{R}}{h} \left(\frac{U_0}{E_\mathrm{R}}\right)^{3/4} \exp\left(-2\sqrt{U_0/E_\mathrm{R}}\right) \tag{6.2}$$

with the potential depth U_0, the recoil energy $E_\mathrm{R} \stackrel{\mathrm{def}}{=} (\hbar k_\mathrm{lat})^2/(2m)$ and the lattice wavevector $k_\mathrm{lat} \stackrel{\mathrm{def}}{=} \pi/d_\mathrm{lat}$. Putting the experimental parameters $d_\mathrm{lat} \approx 7.4\,\mu$m and $U_0/k_\mathrm{B} \approx 20\,\mu$K, the tunneling rate becomes $J/h \sim 10^{-135}\,\mathrm{s}^{-1}$.

Extending the model of the previous section to more than two interfering condensates, one might expect that the interference pattern washes out as in the transition from a superfluid to a Mott phase [270]. Although this is correct in principle, it is not enough to take only a few (say 30) isolated condensates. This can be easily seen from the following model: Again, the total in-trap wavefunction $\psi_\mathrm{tot}(z,0)$ is taken as a superposition of wavefunctions $\psi_j(z,0)$, which are localised on the j^th lattice site. For simplicity each localised wavefunction[153] is assumed to be a Gaussian of width σ_j containing N_j atoms. After the time-of-flight the total wavefunction becomes [268, 272]

$$\begin{aligned} \psi_\mathrm{tot}(z,t_\mathrm{tof}) &\stackrel{\mathrm{def}}{=} \sum_j \psi_j(z,t_\mathrm{tof}) \qquad (6.3)\\ \psi_j(z,t_\mathrm{tof}) &= \int_{-\infty}^{\infty} d\hbar k\; \mathrm{e}^{i2\pi\hbar k z}\, \tilde{\psi}_j(\hbar k,0)\, \exp\left(-\frac{i}{\hbar}\frac{(h\hbar k)^2}{2m}\, t_\mathrm{tof}\right) \\ &= \frac{\sqrt{N_j}\,\mathrm{e}^{i\alpha_j}}{\pi^{1/4}\sqrt{\sigma_j\,(1+it_\mathrm{tof}/t_{0,j})}}\, \exp\left[-\frac{1}{2}\left(\frac{z-z_0-j\,d_\mathrm{lat}}{\ell_j(t_\mathrm{tof})}\right)^2\right] \end{aligned}$$

with the complex *"coherence length"* $\ell_\mathrm{j}(t) \stackrel{\mathrm{def}}{=} \sigma_j\sqrt{1+it/t_{0,j}}$, the time $t_{0,j} \stackrel{\mathrm{def}}{=} m\sigma_j^2/\hbar$, and where z_0 accounts for the relative phase of the two laser beams. Equation (6.3) can be easily checked: By removing the random phases α_j and assuming equal atom numbers N and sizes σ for each lattice site, this situation is equivalent to the diffraction of a plane wave from a grating [273, 274].

[153] The overlap between the wavefunction at neighbouring lattice sites is underestimated, if Gaussians are used instead of Wannier functions. In the asymptotic limit the Wannier functions decay exponentially [271].

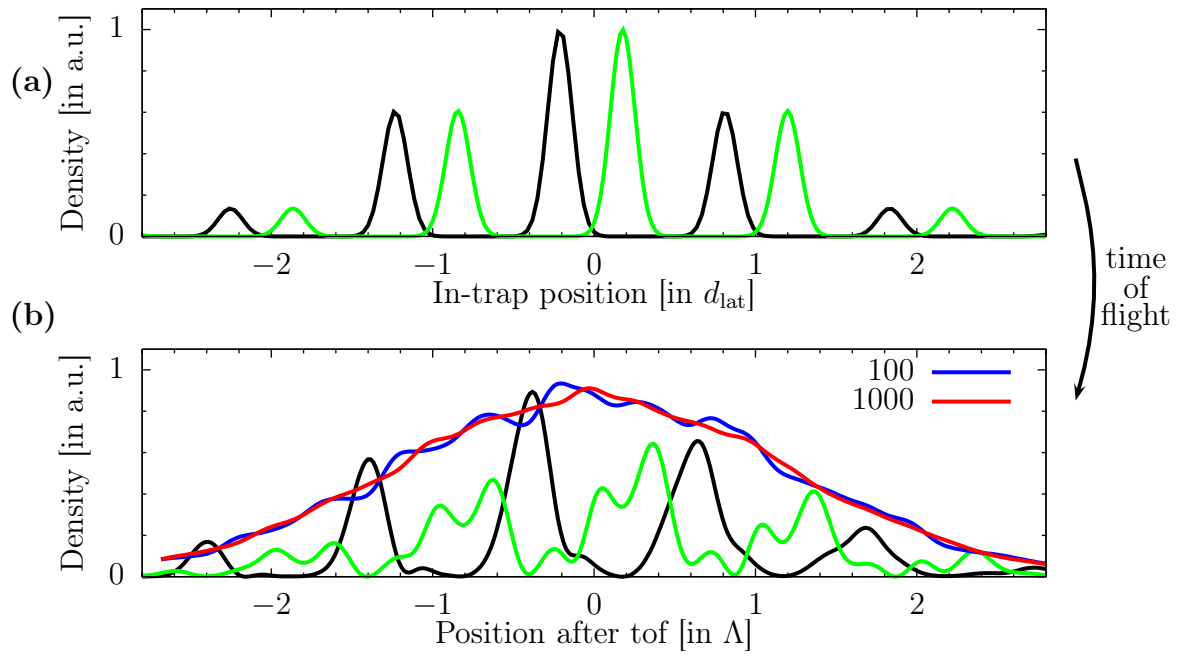

Fig. 6.1, Simulated interference fringes: The in-trap density distribution $|\psi_{\mathrm{tot}}(z, t = 0)|^2$ for two realisations of eq. (6.3) are shown in (a). The envelope function N_j (atom distribution across the lattice sites) as well as the wavefunction on each lattice site ψ_j is a Gaussian. Their $1/e$ radii are $\sigma_N = d_{\mathrm{lat}} = 7.6\,\mu$m and $\sigma_j = 0.8\,\mu$m, respectively. The corresponding densities after $t_{\mathrm{tof}} = 18$ ms of free expansion are presented in (b). Each realisation generates interference fringes (black and green curve) with a periodicity $\sim \Lambda$. If many different realisations are summed, the fringes disappear and only the Gaussian envelope remains. This is shown for $Z = 100$ summands in blue and for $Z = 1000$ in red. Each density distribution is scaled by $1/\sqrt{Z}$.

Figure 6.1 shows the typical interference fringes obtained from simulating eq. (6.3) for our experimental parameters[154]. For a single realisation the interference maxima are clearly visible and separated by approximately Λ. Therefore, we conclude that the "noise" α_j is not sufficient to destroy the underlying order of the lattice. Only if we averaged over many different realisations, the interference fringes wash out such that solely the Gaussian envelope remains.

Figure 6.2(a) shows an absorption image after $t_{\mathrm{tof}} = 18$ ms of free expansion at the background scattering length, $a \simeq 100\,a_{\mathrm{B}}$. The interference pattern is clearly visible. The comparison to the ideal gas model discussed above is done by taking a horizontal cut

[154]In order to take the finite size of the system into account and that we loaded thermal atoms into the lattice the in-trap density distribution is taken to be a Gaussian across the different lattice sites, $N_j \propto \exp[-\frac{1}{2}(j/\sigma_N)^2]$. We checked that a Thomas-Fermi profile and a uniform atom number distribution produces similar fringes. However, the fringes of the uniform distribution disappear first, if different realisations are averaged. This can be understood as follows [268]: The wings of the Thomas-Fermi and the Gaussian profile contain less atoms. Therefore, the "equivalent uniform system" contains fewer condensates. (Internal link to the program 'Interferences.nb'.)

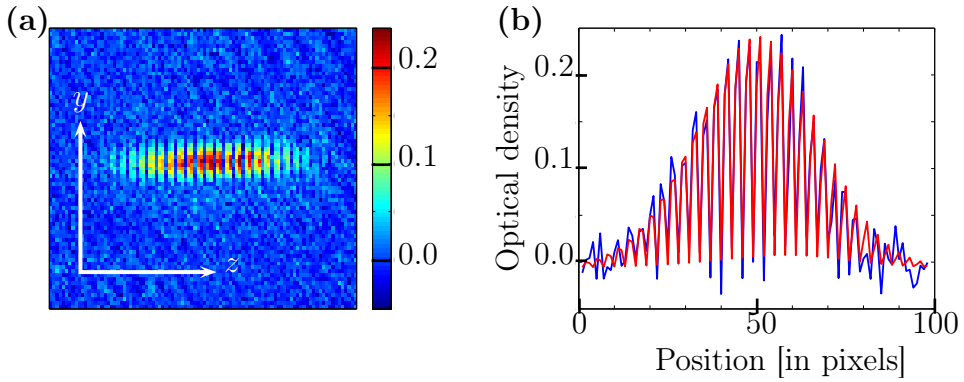

Fig. 6.2, Measured interference fringes of non-collapsed condensates: A single absorption image is shown in (a), the colorbar indicates the optical column density $\mathrm{OD}_{y,z}$. The image is taken after 18 ms of free expansion at the background scattering length. A horizontal cut through the center of this image is presented in (b) as blue curve. In addition, the best fit of eq. (6.4) is shown in red, yielding a fringe spacing $\Lambda_{\mathrm{fit}} \approx 19.3\,\mu\mathrm{m}$ and a contrast $C_{\mathrm{fit}}^{(\mathrm{cut})} \approx 0.94$. The ideal gas model predicts $\Lambda_{\mathrm{theo}} = 18.5\,\mu\mathrm{m}$.

(along the z-direction) through the center of the absorption image, see fig. 6.2(b), and fitting it with the function

$$\begin{aligned} n_{2\mathrm{d}}(y,z) &\stackrel{\mathrm{def}}{=} \int dx\ n_{3\mathrm{d}}(x,y,z) \\ &= A(y)\,\mathrm{e}^{-\left(\frac{z-z_0}{\sigma}\right)^2}\left[1 + C\,\cos\left(\frac{2\pi}{\Lambda}(z-z_0) + \Delta\alpha\right)\right] \end{aligned} \tag{6.4}$$

where $C \stackrel{\mathrm{def}}{=} (n_{\max} - n_{\min})/(n_{\max} + n_{\min})$ is the *contrast*. The fit provides the fringe spacing $\Lambda_{\mathrm{fit}} \approx 19.3\,\mu\mathrm{m}$ and $C_{\mathrm{fit}}^{(\mathrm{cut})} \approx 0.94$. This is in excellent agreement with the ideal gas model, which yields $\Lambda_{\mathrm{theo}} = 18.5\,\mu\mathrm{m}$. The deviation of the contrast $C_{\mathrm{fit}}^{(\mathrm{cut})}$ from unity is attributed to the following three experimental limitations [275, 276]: (*i*) the inhomogeneous trapping potential, (*ii*) the interaction during the time-of-flight, which causes a broadening of the momentum distribution, and (*iii*) the finite expansion time t_{tof}. The first constraint is due to the fact that the atom number is position dependent. This diminishes the contrast, as can be seen from eq. (6.1b). The two other limitations are closely connected. They wash out the interference pattern, because they limit the coherence lengths: The coherence length of each condensate is inversely proportional to the *local* momentum spread. It was shown in [277–279] that for a trapped condensate it is equal to the size of the BEC. However, when the condensate is released from the trapping potential the coherence length grows, because the local momentum spread decreases due to the separation of different velocity classes. Therefore, the contrast increases with the time-of-flight such that even thermal atoms[155] exhibit high contrast interference fringes after sufficient long free expansions [280].

[155] These experiments probed the auto-correlation (self-coherence of a single cloud), whereas we probe the cross-correlation (coherence between different clouds).

6.3 Probing the phase-coherence of collapsed matter-waves

While the last section discussed the phase-coherence of a stack of *stable* condensates, we will show in this section that the phase-coherence is maintained during the collapse. Again, we produce three to five condensates, but now we reduce the scattering length below its critical value and induce the collapse.

Figure 6.3 presents typical absorption images obtained after $t_{\mathrm{tof}} = 18\,\mathrm{ms}$ of free expansion. Whereas the absolute position of the interference fringes changes from shot-to-shot, they can be clearly seen on each image. However, for the holding times[156] $0.2\,\mathrm{ms} \leq t_{\mathrm{hold}} \leq 0.5\,\mathrm{ms}$ the interference fringes are only visible in the wings, but "not" in the central region of the image.

Taking a close look at the *central region* of the absorption images $t_{\mathrm{hold}} = 0.2\,\mathrm{ms}$ and $0.4\,\mathrm{ms}$, we note that

1. Atoms are present in this central region: As the optical density is much larger than the background noise[157] atoms do exist. However, they do not exhibit a periodic high contrast interference pattern.
2. The absorption images are non-uniform in y-direction:
   (a) If horizontal cuts for different y-values are taken, only some exhibit maxima and minima which exceed the noise level.
   (b) If a cut exhibits interference fringes, the fringes seem to be phase shifted with respect to those in the wings[158].
   (c) If cuts for different y-values are compared, the interference fringes are "disorganised": They do not appear at the same z-position.

Hence a single horizontal cut does not reflect the recorded density distribution. Therefore, the lower row in fig. 6.3 does *not* present an horizontal cut through the center of each cloud, but the *one-dimensional optical column densities*

$$\mathrm{OD}_z \stackrel{\mathrm{def}}{=} \sum_y \mathrm{OD}_{y,z} \tag{6.5}$$

where $\mathrm{OD}_{y,z}$ is the two-dimensional optical column density recorded by the imaging system [281]. We checked that for "short" ($t_{\mathrm{hold}} = 0\,\mathrm{ms}$) and "long" ($t_{\mathrm{hold}} \geq 0.6\,\mathrm{ms}$) holding times

[156] We took data in steps of 0.1 ms. Figure 6.3 presents only a part of the measurement.

[157] Using the non-coherent light of a LED (light-emitting diode), we measured the background noise to be 5%, which is only slightly above the $1/\sqrt{N}$ laser shot-noise limit of 3%.

[158] A quantitative statement about the period of the central interference fringes is not possible. The central region is too small.

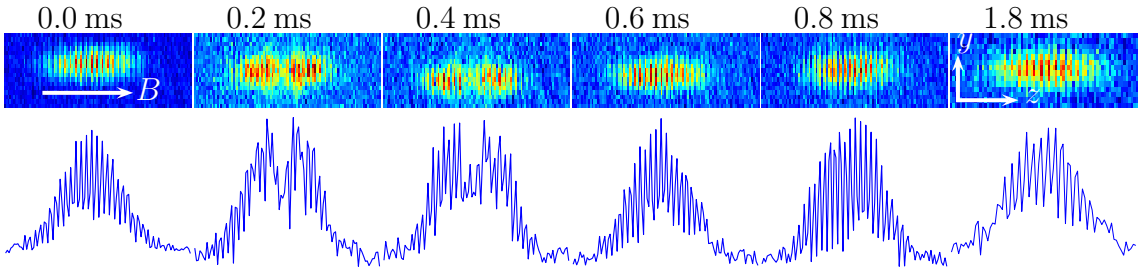

Fig. 6.3, Phase-coherence of collapsed condensates: Single absorption images (upper row) after $t_{\mathrm{tof}} = 18\,\mathrm{ms}$ free expansion for different holding times t_{hold} in the oblate trapping potential $(f_x, f_y, f_z) = (400 \pm 30, 400 \pm 30, 3400 \pm 130)\,\mathrm{Hz}$. The graphs in the lower row show the optical column densities $\sum_y \mathrm{OD}_{y,z}$, which are additionally summed over the y-direction. The field of view is $(y, z) = (110, 690)\,\mu\mathrm{m}$.

the summed optical density of each image provides the same contrast, $C_{\mathrm{fit}}^{(\mathrm{sum})} \approx (0.5 - 0.6)$ as the horizontal cut through the center of the interference pattern[159].

What causes the disorganisation of the interference fringes? A *possible* interpretation is provided by the fact that the collapse does not happen in-trap, but during the time-of-flight: For $t_{\mathrm{hold}} = 0\,\mathrm{ms}$ the condensates do *not* collapse; neither in-trap nor during the time-of-flight. Therefore, the observed fringes are similar to those in fig. 6.2. For $0.2\,\mathrm{ms} \leq t_{\mathrm{hold}} \leq 0.5\,\mathrm{ms}$ the condensates do collapse. However, the collapse happens during the time-of-flight and *after* the clouds overlapped — e.g. for $t_{\mathrm{hold}} = 0.4\,\mathrm{ms}$ the clouds start to overlap at $t_{\mathrm{tof}} = 0.4\,\mathrm{ms}$, but they collapse at $t_{\mathrm{tof}} = 0.8\,\mathrm{ms}$. As the collapse is a violent process, it probably induces a complicated phase distribution in the ensemble. We suspect that this complicated phase distribution is not uniform along the x-direction. Therefore, the integration over the line-of-sight during the imaging process washes-out the interference fringes[160]. On the other hand, if the collapse happens in-trap — e.g. for $t_{\mathrm{hold}} = 0.8\,\mathrm{ms}$ — the fringes are formed by the remnant condensate. Again, we observe the fringes as if the atoms would belong to stable condensates. We checked that for holding times larger than $t_{\mathrm{hold}} = 0.6\,\mathrm{ms}$ (and at least up to[161] $1.8\,\mathrm{ms}$) the fringes in the

[159] These values must be compared to the contrast obtained for non-collapsed condensates. If the optical density in fig. 6.2 is summed up along the y-direction, eq. (6.5), we obtain the contrast $C_{\mathrm{fit}}^{(\mathrm{sum})} \approx 0.71$.

[160] Note that the interference pattern is produced *during* the imaging process [156, 266]. This is true if the condensates are described as a superposition of coherent states, as in eq. (6.1a), but also if they are described by a 2-body Fock state, $\psi \propto |N_1, N_2\rangle$: While in the case of two isolated coherent states the imaging fixes the otherwise unknown relative phase between the condensates, in the case of Fock number states the duration of the imaging process is important. The atoms are not measured simultaneously, but one after the other. The subsequent measurements always reduces the Fock state by one, $|N_1, N_2\rangle \to \sqrt{N_1}|N_1 - 1, N_2\rangle + \sqrt{N_2}|N_1, N_2 - 1\rangle$, which induces quantum correlations of the Hanbury-Brown-Twiss type.

[161] We expect that only the lifetime of the condensates limits the observation of the interference fringes.

central region remain clearly visible. Thus, we have proven that a coherent matter-wave[162] survives the collapse.

Summary

In order to probe the phase-coherence of collapsed condensates we induced the collapse in several (three to five) isolated dipolar condensates simultaneously and let them interfere. For sufficient long holding times we observed high contrast interference fringes, proving the existence of a coherent matter-wave.

[162]We did not check whether the trapped atoms are excited or not.

"Prediction is very difficult, especially about the future."
(Niels Bohr)

7 Summary and outlook

The central subject of the thesis was the time evolution of an unstable chromium condensate. By utilising a Feshbach resonance, we reduced the s-wave scattering length and studied the collapse dynamics in four different trap configurations: (*i*) a strongly prolate trap with trap ratio $\lambda \equiv \omega_z/\omega_\rho \approx 0.12$, (*ii*) a weakly prolate, $\lambda \sim 0.7$, non-cylindrical trap, (*iii*) a non-cylindrical trap which offered a round in-trap $\kappa_{y,z}$-column density, and (*iv*) a strongly oblate trap with $\lambda \approx 8.5$. Being a topic of fundamental research, its aim was two-fold: First, investigating how the symmetry of the interactions (d-wave for the long-range and s-wave for the short-range interactions) influences the collapse dynamics — temporal and spatial evolution of the condensate's density — and second, testing weather or not the standard mean-field theory — the Gross-Pitaevskii equation — can be used to describe condensates in such extreme conditions.

The investigation of collapsing dipolar condensates focused on the anisotropic explosion triggered by the collapse. Instead of reflecting the symmetry of the trapping potential, the remnant cloud exhibited an anisotropic density distribution, which resembled the symmetry of the dipolar interactions. While for both prolate traps, (*i*) and (*ii*), the remnant exploding cloud obtained a dumbbell-like shape after a sufficient long in-trap holding time, the d-wave symmetry of the dipolar interactions manifested itself most clearly in the case of the non-cylindrical trap (*iii*) by displaying a cloverleaf-like shape. This showed not only that the collapse dynamics strongly depends on the character of the mean-field dipolar interaction potential — changing the trapping potential from prolate to oblate transforms the character of the dipolar interactions from "inducing the instability" to "stabilising the condensate against the instability" — but it also was the first time that this most distinctive feature of dipolar interactions was directly observed. Furthermore, we investigated the phase-coherence of the collapsed cloud. Producing an array of three to five condensates, we observed high contrast interference fringes. This demonstrates that the remnant cloud maintains its phase-coherence, if the collapse happens in-trap.

The experimental results were well reproduced by three-dimensional simulations of the Gross-Pitaevskii equation (GPE) including 3-body losses (performed by Masahito Ueda and coworkers), although the simulations do not contain any adjustable parameter. Being a mean-field theory, the GPE does not take correlation into account. Hence, the good agreement between experiment and simulations strongly suggests that the collapse does not induce severe many-body quantum correlations.

Directly related prospects:

The experiments presented in this thesis constitute the basis for many further investigations. Therefore, this work opens numerous perspectives. For example to generate dipolar soliton trains in a prolate trap [246, 247], to induce the collapse in a condensate with spherical density distribution by using an additional laser beam, to obtain experimental evidence for the predicted vortex rings [244] by using e.g. the interferometric technique of section 6, to extend the phononic stability diagram by including the number of condensates, or to investigate the collapse of a structured ground-state by inducing an angular collapse [73]. Since the ongoing experiment focuses on the stability diagram of a stack of dipolar condensates, we like to discuss it in some details. The angular collapse is considered in the subsequent paragraph.

Stability diagram of a stack of dipolar condensates

All our experiments conducted so far focused on the anisotropy of the dipolar interaction. Its long-range character was only probed directly using Rydberg atoms [282–284]. Therefore, the following experiment would be the first demonstration of the long-range character of the dipolar interactions for ground-state atoms.

The stability diagram of a dipolar condensate does not only depend on the aspect ratio of the condensate, but, if it is coupled to other condensates, also on the overall geometry. This can be easily understood as follows: Consider a single cigar-shape dipolar condensate with a trap ratio $\lambda \equiv \omega_z/\omega_\rho = 10^{-2}$. According to the discussion in section 4.2 the condensate becomes unstable against phonons at a critical scattering length $a_{\mathrm{crit}}(\lambda) \approx a_{\mathrm{dd}}$. But, what happens if we slice this single cigar-shape condensate into a stack of many pancake-shape condensates, each having a trap ratio of $\lambda' = 10^2$? Neglecting the inter-site interactions, the critical scattering length of a single condensate is $a_{\mathrm{crit}}(\lambda') \approx -2a_{\mathrm{dd}}$, see section 4.2. However, the long-range dipolar interaction provides a negative energy contribution[163] such that the overall geometry matters. Therefore, a stack of pancake-shape condensates, each having a trap ratio λ', is less stable than the isolated condensate with the same trap ratio λ'. A detailed calculation is given in appendix[164] A.6.2.

Further prospects:

Further perspectives, not directly related to the collapse of a dipolar condensate, but nevertheless on our agenda, are the indirect evidence of the maxon-roton spectrum by observing the characteristic abrupt changes of the Faraday pattern [229, 285], two-dimensional bright solitons [74], or multi-well dipolar physics [78]. As the last perspective is very demanding in terms of optical access and therefore not accessible with the current experimental apparatus (a new set-up is currently build), we will concentrate on the two others in the following. However, note that none is experimentally simple.

[163] Since the on-site dipolar interaction energy in each pancake is positive ("repulsive"), but the total dipolar energy remained constant, the inter-site dipolar energy must be negative ("attractive"). For a numerical confirmation see appendix A.6.

[164] Internal link to the preliminary program 'CollapseLattice.tgz'.

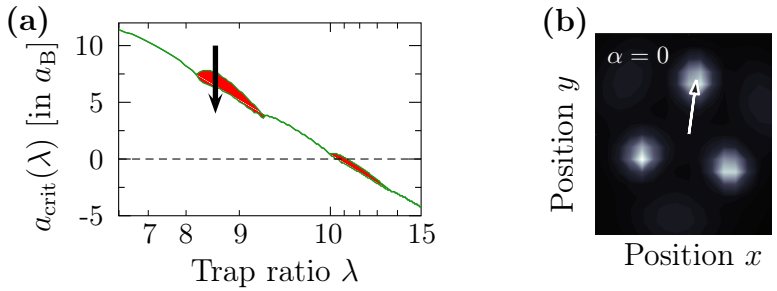

Fig. 7.1, Angular collapse: The red areas in the stability diagram (a) indicate the parameter space where the ground-state has a bi-concave shape. Initiating the collapse by "slowly" ramping the scattering length across this region (from $a_{\rm i} = 10\,a_{\rm B}$ to $a_{\rm f} = 4\,a_{\rm B}$ in 8 ms) results in the absorption image shown in (b). The parameters for the simulations are: mean trap frequency $\bar{\omega}/(2\pi) = 700$ Hz, aspect ratio $\lambda \sim 8$, atom number $N = 2 \times 10^4$, time-of-flight $t_{\rm tof} = 10.5$ ms, 3-body loss coefficient $L_3 = 2 \times 10^{-28}$ cm^6/s, and an overall undetermined angle of rotation of the pattern $\alpha = 0$. (Taken from [73])

Rotons in dipolar condensates

Rotons in dipolar condensates are associated with a characteristic length, which manifests itself in many new physical phenomena. However, since the current experimental set-up does not allow to resolve the in-trap density distributions the condensate has to be expanded before imaging. Unfortunately, the dipolar expansion is non-linear and washes-out many phenomena associated with rotons. Therefore, only two rotonic effects are very promising: the angular collapse [73] and the Faraday pattern [229, 285]. Both utilise the expansion[165].

The *angular collapse* is illustrated in fig. 7.1: In certain parameter regions the ground-state density exhibits a bi-concave density distribution, where the maximum of the density occurs at the periphery of the condensate rather than at its center. This non-trivially structured ground-state is associated with the dipolar roton. The most unstable mode around these structured ground-states is one with $m = 3$, where m is the projection of the quasi-momentum onto the magnetic field axis (taken as z-direction). Ramping the scattering length across this regime results in an absorption image[166] similar to the one shown in 7.1(b).

[165] Strictly speaking, the Faraday pattern presented in [229, 285] are in-trap phenomena, which are not resolvable in the current experimental set-up, due to our limited spatial resolution. However, assuming a time-of-flight, we argue that the abrupt changes in the Faraday patterns transform into abrupt changes of the condensate's size. Therefore, the proposed experiment utilises the time-of-flight to obtain information about the in-trap momentum distribution.

[166] Note that (*i*) the imaging axis in fig. 7.1(b) is parallel to the magnetic field (z-axis), while we usually image along the x-direction, and (*ii*) the density distribution is almost cylindrical symmetric for shorter (7.5 ms) and longer (14.5 ms) free expansion times, see [73, fig. 6]. Therefore, in order to observe this structure using our standard imaging axis the expansion time $t_{\rm tof}$ must be within a certain time-window.

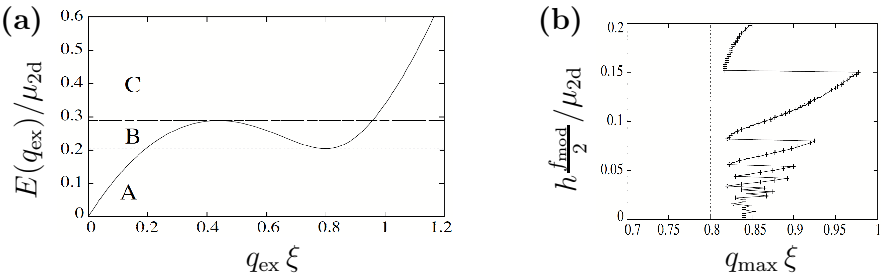

Fig. 7.2, Faraday pattern: The maxon-roton spectrum is shown in (a) in units of the two-dimensional chemical potential $\mu_{2d} \sim k_B 240\,\text{Hz}$ and the healing length $\xi \equiv \hbar/\sqrt{2m\mu_{2d}}$. While the excitation modes are non-degenerated in region "A" and "C", they are three-fold degenerated in region "B". If the non-linearity of the condensate is modulated with a frequency f_{mod}, such that $f_{mod}/2$ lies within the region "A", the most unstable mode $q_{n_{max}}$ is the q_{ex}-mode with the largest wavevector within the region "B", which fulfills the condition for parametric resonances[167]. Therefore, if f_{mod} is decreased such that a new mode moves from "C" to "B", the dominant mode changes abruptly, as shown in (b). As the density after a sufficiently long time-of-flight is related to the in-trap momentum distribution, the abrupt change of the Faraday pattern should be visible as an abrupt change of the condensate's size. (Taken from [229])

Alternatively, the effect of *Faraday patterns*, shown in fig. 7.2, can be used to observe the roton indirectly: The dipoles are assumed to be fully polarised by an external field, which is parallel to the symmetry axis of the confining pancake-shape trap potential. Due to the roton minimum, modes corresponding to different radial wavevectors q_{ex} are three-fold degenerated, see fig. 7.2(a). Surprisingly, this has a severe effect, if we generate excitations by periodically varying the non-linearity (either by modulating the scattering length or the spatial density). Doing so, the most unstable mode is not the fundamental mode ($n = 1$) fulfilling the parametric resonance condition[167], but the higher harmonic ($n \geq 2$) which (*i*) lies in region "B" of fig. 7.2(a) and (*ii*) has the largest wavevector[167] q_n. The reason for this unusual behaviour is that the wavevector corresponding to the higher harmonic ($n \geq 2$) is "abnormally" large, compared to the case of a purely contact interacting condensate[168].

[167] The wavevector q_{ex} and its associated excitation frequency $f_{ex} \stackrel{\text{def}}{=} E(q_{ex})/h$ are assumed to be *continuous* variables and related by eq. (A.30), see page 117. Using a modulation frequency f_{mod}, we excite only the modes which fulfill the parametric resonances condition $f_{ex} = f_n \stackrel{\text{def}}{=} n\, f_{mod}/2$, where $n = 1, 2, \ldots$. Accordingly, for a single modulation frequency f_{mod} we obtain a *discrete* set of wavevectors $\{q_n : n = 1, 2, \ldots\}$. Each q_n is associated with a frequency $f_n = E(q_n)/h$.

[168] Note that it is not the degeneracy but the "abnormal" large wavevector, which makes these modes very unstable: "the most unstable mode for all driving frequencies [f_{mod}] within regime A is given by the largest momenta ... [q_{ex}] compatible with the first harmonic ... [$n = 2$] lying in regime B (or, if none, the first harmonic lying in regime C)." (R. Nath [229]). Mathematically, this is expressed in [229, eq. (9)], where probably a factor 1/16 is missing.

This results in a highly non-trivial dependence of the dominant excitation-mode on the modulation frequency. In order to illustrate fig. 7.2(b) let us assume we start by modulating the spatial density with a frequency f_{mod} such that the modes q_n where $n = 1$ and $n = 2$ are within the region "A" and "B", respectively. According to the above arguments, the $n = 2$ mode is the most unstable, hence, it dominates the Faraday pattern. If we decrease f_{mod} such that the mode $n = 3$ moves from region "C" to "B" — while the mode $n = 2$ is assumed to be still within region "B" —, the most unstable mode n_{max} changes abruptly from $n_{\mathrm{max}} = 2$ to $n_{\mathrm{max}} = 3$. Therefore, the wavevector $q_{n_{\mathrm{max}}}$ (associated with the most unstable mode) jumps from $q_{n_{\mathrm{max}}=2}$ to $q_{n_{\mathrm{max}}=3}$. As discussed in [234], using a stack of pancake-shape condensates rather than a single BEC has two effects: (*i*) it lowers the required spatial density, and (*ii*) it shifts the roton minimum to higher q_{ex}-values and therefore the largest wavevector within region "B" increases. Both effects facilitate the experimental constrains. However, two questions remain open. First, what is the density scales for the Faraday patterns? If the in-trap density varies only on the few percent level, the non-linear dipolar expansion might wash out the effect. And second, do the pattern appear also for shorter modulation times? The publication discusses modulation times on the order of 40 ms at a scattering length $a \sim -10\,\mathrm{a_B}$. This would not be feasible, due to the limited lifetime in the vicinity of the Feshbach resonance.

Two-dimensional anisotropic soliton

The two-dimensional *anisotropic soliton* proposed in [74] is fundamentally different from the solitons in purely contact interacting condensates. This is not only because it is two-dimensional and anisotropic, but also because two colliding solitons would merge and form a single soliton [65].

In order to investigate these dipolar solitons the authors consider a condensate which is fully polarised in z-direction while confined only in the y-direction. Assuming a three-dimensional Gaussian trial wavefunction, the Gross-Pitaevskii energy functional (2.9) [74, eq. (5)][169]

$$\frac{E_{\mathrm{tot}}}{N\hbar\omega_y} \propto \frac{1}{4}\left(\frac{1}{\tilde{\sigma}_x^2}+\frac{1}{\tilde{\sigma}_y^2}+\frac{1}{\tilde{\sigma}_z^2}\right)+\frac{\tilde{\sigma}_y^2}{4}+\frac{N}{\sqrt{2\pi}}\frac{\tilde{a}-\tilde{a}_{\mathrm{dd}}f_{\mathrm{dip}}\left(\tilde{\kappa}_x,\tilde{\kappa}_y\right)}{\tilde{\sigma}_x\tilde{\sigma}_y\tilde{\sigma}_z} \tag{7.1a}$$

$$f_{\mathrm{dip}}(\kappa_x,\kappa_y) \stackrel{\mathrm{def}}{=} 1-3\int_0^1 dx\; x^2\,\frac{\kappa_x}{\sqrt{1+(\kappa_x^2-1)x^2}}\,\frac{\kappa_y}{\sqrt{1+(\kappa_y^2-1)x^2}} \tag{7.1b}$$

is obtained, where the parameters indicated by a tilde are rescaled by the harmonic oscillator length $\ell_y \stackrel{\mathrm{def}}{=} \sqrt{\hbar/(m\omega_y)}$ in the confinement direction. Thus, they are dimensionless[170]. The aspect ratios are defined by $\kappa_x \stackrel{\mathrm{def}}{=} \sigma_x/\sigma_z$ and $\kappa_y \stackrel{\mathrm{def}}{=} \sigma_y/\sigma_z$. The basic idea is to use the

[169] In order to obtain $f_{\mathrm{dip}}(\kappa,\kappa) = f_{\mathrm{dip}}(\kappa)$ we included an additional minus sign in eq. (7.1a).

[170] Notation: Dimensionless condensate's size in j-direction $\tilde{\sigma}_j \equiv \sigma_j/\ell_y$, dimensionless scattering length $\tilde{a} \equiv a/\ell_y$, and dimensionless dipolar interaction strength $\tilde{a}_{\mathrm{dd}} \equiv \mu_0\mu^2 m/(12\pi\hbar^2\ell_y)$.

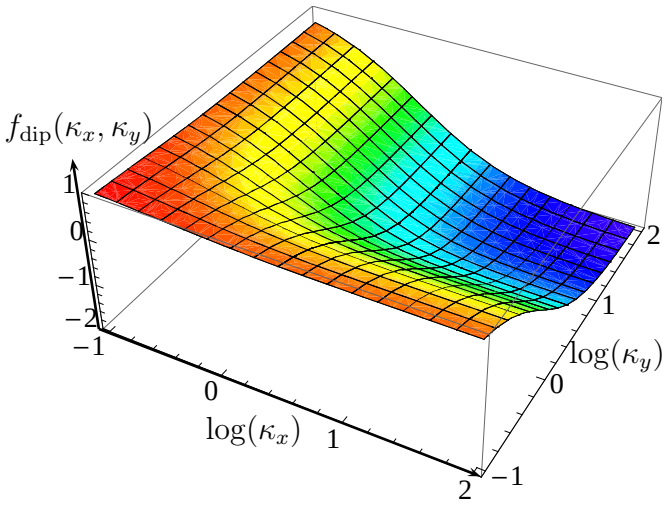

Fig. 7.3, Two-dimensional dipolar anisotropic function: $f_{\rm dip}(\kappa_x, \kappa_y)$ is a monoton decreasing function in both directions, because the condensate becomes more pancake-shape for increasing κ_x or κ_y. It is symmetric in its two parameters,$\kappa_x \leftrightarrow \kappa_y$, and we recover the standard dipolar anisotropic function $f_{\rm dip}(\kappa)$ in the case of a cylindrical symmetric condensate, $\kappa_x = \kappa_y$.

condensate's sizes as variational parameters and to search for a local energy minimum with *finite* condensate sizes, $\sigma_{x,y,z} > 0$.

In order to understand the appearance of the soliton let us study the behaviour of the energy functional. It is analogous to the one discussed in section 4.1.2, except that the dipolar anisotropic function $f_{\rm dip}(\kappa)$ for cylindrical symmetric dipolar condensates (see appendix A.5.5) is replaced by its generalised version $f_{\rm dip}(\kappa_x, \kappa_y)$ for non-cylindrical condensates[169] [161, eq. (17-19)]. Figure 7.3 demonstrates $f_{\rm dip}(\kappa, \kappa)$. Most importantly, it is a monoton decreasing function for κ_x and κ_y — the dipolar energy contribution benefits from being elongated along the polarisation axis compared to both radial directions ($\kappa_x, \kappa_y < 1$). Therefore, $f_{\rm dip}(\kappa, \kappa)$ favours "small" radial sizes, $\tilde{\sigma}_x$ and $\tilde{\sigma}_y$, while a "large" condensate's size in the polarisation direction, z. Hence, we only have to insure that (*i*) the dipolar contribution is dominant (a necessary condition is $\tilde{a} - \tilde{a}_{\rm dd} f_{\rm dip}(0,0) < 0$, where $f_{\rm dip}(0,0) = 1$), and (*ii*) the condensate is stable against the radial shrinking as well as the axial expansion. However, this is straight forward: the quantum pressure (first term in eq. (7.1a)) stabilises the condensate against the radial contracting, while the dipolar energy (last term in eq. (7.1a)) limits the axial expansion, due to its $1/\sigma_z$-scaling. Thus, if the spatial density (or the dipolar interaction strength) is sufficiently high, the energy functional becomes negative at finite condensate sizes $(\sigma_x, \sigma_y, \sigma_z)$, supporting an anisotropic soliton[171].

[171] Note that the arguments above suggest that cylindrical symmetric dipolar solitons might exists even for positive dipolar interaction strength $g_{\rm dd}$. The criterion $g_{\rm dd} < 0$ given in [65, eq. (6)] is based on the limit $\kappa \equiv \sigma_\rho/\sigma_z \to \infty$, which contradicts the condition $\sigma_z > \sigma_\rho$.

How to detect the soliton in an experiment is still an open question. From simulations [286] we know that all three trap frequencies need to be ramped simultaneously in order to form the soliton[172]. This ramping time is $\sim 40\,\mathrm{ms}$ and generates breathing-oscillations of the condensate's sizes. The radial and axial breathing frequencies depend on the scattering length and varies between $(9 - 13)\,\mathrm{Hz}$. Detecting such a small variation of the breathing frequency is experimentally challenging. Therefore, other signatures of the soliton would be desirable.

[172]The standing wave, which produces the confinement in y-direction, would also produce a residual confinement in x and z-direction. The simulations assume a residual confinement of 5 Hz.

A Appendix

A.1 Measured differential ac-Stark shift

This section is not related to the rest of the thesis. We include it nevertheless in order to give a reference to those, who have to re-measure the ac-Stark shift of ^{52}Cr.

The ac-Stark effect is the 1-particle phenomena enabling laser trapping of atoms. It is the energy shift, which an atomic state $|\boldsymbol{\alpha}\rangle$ experiences, if it is exposed to a (classical) light field — the light couples the state of interest $|\boldsymbol{\alpha}\rangle$ to all the other atomic state $|\boldsymbol{\alpha}'\rangle$. Although the ac-Stark shift is a "well know" and widely applied effect, almost every article, phd-thesis, or book discussing its details has some errors or at least a non-SI unit system. Therefore, we present in this section the definitions which we used to calculate the ac-Stark shift for ^{52}Cr based on the NIST-data[173].

The light field, which couples the state of interest[174] $|\boldsymbol{\alpha}\rangle$ to the other atomic states $|\boldsymbol{\alpha}'\rangle$, is provided by a far-detuned[175] Gaussian laser beam of power P_0, waist[176] w_0, wavelength λ_{laser}, and polarisation $\boldsymbol{\epsilon_q}$. In this scenario the *ac-Stark shift* of the state $|\boldsymbol{\alpha}\rangle$ is given by[177] [173, 287–293]

$$\Delta E_{\boldsymbol{\alpha}}^{(\boldsymbol{q})} = \frac{E_0^2}{4\pi\hbar c} \sum_{\boldsymbol{\alpha}'} \text{sign}_{\boldsymbol{\alpha}',\boldsymbol{\alpha}} \ \mu_{\boldsymbol{\alpha}',\boldsymbol{q},\boldsymbol{\alpha}}^2 \frac{\lambda_{\boldsymbol{\alpha}',\boldsymbol{\alpha}} \, \lambda_{\text{laser}}^2}{\lambda_{\text{laser}}^2 - \lambda_{\boldsymbol{\alpha}',\boldsymbol{\alpha}}^2} \tag{A.1a}$$

with the atomic *transition wavelength* $\lambda_{\boldsymbol{\alpha}',\boldsymbol{\alpha}}$ and the (electric dipole) *transition matrix element*

$$\begin{aligned} \mu_{\boldsymbol{\alpha}',\boldsymbol{q},\boldsymbol{\alpha}} &\stackrel{\text{def}}{=} e \, \langle \boldsymbol{\alpha}' | \boldsymbol{r} \cdot \boldsymbol{\epsilon_q} | \boldsymbol{\alpha} \rangle \\ &= e \, \langle \gamma' n' (SL') J' m_{J'} | \boldsymbol{r} \cdot \boldsymbol{\epsilon_q} | \gamma n (SL) J m_J \rangle \end{aligned} \tag{A.1b}$$

The only approximations made are: (*i*) the *electric dipole approximation*, assuming that the size of the atom ($\sim 10\,\text{a}_\text{B}$) is much smaller than the laser wavelength ($\sim 1\,\mu\text{m}$), (*ii*) that each valence electron can be treated independently and therefore the different transitions are summed incoherently, and (*iii*) the atom behaves like a two-level system. For ^{52}Cr, which has a vanishing nuclear spin, only the fine-structure must be considered. However, care has to be taken on how the NIST database defines its physical quantities

[173] Status: 07.2009.

[174] Notation: $\boldsymbol{\alpha}$ is used as a multi-index to select a specific *state*, e.g. $|\text{z}\,^7\text{S}_3, m_J = -3\rangle$.

[175] In the following, we ignore the laser linewidth, because it is much smaller than any other frequency.

[176] We define the waist of a Gaussian laser beam as the $1/e^2$-radius of the intensity. Therefore, the following relations hold: peak intensity $I_0 = 2P_0/(\pi w_0^2)$, peak electric field strength $E_0 = \sqrt{2I_0/(\epsilon_0 c)}$.

[177] The sign of the ac-Stark shift should be put by hand: $\text{sign}_{\boldsymbol{\alpha}',\boldsymbol{\alpha}} = -1$ for the energetically lower state, while it is $+1$ for the upper state. (Internal link to the program 'Stark_Shift.nb').

[289]:

$$\left|\mu_{\boldsymbol{\alpha}',\boldsymbol{q},\boldsymbol{\alpha}}\right|^2 \equiv \left|\langle \gamma' n'(SL')J' m_{J'}|\boldsymbol{d}\cdot\boldsymbol{\epsilon_q}|\gamma n(SL)Jm_J\rangle\right|^2 \tag{A.2a}$$

$$= \left|\langle \gamma' n'(SL')J'||\boldsymbol{d}\cdot\boldsymbol{\epsilon_q}||\gamma n(SL)J\rangle\right|^2 \times \begin{pmatrix} J' & 1 & J \\ -m_{J'} & q & m \end{pmatrix}^2 \tag{A.2b}$$

$$= \frac{3\,\epsilon_0\,h\,\lambda^3_{\boldsymbol{\alpha}',\boldsymbol{\alpha}}}{16\pi^3}\,(2J'+1)A^{(\mathrm{NIST})}_{\boldsymbol{\alpha}',\boldsymbol{\alpha}} \times \begin{pmatrix} J' & 1 & J \\ -m_{J'} & q & m \end{pmatrix}^2 \tag{A.2c}$$

$$= \frac{3\,\epsilon_0\,h\,\lambda^3_{\boldsymbol{\alpha}',\boldsymbol{\alpha}}}{16\pi^3}\,A^{(\mathrm{NIST})}_{\boldsymbol{\alpha}',\boldsymbol{\alpha}} \times \langle \gamma n J\,1\,m_J\,q|\gamma' n'(J1)J'\,m_{J'}\rangle^2 \tag{A.2d}$$

where the round bracket denotes the Wigner-3j symbol, $\langle .||\boldsymbol{d}\cdot\epsilon_{\boldsymbol{q}}||.\rangle$ is the *reduced matrix element*, and $\langle \gamma n JL\,m_J m_L|\gamma' n'(JL)J' m_{J'}\rangle$ refer to the Clebsch-Gordan coefficient. Putting everything together yields[178]

$$E^{(q)}_{\boldsymbol{\alpha}}(P_0) = \frac{h}{16\,\pi^2\,c}\sum_{\boldsymbol{\alpha}'}\ \mathrm{sign}_{\boldsymbol{\alpha}',\boldsymbol{\alpha}}\ A^2_{\boldsymbol{\alpha}',\boldsymbol{\alpha}}\,\frac{P_0}{P_{\mathrm{sat}}}\,\frac{\lambda^2_{\mathrm{laser}}\,\lambda_{\boldsymbol{\alpha}',\boldsymbol{\alpha}}}{\lambda^2_{\mathrm{laser}}-\lambda^2_{\boldsymbol{\alpha}',\boldsymbol{\alpha}}} \times \langle \gamma n J\,1\,m_J\,q|\gamma' n'(J1)J'\,m_{J'}\rangle^2 \tag{A.4}$$

with the ingoing laser power P_0, and the "saturation power" $P_{\mathrm{sat}} \equiv \frac{\pi w_0^2}{2}\,I_{\mathrm{sat}}$. The *saturation intensity* is defined by $I_{\mathrm{sat}} \stackrel{\mathrm{def}}{=} \pi hcA_{\boldsymbol{\alpha}',\boldsymbol{\alpha}}/(3\lambda^3_{\boldsymbol{\alpha}',\boldsymbol{\alpha}})$.

Instead of measuring the ac-Stark shift of a single state, we measured the differential shift between two states. These states are the ground-state $|\mathrm{a}\,^7\mathrm{S}_3, m_J = -3\rangle$ and the excited-state $|\mathrm{z}\,^7\mathrm{P}_4, m_J = -4\rangle$, which is used for imaging. The shift is produced by the ODT1 laser, which is circularly polarised (the quality of the polarisation was measured to be[179] $Q \geq 95\%$), has a wavelength of $\lambda_{\mathrm{laser}} = 1076\,\mathrm{nm}$, and propagates along the z-direction. In order to obtain $\sigma^{\pm}$-light the magnetic offset field $B_{\pm z}$ is chosen to be parallel or anti-parallel to the propagation direction of ODT1. We probe the differential ac-Stark shift $\Delta E^{(q)}_{\boldsymbol{\alpha},\boldsymbol{\alpha}'}(P_0) \stackrel{\mathrm{def}}{=} E^{(q)}_{\boldsymbol{\alpha}'}(P_0) - E^{(q)}_{\boldsymbol{\alpha}}(P_0)$ by determining the resonant absorption

[178] If the nuclear spin I_{spin} does not vanish, the formula is given by [291]

$$E_j = \frac{3\pi}{2}\,c^2\,I\sum_k \frac{A_{k,j}}{\omega^3_{k,j}}\left(\frac{1}{\omega_{k,j}+\omega_{\mathrm{laser}}}+\frac{1}{\omega_{k,j}-\omega_{\mathrm{laser}}}\right) \times (2\,J_k+1)\,(2\,F_j+1)\,(2\,F_k+1) \times \left|\begin{pmatrix} J_k & 1 & J_j \\ -M_k & q & M_j \end{pmatrix}\begin{Bmatrix} J_k & I_{\mathrm{spin}} & F_k \\ F_j & 1 & J_j \end{Bmatrix}\right|^2 \tag{A.3}$$

Notation: The indices j and k are for the energetically lower and upper state, q specifies the polarisation of the light ($q = 0, \pm 1$ for π, $\sigma^{(\pm)}$ light), and the round "$(\dots)$" and curly "$\{\dots\}$" brackets denote the Wigner-3j and Wigner-6j symbols, respectively.

[179] The self-build polarimeter uses a hollow shaft stepper motor (Nanotec: "ST2818L1006-LA", with the driver Nanotec: "SMCI33-1") and a high contrast IR polarisation filter (Edmund: "47327"). The quality of the polarisation was obtained by measuring the contrast $C \equiv (I_{\max} - I_{\min})/(I_{\max} + I_{\min})$ before and after the chamber. The entrance windows do not spoil the contrast by more than 2%. The quality of the polarisation is taken to be $Q \stackrel{\mathrm{def}}{=} 1 - C$.

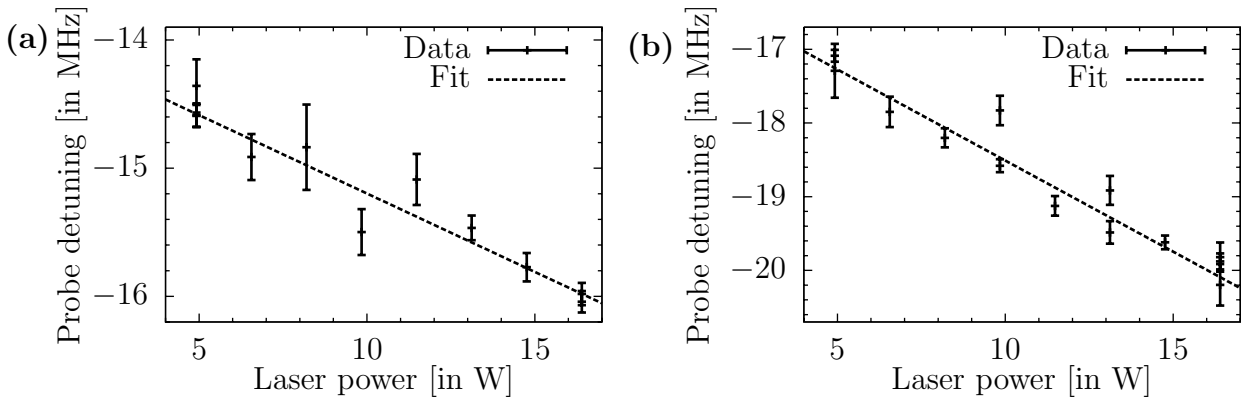

Fig. A.1, Differerential ac-Stark shift measurement 1: The light shift produced on the line component $|a\,^7\mathrm{S}_3, m_\mathrm{J} = -3\rangle \rightarrow |z\,^7\mathrm{P}_3, m_\mathrm{J} = -4\rangle$ is measured for different powers P_0 of the ODT1 laser ($\lambda_\mathrm{laser} = 1076\,\mathrm{nm}$). Graph (a) presents the shift of the resonant probe frequency for σ_1-light[182] at a magnetic offset field $B_z \approx 11\,\mathrm{G}$, yielding $\Delta E^{(\sigma_1)}/(hP_0) = (-0.14 \pm 0.02)\,\mathrm{MHz/W}$, while (b) shows the shift for σ_2-light, $\Delta E^{(\sigma_2)}/(hP_0) = (-0.24 \pm 0.02)\,\mathrm{MHz/W}$, where the magnetic field points in the opposite direction. We obtain the same result if instead of the magnetic field, the ODT1 $\lambda/4$-wave plate is rotated. The probe light is always σ^- polarised, its frequency drift is not included in the errors.

frequency of the imaging laser for different laser powers P_0 of ODT1. The probe beam propagates along the x-direction and is linearly polarised along the y-axis. Therefore, the probe light must be decomposed point-wise into a superposition of σ^+ and σ^- light[180] [172, ch. C.3]. The magnetic offset field $B_z = 11\,\mathrm{G}$ detunes the σ^+ component by 3 natural linewidths. Therefore, the absorption of σ^+-light is suppressed by the factor[181] $\sim 10^3$.

Figure A.1 presents the measured differential ac-Stark shift for the two circular polarisations[182] $\sigma_{1,2}$. The polarisation of the laser is changed by flipping the magnetic field direction[183]. Both measurements are done using thermal atoms with a temperature of a few micro-Kelvins and a "small" magnetic offset field, $B_z \approx 11\,\mathrm{G}$. However, both shifts are negative. Therefore, independent of the polarisation the two states shift closer together, whereas the simulations[184] predict $\Delta E^{(\pm)}/(hP_0) \approx \pm 0.2\,\mathrm{MHz/W}$ for $\sigma^\pm$ light.

[180] In the measurement we neither change the probe intensity, nor its polarisation. Thus, the measured Stark shift is produced only by the 1076 nm light of the ODT1 beam. The 425 nm imaging light merely probes this shift.

[181] The probe intensity was $0.4\,\mathrm{mW/cm^2}$ so that the on-resonant saturation parameter $s_0 \equiv I/I_\mathrm{sat}$ becomes approximately 0.05. This yields a suppression of $(1 + s_0)/[1 + s_0 + (2\delta/\gamma)^2] \approx 35$, see [173, ch. 2.4]. In addition, the square of the Clebsch-Gordan coefficient provides a factor of 28.

[182] We did not measured the absolute polarisation. We only know that one is σ^- and the other is σ^+. Therefore, we denote them as σ_1 and σ_2.

[183] We obtained the same shift, if we rotate the $\lambda/4$-wave plate for the ODT1. However, by flipping the magnetic field we obtained a polarisation of $Q \geq 95\%$, while rotating the $\lambda/4$-wave plate only provides $Q \geq 90\%$.

[184] Internal link to the program 'StarkShift.nb'.

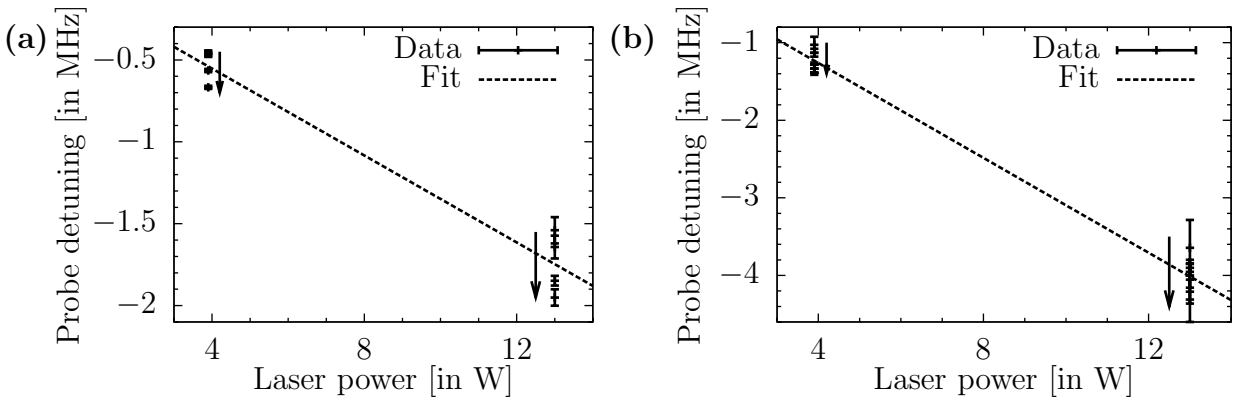

Fig. A.2, Differerential ac-Stark shift measurement 2: In order to rule out any experimental error a $B_z \approx 600\,\mathrm{G}$ offset field is used. The differential Stark shift for the two different polarisations (a, b) are $\Delta E^{(\sigma_1)}/(hP_0) = (-0.14 \pm 0.02)\,\mathrm{MHz/W}$, and $\Delta E^{(\sigma_2)}/(hP_0) = (-0.29 \pm 0.01)\,\mathrm{MHz/W}$. The arrows indicate the frequency drift of the probe laser. The sign problem remains.

A possible explanation for the "wrong" sign is that the atomic sample was not well polarised. Some atoms could have been in different magnetic Zeeman sub-states and not in the absolute ground-state $m_\mathrm{J} = -3$. In order to rule out this experimental error we performed a second measurement shown in fig. A.2. Here, the magnetic offset field is $B_z \approx 600\,\mathrm{G}$. By checking several times during data taking that we obtain a "high-field BEC", we ensured that the sample is fully polarised. Furthermore, instead of measuring the ac-Stark shift for many different ODT1 laser powers, we alternately measured for $P_0 = 4\,\mathrm{W}$ and $P_0 = 13\,\mathrm{W}$ several times. Therefore, we obtain an estimate for the frequency drift of the probe laser. However, the sign problem remains.

A.2 Magnetic fields

The following formulae are useful to estimate the magnetic field strength produced by the coils in our experimental set-up:

- An infinitesimal thick, straight wire ranging from $(x', y', z') = (-a, 0, 0)$ to $(b, 0, 0)$ and carrying the current I produces the magnetic field

$$|\boldsymbol{B}(0,0,z)| = \left| \frac{\mu_0 I}{4\pi} \left[\frac{b}{z\sqrt{b^2+z^2}} + \frac{a}{z\sqrt{a^2+z^2}} \right] \right| \boldsymbol{e}_y \tag{A.5}$$

  at the point $\boldsymbol{r} = (0, 0, z)$.

- An infinitesimal thick, rectangular wire in the (x, y)-plane and centered at the origin (distances between opposite sites are $2a$ and $2b$, respectively) produces the magnetic

field[185] [295]

$$|\boldsymbol{B}(0,0,z)| = \left| \frac{\mu_0 I}{\pi} \frac{a\,b}{\sqrt{a^2+b^2+z^2}} \left[\frac{1}{a^2+z^2} + \frac{1}{b^2+z^2} \right] \right| \boldsymbol{e}_z \tag{A.6}$$

- A circular wire of radius R (otherwise the same specification as the rectangular wire) produces the magnetic field

$$|\boldsymbol{B}(0,0,z)| = \left| \frac{\mu_0 I}{2} \frac{R^2}{(R^2+z^2)^{3/2}} \right| \boldsymbol{e}_z \tag{A.7}$$

- The cloverleaf coils produce the magnetic field [14, ch. 2′3.2]

$$\boldsymbol{B}(x,y,z) \approx B_0 \begin{pmatrix} 0 \\ 0 \\ 1 \end{pmatrix} + b' \begin{pmatrix} x \\ -y \\ 0 \end{pmatrix} - \frac{b''}{2} \begin{pmatrix} x\,z \\ y\,z \\ \frac{x^2+y^2}{2} - z^2 \end{pmatrix} \tag{A.8}$$

[185] Note that a rectangular coil in "Helmholtz configuration" produces a magnetic field, which is almost uniform over a greater volume than a circular Helmholtz coil of comparable dimensions [294].

[186] The fabrication properties of the different coils are documented in [166, page 59+ff], e.g. inner and outer diameter of the coils and the diameter of the used wire. A comprehensive diagram of the coil configuration is given in [172, page 45].

[187] During the time-of-flight at "high magnetic field", $B \sim 600\,\mathrm{G}$, the atoms accelerate with $\sim 10\,\mathrm{m/s}$ in the (negative) z-direction as well. This might be due to a short in one of the offset coils, resulting in a strong axial gradient. (Internal link to the program 'MagneticFields.m' to calculate the magnetic field produced by the offset and pinch coils.)

[188] These are the semiaxes of the ellipse, not the diameters.

[189] Sizes of the rectangular coils.

Tab. A.1, Magnetic coils and there corresponding magnetic fields in radial (ρ) and axial (z) direction, with respect to the symmetry axis of the coils[186]. Measured values are in **bold** font.

coils	**fields**	**windings**	**diameter** [in mm]	**distance** [in mm]
offset[187]		17	133	133/2
bias field B_0/I	1.67 G/A			
curvature b''_z/I	**0.044** G/(cm^{2}A)	ref. [172]		
pinch		8	29	26
bias field B_0/I	1.72 G/A			
curvature b''_z/I	**1.09** G/(cm^{2}A)	ref. [166]		
cloverleaf		16	(22, 36)[188]	26
gradient b'_ρ/I	**0.73** G/(cmA)	ref. [166]		
curvature b''/I	??? G/(cm^{2}A)			
add. offset X		~ 40	~ 100	~ 190
bias field B_0/I	~ 0.4 G/A			
add. offset Y		~ 40	$\sim (160, 120)$[189]	~ 300
bias field B_0/I	~ 1 G/A			

"Two Pi or not two Pi: That is the question!" (Robert Löw)

A.3 Mathematical definitions

- **Fourier transformation:** Throughout the manuscript we use the definition of [296]: Suppose $f(x)$ is an arbitrary function defined on the real axis $(-\infty, \infty)$. First, we define a periodic function $f_\ell(x)$ with period 2ℓ, which coincides with $f(x)$ in the interval $(-\ell, \ell)$. The *Fourier series* of $f_\ell(x)$ is defined by

$$f_\ell(x) \stackrel{\text{def}}{=} \frac{1}{2\ell} \sum_{n=-\infty}^{\infty} \mathrm{e}^{i2\pi k_n x}\, \tilde{f}_\ell(k_n) \tag{A.9a}$$

where $k_n \stackrel{\text{def}}{=} n/(2\ell)$ and

$$\tilde{f}_\ell(k_n) = \int_{-\ell}^{\ell} dx\, \mathrm{e}^{-i2\pi k_n x}\, f(x) \tag{A.9b}$$

is the *Fourier transform* of $f_\ell(x)$. In the limit $\ell \to \infty$ we obtain[190]

$$f(x) \stackrel{\text{def}}{=} \mathcal{F}[\tilde{f}](x) \stackrel{\text{def}}{=} \int_{-\infty}^{\infty} dk\, \mathrm{e}^{i2\pi kx} \tilde{f}(k) \tag{A.10a}$$

$$\tilde{f}(k) \stackrel{\text{def}}{=} \mathcal{F}^{-1}[f](k) \stackrel{\text{def}}{=} \int_{-\infty}^{\infty} dx\, \mathrm{e}^{-i2\pi kx} f(x) \tag{A.10b}$$

In this notation the Dirac δ-distribution is given by

$$\delta(x - x_0) \stackrel{\text{def}}{=} \int_{-\infty}^{+\infty} dk\, \mathrm{e}^{+i2\pi k(x-x_0)} \quad \text{with} \quad \tilde{\delta}(k) = \mathrm{e}^{-i2\pi kx_0} \tag{A.11a}$$

and consequently

$$\delta(k - k_0) \stackrel{\text{def}}{=} \int_{-\infty}^{+\infty} dx\, \mathrm{e}^{-i2\pi(k-k_0)x} \quad \text{with} \quad \tilde{\delta}(x) = \mathrm{e}^{+i2\pi k_0 x} \tag{A.11b}$$

- **Hankel transformation:** The *Hankel transformation* and its inverse are given by

$$g(k) \stackrel{\text{def}}{=} 2\pi \int_0^{\infty} dr\, r\, f(r)\, J_0(2\pi kr) \tag{A.12a}$$

$$f(r) \stackrel{\text{def}}{=} 2\pi \int_0^{\infty} dk\, k\, g(k)\, J_0(2\pi kr) \tag{A.12b}$$

where $J_0(z)$ is the Bessel function of first kind and zero order [297, ch. 9.1.20].

[190] The notation k emphasises the factor 2π, which is used to get an angular frequency ω from a frequency ν, $f(t) \stackrel{\text{def}}{=} \mathcal{F}[\tilde{f}](t) \stackrel{\text{def}}{=} \int_{-\infty}^{\infty} d\nu\, \mathrm{e}^{i2\pi\nu t} \tilde{f}(\nu)$.

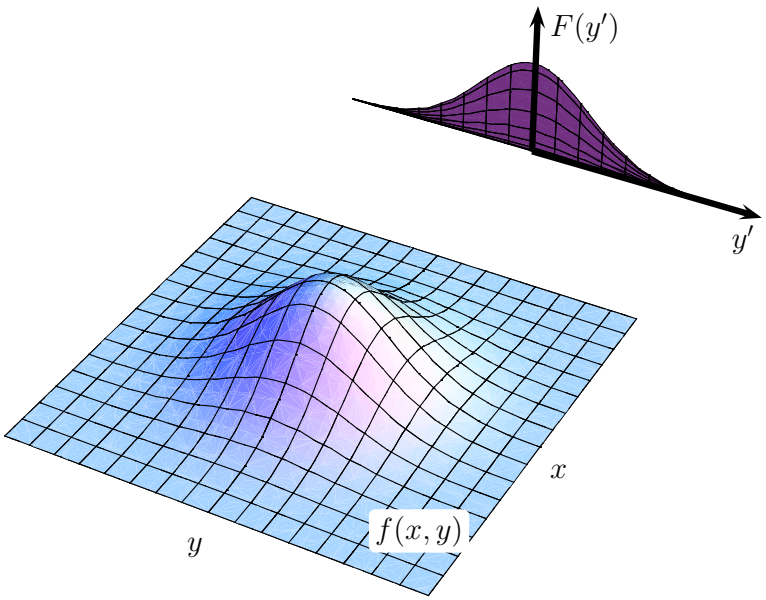

Fig. A.3, Inverse Abel transformation: Integrating the two-dimensional, cylindrical symmetric density distribution $f(x, y)$ along the x-direction maintains the full two-dimensional information. Therefore, $f(x, y)$ can be reconstructed from the one-dimensional projection $F(y')$ using the inverse Abel transformation (A.13).

A.4 Inverse Abel transformation

Symmetries reduce the degrees of freedom and hence simplify the system. E.g., a three-dimensional, cylindrical symmetric density distribution $f(\boldsymbol{r}) = f(r, \vartheta)$ is fully characterizes by only two variables. Hence, if $f(\boldsymbol{r})$ is integrated along an axis perpendicular to the symmetry axis (here taken to be the z-direction) the three-dimensional information is maintained. Therefore, the three-dimensional density distribution $f(r, \vartheta)$ can be reconstructed from the two-dimensional projection $F(y', z)$. This is commonly done by the inverse Abel transformation

$$f(x, y, z) = \frac{1}{2\pi} \int_0^\infty dk\ k \cdot J_0(k \cdot \rho) \int_{-\infty}^{+\infty} dy'\ F(y', z)\ \mathrm{e}^{-ik \cdot y'} \tag{A.13}$$

with the polar coordinate $\rho \stackrel{\text{def}}{=} \sqrt{x^2 + y^2}$.

Explicit calculation:
In order to use the Abel transformation the projection axis (x-direction) must be perpendicular to the symmetry axis (z-direction). In the following we simplify the notation and discuss how to obtain the two-dimensional spatial density $f(x, y, z_0)$ for an arbitrary but fixed z_0 from the one-dimensional projection $F(y', z_0)$ as sketched in fig. A.3. Carrying out the procedure for each z_0-plane separately yields the three-dimensional spatial density distribution $f(x, y, z)$. From now on, the index z_0 will be omitted.

The projection, which we want to invert, is given by[191]

$$F(y') \stackrel{\text{def}}{=} \int_{-\infty}^{\infty} dx \int_{-\infty}^{\infty} dy\; f(x,y)\,\delta(y'-y) \tag{A.14a}$$

$$\stackrel{(A.11)}{=} \int dxdy \int_{-\infty}^{\infty} d\hbar\; f(x,y)\,\mathrm{e}^{+i2\pi\hbar\cdot(y'-y)}$$

$$\stackrel{\text{def}}{=} \int d\hbar\; \mathrm{e}^{+i2\pi\hbar\, y'}\, h(\hbar) \tag{A.14b}$$

where we defined $h(\hbar)$ such that on the one hand side it is the Fourier transform of $F(y')$

$$h(\hbar) \stackrel{(A.14b)}{=} \tilde{F}(\hbar) \equiv \int_{-\infty}^{+\infty} dy'\; \mathrm{e}^{-i2\pi\hbar\, y'} F(y') \tag{A.14c}$$

while on the other hand side it is given by

$$\begin{aligned} h(\hbar) &\equiv \int dxdy\; f(x,y)\,\mathrm{e}^{-i2\pi\hbar\, y} \\ &= \int_0^{\infty} d\rho \int_0^{2\pi} d\varphi\; \rho\, f(\rho)\,\mathrm{e}^{-i2\pi\hbar\cdot\rho\sin\varphi} \\ &\equiv 2\pi \int d\rho\, \rho\, f(\rho)\, J_0(2\pi\hbar\cdot\rho) \end{aligned} \tag{A.14d}$$

Here, the integral representation of the Bessel function $J_0(z)$ of first kind and zeroth order was used[192]. The last expression is just the Hankel transformation, hence,

$$\begin{aligned} f(x,y) \mathrel{\widehat{=}} f(\rho) &\stackrel{(A.12b)}{=} 2\pi \int_0^{\infty} d\hbar\, \hbar\, J_0(2\pi\hbar\cdot\rho)\, h(\hbar) \\ &\stackrel{(A.14c)}{=} 2\pi \int d\hbar\, \hbar\, J_0(2\pi\hbar\cdot\rho) \int dy'\; \mathrm{e}^{-i2\pi\hbar y'}\, F(y') \end{aligned}$$

which provides eq. (A.13) with $\hbar \stackrel{\text{def}}{=} k/(2\pi)$. The alternative form [298]

$$f(x,y) = -\frac{1}{\pi} \int_{\rho}^{\infty} dy'\; \frac{\partial F}{\partial y'} \frac{1}{\sqrt{y'^2-\rho^2}} \tag{A.14e}$$

is obtained, by using the identity $k\,\mathrm{e}^{-iky'} = i\frac{\partial}{\partial y'}\left(\mathrm{e}^{-iky'}\right)$, integrating by parts[193], and Fourier transforming the Bessel function. However, in eq. (A.14e) the derivative of $F(y')$ must be calculated numerically, which produces additional errors and also complicates the usage of filters [299].

[191] Since the integral boundaries do not change, they are explicitly written only when they appear for the first time.

[192] Use $J_0(z) \stackrel{\text{def}}{=} \frac{1}{\pi}\int_0^{\pi} d\varphi\; \mathrm{e}^{iz\cos\varphi}$ (see [297, ch. 9.1.20]), then $2\int_0^{\pi} ... = \int_0^{2\pi} ...$ and replace $\cos\varphi$ by $\sin\varphi$. Thus, $J_0(z) \stackrel{\text{def}}{=} \frac{1}{2\pi}\int_0^{2\pi} d\varphi\; \mathrm{e}^{iz\sin\varphi}$. Finally note that $J_0(z)$ is an even function, $J_0(z) = J_0(-z)$.

[193] Use that the spatial density distribution $F(y')$ vanishes for $y \to \pm\infty$.

A.5 Dipolar interactions: Some basic calculations

This section contains some detailed calculations for dipolar condensates. None of these calculations is new and presumably none is mathematically rigorous. Nevertheless, they deepened my understanding of the system at hand and might be useful to others.

A.5.1 Dipole-dipole interaction in position space

The *dipole-dipole interaction potential* (bare as well as pseudo)

$$V_{\mathrm{dd}}(\boldsymbol{r}) = \frac{\mu_0}{4\pi}\,\frac{\boldsymbol{\mu}_{\mathrm{m}_1}\cdot\boldsymbol{\mu}_{\mathrm{m}_2} - 3\,(\boldsymbol{\mu}_{\mathrm{m}_1}\cdot\boldsymbol{e}_r)\cdot(\boldsymbol{\mu}_{\mathrm{m}_2}\cdot\boldsymbol{e}_r)}{r^3} - \frac{2}{3}\,\mu_0\,\mu_{\mathrm{m}}^2\,\delta(\boldsymbol{r}) \tag{A.15a}$$

describes the interaction of two permanent magnetic dipoles $\boldsymbol{\mu}_{\mathrm{m}_1}$ and $\boldsymbol{\mu}_{\mathrm{m}_2}$, which are separated by $\boldsymbol{r} \stackrel{\mathrm{def}}{=} r\,\boldsymbol{e}_r$. If the dipoles are polarised in the z-direction the interaction potential becomes

$$\begin{aligned} V_{\mathrm{dd}}(\boldsymbol{r}) &= \frac{\mu_0\,\mu_{\mathrm{m}}^2}{4\pi}\,\frac{1-3\,(z/r)^2}{r^3} - \frac{2}{3}\,\mu_0\,\mu_{\mathrm{m}}^2\,\delta(\boldsymbol{r}) \\ &= g_{\mathrm{dd}}\left(\frac{3}{4\pi}\,\frac{1-3\,\cos^2\vartheta}{r^3} - 2\,\delta(\boldsymbol{r})\right) \end{aligned} \tag{A.15b}$$

where $g_{\mathrm{dd}} \equiv 4\pi\hbar^2\,a_{\mathrm{dd}}/m \equiv g\,\epsilon_{\mathrm{dd}}$. It consists of two terms: a long-range term, which is proportional to the spherical harmonic $Y_{2,0}(\vartheta)$, and a short-range term, which incorporates the view that the magnetic moment stems from a "current loop" of infinitesimal size [300, 301].

Derivation *via* the "magnetic potential"
A simple way to motivate the interaction potential for magnetic DDIs, eq. (A.15b), is to stress the similarity with electric dipoles [300].

The standard derivation of the conservative (irrotational) electric DDI considers two opposite electric charges $\pm e$ placed at the origin and separated by the vector $\boldsymbol{r}_{12}$. The electrical dipole moment $\boldsymbol{d} = e\boldsymbol{r}_{12}$ produces an *electric potential*

$$\varphi_{\mathrm{el}}(\boldsymbol{r}) = -\frac{1}{4\pi\epsilon_0}\boldsymbol{d}\cdot\boldsymbol{\nabla}\frac{1}{|\boldsymbol{r}|} \tag{A.16}$$

at the position $\boldsymbol{r}$ if $r \gg r_{12}$. The electric field is defined by $\boldsymbol{E}(\boldsymbol{r}) = -\boldsymbol{\nabla}\varphi_{\mathrm{el}}(\boldsymbol{r})$. In order to obtain the electric potential assume to place a fictive test dipole $\boldsymbol{d}'$ at the position $\boldsymbol{r}$. The fictive dipole does not have any effect on $\boldsymbol{d}$, but only probes the electric interaction potential, which is given by $V_{\mathrm{dd}}(\boldsymbol{r}) = -\boldsymbol{d}'\cdot\boldsymbol{E}(\boldsymbol{r})$.

Although tempting, the magnetic potential $\varphi_{\mathrm{mag}}(\boldsymbol{r})$ produced by a magnetic dipole is not obtained by just replacing $\{\boldsymbol{d}, \epsilon_0\} \to \{\boldsymbol{\mu}_{\mathrm{m}}, 1/\mu_0\}$, but we have to allow for an extra term in order to fulfill Maxwell's equation of the non-existence of magnetic monopoles,

$\boldsymbol{\nabla}\cdot\boldsymbol{B}=0$. Therefore, we start with the ansatz

$$\boldsymbol{B}(\boldsymbol{r}) = -\boldsymbol{\nabla}\varphi_{\mathrm{B}}(\boldsymbol{r}) = -\boldsymbol{\nabla}\varphi_{\mathrm{mag}}(\boldsymbol{r}) + \boldsymbol{f}_{\mathrm{B}}(\boldsymbol{r}) \tag{A.17a}$$

where the "*magnetic potential*" is defined as[194]

$$\varphi_{\mathrm{B}}(\boldsymbol{r}) \stackrel{\mathrm{def}}{=} \varphi_{\mathrm{mag}}(\boldsymbol{r}) - F_{\mathrm{B}}(\boldsymbol{r}) \tag{A.17b}$$

with

$$\varphi_{\mathrm{mag}}(\boldsymbol{r}) \stackrel{\mathrm{def}}{=} -\frac{\mu_0}{4\pi}\boldsymbol{\mu}_{\mathrm{m}}\cdot\boldsymbol{\nabla}\frac{1}{|\boldsymbol{r}|} \tag{A.17c}$$

and some unknown vector $\boldsymbol{f}_{\mathrm{B}}(\boldsymbol{r}) \stackrel{\mathrm{def}}{=} \boldsymbol{\nabla}F_{\mathrm{B}}(\boldsymbol{r})$. This unknown vector needs to be specified from[195] $0=\boldsymbol{\nabla}\cdot\boldsymbol{B}(\boldsymbol{r})=\boldsymbol{\nabla}\cdot\left[-\mu_0\boldsymbol{\mu}_{\mathrm{m}}\delta(\boldsymbol{r})+\boldsymbol{f}_{\mathrm{B}}(\boldsymbol{r})\right]$. Doing so, the magnetic field[196]

$$\begin{aligned}\boldsymbol{B}(\boldsymbol{r}) &= -\boldsymbol{\nabla}\varphi_{\mathrm{mag}}(\boldsymbol{r}) + \mu_0\boldsymbol{\mu}_{\mathrm{m}}\delta(\boldsymbol{r}) \\ &= -\frac{\mu_0}{4\pi}\frac{r^2\boldsymbol{\mu}_{\mathrm{m}} - 3(\boldsymbol{\mu}_{\mathrm{m}}\cdot\boldsymbol{r})\,\boldsymbol{r}}{r^5} + \frac{2}{3}\,\mu_0\boldsymbol{\mu}_{\mathrm{m}}\delta(\boldsymbol{r})\end{aligned}$$

produced by the magnetic moment $\boldsymbol{\mu}_{\mathrm{m}}$ is obtained. If a fictive magnetic test dipole $\boldsymbol{\mu}_{\mathrm{m}'}=\boldsymbol{\mu}_{\mathrm{m}}$ is placed at the position $\boldsymbol{r}$, the dipole-dipole interaction potential is given by

$$\begin{aligned}V_{\mathrm{dd}}(\boldsymbol{r}) &= -\boldsymbol{\mu}_{\mathrm{m}'}\cdot\boldsymbol{B}(\boldsymbol{r}) = -\frac{\mu_0}{4\pi}\,(\boldsymbol{\mu}_{\mathrm{m}}\cdot\boldsymbol{\nabla})^2\frac{1}{|\boldsymbol{r}|} - \mu_0\mu_{\mathrm{m}}^2\delta(\boldsymbol{r}) \\ &= -\frac{\mu_0}{4\pi}\,\mu_{\mathrm{m}}^2\frac{\partial^2}{\partial z^2}\frac{1}{|\boldsymbol{r}|} - \mu_0\mu_{\mathrm{m}}^2\delta(\boldsymbol{r}) \\ &= \frac{\mu_0\,\mu_{\mathrm{m}}^2}{4\pi}\,\frac{1-3\,(z/r)^2}{r^3} - \frac{2}{3}\,\mu_0\,\mu_{\mathrm{m}}^2\,\delta(\boldsymbol{r})\end{aligned} \tag{A.18}$$

In the last two equations the dipoles are assumed to be polarised in z-direction.

[194] To emphasise that this is only a construction, which simplifies the mathematics, we refer to eq. (A.17b) by putting the term 'magnetic potential' in quotes.

[195] Use: $(\boldsymbol{\nabla}\cdot\boldsymbol{\nabla})(\boldsymbol{\mu}\cdot\boldsymbol{\nabla})=\nabla^2(\boldsymbol{\mu}\cdot\boldsymbol{\nabla})=(\boldsymbol{\mu}\cdot\boldsymbol{\nabla})\nabla^2=\boldsymbol{\nabla}\cdot(\boldsymbol{\mu}\nabla^2)$ and $\nabla^2 1/|\boldsymbol{r}|=-4\pi\delta(\boldsymbol{r})$, see [301, ch. 1.7].

[196] The function $1/r$ is singular at the origin and has to be replaced by a function which is regular everywhere, e.g. $1/r=\lim_{\epsilon\to 0}1/\sqrt{r^2+\epsilon^2}$. Use [159]

$$\frac{\partial^2}{\partial x_i\partial x_j}\,\frac{1}{r} = \frac{3\,x_i x_j - r^2\,\delta_{i,j}}{r^5} - \lim_{\epsilon\to 0} g_\epsilon(\boldsymbol{r})$$

where $g_\epsilon(\boldsymbol{r}) \stackrel{\mathrm{def}}{=} \epsilon^2/(r^2+\epsilon^2)^{5/2}$ and show that this function tends to $\frac{4\pi}{3}\,\delta(\boldsymbol{r})$ in the limit $\epsilon\to 0$. The simplest way to convince oneself, is to integrate it over a sphere of radius $R>0$.

A.5.2 Dipole-dipole interaction in Fourier space

Since the short-range contribution of the DDI (A.15b) can be absorbed by the contact interaction, we will concentrate on the long-range term[197]

$$V'_{\mathrm{dd}}(\boldsymbol{r}) \stackrel{\mathrm{def}}{=} \frac{\mu_0}{4\pi}\,\frac{r^2\,\mu_{\mathrm{m}}^2 - 3\,(\boldsymbol{\mu}_{\mathrm{m}}\cdot\boldsymbol{r})^2}{r^5} \tag{A.19a}$$

$$\stackrel{(A.18)}{=} -\frac{\mu_0}{4\pi}\,(\boldsymbol{\mu}_{\mathrm{m}}\cdot\boldsymbol{\nabla})^2\frac{1}{r} - \frac{\mu_0\,\mu_{\mathrm{m}}^2}{3}\,\delta(\boldsymbol{r}) \tag{A.19b}$$

The aim of this section is to derive its Fourier transform

$$\tilde{V}'_{\mathrm{dd}}(\boldsymbol{k}) = -\frac{\mu_0}{3}\left(\mu_{\mathrm{m}}^2 - 3\frac{(\boldsymbol{\mu}_{\mathrm{m}}\cdot\boldsymbol{k})^2}{|\boldsymbol{k}|^2}\right) = -g_{\mathrm{dd}}\left(1 - 3\,(\boldsymbol{e}_{\mu_{\mathrm{m}}}\cdot\boldsymbol{e}_k)^2\right) \tag{A.20}$$

which was first done in [69]. In the following two different derivations are presented.

Brute force integration

Here the regularised expression of the DDI (A.19a) is used and the integrals are evaluated step by step. We found this derivation in Axel Pelster's lecture notes [302].

The Fourier transformation is defined in eq. (A.10). Due to the symmetry of the DDI, spherical coordinates

$$\boldsymbol{e}_{\bar{k}} \stackrel{\mathrm{def}}{=} \begin{pmatrix} 0 \\ 0 \\ 1 \end{pmatrix}, \qquad \boldsymbol{e}_{\mu_{\mathrm{m}}} \stackrel{\mathrm{def}}{=} \begin{pmatrix} \sin\vartheta\cos\varphi \\ \sin\vartheta\sin\varphi \\ \cos\vartheta \end{pmatrix}, \qquad \boldsymbol{e}_r \stackrel{\mathrm{def}}{=} \begin{pmatrix} \sin\alpha\cos\beta \\ \sin\alpha\sin\beta \\ \cos\alpha \end{pmatrix}$$

are appropriate. Expressing the Fourier transform of eq. (A.19a) in these coordinates results in

$$\begin{aligned}
\tilde{V}'_{\mathrm{dd}}(\bar{\boldsymbol{k}}, a) &\stackrel{\mathrm{def}}{=} \int_a^\infty dr \int_0^\pi d\alpha \int_0^{2\pi} d\beta\; r^2 \sin\alpha\, V'_{\mathrm{dd}}(\boldsymbol{r})\; \mathrm{e}^{-i\,2\pi\bar{\boldsymbol{k}}\cdot\boldsymbol{r}} \\
&= -\frac{\mu_0\mu_{\mathrm{m}}^2}{4\pi}\int_a^\infty \frac{dr}{r}\int_0^\pi d\alpha\;\sin\alpha\;\mathrm{e}^{-i\,2\pi\,\bar{k}r\cos\alpha}\int_0^{2\pi} d\beta \\
&\quad\times\Big\{3\sin^2\vartheta\sin^2\alpha\left[\cos^2\varphi\cos^2\beta + 2\sin\varphi\cos\varphi\sin\beta\cos\beta + \sin^2\varphi\cos^2\beta\right] \\
&\qquad + 6\sin\vartheta\cos\vartheta\sin\alpha\cos\alpha\left[\cos\varphi\cos\beta + \sin\varphi\sin\beta\right] \\
&\qquad + 3\cos^2\vartheta\cos^2\alpha - 1\Big\}
\end{aligned} \tag{A.21}$$

[197] Notation: The prime indicates that only the long-range part of the dipole-dipole interaction (A.15b) is used.

where the cut-off parameter a is introduced to regularise UV divergences[198]. Evaluating the β-integral reduces eq. (A.21) to

$$\tilde{V}'_{\rm dd}(\boldsymbol{\hbar}, a) = \frac{\mu_0 \mu_{\rm m}^2}{4} \left(1 - 3\cos^2\vartheta\right) \int_a^\infty \frac{dr}{r} \int_0^\pi d\alpha \, \sin\alpha \, \mathrm{e}^{-i\,2\pi\,\hbar r \cos\alpha} \left(3\cos^2\alpha - 1\right)$$

and the α-integration provides

$$\tilde{V}'_{\rm dd}(\boldsymbol{\hbar}, a) = \mu_0 \mu_{\rm m}^2 \left(1 - 3\cos^2\vartheta\right) \int_a^\infty \frac{dr}{r} \left\{ 3\frac{\cos kr}{(kr)^2} - 3\frac{\sin kr}{(kr)^3} + \frac{\sin kr}{kr} \right\}$$

with $k \equiv 2\pi\hbar$. The final r-integral is evaluated using partial integration,

$$\tilde{V}'_{\rm dd}(\boldsymbol{\hbar}, a) = \mu_0 \mu_{\rm m}^2 \left(1 - 3\cos^2\vartheta\right) \left\{ \frac{\cos ka}{(ka)^2} - \frac{\sin ka}{(ka)^3} \right\} \tag{A.22}$$

which is the intermediate result stated in [69]. Since the final results must not depend on the cut-off parameter, it is now removed by taking the limit $a \to 0^+$. Using $\cos\vartheta = \boldsymbol{\mu}_{\rm m} \cdot \boldsymbol{k}/(\mu_{\rm m} k)$, we obtain eq. (A.20).

Utilising the "magnetic potential"

As in the derivation of the DDI potential *via* the "magnetic potential" (see section A.5.1) we encounter the problem that $1/r$ is singular at the origin and therefore its derivative must be evaluated carefully. However, derivatives become simple in Fourier space, and this is the trick we gone use.

The challenge is to calculate the the Fourier transformation of $1/r$. Fortunately, this is just the Fourier transform of the Coulomb potential, which is well known in atomic physics. Inserting[199]

$$\frac{1}{r} = \int d^3\hbar \, \mathrm{e}^{+i\,2\pi\boldsymbol{\hbar}\cdot\boldsymbol{r}} \frac{1}{\pi\,\hbar^2}$$

into eq. (A.19b) the Fourier transformation (A.10) yields

$$\tilde{V}'_{\rm dd}(\boldsymbol{\hbar}') = -\frac{\mu_0\,\mu_{\rm m}^2}{3} - \frac{\mu_0}{4\pi} \int d^3r \, \mathrm{e}^{-i\,2\pi\boldsymbol{\hbar}'\cdot\boldsymbol{r}} (\boldsymbol{\mu}_{\rm m} \cdot \boldsymbol{\nabla})^2 \left[\int d^3\hbar \, \mathrm{e}^{+i\,2\pi\boldsymbol{\hbar}\cdot\boldsymbol{r}} \frac{1}{\pi\,\hbar^2} \right]$$

The rest is simple. Just evaluate the derivative

$$\tilde{V}'_{\rm dd}(\boldsymbol{\hbar}') = -\frac{\mu_0\,\mu_{\rm m}^2}{3} - \frac{\mu_0}{4\pi} \int d^3r \int d^3\hbar \, \frac{(\boldsymbol{\mu}_{\rm m} \cdot i\,2\pi\,\boldsymbol{\hbar})^2}{\pi\,\hbar^2} \, \mathrm{e}^{i\,2\pi(\boldsymbol{\hbar}-\boldsymbol{\hbar}')\cdot\boldsymbol{r}}$$

[198] Physically, the cut-off parameter a accounts for the fact that two atoms can not overlap. Hence, it is identified with twice the atomic radius.

[199] In order to get an expression which is regular everywhere calculate the Fourier transform of $\mathrm{e}^{-\lambda r}/r$ and take the limit $\lambda \to 0^+$.

and use the Fourier representation of the Dirac δ-distribution, eq. (A.11b), to obtain[200]

$$\tilde{V}'_{\mathrm{dd}}(\boldsymbol{\hbar k}') = -\frac{\mu_0\,\mu_{\mathrm{m}}^2}{3} + \mu_0 \int d^3\hbar k \, \left(\boldsymbol{\mu}_{\mathrm{m}} \cdot \frac{\boldsymbol{\hbar k}}{\hbar k}\right)^2 \delta(\boldsymbol{\hbar k} - \boldsymbol{\hbar k}')$$

This results in eq. (A.20).

A.5.3 Dipolar coupling of different atomic states

The underlying mechanism of Feshbach resonances is the coupling of different molecular states. In the case of ^{52}Cr the dominant contribution comes from the DDI [126, 127]. The DDI mixes states with different orbital angular momentum $\boldsymbol{l} \stackrel{\mathrm{def}}{=} \boldsymbol{r} \times \boldsymbol{p}$ and/or magnetic quantum number m_l. Therefore, if two atoms meet, which were initially in the asymptotic 2-body state $|l, m_l\rangle$, they may end up in the state $|l', m_{l'}\rangle$ after the scattering process. The same mechanism is responsible for dipolar relaxations [119, 123, 170, 189].

Consider two atoms $n = 1, 2$. Each atom exhibits a total angular momentum $\boldsymbol{J}_n = (J_{nx}, J_{ny}, J_{nz})$, which translates into a magnetic moment $\boldsymbol{\mu}_{\mathrm{m}_n} \equiv g_n \mu_{\mathrm{B}}\, \boldsymbol{J}_n/\hbar$. The two particles are separated by $\boldsymbol{r} \stackrel{\mathrm{def}}{=} \boldsymbol{r}_2 - \boldsymbol{r}_1$. In order to convince oneself that the DDI mixes states with different orbital angular momentum we can assume a fully polarised sample and therefore use eq. (A.15b). Noting that the spherical harmonics $Y_{2,0}(\vartheta)$ is proportional to $1 - 3\cos^2\vartheta$, we immediately see that states with orbital angular momentum $\boldsymbol{l}$ and $\boldsymbol{l}' = \boldsymbol{l} \pm 2$ are mixed (the details are presented below). However, to see that the magnetic quantum numbers m_l get mixed as well, we need to use the non-polarised version of the dipole-dipole potential instead, eq. (A.15a).

The calculation is tedious, but straight forward. We express the relative position vector $\boldsymbol{r}$ from eq. (A.15a) in spherical coordinates (r, ϑ, φ) and use the ladder operators $\hat{\mathrm{J}}_{n\pm} \stackrel{\mathrm{def}}{=} \hat{\mathrm{J}}_{nx} \pm i\,\hat{\mathrm{J}}_{ny}$ to obtain [119, 123, 189]

$$\hat{\mathrm{H}}_{\mathrm{dd}} = -\frac{\mu_0}{4\pi r^3} \frac{{\mu_{\mathrm{B}}}^2 g_1 g_2}{\hbar^2} \cdot \sqrt{\frac{6\,\pi}{5}} \sum_{l,\,m_l} \hat{\mathcal{T}}_{l,m_l} \tag{A.23}$$

where

$$\begin{aligned}\sum_{l,\,m_l} \hat{\mathcal{T}}_{l,m_l} = {} & Y_{2,-2}\,\hat{\mathrm{J}}_{1+}\,\hat{\mathrm{J}}_{2+} + Y_{2,-1}\,(\hat{\mathrm{J}}_{1z}\,\hat{\mathrm{J}}_{2+} + \hat{\mathrm{J}}_{1+}\,\hat{\mathrm{J}}_{2z}) \\ & + 4\sqrt{\frac{1}{6}}\,Y_{2,0}\,\hat{\mathrm{J}}_{1z}\,\hat{\mathrm{J}}_{2z} - \sqrt{\frac{1}{6}}\,Y_{2,0}\left(\hat{\mathrm{J}}_{1+}\,\hat{\mathrm{J}}_{2-} + \hat{\mathrm{J}}_{1-}\,\hat{\mathrm{J}}_{2+}\right) \\ & - Y_{2,1}\,(\hat{\mathrm{J}}_{1z}\,\hat{\mathrm{J}}_{2-} + \hat{\mathrm{J}}_{1-}\,\hat{\mathrm{J}}_{2z}) + Y_{2,2}\,\hat{\mathrm{J}}_{1-}\,\hat{\mathrm{J}}_{2-}\end{aligned}$$

[200] Note $\delta(\alpha z) = \delta(z)/|\alpha|$, which provides $\delta(-z) = \delta(z)$.

is the so called *tensor interaction*[201]. In this representation it is obvious that the DDI does neither preserve the magnetic quantum numbers $m_{\mathrm{J}_1}, m_{\mathrm{J}_2}$ — because $\hat{\mathrm{J}}_{n\pm}|m_n\rangle \propto |m_n \pm 1\rangle$ — nor the relative orbital angular momentum l of the two particles — because $\int d^3r\, Y^{\star}_{l',m_{l'}} Y_{2,q} Y_{l,m}$ is non-vanishing only if[202] $|l - l'| = 0, 2$ and $m_{l'} = m_l + q$ (except for $l = l' = 0$, because the vectors must build a triangle: $\boldsymbol{l'} = \boldsymbol{l} + \text{"}\boldsymbol{2}\text{"}$). Therefore, the 2-body state $|n, l, m_l\rangle\,|m_{\mathrm{J}_1}; m_{\mathrm{J}_2}\rangle$ is coupled *via* the DDI to $|n', l', m_{l'}\rangle\,|m_{\mathrm{J}'_1}; m_{\mathrm{J}'_2}\rangle$.

Let us now specify to the system at hand: Consider two ^{52}Cr atoms, which are well separated and polarised by a strong external magnetic field $\boldsymbol{B}$. Since the energy of the different molecular potentials is dominated by the Zeeman energy, each atom is in its 1-body ground-state $|^7\mathrm{S}_3, m_{\mathrm{J}_n} = -3\rangle$ with $n = 1, 2$. Hence, the asymptotic molecular state is given by $|l, m_l\rangle|j, m_j\rangle = |l, m_l\rangle|6, -6\rangle$, where the quantum numbers j corresponds to the 2-body total angular momentum[203] $\boldsymbol{j} \stackrel{\text{def}}{=} \boldsymbol{J_1} + \boldsymbol{J_2}$.

However, if the two atoms approach each other, we have just seen that the DDI couples this state to different molecular states $|l', m_{l'}\rangle|j', m_{j'}\rangle$, with $l' - l = 0, \pm 2$ and $m_{l'} + m_{j'} = m_l + m_j$. Hence, we expand the initial 2-body state into the 1-body basis,

$$|j, m_j\rangle = \sum_{m_{\mathrm{J}_1}, m_{\mathrm{J}_2}} \langle J_1, m_{\mathrm{J}_1}, J_2, m_{\mathrm{J}_2}\,|\,j, m_j\rangle\,|J_1, m_{\mathrm{J}_1}, J_2, m_{\mathrm{J}_2}\rangle \tag{A.24}$$

where $\langle J_1, m_{\mathrm{J}_1}, J_2, m_{\mathrm{J}_2}\,|\,j, m_j\rangle$ denotes the Clebsch-Gordan coefficient. Using eq. (A.23), Mathematica easily evaluates the overlap between different molecular states[204].

A.5.4 Mean-field dipolar interaction energy

If, instead of only two dipoles, (macroscopic) many dipoles are interacting *via* the DDI, the different 2-particle potentials are averaged and a mean-field potential arises. Each particle can be thought of moving in a potential, which is produced by the other dipoles.

[201] The position vector $\boldsymbol{r}$ is the relative vector of the two particles, and hence the spherical harmonics $Y_{l,m}$ act on the *relative* orbital angular momentum l. The quantum numbers J_1 and J_2 correspond to the total angular momenta of the single particles.

[202] Use the relation

$$\int d^2\Omega\, Y_{l',m'}\, Y_{l_{\mathrm{q}},m_{\mathrm{q}}}\, Y_{l,m} = \sqrt{\frac{(2\,l'+1)\,(2\,l_{\mathrm{q}}+1)\,(2\,l+1)}{4\,\pi}} \begin{pmatrix} l' & l_{\mathrm{q}} & l \\ 0 & 0 & 0 \end{pmatrix} \begin{pmatrix} l' & l_{\mathrm{q}} & l \\ m' & m_{\mathrm{q}} & m \end{pmatrix}$$

where the brackets denote the Wigner $3j$-symbols.

[203] Since ^{52}Cr atoms do not have a nuclear spin ($I = 0$) and the orbital angular momentum in the ground-state vanishes ($L = 0$), its total angular momentum is given by the atomic spin, $\boldsymbol{J} = \boldsymbol{S}$. Therefore, the potentials are most often labeled by S.

[204] For example, consider the state $|l, m_l\rangle|j, m_j\rangle = |0, 0\rangle|6, -6\rangle$. It is coupled by the term $Y_{2,-2}\,\hat{\mathrm{J}}_{1+}\,\hat{\mathrm{J}}_{2+}$ to $\langle l', m_{l'}|\langle j', m_{j'}| = \langle 2, -2|\langle 4, -4|$ and to $\langle 2, -2|\langle 6, -4|$, while $Y_{2,-1}\,(\hat{\mathrm{J}}_{1z}\,\hat{\mathrm{J}}_{2+} + \hat{\mathrm{J}}_{1+}\,\hat{\mathrm{J}}_{2z})$ couples it only to $\langle 2, -1|\langle 6, -5|$. The coupling of the latter term to $\langle 2, -1|\langle 5, -5|$ is canceled, because the associated Clebsch-Gordan coefficients interfere destructively.

In this section we will show that the *dipolar mean-field energy*[205]

$$E_{\text{dip}} \stackrel{\text{def}}{=} \frac{1}{2} \int d^3r \; n(\boldsymbol{r}) \Phi_{\text{dip}}^{(N)}(\boldsymbol{r}) \tag{A.25a}$$

where

$$\Phi_{\text{dip}}^{(N)}(\boldsymbol{r}) \stackrel{\text{def}}{=} \int d^3r' \; V_{\text{dd}}(\boldsymbol{r} - \boldsymbol{r}') n(\boldsymbol{r}') \tag{A.25b}$$

is the *dipolar mean-field potential*[206], can be expressed as

$$E_{\text{dip}} = \frac{1}{2} \int d^3\boldsymbol{k} \; |\tilde{n}(\boldsymbol{k})|^2 \, \tilde{V}_{\text{dd}}(\boldsymbol{k}) \tag{A.26}$$

in Fourier space. This is a neat result, because the double three-dimensional integral in eq. (A.25a) is reduced to a single three-dimensional integral.

Proof
As in the previous section, we will make use of the Fourier transform. However, this time we use that the dipolar potential (A.25b) is a convolution and Fourier transforms of convolutions are easy to evaluate.

Using Parseval's theorem[207] and that the density has to be real, eq. (A.25a) reads

$$E_{\text{dip}} = \frac{1}{2} \int d^3\boldsymbol{k} \; \tilde{n}^\star(\boldsymbol{k}) \, \tilde{\Phi}_{\text{dip}}^{(N)}(\boldsymbol{k})$$

where the tilde ($\tilde{}$) indicates the Fourier transform, and the star ($\star$) the complex conjugate of the corresponding function. Using the convolution theorem[208] we end up with eq. (A.26).

A.5.5 Anisotropic function for cylindrical symmetric dipolar condensates

A Gaussian density distribution describes most of the effects observed in dipolar condensates. Remarkably, it agrees not only qualitatively, but also quantitatively. Therefore,

[205] The derivation of eq. (A.25a) is analog to the case of a purely contact interacting condensate [63, 119, 151]. The two requirements for its derivation are that (*i*) the potential $V_{\text{dd}}(\boldsymbol{r})$ considers 2-body interactions only, and (*ii*) the screened of the dipole-dipole interaction (by other dipoles lying between the two interacting dipoles) is negligible.

[206] Different notations are found in the literature and even within the Stuttgart group: $\Phi_{\text{dd}}, V_{\text{dd}}, U_{\text{dd}}$. In this thesis we refer to it as Φ_{dip} (or $\Phi_{\text{dip}}^{(N)}$, if the N-particle nature is emphasise), whereas we use V_{dd} for the 2-particle DDI only.

[207] Parseval's theorem states that $\int dx \; f(x)\, g^\star(x) = \int d\boldsymbol{k} \; \tilde{f}(\boldsymbol{k})\, \tilde{g}^\star(\boldsymbol{k})$, where the star indicates complex conjugation [296, ch. 2.1].

[208] A convolution of two functions $f(t)$ and $g(t)$ is defined as $[f \star g]\,(t) \stackrel{\text{def}}{=} \int_{-\infty}^{\infty} dt' \; f(t - t')\, g(t')$ and its Fourier transform is the product of the individual Fourier transforms, $\mathcal{F}\{f \star g\}(x) = \mathcal{F}\{f\}(x) \cdot \mathcal{F}\{g\}(x)$. The last identity is named *convolution theorem*.

it is worth to calculate the dipolar mean-field interaction energy, eq. (A.26), for a in z-direction polarised, dipolar interacting, pure condensate in a cylindrical symmetric harmonic potential. Again, only the long-range term of the DDI is considered, which yields

$$E'_{\rm dip} = -\frac{N^2\,\hbar\bar{\omega}}{\sqrt{2\pi}}\,\frac{a_{\rm dd}}{\sigma_z}\left(\frac{a_{\rm ho}}{\sigma_\rho}\right)^2 f_{\rm dip}(\kappa) \tag{A.27a}$$

$$= -\frac{N^2\,g_{\rm dd}}{\sqrt{2\pi}}\,\frac{1}{\sigma_z\,\sigma_\rho^2}\,\frac{f_{\rm dip}(\kappa)}{4\pi} \tag{A.27b}$$

with the *dipolar anisotropic function*[209] [133, 159]

$$f_{\rm dip}(\kappa) \stackrel{\rm def}{=} \frac{1+2\kappa^2}{1-\kappa^2} - \frac{3\kappa^2 {\rm arctanh}[\sqrt{1-\kappa^2}]}{(1-\kappa^2)^{3/2}} \tag{A.27c}$$

the mean trapping energy $\hbar\bar{\omega} \stackrel{\rm def}{=} \hbar(\omega_\rho^2\omega_z)^{1/3}$, the harmonic oscillator length $a_{\rm ho} \stackrel{\rm def}{=} \sqrt{\hbar/(m\bar{\omega})}$, the dipolar lengths $a_{\rm dd} \stackrel{\rm def}{=} m\,\mu_0\mu_{\rm m}^2/(12\pi\hbar^2)$, the Gaussian widths of the wavefunction in transversal σ_ρ and longitudinal σ_z direction, and the aspect ratio $\kappa \stackrel{\rm def}{=} \sigma_\rho/\sigma_z$. Note that eq. (A.27c) holds in cylindrical symmetric traps for Gaussian as well as Thomas-Fermi wavefunctions. A three-dimensional version is given in [161].

Explicit calculation

We assume that the wavefunction of the condensate is given by

$$\psi(\boldsymbol{r}) = \sqrt{N}\,g^{(\sigma_x)}(x)\,g^{(\sigma_y)}(y)\,g^{(\sigma_z)}(z)$$

where $g^{(\sigma)}(x) \stackrel{\rm def}{=} \frac{1}{\pi^{1/4}\,\sigma^{1/2}}\,\exp\left[-x^2/(2\sigma^2)\right]$ is a Gaussian normalised to one, $\int dx|g^{(\sigma)}(x)|^2 = 1$, and N is the atom number. Using eq. (A.26) and that the density is given by $n(\boldsymbol{r}) \stackrel{\rm def}{=} |\psi(\boldsymbol{r})|^2$, and therefore $\tilde{n}(\boldsymbol{\bar{k}}) = N\,\exp\left[-(\pi\,\boldsymbol{\sigma}\cdot\boldsymbol{\bar{k}})^2\right]$, we obtain

$$\begin{aligned}
E_{\rm dip} &= -N^2\,\frac{g_{\rm dd}}{2}\int d^3\bar{k}\,(1-3\cos^2\vartheta)\,{\rm e}^{-2(\pi\,\boldsymbol{\sigma}\cdot\boldsymbol{\bar{k}})^2} \\
&= -N^2\,\frac{g_{\rm dd}}{2}\int_0^\infty d\bar{k}\int_{-1}^{+1} d\xi\int_0^{2\pi} d\varphi\,(1-3\,\xi^2)\,{\rm e}^{-2\bar{k}^2\,(\pi\,\sigma_\rho)^2\left[(1-\xi^2)+\xi^2/\kappa^2\right]} \\
&= -N^2\,\frac{g_{\rm dd}}{\sqrt{2\pi}\,\sigma_\rho^2\,\sigma_z}\,\frac{1}{8\pi\,\kappa}\int_{-1}^{+1} d\xi\frac{1-3\,\xi^2}{\left[1+(\frac{1}{\kappa^2}-1)\xi^2\right]^{3/2}}
\end{aligned}$$

where in the second line we used spherical coordinates and substituted $\xi = \cos\vartheta$. The final integral is tedious to calculate, however, it is not complicated[210] and yields eq. (A.27).

[209] Note that many authors include an additional minus sign in the definition of $f_{\rm dip}(\kappa)$. Although I agree that this sign convention simplifies discussions involving the dipolar mean-field energy, I use eq. (A.27c) nevertheless in order to be consistent with our publication [237].

[210] Subsequent substitute (i) $\sqrt{a}\xi = \sinh y$, with $a = \kappa^{-2}-1$, and (ii) $z = \tanh y$. Use $\frac{\partial}{\partial\xi}\frac{\xi}{(1+a\xi^2)^{1/2}} = \frac{1}{(1+a\xi^2)^{3/2}}$ to evaluate the integrals. Finally, in order to to obtain ${\rm arcsinh}(\sqrt{a}) = {\rm arctanh}(\sqrt{1-\kappa^2})$

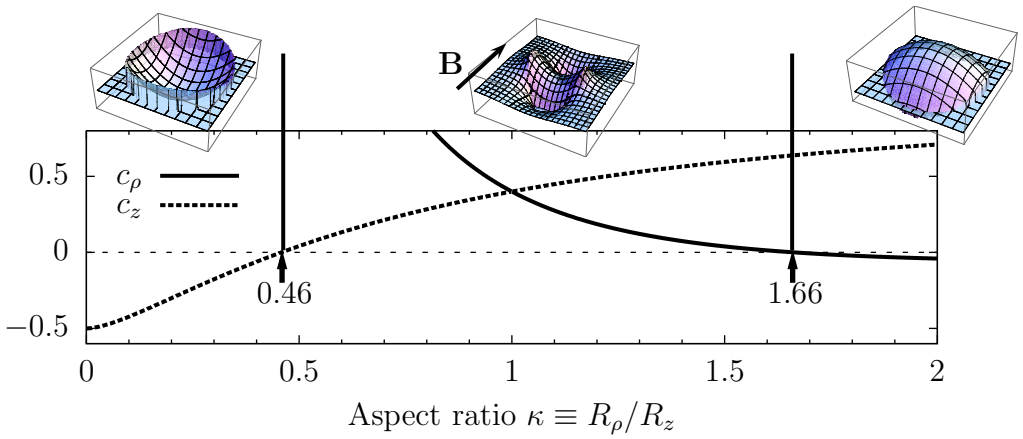

Fig. A.4, Thomas-Fermi dipolar potential: The shape of the dipolar mean-field potential (in the TF limit) depends on the signs of the coefficients c_ρ and c_z in eq. (A.28a). If we increase κ starting at small κ, the mean-field potential has initially the shape of a positive curves parabola. When c_z becomes positive at $\kappa \approx 0.46$, it becomes a saddle and finally, when c_ρ becomes negative at $\kappa \approx 1.66$, we obtain a negative curved parabola.

A.5.6 Mean-field dipolar potential in the Thomas-Fermi limit

The long-range part of the dipolar mean-field potential (of a pure condensate in the Thomas-Fermi limit and confined in a cylindrical symmetric harmonic trap) is [159, 162, 163]

$$\Phi_{\rm dip}^{\prime({\rm TF})}(\boldsymbol{r}) = n_0\, g_{\rm dd} \left[-f_{\rm dip}(\kappa) + \frac{c_\rho\, \rho^2 - 2\, c_z\, z^2}{R_z^2} \right] \tag{A.28a}$$

inside the BEC[211], $(\rho/R_\rho)^2 + (z/R_z)^2 < 1$. The Thomas-Fermi radius in z-direction[212] is R_z and the coefficients c_ρ and c_z are given by

$$c_\rho \stackrel{\rm def}{=} \frac{1}{\kappa^2} + \frac{3}{2}\, \frac{f_{\rm dip}(\kappa)}{\kappa^2 - 1} \tag{A.28b}$$

$$c_z \stackrel{\rm def}{=} 1 + \frac{3}{2}\, \frac{f_{\rm dip}(\kappa)}{\kappa^2 - 1} \tag{A.28c}$$

This is a "saddle potential" only in a small region around $\kappa = 1$: In order to obtain a saddle potential the coefficients c_ρ and c_z must have the same sign — the additional term $f_{\rm dip}(\kappa)$ is unimportant, because it just produces an offset. Figure A.4 shows that both

we make use of the two identities (i) $\operatorname{arcsinh}(x) = \ln(x + \sqrt{1+x^2})$ and (ii) $\operatorname{arctanh}(x) = \frac{1}{2}\,[\ln(1+z) - \ln(1-z)]$.

[211] The Thomas-Fermi dipolar potential outside of the condensate is give in [159, 163].

[212] The dipoles are assumed to be polarised in z-direction.

coefficients are monoton and each has a single root. Therefore, the potential has the shape of a saddle only if the aspect ratio κ lies within the range $\sim (0.46, 1.66)$.

A.5.7 Dipolar interactions for isotropic density distributions

The dipolar anisotropic function $f_{\mathrm{dip}}(\kappa)$ vanishes for $\kappa = 1$. Thus, for an isotropic Gaussian or Thomas-Fermi density profile the long-range part of the dipolar mean-field energy E'_{dip} vanishes, see eq. (4.7) (page 63). In the following we will show that this is a general property of the DDI, and therefore true for *any* spherical symmetric wavefunction[213].

Proof
If the spatial density distribution (not the trapping potential, because the dipoles elongate along the z-direction) is spherical symmetric, we can easily show that the long-range part of the dipole-dipole potential vanishes, eq. (A.15b). Just use

$$-4\pi\delta(\boldsymbol{r}) = \nabla^2 \frac{1}{|\boldsymbol{r}|} = \left(\frac{\partial^2}{\partial x^2} + \frac{\partial^2}{\partial y^2} + \frac{\partial^2}{\partial z^2}\right) \frac{1}{|\boldsymbol{r}|} = 3\frac{\partial^2}{\partial z^2}\frac{1}{|\boldsymbol{r}|} \tag{A.29a}$$

and insert it into

$$\frac{1-3(z/r)^2}{r^3} = -\frac{4\pi}{3}\delta(\boldsymbol{r}) - \frac{\partial^2}{\partial z^2}\frac{1}{|\boldsymbol{r}|} \tag{A.29b}$$

A.5.8 Dipolar Bogoliubov spectrum

In this appendix we explicitly derive the famous (phononic) *Bogoliubov spectrum* for homogeneous dipolar condensates [159]

$$E(\boldsymbol{q}) = \sqrt{E_{\mathrm{free}}(\boldsymbol{q})\Big(E_{\mathrm{free}}(\boldsymbol{q}) + 2n_{\mathrm{eq}}\,[g - g_{\mathrm{dd}}(1-3\cos^2\alpha)]\Big)} \tag{A.30}$$

where $E_{\mathrm{free}}(\boldsymbol{q}) \stackrel{\mathrm{def}}{=} (\hbar\boldsymbol{q})^2/(2m)$ is the free particle dispersion relation, n_{eq} the equilibrium value of the spatial density, and α is the angle between the fully polarised magnetic moments $\boldsymbol{\mu}_{\mathrm{m}}$ and the wavevector $\boldsymbol{q}$ of the phonon. The steps of the calculations are identical to those without dipolar interactions, the only difference is to take the Fourier transform of both interaction potentials, contact and dipolar, instead of only the contact potential.

Method 1: Using the hydro-dynamical equation
This paragraph emphasises the collective character of the excitation. The starting point

[213] This implies that the long-range part of the dipolar mean-field potential $\Phi'_{\mathrm{dip}}(\boldsymbol{r})$, eq. (A.25b), vanishes at the origin, $\boldsymbol{r} = 0$. It does not vanish everywhere, e.g. in the Thomas-Fermi limit we obtain the saddle potential shown in fig. A.4.

is the time-dependent GPE (2.7a)

$$i\hbar\frac{\partial}{\partial t}\Psi = \left(-\frac{\hbar^2}{2m}\nabla^2 + V_{\text{trap}} + \Phi_{\text{int}}^{(N)}\right)\Psi$$

By expressing the wavefunction into an amplitude and a phase[214], $\Psi = \sqrt{n}\,\mathrm{e}^{iS}$, we obtain for the imaginary part

$$\frac{\partial\, n}{\partial t} = -\frac{\hbar}{m}\boldsymbol{\nabla}\cdot(n\,\boldsymbol{\nabla}S)$$

which is equivalent to the *continuity equation*[215]

$$\frac{\partial\, n}{\partial t} + \boldsymbol{\nabla}\cdot(n\boldsymbol{v}) = 0 \tag{A.31a}$$

and for the real part

$$-\hbar\frac{\partial\, S}{\partial t} = -\frac{\hbar^2}{2m}\frac{\nabla^2\sqrt{n}}{\sqrt{n}} + \frac{1}{2}\,mv^2 + V_{\text{trap}} + \Phi_{\text{int}}^{(N)} \tag{A.31b}$$

where $v = |\boldsymbol{v}|$. Taking the gradient of eq. (A.31b), provides the *hydrodynamic equation of motion*[216]

$$m\frac{\partial\,\boldsymbol{v}}{\partial t} = -\boldsymbol{\nabla}\left(V_{\text{qp}} + V_{\text{kin}} + V_{\text{trap}} + \Phi_{\text{int}}^{(N)}\right) \tag{A.32a}$$

with the quantum pressure, kinetic energy, and the mean-field interaction potential

$$V_{\text{zero}} \equiv V_{\text{qp}} \stackrel{\text{def}}{=} -\frac{\hbar^2}{2m}\frac{\boldsymbol{\nabla}^2\sqrt{n(\boldsymbol{r})}}{\sqrt{n(\boldsymbol{r})}} \tag{A.32b}$$

$$V_{\text{kin}} \stackrel{\text{def}}{=} \frac{1}{2}\,mv^2(\boldsymbol{r}) \tag{A.32c}$$

$$\Phi_{\text{int}}^{(N)} \stackrel{\text{def}}{=} \Phi_{\text{contact}}^{(N)}(\boldsymbol{r}) + \Phi_{\text{dip}}^{(N)}(\boldsymbol{r}) \tag{A.32d}$$

where $\Phi_{\text{contact}}^{(N)}(\boldsymbol{r})$ is defined analogously to $\Phi_{\text{dip}}^{(N)}(\boldsymbol{r})$ — just replace the dipole-dipole potential $V_{\text{dd}}(\boldsymbol{r})$ in eq. (A.25b) by the 2-body contact potential, eq. (2.3).

As in the purely contact interacting case, elementary excitations can be investigated by considering small perturbations of the equilibrium state. Therefore, the continuity equation (A.31a) and the hydrodynamic equation of motion (A.32a) are linearised in the velocity, $\boldsymbol{v} = \boldsymbol{v}_{\text{eq}} + \delta\boldsymbol{v} \approx \delta\boldsymbol{v}$, and density, $n = n_{\text{eq}} + \delta n$, around their equilibrium values. Taking the time derivative of eq. (A.31a) and eliminating the velocity by using eq. (A.32a),

[214] Choosing the global phase of the wavefunction formally breaks the gauge symmetry.

[215] Here $n \stackrel{\text{def}}{=} |\Psi(\boldsymbol{r})|^2$ is the spatial density and $\boldsymbol{v} \stackrel{\text{def}}{=} \frac{\hbar}{2m\,i}\cdot\frac{\Psi^\star\boldsymbol{\nabla}\Psi - \Psi\boldsymbol{\nabla}\Psi^\star}{n} = \frac{\hbar}{m}\boldsymbol{\nabla}S$ is the *velocity of the condensate*. Use $\nabla^2\Psi = \left[\nabla^2 f - f\,(\boldsymbol{\nabla}S)^2 + i\,f\,\nabla^2 S + 2i(\boldsymbol{\nabla}S)\cdot(\boldsymbol{\nabla}f)\right]\mathrm{e}^{iS}$.

[216] Apart from the so quantum pressure, it has the form of the Navier-Stokes equation used in classical hydrodynamics.

the hydrodynamic equation for the perturbation[217]

$$m\frac{\partial^2}{\partial t^2}\Big(\delta n\Big) = \boldsymbol{\nabla}\cdot\left(n_{\mathrm{eq}}\,\boldsymbol{\nabla}\delta\mu\right) \tag{A.33}$$

is obtained, with the chemical potential $\mu \overset{\mathrm{def}}{=} V_{\mathrm{qp}}(\boldsymbol{r}) + V_{\mathrm{trap}}(\boldsymbol{r}) + \Phi^{(N)}_{\mathrm{int}}(\boldsymbol{r})$. Now, beside of specifying these equations for the case of a homogeneous condensate ($n_{\mathrm{eq}}(\boldsymbol{r}) = \mathrm{const}$ and $V_{\mathrm{trap}}(\boldsymbol{r}) = 0$) one has to choose an appropriate ansatz for the solution one is interested in. Here, we choose a perturbativ ansatz, $n(\boldsymbol{r}) \equiv n_{\boldsymbol{q}}(\boldsymbol{r}) = n_{\mathrm{eq}} + \delta n_{\boldsymbol{q}}(\boldsymbol{r})$, and because we are interested in phonon-solutions, we use[218] plane waves with momentum $\hbar\boldsymbol{q}$ and energy $\hbar\omega$ as perturbations[219], $\delta n_{\boldsymbol{q}}(\boldsymbol{r}) = u_{\boldsymbol{q}}\cdot\exp\left[i(\boldsymbol{q}\cdot\boldsymbol{r}-\omega t)\right] + v_{-\boldsymbol{q}}\cdot\exp\left[-i(\boldsymbol{q}\cdot\boldsymbol{r}-\omega t)\right]$.

Insert this ansatz into the the chemical potential and retaining only first order terms[220] yields[221]

$$\delta\mu \equiv \delta\mu_{\boldsymbol{q}}(\boldsymbol{r}) = \delta V_{\mathrm{qp}}(\boldsymbol{r}) + \delta\Phi^{(N)}_{\mathrm{contact}}(\boldsymbol{r}) + \delta\Phi^{(N)}_{\mathrm{dip}}(\boldsymbol{r}) \tag{A.34a}$$

$$\delta V_{\mathrm{qp}}(\boldsymbol{r}) = +\frac{(\hbar\, q)^2}{4\,m\,n_{\mathrm{eq}}}\delta n_{\boldsymbol{q}}(\boldsymbol{r}) \tag{A.34b}$$

$$\delta\Phi^{(N)}_{\mathrm{contact}}(\boldsymbol{r}) = g\,\delta n_{\boldsymbol{q}}(\boldsymbol{r}) \tag{A.34c}$$

$$\delta\Phi^{(N)}_{\mathrm{dip}}(\boldsymbol{r}) = \tilde{V}_{\mathrm{dd}}(\boldsymbol{q})\,\delta n_{\boldsymbol{q}}(\boldsymbol{r}) \tag{A.34d}$$

where $\tilde{V}_{\mathrm{dd}}(\boldsymbol{q})$ is the Fourier transform of the DDI (A.20). Since $\delta\mu_{\boldsymbol{q}}(\boldsymbol{r})$ is linear in $\delta n_{\boldsymbol{q}}(\boldsymbol{r})$ with a pre-factor, which is independent of the position $\boldsymbol{r}$, inserting eq. (A.34a) into eq. (A.33) is straight forward[222], resulting in eq. (A.30).

Method 2: Using quantum field theory

Deriving the Bogoliubov spectrum using the quantum field theoretical description emphasises the single particle character of the excitation. The collective excitation is described by a single quasi-particle, the phonon. This is a mean-field description in the sense that there is no interaction between two phonons and therefore there are no phonon-phonon

[217] $\delta\mu$ indicates the (linear) perturbation of the chemical potential.

[218] It is crucial to understand that this ansatz limits the obtainable solutions. One can only find what one is looking for.

[219] Since an infinite, homogeneous BEC is translation invariant, one expects the eigenstates of the system to be eigenstates of the momentum operator (plane waves). If inhomogeneous systems are considered, the coefficients $\{u_{\boldsymbol{q}}, v_{-\boldsymbol{q}}\}$ become position dependent $\{u_{\boldsymbol{q}}(\boldsymbol{r}), v_{-\boldsymbol{q}}(\boldsymbol{r})\}$, whereas if the particle number is not conserved, they become complex (recall, $\boldsymbol{v} \propto \Psi\boldsymbol{\nabla}\Psi^\star - h.c.$). Note that in our ansatz both plane waves travel in the same direction.

[220] The zero order terms fulfills the hydrodynamic equation of motion (A.33). Therefore, they cancel each other.

[221] Taylor expand the square root for the quantum pressure term, $\frac{1}{\sqrt{n}}\boldsymbol{\nabla}^2\sqrt{n} \approx \frac{1}{2\,n_{\mathrm{eq}}}\boldsymbol{\nabla}^2\delta n_{\boldsymbol{q}}$, and use that the Fourier transform of the dipole-dipole potential does only depend on the angle between the magnetic moments $\boldsymbol{\mu}_{\mathrm{m}}$ and the wavevector $\boldsymbol{q}$ of the excitation, but neither on the magnitude nor the sign of $\boldsymbol{q}$.

[222] Use $m\frac{\partial^2}{\partial t^2}\big(\delta n_{\boldsymbol{q}}\big) = -m\omega^2\delta n_{\boldsymbol{q}}$ and $\boldsymbol{\nabla}^2\big(\delta n_{\boldsymbol{q}}\big) = -\boldsymbol{q}^2\delta n_{\boldsymbol{q}}$.

correlations. The calculation for a purely contact interacting condensate is given in [63, 119]. The dipolar case is done in [303] using the Green's function method.

Starting point is the field theoretical Hamilton operator [134]

$$\hat{\mathrm{H}} = \int d^3r \, \Big[-\frac{\hbar^2}{2m} \left|\boldsymbol{\nabla}\hat{\Psi}(\boldsymbol{r})\right|^2 - \mu\hat{\Psi}^\dagger(\boldsymbol{r})\hat{\Psi}(\boldsymbol{r}) + \frac{1}{2}\int d^3r' \; \hat{\Psi}^\dagger(\boldsymbol{r})\hat{\Psi}^\dagger(\boldsymbol{r}')V_{\mathrm{int}}^{(2)}(\boldsymbol{r}-\boldsymbol{r}')\hat{\Psi}(\boldsymbol{r}')\hat{\Psi}(\boldsymbol{r})\Big] \tag{A.35}$$

with the 2-body interaction potential $V_{\mathrm{int}}^{(2)}(\boldsymbol{r}) \stackrel{\mathrm{def}}{=} g\delta(\boldsymbol{r}) + V_{\mathrm{dd}}(\boldsymbol{r})$ and the field operator in Fourier representation[223] $\hat{\Psi}(\boldsymbol{r}) \stackrel{\mathrm{def}}{=} \frac{1}{\sqrt{V}}\sum_{\boldsymbol{k}} \hat{\mathrm{a}}_{\boldsymbol{k}}\, \mathrm{e}^{i\boldsymbol{k}\cdot\boldsymbol{r}}$, where V is the volume of the system. The annihilation (creation) operator $\hat{\mathrm{a}}_{\boldsymbol{k}}$ ($\hat{\mathrm{a}}_{\boldsymbol{k}}^\dagger$) destroys (creates) one quantum[224] in the state $|\boldsymbol{k}\rangle$, which is a plane wave with momentum $\hbar\boldsymbol{k}$ in the position representation, $\langle\boldsymbol{r}|\boldsymbol{k}\rangle = \mathrm{e}^{i\boldsymbol{k}\cdot\boldsymbol{r}}$. They satisfy the bosonic algebra

$$\begin{aligned} [\hat{\mathrm{a}}_{\boldsymbol{k}}, \hat{\mathrm{a}}_{\boldsymbol{k}'}^\dagger] &= \delta_{\boldsymbol{k},\boldsymbol{k}'} \\ [\hat{\mathrm{a}}_{\boldsymbol{k}}, \hat{\mathrm{a}}_{\boldsymbol{k}'}] &= 0 = [\hat{\mathrm{a}}_{\boldsymbol{k}}^\dagger, \hat{\mathrm{a}}_{\boldsymbol{k}'}^\dagger] \end{aligned} \tag{A.36}$$

Defining the number state of the $\boldsymbol{k}$-th mode by $|N_{\boldsymbol{k}}\rangle \stackrel{\mathrm{def}}{=} (\hat{\mathrm{a}}_{\boldsymbol{k}}^\dagger)^{N_{\boldsymbol{k}}}|0\rangle/\sqrt{N_{\boldsymbol{k}}!}$, where $|0\rangle$ is the vacuum state, and expressing the Hamilton operator in this basis, $\hat{\mathrm{H}} = \sum_{\boldsymbol{k},\boldsymbol{k}'} |\boldsymbol{k}\rangle\langle\boldsymbol{k}|\hat{\mathrm{H}}|\boldsymbol{k}'\rangle\langle\boldsymbol{k}'|$, eq. (A.35) becomes [155]

$$\hat{\mathrm{H}} = \sum_{\boldsymbol{k}} \Big(E_{\mathrm{free}}(\boldsymbol{k}) - \mu\Big)\, \hat{\mathrm{a}}_{\boldsymbol{k}}^\dagger\hat{\mathrm{a}}_{\boldsymbol{k}} + \frac{1}{2V}\sum_{\boldsymbol{k},\boldsymbol{k}',\boldsymbol{q}} \tilde{V}_{\mathrm{int}}^{(2)}(\boldsymbol{q})\, \hat{\mathrm{a}}_{\boldsymbol{k}+\boldsymbol{q}}^\dagger\hat{\mathrm{a}}_{\boldsymbol{k}'-\boldsymbol{q}}^\dagger\hat{\mathrm{a}}_{\boldsymbol{k}'}\hat{\mathrm{a}}_{\boldsymbol{k}} \tag{A.37}$$

where $E_{\mathrm{free}}(\boldsymbol{k}) \stackrel{\mathrm{def}}{=} (\hbar\boldsymbol{k})^2/(2m)$ is the free particle dispersion relation and $\tilde{V}_{\mathrm{int}}^{(2)}(\boldsymbol{q})$ is the Fourier transform of the 2-body interaction potential. Note that the creation and annihilation operators occur in such a way that they maintain the total momentum.

Now we use the *Bogoliubov approximation*, which assumes that

1. almost all particles are in the ground-state[225], $N_{\mathrm{tot}} \approx N_0 \stackrel{\mathrm{def}}{=} N_{\boldsymbol{k}=0} \gg 1$, so that $\langle N_0+1|\hat{\mathrm{a}}_0^\dagger|N_0\rangle = \sqrt{N_0+1} \approx \sqrt{N_0}$. Therefore, we replace the operators[226] $\hat{\mathrm{a}}_0$ and $\hat{\mathrm{a}}_0^\dagger$ by the number $\sqrt{N_0}$. This is equivalent to the statement that the ground-state operators commute, $[\hat{\mathrm{a}}_0, \hat{\mathrm{a}}_0^\dagger] = 0$, while the creation and annihilation operators for modes with $\boldsymbol{k} \neq 0$ still obey the standard bosonic commutation relation (A.36).

[223] Each Fourier mode $\boldsymbol{k}$ of the field is treated as an independent oscillator with its own creation and annihilation operator.

[224] Since they create/destroy one discrete entity the excitation is often called a "particle". These particles are not localised in position space: $\hat{\mathrm{a}}_{\boldsymbol{k}}^\dagger$ creates a particle in the momentum eigenstate $|\boldsymbol{k}\rangle$.

[225] This implies a low temperature.

[226] *Only* the creation and annihilation operators for the ground-state are replaced. Those for excited-states ($\boldsymbol{k} \neq 0$) remain operators.

2. the interaction between two excitations is negligible, because the gas is very dilute and the number of excitations is small compared to total atom number.

Using these two assumptions and separating the "ground-state" ($\boldsymbol{k} = 0$) from the "excitations" ($\boldsymbol{k} \neq 0$), we find[227]

$$\begin{aligned}\hat{\mathrm{H}} =& -N_0\mu + \frac{N_0^2\tilde{V}_{\mathrm{int}}(0)}{2V} \\ &+ \sum_{\boldsymbol{q}\neq 0}\left[\left(E_{\mathrm{free}}(\boldsymbol{q}) + n_0[\tilde{V}_{\mathrm{int}}(0) + \tilde{V}_{\mathrm{int}}(\boldsymbol{q})] - \mu\right)\hat{\mathrm{a}}_{\boldsymbol{q}}^\dagger\hat{\mathrm{a}}_{\boldsymbol{q}} + \frac{n_0\tilde{V}_{\mathrm{int}}(\boldsymbol{q})}{2}\left(\hat{\mathrm{a}}_{\boldsymbol{q}}^\dagger\hat{\mathrm{a}}_{-\boldsymbol{q}}^\dagger + \hat{\mathrm{a}}_{\boldsymbol{q}}\hat{\mathrm{a}}_{-\boldsymbol{q}}\right)\right]\end{aligned} \tag{A.38}$$

with the ground-state density n_0. Finally, we use that for a homogeneous condensate the chemical potential is given by $\mu = n_0\,\tilde{V}_{\mathrm{int}}(0)$ and that the Fourier transform of the interaction potential does neither depend on the magnitude nor sign of $\boldsymbol{q}$ so that we symmetrise $\hat{\mathrm{a}}_{\boldsymbol{q}}^\dagger\hat{\mathrm{a}}_{\boldsymbol{q}} \to (\hat{\mathrm{a}}_{\boldsymbol{q}}^\dagger\hat{\mathrm{a}}_{\boldsymbol{q}} + \hat{\mathrm{a}}_{-\boldsymbol{q}}^\dagger\hat{\mathrm{a}}_{-\boldsymbol{q}})/2$ to write the Hamiltonian in the bilinear form

$$\hat{\mathrm{H}} = -\mu N_0 + \frac{N_0^2}{2V} + \frac{1}{2}\sum_{\boldsymbol{q}\neq 0}\begin{pmatrix}\hat{\mathrm{a}}_{\boldsymbol{q}}^\dagger & \hat{\mathrm{a}}_{-\boldsymbol{q}}\end{pmatrix}\begin{pmatrix}\epsilon_1 & \epsilon_2\\ \epsilon_2 & \epsilon_1\end{pmatrix}\begin{pmatrix}\hat{\mathrm{a}}_{\boldsymbol{q}}^\dagger\\ \hat{\mathrm{a}}_{-\boldsymbol{q}}\end{pmatrix} \tag{A.39}$$

with $\epsilon_1 \overset{\mathrm{def}}{=} E_{\mathrm{free}}(\boldsymbol{q}) + n_0\tilde{V}_{\mathrm{int}}(\boldsymbol{q})$ and $\epsilon_2 \overset{\mathrm{def}}{=} n_0\tilde{V}_{\mathrm{int}}(\boldsymbol{q})$. The rest, although tedious, is the standard Bogoliubov transformation and can be found e.g. in [119, ch. 8]:

1. Define new creation/annihilation operators

$$\begin{pmatrix}\hat{\mathrm{b}}_{\boldsymbol{q}}\\ \hat{\mathrm{b}}_{-\boldsymbol{q}}^\dagger\end{pmatrix} \overset{\mathrm{def}}{=} \begin{pmatrix}u_{\boldsymbol{q}} & v_{\boldsymbol{q}}\\ v_{\boldsymbol{q}} & u_{\boldsymbol{q}}\end{pmatrix}\begin{pmatrix}\hat{\mathrm{a}}_{\boldsymbol{q}}\\ \hat{\mathrm{a}}_{-\boldsymbol{q}}^\dagger\end{pmatrix} \tag{A.40}$$

2. Demand that the new operators fulfill the standard bosonic algebra[228], analog to eq. (A.36)

3. Choose $\{u_{\boldsymbol{q}}, v_{\boldsymbol{q}}\}$ such that the Hamilton operator becomes diagonal[229]

$$\hat{\mathrm{H}} = (\text{some terms})\hat{\mathbb{1}} + \sum_{q\neq 0} E(\boldsymbol{q})\hat{\mathrm{b}}_{\boldsymbol{q}}^\dagger\hat{\mathrm{b}}_{\boldsymbol{q}} \tag{A.41}$$

where $E(\boldsymbol{q})$ is given by eq. (A.30).

[227] The Fourier transform of the DDI is evaluated at the origin, where it is ill defined. Therefore, we average over the directions of the wavevector $\boldsymbol{q}$, which yields $\tilde{V}_{\mathrm{int}}(0) = g\,n$.

[228] This leads to the condition $u_{\boldsymbol{q}}^2 - v_{\boldsymbol{q}}^2 = 1$, if $u_{\boldsymbol{q}}, v_{\boldsymbol{q}} \in \mathbb{R}$. Therefore, the transformation is a hyperbolic rotation and by choosing the convention $u_{\boldsymbol{q}} \geq 0$, we define the angle $\theta_{\boldsymbol{q}}$ by $\{u_{\boldsymbol{q}}, v_{\boldsymbol{q}}\} \overset{\mathrm{def}}{=} \{\sinh\theta_{\boldsymbol{q}}, \cosh\theta_{\boldsymbol{q}}\}$.

A.5.9 Corrected dipolar expansion formulae

To calibration the scattering length we used the hydrodynamic equations in the Thomas-Fermi limit. Unfortunately, the in-trap formulae [161, eq. (20) – (22)] are wrong. They should read

$$\begin{aligned}
\omega_x^2 &= \bar{\omega}_x^2 \left[1 - \epsilon_{\mathrm{dd}} \left(f_{\mathrm{dip}} + \kappa_{xy} \frac{\partial f_{\mathrm{dip}}}{\partial \kappa_{xy}} + \kappa_{xz} \frac{\partial f_{\mathrm{dip}}}{\partial \kappa_{xz}} \right)\right] \\
\omega_y^2 &= \bar{\omega}_y^2 \left[1 - \epsilon_{\mathrm{dd}} \left(f_{\mathrm{dip}} - \kappa_{xy} \frac{\partial f_{\mathrm{dip}}}{\partial \kappa_{xy}} \right)\right] \\
\omega_z^2 &= \bar{\omega}_z^2 \left[1 - \epsilon_{\mathrm{dd}} \left(f_{\mathrm{dip}} - \kappa_{xz} \frac{\partial f_{\mathrm{dip}}}{\partial \kappa_{xz}} \right)\right]
\end{aligned}$$

where $f_{\mathrm{dip}} \stackrel{\mathrm{def}}{=} f_{\mathrm{dip}}(\kappa_{xy}, \kappa_{xz})$, $n_0 \stackrel{\mathrm{def}}{=} 15N/(8\pi\, R_x R_y R_z)$, and $\bar{\omega}_j^2 \stackrel{\mathrm{def}}{=} 2\, g\, n_0/(m\, R_j^2)$ with $j = x, y, z$. Note that in these formulae the polarisation axis is chosen to be the x-direction. The sign problem is present throughout the publication and results in wrong expansion equations [161, eq. (31)]. The set of differential equations should read[230]

$$\frac{\partial^2 b_x}{\partial t^2} = \frac{\bar{\omega}_x^2}{b_x^2\, b_y\, b_z} \left[1 - \epsilon_{\mathrm{dd}}\, f(\frac{b_y}{b_x}\kappa_y^0, \frac{b_z}{b_x}\kappa_z^0) + \epsilon_{\mathrm{dd}}\, b_x \frac{\partial\, f(\frac{b_y}{b_x}\kappa_y^0, \frac{b_z}{b_x}\kappa_z^0)}{\partial b_x}\right] \tag{A.42a}$$

$$\frac{\partial^2 b_y}{\partial t^2} = \frac{\bar{\omega}_y^2}{b_x\, b_y^2\, b_z} \left[1 - \epsilon_{\mathrm{dd}}\, f(\frac{b_y}{b_x}\kappa_y^0, \frac{b_z}{b_x}\kappa_z^0) + \epsilon_{\mathrm{dd}}\, b_y \frac{\partial\, f(\frac{b_y}{b_x}\kappa_y^0, \frac{b_z}{b_x}\kappa_z^0)}{\partial b_y}\right] \tag{A.42b}$$

$$\frac{\partial^2 b_z}{\partial t^2} = \frac{\bar{\omega}_z^2}{b_x\, b_y\, b_z^2} \left[1 - \epsilon_{\mathrm{dd}}\, f(\frac{b_y}{b_x}\kappa_y^0, \frac{b_z}{b_x}\kappa_z^0) + \epsilon_{\mathrm{dd}}\, b_z \frac{\partial\, f(\frac{b_y}{b_x}\kappa_y^0, \frac{b_z}{b_x}\kappa_z^0)}{\partial b_z}\right] \tag{A.42c}$$

[229] Expressing the "old" operators in the "new" basis,

$$\begin{aligned}
\hat{\mathrm{a}}_{\boldsymbol{q}}^\dagger \hat{\mathrm{a}}_{\boldsymbol{q}} &= u_{\boldsymbol{q}}^2 \hat{\mathrm{b}}_{\boldsymbol{q}}^\dagger \hat{\mathrm{b}}_{\boldsymbol{q}} + v_{\boldsymbol{q}}^2 \hat{\mathrm{b}}_{-\boldsymbol{q}} \hat{\mathrm{b}}_{-\boldsymbol{q}}^\dagger - u_{\boldsymbol{q}} v_{\boldsymbol{q}} (\hat{\mathrm{b}}_{\boldsymbol{q}} \hat{\mathrm{b}}_{-\boldsymbol{q}} + \hat{\mathrm{b}}_{\boldsymbol{q}}^\dagger \hat{\mathrm{b}}_{-\boldsymbol{q}}^\dagger) \\
\hat{\mathrm{a}}_{-\boldsymbol{q}}^\dagger \hat{\mathrm{a}}_{-\boldsymbol{q}} &= u_{\boldsymbol{q}}^2 \hat{\mathrm{b}}_{-\boldsymbol{q}}^\dagger \hat{\mathrm{b}}_{-\boldsymbol{q}} + v_{\boldsymbol{q}}^2 \hat{\mathrm{b}}_{\boldsymbol{q}} \hat{\mathrm{b}}_{\boldsymbol{q}}^\dagger - u_{\boldsymbol{q}} v_{\boldsymbol{q}} (\hat{\mathrm{b}}_{\boldsymbol{q}} \hat{\mathrm{b}}_{-\boldsymbol{q}} + \hat{\mathrm{b}}_{\boldsymbol{q}}^\dagger \hat{\mathrm{b}}_{-\boldsymbol{q}}^\dagger) \\
\hat{\mathrm{a}}_{\boldsymbol{q}} \hat{\mathrm{a}}_{-\boldsymbol{q}} &= u_{\boldsymbol{q}}^2 \hat{\mathrm{b}}_{\boldsymbol{q}} \hat{\mathrm{b}}_{-\boldsymbol{q}} + v_{\boldsymbol{q}}^2 \hat{\mathrm{b}}_{\boldsymbol{q}}^\dagger \hat{\mathrm{b}}_{-\boldsymbol{q}}^\dagger - u_{\boldsymbol{q}} v_{\boldsymbol{q}} (\hat{\mathrm{b}}_{\boldsymbol{q}} \hat{\mathrm{b}}_{\boldsymbol{q}}^\dagger + \hat{\mathrm{b}}_{-\boldsymbol{q}}^\dagger \hat{\mathrm{b}}_{-\boldsymbol{q}}) \\
\hat{\mathrm{a}}_{\boldsymbol{q}}^\dagger \hat{\mathrm{a}}_{-\boldsymbol{q}}^\dagger &= v_{\boldsymbol{q}}^2 \hat{\mathrm{b}}_{\boldsymbol{q}} \hat{\mathrm{b}}_{-\boldsymbol{q}} + u_{\boldsymbol{q}}^2 \hat{\mathrm{b}}_{\boldsymbol{q}}^\dagger \hat{\mathrm{b}}_{-\boldsymbol{q}}^\dagger - u_{\boldsymbol{q}} v_{\boldsymbol{q}} (\hat{\mathrm{b}}_{\boldsymbol{q}} \hat{\mathrm{b}}_{\boldsymbol{q}}^\dagger + \hat{\mathrm{b}}_{-\boldsymbol{q}}^\dagger \hat{\mathrm{b}}_{-\boldsymbol{q}})
\end{aligned}$$

one finds

$$\begin{aligned}
\tanh(2\theta_{\boldsymbol{q}}) &= \frac{2\tanh\theta_{\boldsymbol{q}}}{1+\tanh^2\theta_{\boldsymbol{q}}} = \frac{\epsilon_2}{\epsilon_1} \\
v_{\boldsymbol{q}} &= \sinh\theta_{\boldsymbol{q}} = \sqrt{\frac{1}{2}\left(\frac{\epsilon_1}{E(\boldsymbol{q})} - 1\right)} \\
u_{\boldsymbol{q}} &= \cosh\theta_{\boldsymbol{q}} = \sqrt{\frac{1}{2}\left(\frac{\epsilon_1}{E(\boldsymbol{q})} + 1\right)}
\end{aligned}$$

with $E(\boldsymbol{q}) \stackrel{\mathrm{def}}{=} +\sqrt{\epsilon_1^2 - \epsilon_2^2}$. This $E(\boldsymbol{q})$ becomes the excitation energy of the Bogoliubov spectrum (A.30).

[230] Internal link to the program 'TOF-DipolarExpansion02.nb'.

where the trap is assumed to be switched off completely, $\boldsymbol{\omega}(t) = 0$ for $t \geq 0\,\mathrm{s}$.

A.6 Inter-site dipolar interactions in an optical lattice

So far we were concerned about the description of a single condensate confined in a cylindrical symmetric trap. Now we extend this description by considering stacks of pancake-shape dipolar condensates, which are coupled by the long-range part of the dipolar interactions, see fig. A.5(a). First, we calculate the inter-site dipolar mean-field potential $\Phi'_{\mathrm{dip}}(\boldsymbol{r})$ for a pair of two-dimensional discs, see fig. A.5(b). The dipoles are assumed to be polarised either parallel or perpendicular to the symmetry axis of the confinement. In the second part of this section we derive the Gross-Pitaevskii energy functional E'_{dip} for a stack of three-dimensional Gaussian wavefunctions.

A.6.1 Inter-site dipolar mean-field potential

Consider a stack of dipolar condensates, which are confined on adjacent sites of a one-dimensional optical lattice. Due to the dipolar coupling between the sites the properties of each condensate depend on the overall geometry of the stack. This can be seen as follows: Whereas each condensate has a pancake-shape aspect ratio $\kappa > 1$, the stacking leads to a cigar-shape overall geometry. Hence, in the limit of infinitesimal lattice spacing, $d_{\mathrm{lat}} \to 0$, the stack becomes a single cigar-shape condensate. Thus, the dipolar mean-field energy changes from being "repulsive" to "attractive" and the condensate becomes less stable, see section 5. In the following we calculate the inter-site dipolar mean-field potential $\Phi'_{\mathrm{dip}}(\boldsymbol{r})$, eq. (A.25b), for a pair of condensates.

In order to understand the inter-site interactions it is useful to start with a simple model and to increase the complexity gradually. Therefore, consider the interactions between two discs of radius R and vanishing axial extension, see fig. A.5(b). Their spatial density distribution (uniform in two-dimensions) is given by

$$n_{3\mathrm{d}}(\boldsymbol{r}) = \sum_{j=1,2} n_{2\mathrm{d}}\,\Theta(\rho - R)\,\delta(z - j \cdot d_{\mathrm{lat}}) \tag{A.43}$$

where $\Theta(\rho)$ is the Heaviside function and the dipoles are assumed to be fully polarised in the z-direction.

Figure A.5(c) presents the inter-site dipolar mean-field potential (A.25b) produced by a uniform area-density, $n_{2\mathrm{d}} = N_{\mathrm{atoms}}/(\pi R^2)$. In the trap center[231] the potential is *negative* ("attractive") and almost constant. The reason for this behaviour is the interplay between the anisotropy of the dipolar interactions and its $1/r^3$-dependence: Only the part of the

[231] The inter-site potential at the trap center given by $\Phi'_{\mathrm{dip}}(\rho = 0) = -\frac{\mu_0\,\mu_{\mathrm{m}}^2\,n_{2\mathrm{d}}\,R^2}{2\,(R^2+d_{\mathrm{lat}}^2)^{3/2}}$ and therefore $\Phi'_{\mathrm{dip}}(0) \approx -\frac{3}{2}\,g_{\mathrm{dd}}\,\frac{n_{2d}}{R}$ for $R \gg d_{\mathrm{lat}}$.

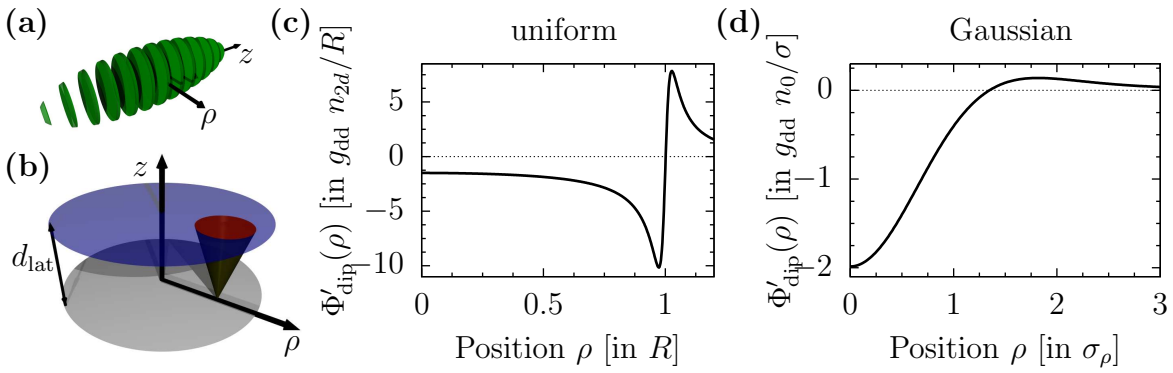

Fig. A.5, Inter-site potential for dipoles polarised in z-direction: If a cigar-shape condensate is sliced into a stack of pancake-shape BECs, as shown in (a), the inter-site dipolar potential is not negligible. Calculating the dipolar interaction potential (A.25b) between two in z-direction polarised dipolar BECs at a point ρ, only the red area sketched in (b) provides a negative contribution. In (c) the inter-site potential is calculated[233] for a pair of two-dimensional discs of radius R with uniform spatial density, eq. (A.43), whereas in (d) a two-dimensional Gaussian density, eq. (A.44), is considered.

upper disc which lies within the magic angle $0 \leq \vartheta \leq \vartheta_{\text{magic}}$ (indicated in fig. A.5(b) by the red area) gives an "attractive" contribution to the inter-site potential at a point ρ of the lower disc. Therefore, most dipoles interact "repulsively". However, the points within the magic angle are closer to the "receiving point" ρ, their contributions are weighted stronger. Thus, the mean-field potential is still negative, the inter-site interaction *destabilises* the condensates. That the potential is not constant, but decreases with increasing ρ, is a finite size effect[232].

Next, let us redefining the model to assimilate with the experiment. Therefore, we assume a spatial density distribution

$$n(\boldsymbol{r}) = \sum_{j=1,2} g_{2d}^{(\sigma_\rho)}(\rho)\, \delta(z - j \cdot d_{\text{lat}}) \tag{A.44}$$

where $g_{2d}^{(\sigma_\rho)}(\rho) = n_0 \exp\left(-\rho^2/\sigma_\rho^2\right)$ is a two-dimensional Gaussian, with peak density $n_0 = N_{\text{atoms}}/(\pi\sigma_\rho^2)$. Fig. A.5(d) presents the dipolar mean-field potential produced by the site $j = 2$ at the position of the neighbouring site $j = 1$. As expected, the inter-

[232] Moving the "receiving point" $\rho = \rho_{disc1}$ towards the edge of the disc, maintains the "attractive" contribution as long as the area covered by the magic angle lies within the upper disc. However, it decreases the "repulsive" contribution, because it increases the distance to the dipoles sitting at the opposite edge. The potential reaches its minimum at a distance $\rho_{\text{disc1}} = R - \rho_{\text{ext}}$ from the center, where $\rho_{\text{ext}}/d_{\text{lat}} = \tan\vartheta_{\text{magic}} \approx 0.82$. Moving further outwards, decreases the "attractive" contributions as well. Thus, the inter-site potential has a maximum at $\rho = R + \rho_{\text{ext}}$, which lies outside of the disc. The same reasoning explains, why the modulus of the minimum value and the maximum are unequal.

[233] These calculations are made for a lattice spacing of $d_{\text{lat}} = (532/2)$ nm, a disc radius $R = 10\,\mu$m , and a Gaussian width $\sigma_\rho = 2\,\mu$m, but the scaling of the potential make it quite robust.

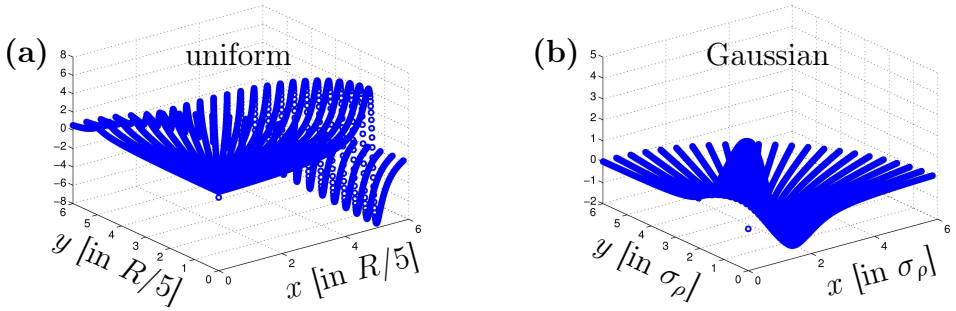

Fig. A.6, Inter-site potential with dipoles polarised in x-direction: (a, b) The inter-site dipolar mean-field potential (A.25b) between a pair of condensates (in units of $g_{\rm dd}\, n_{2d}/R$ and $g_{\rm dd}\, n_0/R$, respectively). The spatial density is given by (A.43) and eq. (A.44), respectively. The parameters for the calculations are: $d_{\rm lat} = 532/2\,\text{nm}$, $\sigma_\rho = 2\,\mu$m, and $R = 10\,\mu$m.

site potential has a minimum at the center[234]. Furthermore, as the spatial density decreases with increasing radial coordinate, the finite size effect is strongly suppressed. The potential vanishes at[235] $\rho_0 \approx 1.35\,\sigma_\rho$ and becomes only "slightly" positive for $\rho > \rho_0$. The central region of the inter-site potential is well described by a Gaussian with a width $\sigma_{\rm dd}/\sigma_\rho = 0.82 < 1$. Hence, despite its simplicity the model incorporates the elongation of a three-dimensional dipolar condensate along the polarisation direction.

Figure A.6 presents the inter-site dipolar mean-field potential for the case, where the dipoles are polarised perpendicular to the normal axis of the optical lattice. The arguments which explain the shape of the potentials are similar to those above.

A.6.2 Instability for a stack of dipolar condensates

In this section we derive the inter-site mean-field interaction energy $E'_{\rm dip}$, eq. (A.25a), for a stack of dipolar condensates. A possible experimental set-up is sketched in fig. A.7. This work is closely related to [237], only the mean-field dipolar *inter-site* interaction is added. Because the zero-point energy, the potential trapping energy, and the energy arising from the contact interaction are straight forward to calculate[236], solely the long-range part of the dipolar interactions is treated in the following section.

[234] $\Phi'_{\rm dip}(\rho = 0) = -\frac{\mu_0 \mu_{\rm m}^2\, n_0}{2\sigma}\left[-2\frac{d_{\rm lat}}{\sigma} + \sqrt{\pi}\left(1 + 2\frac{d_{\rm lat}^2}{\sigma^2}\right)\exp\left(d_{\rm lat}^2/\sigma^2\right)\Gamma\left(\frac{d_{\rm lat}}{\sigma}\right)\right]$.

[235] The zero crossing of the inter-site potential is larger than $\rho = \sigma_\rho + d_{\rm lat}\,\tan\vartheta_{\rm magic}$, because the spatial density decreases continuously, rather than abruptly as in the disc case.

[236] As these energies do not depend on the inter-site interactions, they are given in [237].

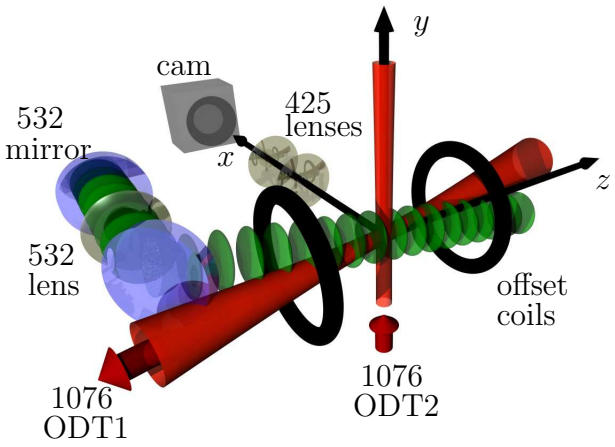

Fig. A.7, Sketch of the experimental setup: The coordinate system is defined by the offset coils (z-direction), the imaging axis (x-direction) and the propagation direction of ODT2 (y-direction). ODT1 propagates in the (x, z)-plane, whereas the 532-OL forms in the (y, z)-plane. Both beams are tilted with respect to the polarisation axis of the atoms (z-direction). However, these tilts are neglected in the calculations, because they are expected to only perturb the results within the experimental uncertainties, while increasing the numerical effort tremendously.

The inter-site interaction energy

$$E'^{(\ell,j)}_{\text{dip}} \overset{(A.25a)}{=} \int d^3\boldsymbol{r}\; n_\ell(\boldsymbol{r}) \times \int d^3r'\; V'_{\text{dd}}(\boldsymbol{r}-\boldsymbol{r}')n_j(\boldsymbol{r}') \tag{A.45a}$$

$$\overset{(A.26)}{=} \int d^3\tilde{k}\; \tilde{n}^\star_\ell(\tilde{\boldsymbol{k}}) \cdot \tilde{n}_j(\tilde{\boldsymbol{k}})\tilde{V}'_{\text{dd}}(\tilde{\boldsymbol{k}}) \tag{A.45b}$$

contains the Fourier transform of the atomic densities of the two interacting sites j and ℓ. We start simplifying the integral by making the following assumptions:

1. The wavefunction of the condensate on the ℓ^{th} lattice site is given by[237]

$$\psi^{(\ell)}(\boldsymbol{r}) \overset{\text{def}}{=} \sqrt{N^{(\ell)}_{\text{atoms}}}\; g^{(\sigma_{x,\ell})}(x)\, g^{(\sigma_{y,\ell})}(y)\, g^{(\sigma_{z,\ell})}(z) \tag{A.46}$$

   where $g^{(\sigma)}(x) \overset{\text{def}}{=} \frac{1}{\pi^{1/4}\sigma^{1/2}} \exp\left(-\frac{x^2}{2\sigma^2}\right)$ is a Gaussian with width σ and normalised to one, $\int_{-\infty}^{\infty} dx\; |g^{(\sigma)}(x)|^2 = 1$.

2. The wavefunction is cylindrical symmetric: $\sigma_{\rho,\ell} \overset{\text{def}}{=} \sigma_{x,\ell} = \sigma_{y,\ell}$.

[237] The gravitational sag is neglected, because it is expected to not alter the results, if tight enough trapping potentials are used. A Gaussian distribution of the atom numbers over the different lattice sites is easily included at this point.

3. The lattice spacing in z-direction is d_{lat}, each lattice site is occupied by the same atom number, $N_{\mathrm{atoms}}^{(\ell)} \to N_{\mathrm{atoms}}$, and their widths are site-independent, $\sigma_{\rho,\ell} \to \sigma_\rho$ and $\sigma_{z,\ell} \to \sigma_z$.

4. The wavefunction of individual sites do not overlap[238].

Using these assumptions, the Fourier transformation of the density separates into three terms

$$\tilde{n}^{(\ell)}(\boldsymbol{\hbar}) = \tilde{n}_x(\hbar_x) \cdot \tilde{n}_y(\hbar_y) \cdot \tilde{n}_z^{(\ell)}(\hbar_z) \tag{A.47}$$

with

$$\begin{aligned} \tilde{n}_x(\hbar) = \tilde{n}_y(\hbar) &\stackrel{\mathrm{def}}{=} N_{\mathrm{atoms}}^{1/3}\, \mathrm{e}^{-(\pi\,\sigma_\rho\,\hbar)^2} \\ \tilde{n}_z^{(\ell)}(\hbar) &\stackrel{\mathrm{def}}{=} N_{\mathrm{atoms}}^{1/3}\, \mathrm{e}^{-(\pi\,\sigma_z\,\hbar)^2} \cdot \mathrm{e}^{i2\pi\hbar\ell d_{\mathrm{lat}}} \end{aligned}$$

Hence, the inter-site dipolar energy for the ℓ^{th} lattice site

$$\begin{aligned} E_{\mathrm{dip}}'^{(\ell)} &= \sum_{j\neq\ell} E_{\mathrm{dip}}'^{(\ell,j)} \\ &= \underbrace{\frac{1}{2}\int d^3\hbar\ \left|\tilde{n}(\boldsymbol{\hbar})\right|^2 \tilde{V}_{\mathrm{dd}}'(\boldsymbol{\hbar})}_{\text{standard on-site DDI}} \times 2 \sum_{j\neq\ell} \mathrm{e}^{i2\pi\hbar_z d_{\mathrm{lat}}(\ell-j)} \end{aligned} \tag{A.48}$$

consists of two factors: the standard on-site dipolar interactions and a "lattice factor". Knowing from the previous section that the inter-site dipolar energy lowers the total energy, we concentrate in the following on the central lattice site ($\ell = 0$), because here the instability occurs first. Using the geometric series $\sum_{n=0}^{j_{\mathrm{lat}}} q^n = (1 - q^{1+j_{\mathrm{lat}}})/(1-q)$ with $q = \mathrm{e}^{i2\alpha}$ the "lattice factor" simplifies to

$$\begin{aligned} -1 + \sum_{n=-j_{\mathrm{lat}}}^{j_{\mathrm{lat}}} q^n &= -2 + \sum_{n=0}^{j_{\mathrm{lat}}} q^n + \sum_{n=0}^{j_{\mathrm{lat}}} q^{-n} \\ &= \ldots = -1 + \frac{\sin\left(\alpha[2j_{\mathrm{lat}}+1]\right)}{\sin\left(\alpha\right)} = -1 + \frac{\sin\left(N_{\mathrm{lat}}\alpha\right)}{\sin\left(\alpha\right)} \end{aligned}$$

[238]The total density is given by

$$\begin{aligned} n_{\mathrm{tot}}(\boldsymbol{r}) &\stackrel{\mathrm{def}}{=} |\psi_{\mathrm{tot}}|^2 \approx \sum_{\ell=-j_{\mathrm{lat}}}^{j_{\mathrm{lat}}} |\psi^{(\ell)}(\boldsymbol{r})|^2 \\ &= N_{\mathrm{atoms}}\, |g^{(\sigma_x)}(x)|^2\, |g^{(\sigma_y)}(y)|^2 \sum_{\ell=-j_{\mathrm{lat}}}^{j_{\mathrm{lat}}} |g^{(\sigma_z)}(z+\ell d_{\mathrm{lat}})|^2 \end{aligned}$$

which, in the limit $j_{\mathrm{lat}} \to \infty$, is equivalent to a convolution of a Gaussian $g^{(\sigma_z)}(z)$ with an Dirac comb $d^{(d_{\mathrm{lat}})}(z) \stackrel{\mathrm{def}}{=} \sum_{\ell=-\infty}^{\infty} \delta(z - \ell d_{\mathrm{lat}})$.

The last term is well known from linear optics: Its the diffraction term of a plane wave from a grating, see e.g. [273, ch. 52.4.2]. In the limit $N_{\mathrm{lat}} \to \infty$ it simplifies further to a Dirac comb[239].

Cylindrical coordinates are especially suited to evaluate the resulting integral. The integrand does not depend on the azimuthal reciprocal angle $\bar{k}_\varphi$ and the $\bar{k}_\rho$-integration is the same standard integral[240] as in [237]. So we are left with the $\bar{k}_z$-integral, which after rescaling to a dimensionless form ($\xi \stackrel{\mathrm{def}}{=} \sqrt{2}\pi\sigma_z\bar{k}_z$) yields the total (on-site and inter-site) dipolar energy per atom in units of $\hbar\bar{\omega}$

$$\frac{E'^{(\ell=0)}_{\mathrm{dip}}}{N_{\mathrm{atoms}}\,\hbar\bar{\omega}} = \frac{N_{\mathrm{atoms}}}{\sqrt{2\pi}}\,\frac{a_{\mathrm{dd}}}{\sigma_z}\left(\frac{a_{\mathrm{ho}}}{\sigma_\rho}\right)^2 \int_{-\infty}^{\infty}\frac{d\xi}{\sqrt{\pi}}\,\mathrm{e}^{-\xi^2}\left\{-1+3\kappa^2\xi^2\,\mathrm{e}^{+\kappa^2\xi^2}\,\Gamma\left[0,\kappa^2\xi^2\right]\right\} \times\left(-1+2\,\frac{\sin\left[N_{\mathrm{lat}}\cdot\alpha(\xi)\right]}{\sin\left[\alpha(\xi)\right]}\right) \tag{A.49}$$

with $\alpha(\xi) \stackrel{\mathrm{def}}{=} \xi\, d_{\mathrm{lat}}/(\sqrt{2}\,\sigma_z)$, the harmonic oscillator length $a_{\mathrm{ho}} \stackrel{\mathrm{def}}{=} \sqrt{\hbar/(m\bar{\omega})}$, the upper incomplete Gamma function[241] $\Gamma\left[\alpha,x\right] \stackrel{\mathrm{def}}{=} \int_x^\infty dt\; t^{\alpha-1}\mathrm{e}^{-t}$ for $\alpha = 0$, the aspect ratio $\kappa \stackrel{\mathrm{def}}{=} \sigma_\rho/\sigma_z$, the dipolar length $a_{\mathrm{dd}} \stackrel{\mathrm{def}}{=} \mu_0\,\mu_{\mathrm{m}}^2\,m/(12\pi\hbar^2)$, and the mean trap energy $\hbar\bar{\omega} \stackrel{\mathrm{def}}{=} \hbar(\omega_z\omega_\rho^2)^{1/3}$. For $N_{\mathrm{lat}} \to 1$ the integral in eq. (A.49) reduces to $-f_{\mathrm{dip}}(\kappa)$ and the result of [237] is obtained. In the opposite limit, $N_{\mathrm{lat}} \to \infty$, the "lattice factor" becomes a Dirac comb, resulting in

$$\lim_{N_{\mathrm{lat}}\to\infty}\frac{E'^{(\ell=0)}_{\mathrm{dip}}}{N_{\mathrm{atoms}}\,\hbar\bar{\omega}} = \frac{N_{\mathrm{atoms}}}{\sqrt{2\pi}}\,\frac{a_{\mathrm{dd}}}{\sigma_z}\left(\frac{a_{\mathrm{ho}}}{\sigma_\rho}\right)^2\Bigg[+f_{\mathrm{dip}}(\kappa) + \frac{2}{\sqrt{\pi}}\,\phi\lim_{j_{\mathrm{lat}}\to\infty}\sum_{j=-j_{\mathrm{lat}}}^{j_{\mathrm{lat}}}\mathrm{e}^{-\phi_j^2}\left\{-1+3\kappa^2\phi_j^2\,\mathrm{e}^{+\kappa^2\phi_j^2}\,\Gamma\left[0,\kappa^2\phi_j^2\right]\right\}\Bigg] \tag{A.50}$$

with $\phi \stackrel{\mathrm{def}}{=} \sqrt{2}\pi\sigma_z/d_{\mathrm{lat}}$ and $\phi_j \stackrel{\mathrm{def}}{=} \phi\cdot j$. As expected, the dipolar energy does depend on the aspect ration κ and on the ratio $\phi \propto \sigma_z/d_{\mathrm{lat}}$. The other energy functionals are as in [237][242]

[239] As stated above, in this limit the total density is given by a convolution of a Gaussian and a Dirac comb. The Fourier transform of a Dirac comb is a Dirac comb: $\lim_{N_{\mathrm{lat}}\to\infty}\frac{\sin\left(N_{\mathrm{lat}}\alpha\right)}{\sin\left(\alpha\right)} = d^{(2\pi/d_{\mathrm{lat}})}(\bar{k}_z)$. Simpler, $\mathcal{F}\left\{\sum_{n=-\infty}^{\infty}c_n\mathrm{e}^{i2\pi z/\ell}\right\}(\bar{k}) = \sum_{n=-\infty}^{\infty}c_n\delta(\bar{k}-n/\ell)$, see e.g. [296, ch. 5.1].

[240] Here we use the substitution $\chi^2 \stackrel{\mathrm{def}}{=} \bar{k}_\rho^2 + \bar{k}_z^2$ for the $\bar{k}_\rho$-integration. This shifts the coupling of $\bar{k}_\rho$ and $\bar{k}_z$ from the denominator into the lower boundary of the χ-integral and provides the incomplete Gamma function.

[241] In order to simplify the numerical calculation the asymptotic expansion [304] $\Gamma[0,x] \sim x^{-1}\,\mathrm{e}^{-x}\big(1 - 1/x + 2/x^2 + \ldots\big)$ is used for "large" values of $\kappa\,\xi$, and the Taylor series $x\,\mathrm{e}^x\Gamma[0,x] \sim -[\gamma+\ln(x)]\,x + [1-\gamma-\ln(x)]\,x^2 + \frac{1}{4}[3-2\gamma-2\ln(x)]x^3 + \mathcal{O}(x^4)$, where $\gamma \approx 0.577$ is the Euler-Mascheroni constant, for "small" values, respectively.

[242] Recall: The atom number per lattice site is N_{atoms}, while the total atom number is N_{tot}.

- zero-point energy

$$\frac{E_{\text{zero}}}{N_{\text{tot}}\hbar\bar{\omega}} = \frac{1}{N_{\text{atoms}}\hbar\bar{\omega}}\,\frac{\hbar^2}{2m}\int d^3r\;|\boldsymbol{\nabla}\psi_\ell|^2 = \frac{a_{\text{ho}}^2}{4}\left(\frac{1}{\sigma_z^2}+\frac{2}{\sigma_\rho^2}\right) \tag{A.51}$$

- trapping potential[243]

$$\frac{E_{\text{trap}}}{N_{\text{tot}}\hbar\bar{\omega}} = \frac{1}{N_{\text{atoms}}\hbar\bar{\omega}}\;\int d^3r\;V_{\text{trap}}\,n_\ell(\boldsymbol{r}) = \frac{2\sigma_\rho^2+\lambda^2\sigma_z^2}{4\;a_{\text{ho}}^2\;\lambda^{2/3}} \tag{A.52}$$

- contact interaction energy

$$\frac{E_{\text{contact}}}{N_{\text{tot}}\hbar\bar{\omega}} = \frac{1}{N_{\text{atoms}}\hbar\bar{\omega}}\;\frac{1}{2}\int d^3r\;g\,n_\ell^2(\boldsymbol{r}) = N_{\text{atoms}}\,\frac{a}{\sqrt{2\pi}\,\sigma_z}\left(\frac{a_{\text{ho}}}{\sigma_\rho}\right)^2 \tag{A.53}$$

  which is the pre-factor of eq. (A.49) if the scattering length a is replaced by the dipolar length a_{dd}.

[243] Ratio of the trapping frequencies $\lambda \stackrel{\text{def}}{=} \omega_z/\omega_r$.

References*

[1] A. J. Leggett: "*Superfluidity.*" Rev. Mod. Phys. **71**, 318 (1999)

[2] L. Hoddeson, G. Baym, and M. Eckert: "*The development of the quantum-mechanical electron theory of metals: 1928-1933.*" Rev. Mod. Phys. **59**, 287 (1987)

[3] P. W. Anderson: "*Absence of Diffusion in Certain Random Lattices.*" Phys. Rev. **109**, 1492 (1958)

[4] P. W. Anderson: "Local moments and localized states." in: *Physics 1971-1980: Nobel lectures.* (World Scientific, Singapore, 1992)

[5] B. A. van Tiggelen: "Localization of Waves." in: *Diffuse waves in complex media.* (Kluwer, Dordrecht, 1999)

[6] M. Girardeau: "*Relationship between Systems of Impenetrable Bosons and Fermions in One Dimension.*" J. Math. Phys. **1**, 516 (1960)

[7] K. B. Davis, M.-O. Mewes, M. R. Andrews, N. J. Druten, D. S. Durfee, D. M. Kurn, and W. Ketterle: "*Bose-Einstein condensation in a gas of sodium atoms.*" Phys. Rev. Lett. **75**, 3969 (1995)

[8] M. H. Anderson, J. R. Ensher, M. R. Matthews, C. E. Wieman, and E. A. Cornell: "*Observation of Bose-Einstein Condensation in a Dilute Atomic Vapor.*" Science **269**, 198 (1995)

[9] C. C. Bradley, C. A. Sackett, J. J. Tollett, and R. G. Hulet: "*Evidence of Bose-Einstein Condensation in an Atomic Gas with Attractive Interactions.*" Phys. Rev. Lett. **75**, 1687 (1995) Note: See erratum [10].

[10] C. C. Bradley, C. A. Sackett, J. J. Tollett, and R. G. Hulet: "*Erratum: Evidence of Bose-Einstein Condensation in an Atomic Gas with Attractive Interactions [9].*" Phys. Rev. Lett. **79**, 1170 (1997)

[11] C. C. Bradley, C. A. Sackett, and R. G. Hulet: "*Bose-Einstein Condensation of Lithium: Observation of Limited Condensate Number.*" Phys. Rev. Lett. **78**, 985 (1997)

[12] E. A. Cornell, and C. E. Wieman: "*Nobel Lecture: Bose-Einstein condensation in a dilute gas, the first 70 years and some recent experiments.*" Rev. Mod. Phys. **74**, 875–893 (2002)

[13] W. Ketterle: "*Nobel lecture: When atoms behave as waves: Bose-Einstein condensation and the atom laser.*" Rev. Mod. Phys. **74**, 1131–1151 (2002)

*Most references are linked to the internet: The first author to the digital object identifier (doi) and the journal name to the URL-adress.

[14] W. Ketterle, D. S. Durfee, and D. M. Stamper-Kurn: "Making, probing and understanding Bose-Einstein condensates." in: *Proceedings of the International School of Physics Enrico Fermi, Course CXL: Bose-Einstein condensation in atomic gases.* (IOS, Amsterdam, 1999)

[15] B. DeMarco, and D. Jin: "*Onset of Fermi degeneracy in a trapped atomic gas.*" Science **285**, 1703 (1999)

[16] F. Schreck, L. Khaykovich, K. L. Corwin, G. Ferrari, T. Bourdel, J. Cubizolles, and C. Salomon: "*Quasipure Bose-Einstein Condensate Immersed in a Fermi Sea.*" Phys. Rev. Lett. **87**, 080403 (2001)

[17] A. G. Truscott, K. E. Strecker, W. I. McAlexander, G. B. Partridge, and R. G. Hulet: "*Observation of Fermi Pressure in a Gas of Trapped Atoms.*" Science **291**, 2570–2572 (2001)

[18] W. Ketterle, and M. W. Zwierlein: "Making, probing and understanding ultracold Fermi gases." in: *Proceedings of the International School of Physics "Enrico Fermi", Course CLXIV: Ultracold Fermi Gases.* (IOS, Amsterdam, 2008)

[19] R. P. Feynman: "*Simulating Physics with Computers.*" Int. J. Theo. Phys. **21**, 467 (1982)

[20] I. Bloch, J. Dalibard, and W. Zwerger: "*Many-body physics with ultracold gases.*" Rev. Mod. Phys. **80**, 885 (2008)

[21] S. Bose: "*Plancks Gesetz und Lichtquantenhypothese.*" Zeitschrift für Physik **26**, 178 (1924)

[22] O. Theimer, and B. Ram: "*The beginning of quantum statistics: A translation of: Planck's law and the light quantum hypothesis.*" Am. J. Phys. **44**, 1056 (1976)

[23] A. Einstein: "*Quantentheorie des Einatomigen idealen Gases.*" Sitzungsbericht der preussischen Akademie der Wissenschaft 261–267 (1924)

[24] A. Einstein: "*Quantentheorie des einatomigen idealen Gases, zweite Abhandlung.*" Berliner Berichte 3–14 (1925)

[25] W. Ketterle, and N. J. Druten: "*Bose-Einstein condensation of a finite number of particles trapped in one or three dimensions.*" Phys. Rev. A **54**, 656 (1996)

[26] E. A. Cornell, J. R. Ensher, and C. E. Wieman: "*Experiments in Dilute Atomic Bose-Einstein Condensation.*" arXiv:cond-mat/9903109v1 (1999)

[27] D. M. Stamper-Kurn, and W. Ketterle: "Spinor condensates and light scattering from Bose-Einstein condensates." in: *Les Houches Summer School, session LXXII: Coherent atomic matter waves.* (Springer, Berlin, 2001)

[28] V. N. Efimov: "*Energy levels arising from resonant two-body forces in a three-body system.*" Phys. Lett. B **33**, 563–564 (1970)

[29] V. N. Efimov: "*Weakly-bound states of three resonantly-interacting particles.*" Sov. J. Nucl. Phys. **12**, 589–595 (1971)

[30] T. Kraemer, M. Mark, P. Waldburger, J. G. Danzl, C. Chin, B. Engeser, A. D. Lange, K. Pilch, A. Jaakkola, H.-C. Nägerl, and R. Grimm: "*Evidence for Efimov quantum states in an ultracold gas of caesium atoms.*" Nature **440**, 315 (2006)

[31] F. Ferlaino, and R. Grimm: "*Forty years of Efimov physics: How a bizarre prediction turned into a hot topic.*" Physics **3**, 9 (2010)

[32] M. Zaccanti, B. Deissler, C. D'Errico, M. Fattori, M. Jona-Lasinio, S. Müller, G. Roati, M. Inguscio, and G. Modugno: "*Observation of an Efimov spectrum in an atomic system.*" Nature Physics **5**, 586 (2009)

[33] F. Brennecke, T. Donner, S. Ritter, T. Bourdel, M. Köhl, and T. Esslinger: "*Cavity QED with a Bose-Einstein condensate.*" Nature **450**, 268 (2007)

[34] H. J. Kimble: "*The quantum internet.*" Nature **453**, 1023–30 (2008)

[35] P. Treutlein, D. Hunger, S. Camerer, T. W. Hänsch, and J. Reichel: "*Bose-Einstein Condensate Coupled to a Nanomechanical Resonator on an Atom Chip.*" Phys. Rev. Lett. **99**, 140403 (2007)

[36] D. Hunger, S. Camerer, T. W. Hänsch, D. König, J. P. Kotthaus, J. Reichel, and P. Treutlein: "*Resonant Coupling of a Bose-Einstein Condensate to a Micromechanical Oscillator.*" Phys. Rev. Lett. **104**, 143002 (2010)

[37] L. Kocbach, and S. Lubbad: "*Geometrical simplification of the dipole-dipole interaction formula.*" Physics Education **45**, 345–351 (2010)

[38] C. Klempt, O. Topic, G. Gebreyesus, M. Scherer, T. Henninger, P. Hyllus, W. Ertmer, L. Santos, and J. J. Arlt: "*Multiresonant Spinor Dynamics in a Bose-Einstein Condensate.*" Phys. Rev. Lett. **103**, 195302 (2009)

[39] C. Klempt, O. Topic, G. Gebreyesus, M. Scherer, T. Henninger, P. Hyllus, W. Ertmer, L. Santos, and J. J. Arlt: "*Parametric Amplification of Vacuum Fluctuations in a Spinor Condensate.*" Phys. Rev. Lett. **104**, 195303 (2010)

[40] J. M. Higbie, L. E. Sadler, S. Inouye, A. P. Chikkatur, S. R. Leslie, K. L. Moore, V. Savalli, and D. M. Stamper-Kurn: "*Direct, Non-Destructive Imaging of Magnetization in a Spin-1 Bose Gas.*" Phys. Rev. Lett. **95**, 050401 (2005)

[41] L. E. Sadler, J. M. Higbie, S. R. Leslie, M. Vengalattore, and D. M. Stamper-Kurn: "*Spontaneous symmetry breaking in a quenched ferromagnetic spinor Bose-Einstein condensate.*" Nature **443**, 312 (2006)

[42] M. Vengalattore, S. R. Leslie, J. Guzman, and D. M. Stamper-Kurn: "*Spontaneously modulated spin textures in a dipolar spinor Bose-Einstein condensate.*" Phys. Rev. Lett. **100**, 170403 (2008)

[43] M. Vengalattore, J. Guzman, S. Leslie, F. Serwane, and D. M. Stamper-Kurn: "*Crystalline Magnetic Order in a Dipolar Quantum Fluid.*" arXiv:cond-mat.other/0901.3800v1 (2009)

[44] J. Stuhler, A. Griesmaier, T. Koch, M. Fattori, T. Pfau, S. Giovanazzi, P. Pedri, and L. Santos: "*Observation of Dipole-Dipole Interaction in a Degenerate Quantum Gas.*" Phys. Rev. Lett. **95**, 150406 (2005)

[45] A. Griesmaier, J. Stuhler, T. Koch, M. Fattori, T. Pfau, and S. Giovanazzi: "*Comparing Contact and Dipolar Interactions in a Bose-Einstein Condensate.*" Phys. Rev. Lett. **97**, 250402 (2006)

[46] M. Fattori, T. Koch, S. Götz, A. Griesmaier, S. Hensler, J. Stuhler, and T. Pfau: "*Demagnetization cooling of a gas.*" Nature Physics **2**, 765 (2006)

[47] Q. Beaufils, R. Chicireanu, A. Pouderous, W. Souza Melo, B. Laburthe-Tolra, E. Maréchal, L. Vernac, J. C. Keller, and O. Gorceix: "*Averaging out magnetic forces with fast rf sweeps in an optical trap for metastable chromium atoms.*" Phys. Rev. A **77**, 053413 (2008)

[48] B. Pasquiou, G. Bismut, Q. Beaufils, A. Crubellier, E. Maréchal, P. Pedri, L. Vernac, O. Gorceix, and B. Laburthe-Tolra: "*Control of dipolar relaxation in external fields.*" Phys. Rev. A **81**, 042716 (2010)

[49] M. Fattori, G. Roati, B. Deissler, C. D'Errico, M. Zaccanti, M. Jona-Lasinio, L. Santos, M. Inguscio, and G. Modugno: "*Magnetic Dipolar Interaction in a Bose-Einstein Condensate Atomic Interferometer.*" Phys. Rev. Lett. **101**, 190405 (2008)

[50] S. E. Pollack, D. Dries, M. Junker, Y. P. Chen, T. A. Corcovilos, and R. G. Hulet: "*Extreme Tunability of Interactions in a ^{7}Li Bose-Einstein Condensate.*" Phys. Rev. Lett. **102**, 90402 (2009)

[51] M. A. Baranov: "*Theoretical progress in many-body physics with ultracold dipolar gases.*" Phys. Rep. **464**, 71 (2008)

[52] T. Lahaye, C. Menotti, L. Santos, M. Lewenstein, and T. Pfau: "*The physics of dipolar bosonic quantum gases.*" Rep. Prog. Phys. **72**, 6401 (2009)

[53] C. A. Sackett, H. T. C. Stoof, and R. G. Hulet: "*Growth and Collapse of a Bose-Einstein Condensate with Attractive Interactions.*" Phys. Rev. Lett. **80**, 2031 (1998)

[54] C. A. Sackett, J. M. Gerton, M. Welling, and R. G. Hulet: "*Measurements of Collective Collapse in a Bose-Einstein Condensate with Attractive Interactions.*" Phys. Rev. Lett. **82**, 876 (1999)

[55] C. A. Sackett: "*Dynamics of Bose-Einstein Condensation in ^{7}Li.*" (PhD thesis, Huston, 2001)

[56] J. M. Gerton, D. Strekalov, I. Prodan, and R. G. Hulet: "*Direct observation of growth and collapse of a Bose-Einstein condensate with attractive interactions.*" Nature **408**, 692–5 (2000)

[57] E. A. Donley, N. R. Claussen, S. L. Cornish, J. L. Roberts, E. A. Cornell, and C. E. Wieman: "*Dynamics of collapsing and exploding Bose-Einstein condensates.*" Nature **412**, 295 (2001)

[58] N. R. Claussen: "*Dynamics of Bose-Einstein condensates near a Feshbach resonance in ^{85}Rb.*" (PhD thesis, Boulder, 2003)

[59] J. L. Roberts, N. R. Claussen, S. L. Cornish, E. A. Donley, E. A. Cornell, and C. E. Wieman: "*Controlled Collapse of a Bose-Einstein Condensate.*" Phys. Rev. Lett. **86**, 4211 (2001)

[60] J. L. Roberts: "*Bose-Einstein Condensates with Tunable Atom-atom Interactions: The First Experiments with ^{85}Rb BECs.*" (PhD thesis, Boulder, 2001)

[61] G. Modugno, G. Roati, F. Riboli, F. Ferlaino, R. J. Brecha, and M. Inguscio: "*Collapse of a Degenerate Fermi Gas.*" Science **297**, 2240 (2002)

[62] C. Ospelkaus, S. Ospelkaus, K. Sengstock, and K. Bongs: "*Interaction-Driven Dynamics of ^{40}K-^{87}Rb Fermion-Boson Gas Mixtures in the Large-Particle-Number Limit.*" Phys. Rev. Lett. **96**, 20401 (2006)

[63] F. Dalfovo, S. Giorgini, L. P. Pitaevskii, and S. Stringari: "*Theory of Bose-Einstein condensation in trapped gases.*" Rev. Mod. Phys. **71**, 463 (1999)

[64] L. Santos, G. V. Shlyapnikov, and M. Lewenstein: "*Roton-Maxon Spectrum and Stability of Trapped Dipolar Bose-Einstein Condensates.*" Phys. Rev. Lett. **90**, 250403 (2003)

[65] P. Pedri, and L. Santos: "*Two-Dimensional Bright Solitons in Dipolar Bose-Einstein Condensates.*" Phys. Rev. Lett. **95**, 200404 (2005)

[66] U. R. Fischer: "*Stability of quasi-two-dimensional Bose-Einstein condensates with dominant dipole-dipole interactions.*" Phys. Rev. A **73**, 31602 (2006)

[67] R. M. Wilson, S. Ronen, J. L. Bohn, and H. Pu: "*Manifestations of the Roton Mode in Dipolar Bose-Einstein Condensates.*" Phys. Rev. Lett. **100**, 245302 (2008)

[68] R. M. Wilson, S. Ronen, and J. L. Bohn: "*Dipolar Bose-Einstein condensates as discrete superfluids.*" arXiv:cond-mat.quant-gas/0912.5261v1 (2009)

[69] K. Góral, K. Rzazewski, and T. Pfau: "*Bose-Einstein condensation with magnetic dipole-dipole forces.*" Phys. Rev. A **61**, 051601 (2000) Note: See comment [305].

[70] S. Ronen, D. C. E. Bortolotti, and J. L. Bohn: "*Radial and Angular Rotons in Trapped Dipolar Gases.*" Phys. Rev. Lett. **98**, 30406 (2007)

[71] P. Köberle, and G. Wunner: "*Phonon instability and self-organized structures in multi-layer stacks of confined dipolar Bose-Einstein condensates in optical lattices.*" Phys. Rev. A **80**, 063601 (2009)

[72] O. Dutta, and P. Meystre: "*Ground-state structure and stability of dipolar condensates in anisotropic traps.*" Phys. Rev. A **75**, 53604 (2007)

[73] R. M. Wilson, S. Ronen, and J. L. Bohn: "*Angular collapse of dipolar Bose-Einstein condensates.*" Phys. Rev. A **80**, 23614 (2009)

[74] I. Tikhonenkov, B. A. Malomed, and A. Vardi: "*Anisotropic Solitons in Dipolar Bose-Einstein Condensates.*" Phys. Rev. Lett. **100**, 90406 (2008)

[75] K. Góral, L. Santos, and M. Lewenstein: "*Quantum Phases of Dipolar Bosons in Optical Lattices.*" Phys. Rev. Lett. **88**, 170406 (2002)

[76] G. E. Astrakharchik, and Y. E. Lozovik: "*Super-Tonks-Girardeau regime in trapped one-dimensional dipolar gases.*" Phys. Rev. A **77**, 13404 (2008)

[77] R. Citro, S. DePalo, E. Orignac, P. Pedri, and M.-L. Chiofalo: "*Luttinger hydrodynamics of confined one-dimensional Bose gases with dipolar interactions.*" New J. Phys. **10**, 5011 (2008)

[78] T. Lahaye, T. Pfau, and L. Santos: "*Mesoscopic ensembles of polar bosons in triple-well potentials.*" Phys. Rev. Lett. **104**, 170404 (2010)

[79] J. J. McClelland, and J. L. Hanssen: "*Laser Cooling without Repumping: A Magneto-Optical Trap for Erbium Atoms.*" Phys. Rev. Lett. **96**, 143005 (2006)

[80] M. Lu, S. H. Youn, and B. L. Lev: "*Trapping Ultracold Dysprosium: A Highly Magnetic Gas for Dipolar Physics.*" Phys. Rev. Lett. **104**, 63001 (2010)

[81] K.-K. Ni, S. Ospelkaus, M. H. G. Miranda, A. Pe'er, B. Neyenhuis, J. J. Zirbel, S. Kotochigova, P. S. Julienne, D. S. Jin, and J. Ye: "*A High Phase-Space-Density Gas of Polar Molecules.*" Science **322**, 231 (2008)

[82] K.-K. Ni, S. Ospelkaus, D. Wang, G. Quéméner, B. Neyenhuis, M. H. G. Miranda, J. L. Bohn, J. Ye, and D. S. Jin: "*Dipolar collisions of polar molecules in the quantum regime.*" Nature **464**, 1324–8 (2010)

[83] S. Ospelkaus, A. Pe'er, K.-K. Ni, J. J. Zirbel, B. Neyenhuis, S. Kotochigova, P. S. Julienne, J. Ye, and D. S. Jin: "*Efficient state transfer in an ultracold dense gas of heteronuclear molecules.*" Nature Physics **4**, 622 (2008)

[84] S. Ospelkaus, K.-K. Ni, G. Quéméner, B. Neyenhuis, D. Wang, M. H. G. Miranda, J. L. Bohn, J. Ye, and D. S. Jin: "*Controlling the Hyperfine State of Rovibronic Ground-State Polar Molecules.*" Phys. Rev. Lett. **104**, 30402 (2010)

[85] S. Ospelkaus, K.-K. Ni, D. Wang, M. H. G. Miranda, B. Neyenhuis, G. Quéméner, P. S. Julienne, J. L. Bohn, D. S. Jin, and J. Ye: "*Quantum-state controlled chemical reactions of ultracold potassium-rubidium molecules.*" Science **327**, 853–7 (2010)

[86] J. Deiglmayr, A. Grochola, M. Repp, K. Mörtlbauer, C. Glück, J. Lange, O. Dulieu, R. Wester, and M. Weidemüller: "*Formation of Ultracold Polar Molecules in the Rovibrational Ground State.*" Phys. Rev. Lett. **101**, 133004 (2008)

[87] J. M. Sage, S. Sainis, T. Bergeman, and D. Demille: "*Optical Production of Ultracold Polar Molecules.*" Phys. Rev. Lett. **94**, 203001 (2005)

[88] G. Pupillo, A. Micheli, M. Boninsegni, I. Lesanovsky, and P. Zoller: "*Strongly Correlated Gases of Rydberg-Dressed Atoms: Quantum and Classical Dynamics.*" Phys. Rev. Lett. **104**, 223002 (2010)

[89] H. P. Büchler, E. Demler, M. Lukin, A. Micheli, N. Prokof'ev, G. Pupillo, and P. Zoller: "*Strongly Correlated 2D Quantum Phases with Cold Polar Molecules: Controlling the Shape of the Interaction Potential.*" Phys. Rev. Lett. **98**, 60404 (2007)

[90] H. P. Büchler, A. Micheli, and P. Zoller: "*Three-body interactions with cold polar molecules.*" Nature Physics **3**, 726 (2007)

[91] N. R. Cooper, and G. V. Shlyapnikov: "*Stable Topological Superfluid Phase of Ultracold Polar Fermionic Molecules.*" Phys. Rev. Lett. **103**, 155302 (2009)

[92] M. Ueda, and Y. Kawaguchi: "*Spinor Bose-Einstein condensates.*" arXiv:cond-mat.quant-gas/1001.2072v1 (2010)

[93] S. Jochim, M. Bartenstein, A. Altmeyer, G. Hendl, S. Riedl, C. Chin, J. H. Denschlag, and R. Grimm: "*Bose-Einstein Condensation of Molecules.*" Science **302**, 2101 (2003)

[94] M. W. Zwierlein, C. A. Stan, C. H. Schunck, S. M. Raupach, S. Gupta, Z. Hadzibabic, and W. Ketterle: "*Observation of Bose-Einstein Condensation of Molecules.*" Phys. Rev. Lett. **91**, 250401 (2003)

[95] J. Kasprzak, M. Richard, S. Kundermann, A. Baas, P. Jeambrun, J. M. J. Keeling, F. M. Marchetti, M. H. Szymańska, R. André, J. L. Staehli, V. Savona, P. B. Littlewood, B. Deveaud, and L. S. Dang: "*Bose-Einstein condensation of exciton polaritons.*" Nature **443**, 409 (2006)

[96] W. Pauli: "*The Connection Between Spin and Statistics.*" Phys. Rev. **58**, 716 (1940)

[97] V. Bagnato, D. E. Pritchard, and D. Kleppner: "*Bose-Einstein condensation in an external potential.*" Phys. Rev. A **35**, 4354 (1987)

[98] D. Stamper-Kurn: "*Peeking and poking at a new quantum fluid: studies of gaseous Bose–Einstein condensates in magnetic and optical traps.*" (PhD thesis, MIT, 1999)

[99] Y. Castin: "*Bose-Einstein condensates in atomic gases: simple theoretical results.*" arXiv:cond-mat/0105058v1 (2001)

[100] A. Griffin: "A Brief History of Our Understanding of BEC: From Bose to Beliaev." in: *Proceedings of the International School of Physics Enrico Fermi, Course CXL: Bose-Einstein condensation in atomic gases.* (IOS, Amsterdam, 1999)

[101] C. Hecht: "*The possible superfluid behaviour of hydrogen atom gases and liquids.*" Physica **25**, 1159 (1959)

[102] W. C. Stwalley, and L. H. Nosanow: "*Possible "New" Quantum Systems.*" Phys. Rev. Lett. **36**, 910 (1976)

[103] W. C. Stwalley: "*Stability of Spin-Aligned Hydrogen at Low Temperatures and High Magnetic Fields: New Field-Dependent Scattering Resonances and Predissociations.*" Phys. Rev. Lett. **37**, 1628 (1976)

[104] D. G. Fried, T. C. Killian, L. Willmann, D. Landhuis, S. C. Moss, D. Kleppner, and T. J. Greytak: "*Bose-Einstein Condensation of Atomic Hydrogen.*" Phys. Rev. Lett. **81**, 3811 (1998)

[105] A. Robert, O. Sirjean, A. Browaeys, J. Poupard, S. Nowak, D. Boiron, C. I. Westbrook, and A. Aspect: "*A Bose-Einstein condensate of metastable atoms.*" Science **292**, 461–4 (2001)

[106] F. P. D. Santos, J. Léonard, J. Wang, C. J. Barrelet, F. Perales, E. Rasel, C. S. Unnikrishnan, M. Leduc, and C. Cohen-Tannoudji: "*Bose-Einstein Condensation of Metastable Helium.*" Phys. Rev. Lett. **86**, 3459 (2001)

[107] G. Roati, M. Zaccanti, C. D'Errico, J. Catani, M. Modugno, A. Simoni, M. Inguscio, and G. Modugno: "^{39}K *Bose-Einstein Condensate with Tunable Interactions.*" Phys. Rev. Lett. **99**, 10403 (2007)

[108] G. Modugno, G. Ferrari, G. Roati, R. J. Brecha, A. Simoni, and M. Inguscio: "*Bose-Einstein condensation of potassium atoms by sympathetic cooling.*" Science **294**, 1320–2 (2001)

[109] S. Kraft, F. Vogt, O. Appel, F. Riehle, and U. Sterr: "*Bose-Einstein Condensation of Alkaline Earth Atoms:* ^{40}Ca." Phys. Rev. Lett. **103**, 130401 (2009)

[110] A. Griesmaier, J. Werner, S. Hensler, J. Stuhler, and T. Pfau: "*Bose-Einstein Condensation of Chromium.*" Phys. Rev. Lett. **94**, 160401 (2005)

[111] Y. N. M. Escobar, P. G. Mickelson, M. Yan, B. J. Desalvo, S. B. Nagel, and T. C. Killian: "*Bose-Einstein Condensation of* ^{84}Sr." Phys. Rev. Lett. **103**, 200402 (2009)

[112] S. Stellmer, M. K. Tey, B. Huang, R. Grimm, and F. Schreck: "*Bose-Einstein Condensation of Strontium.*" Phys. Rev. Lett. **103**, 200401 (2009)

[113] S. L. Cornish, N. R. Claussen, J. L. Roberts, E. A. Cornell, and C. E. Wieman: "*Stable* ^{85}Rb *Bose-Einstein Condensates with Widely Tunable Interactions.*" Phys. Rev. Lett. **85**, 1795 (2000)

[114] T. Weber, J. Herbig, M. Mark, H.-C. Nägerl, and R. Grimm: "*Bose-Einstein Condensation of Cesium.*" Science **299**, 232 (2003)

[115] T. Fukuhara, S. Sugawa, and Y. Takahashi: "*Bose-Einstein condensation of an ytterbium isotope.*" Phys. Rev. A **76**, 51604 (2007)

[116] Y. Takasu, K. Maki, K. Komori, T. Takano, K. Honda, M. Kumakura, T. Yabuzaki, and Y. Takahashi: "*Spin-Singlet Bose-Einstein Condensation of Two-Electron Atoms.*" Phys. Rev. Lett. **91**, 40404 (2003)

[117] T. Fukuhara, S. Sugawa, Y. Takasu, and Y. Takahashi: "*All-optical formation of quantum degenerate mixtures.*" Phys. Rev. A **79**, 21601 (2009)

[118] E. A. Burt, R. W. Ghrist, C. J. Myatt, M. J. Holland, E. A. Cornell, and C. E. Wieman: "*Coherence, Correlations, and Collisions: What One Learns about Bose-Einstein Condensates from Their Decay.*" Phys. Rev. Lett. **79**, 337 (1997)

[119] C. J. Pethick, and H. Smith: "*Bose-Einstein Condensation in Dilute Gases.*" (Cambridge University Press, Cambridge, 2001)

[120] Y. Kagan, B. V. Svistunov, and G. V. Shlyapnikov: "*Effect of Bose condensation on inelastic processes in gases.*" JETP Lett. **42**, 209 (1985)

[121] J. Weiner, V. S. Bagnato, S. Zilio, and P. S. Julienne: "*Experiments and theory in cold and ultracold collisions.*" Rev. Mod. Phys. **71**, 1 (1999)

[122] D. J. Heinzen: "Bose-Einstein condensation in atomic gases." in: *Proceedings of the International School of Physics-Enrico Fermi, Course CXL.* (IOS, Bologna, 1998)

[123] C. Cohen-Tannoudji, B. Diu, and F. Laloe: "*Quantenmechanik 2.*" (de Gruyter, Berlin, 1999)

[124] J. Dalibard: "Collisional dynamics of ultra-cold atomic gases." in: *Proceedings of the International School of Physics Enrico Fermi, Course CXL: Bose-Einstein condensation in gases.* (IOS, Amsterdam, 1998)

[125] E. Hecht: "*Optics.*" (Addison-Wesley, Massachusetts, 1998)

[126] J. Werner, A. Griesmaier, S. Hensler, J. Stuhler, T. Pfau, A. Simoni, and E. Tiesinga: "*Observation of Feshbach Resonances in an Ultracold Gas of* ^{52}*Cr.*" Phys. Rev. Lett. **94**, 183201 (2005)

[127] J. Werner: "*Observation of Feshbach resonances in an ultracold gas of* ^{52}*Cr.*" (PhD thesis, Stuttgart, 2006)

[128] C. Chin, R. Grimm, P. Julienne, and E. Tiesinga: "*Feshbach Resonances in Ultracold Gases.*" Rev. Mod. Phys. **82**, 1225–1286 (2010)

[129] C. Buggle, J. Léonard, W. V. Klitzing, and J. T. Walraven: "*Interferometric Determination of the s and d-Wave Scattering Amplitudes in* ^{87}*Rb.*" Phys. Rev. Lett. **93**, 173202 (2004)

[130] N. R. Thomas, N. Kjærgaard, P. S. Julienne, and A. C. Wilson: "*Imaging of s and d Partial-Wave Interference in Quantum Scattering of Identical Bosonic Atoms.*" Phys. Rev. Lett. **93**, 173201 (2004)

[131] H. Davies: "*On the convergence of the born approximation.*" Nuclear Physics **14**, 465 (1960)

[132] K. Huang: "*Statistical mechnics.*" (John Wiley, New York, 1987)

[133] S. Yi, and L. You: "*Trapped atomic condensates with anisotropic interactions.*" Phys. Rev. A **61**, 41604 (2000)

[134] S. Yi, and L. You: "*Trapped condensates of atoms with dipole interactions.*" Phys. Rev. A **63**, 53607 (2001)

[135] A. Derevianko: "*Anisotropic pseudopotential for polarized dilute quantum gases.*" Phys. Rev. A **67**, 33607 (2003)

[136] T. Koch: "*Enhancing the dipolar character of a Bose-Einstein condensate: From perturbative effects to a purely dipolar quantum gas.*" (PhD thesis, Stuttgart, 2008)

[137] H. B. G. Casimir, and D. Polder: "*Influence of Retardation on the London-van der Waals Forces.*" Nature **158**, 787 (1946)

[138] T. G. Walker, and M. Saffman: "*Consequences of Zeeman degeneracy for the van der Waals blockade between Rydberg atoms.*" Phys. Rev. A **77**, 32723 (2008)

[139] M. Fowler: "*Van der Waals Forces Between Atoms.*" (unpublished, University of Virginia, 2007)

[140] D. L. Andrews, and D. S. Bradshaw: "*Virtual photons, dipole fields and energy transfer: a quantum electrodynamical approach.*" Eur. J. Phys. **25**, 845–858 (2004)

[141] G. V. Shlyapnikov, J. T. M. Walraven, U. M. Rahmanov, and M. W. Reynolds: "*Decay kinetics and Bose condensation in a gas of spin-polarized triplet helium.*" Phys. Rev. Lett. **73**, 3247 (1994)

[142] K. Xu, Y. Liu, D. E. Miller, J. K. Chin, W. Setiawan, and W. Ketterle: "*Observation of Strong Quantum Depletion in a Gaseous Bose-Einstein Condensate.*" Phys. Rev. Lett. **96**, 180405 (2006)

[143] M. Baranov, Å. G. Dobrek, K. Góral, L. Santos, and M. Lewenstein: "*Ultracold Dipolar Gases — a Challenge for Experiments and Theory.*" Physica Scripta **102**, 74 (2002)

[144] L. Santos, G. V. Shlyapnikov, P. Zoller, and M. Lewenstein: "*Bose-Einstein Condensation in Trapped Dipolar Gases.*" Phys. Rev. Lett. **85**, 1791 (2000) Note: See erratum [145].

[145] L. Santos, G. V. Shlyapnikov, P. Zoller, and M. Lewenstein: "*Erratum: Bose-Einstein Condensation in Trapped Dipolar Gases [144].*" Phys. Rev. Lett. **88**, 139904 (2002)

[146] D. C. E. Bortolotti, S. Ronen, J. L. Bohn, and D. Blume: "*Scattering Length Instability in Dipolar Bose-Einstein Condensates.*" Phys. Rev. Lett. **97**, 160402 (2006)

[147] S. Ronen, D. C. E. Bortolotti, D. Blume, and J. L. Bohn: "*Dipolar Bose-Einstein condensates with dipole-dependent scattering length.*" Phys. Rev. A **74**, 33611 (2006)

[148] C. Huepe, S. Métens, G. Dewel, P. Borckmans, and M. E. Brachet: "*Decay Rates in Attractive Bose-Einstein Condensates.*" Phys. Rev. Lett. **82**, 1616 (1999)

[149] P. Köberle, H. Cartarius, T. Fabčič, J. Main, and G. Wunner: "*Bifurcations, order and chaos in the Bose-Einstein condensation of dipolar gases.*" New J. Phys. **11**, 3017 (2009) Note: The characteristic dipolar length scale a_{dd} differs from the one used in this thesis.

[150] S. L. Rolston, and W. D. Phillips: "*Nonlinear and quantum atom optics.*" Nature **416**, 219–224 (2002)

[151] B. D. Esry: "*Many-body effects in Bose-Einstein Condensates of dilute atomic gases.*" (PhD thesis, Colorado, 1997)

[152] J. J. Sakurai: "*Modern Quantum Mechanics.*" (Addison-Wesley, Massachusetts, 1985)

[153] M. E. Peskin, and D. V. Schroeder: "*An Introduction to Quantum Field Theory.*" (Addison-Wesley, Massachusetts, 1997)

[154] L. E. Ballentine: "*Equation of motion for the statistical operator.*" Am. J. Phys. **52**, 74 (1984)

[155] F. Schwabl: "*Advanced quantum mechanics.*" (Springer, Berlin, 2005)

[156] M. Naraschewski, H. Wallis, A. Schenzle, J. I. Cirac, and P. Zoller: "*Interference of Bose condensates.*" Phys. Rev. A **54**, 2185 (1996)

[157] L. Pitaevskii, and S. Stringari: "*Bose-Einstein condensation.*" (Clarendon, Oxford, 2003)

[158] G. Cook, and R. H. Dickerson: "*Understanding the chemical potential.*" Am. J. Phys. **63**, 737 (1995)

[159] C. Eberlein, S. Giovanazzi, and D. H. O'Dell: "*Exact solution of the Thomas-Fermi equation for a trapped Bose-Einstein condensate with dipole-dipole interactions.*" Phys. Rev. A **71**, 33618 (2005)

[160] N. G. Parker, and D. H. J. O'Dell: "*Thomas-Fermi versus one- and two-dimensional regimes of a trapped dipolar Bose-Einstein condensate.*" Phys. Rev. A **78**, 41601 (2008)

[161] S. Giovanazzi, P. Pedri, L. Santos, A. Griesmaier, M. Fattori, T. Koch, J. Stuhler, and T. Pfau: "*Expansion dynamics of a dipolar Bose-Einstein condensate.*" Phys. Rev. A **74**, 13621 (2006)

[162] D. H. O'Dell, S. Giovanazzi, and C. Eberlein: "*Exact Hydrodynamics of a Trapped Dipolar Bose-Einstein Condensate.*" Phys. Rev. Lett. **92**, 250401 (2004)

[163] S. Giovanazzi, A. Görlitz, and T. Pfau: "*Tuning the Dipolar Interaction in Quantum Gases.*" Phys. Rev. Lett. **89**, 130401 (2002)

[164] Y. Castin, and R. Dum: "*Bose-Einstein Condensates in Time Dependent Traps.*" Phys. Rev. Lett. **77**, 5315 (1996)

[165] T. Lahaye, T. Koch, B. Fröhlich, M. Fattori, J. Metz, A. Griesmaier, S. Giovanazzi, and T. Pfau: "*Strong dipolar effects in a quantum ferrofluid.*" Nature **448**, 672 (2007)

[166] A. Griesmaier: "*Aufbau einer kombinierten magneto-optischen Falle für Chrom und Rubidium.*" (MA thesis, Stuttgart, 2002)

[167] A. Griesmaier: "*Dipole-dipole interaction in a degenerate quantum gas Bose–Einstein condensation of chromium atoms.*" (PhD thesis, Stuttgart, 2006)

[168] P. O. Schmidt: "*Scattering properties of ultra-cold chromium atoms.*" (PhD thesis, Stuttgart, 2003)

[169] J. Stuhler: "*Kontinuierliches Laden einer Magnetfalle mit lasergekühlten Chromatomen.*" (PhD thesis, Stuttgart, 2001)

[170] S. Hensler: "*Wechselwirkungen in ultrakalten dipolaren Gasen.*" (PhD thesis, Stuttgart, 2004)

[171] J. Werner: "*Kontinuierliches Laden einer Magnetfalle mit lasergekühlten Chromatomen.*" (MA thesis, Konstanz, 2000)

[172] B. Fröhlich: "*Strong Dipolar Effects in a Chromium Bose-Einstein Condensate.*" (MA thesis, Stuttgart, 2007)

[173] H. J. Metcalf, and P. Straten: "*Laser Cooling and Trapping.*" (Springer, New York, 1999)

[174] J. V. Prodan, W. D. Phillips, and H. Metcalf: "*Laser Production of a Very Slow Monoenergetic Atomic Beam.*" Phys. Rev. Lett. **49**, 1149 (1982)

[175] C. J. Dedman, J. Nes, T. M. Hanna, R. G. Dall, K. G. H. Baldwin, and A. G. Truscott: "*Optimum design and construction of a Zeeman slower for use with a magneto-optic trap.*" Rev. Sci. Inst. **75**, 5136 (2004)

[176] W. Ketterle, and D. E. Pritchard: "*Atom cooling by time-dependent potentials.*" Phys. Rev. A **46**, 4051 (1992) Note: This is only true for an ideal gas [193].

[177] Y. Wan: "*Aufbau von hochstabilen optischen Gittern für dipolare Quantengase.*" (MA thesis, Stuttgart, 2010)

[178] A. S. Arnold, and P. J. Manson: "*Atomic density and temperature distributions in magneto-optical traps.*" J. Opt. Soc. Am. B **17**, 497 (2000)

[179] C. G. Townsend, N. H. Edwards, C. J. Cooper, K. P. Zetie, C. J. Foot, A. M. Steane, P. Szriftgiser, H. Perrin, and J. Dalibard: "*Phase-space density in the magneto-optical trap.*" Phys. Rev. A **52**, 1423 (1995)

[180] C. Kittel: "*Einführung in die Festkörperphysik.*" (Oldenbourg, München, 1996)

[181] H. Ibach, and H. Lüth: "*Solid-state physics: An introduction to principles of materials science.*" (Springer, Berlin, 2009)

[182] A. S. Bell, J. Stuhler, S. Locher, S. Hensler, J. Mlynek, and T. Pfau: "*A magneto-optical trap for chromium with population repumping via intercombination lines.*" Eur. Phys. Lett. **45**, 156 (1999)

[183] P. O. Schmidt, S. Hensler, J. Werner, T. Binhammer, A. Görlitz, and T. Pfau: "*Continuous loading of cold atoms into a Ioffe-Pritchard magnetic trap.*" J. Opt. B **5**, 170 (2002)

[184] J. Stuhler, P. O. Schmidt, S. Hensler, J. Werner, J. Mlynek, and T. Pfau: "*Continuous loading of a magnetic trap.*" Phys. Rev. A **64**, 31405 (2001)

[185] P. O. Schmidt, S. Hensler, J. Werner, T. Binhammer, A. Görlitz, and T. Pfau: "*Doppler cooling of an optically dense cloud of magnetically trapped atoms.*" Opt. Soc. Am. J. B **20**, 960 (2003)

[186] E. A. L. Henn, J. A. Seman, E. R. F. Ramos, A. H. Iavaronni, T. Amthor, and V. S. Bagnato: "*Evaporation in atomic traps: A simple approach.*" Am. J. Phys. **75**, 907 (2007)

[187] C. A. Sackett, C. C. Bradley, and R. G. Hulet: "*Optimization of evaporative cooling.*" Phys. Rev. A **55**, 3797 (1997)

[188] K. B. Davis, M.-O. Mewes, and W. Ketterle: "*An analytical model for evaporative cooling of atoms.*" App. Phys. B **60**, 155 (1995)

[189] S. Hensler, J. Werner, A. Griesmaier, P. O. Schmidt, A. Görlitz, T. Pfau, S. Giovanazzi, and K. Rzażewski: "*Dipolar relaxation in an ultra-cold gas of magnetically trapped chromium atoms.*" Appl. Phys. B **77**, 765 (2003)

[190] D. Guéry-Odelin, J. Söding, P. Desbiolles, and J. Dalibard: "*Is Bose-Einstein condensation of atomic cesium possible?*" Eur. Phys. Lett. **44**, 25 (1998)

[191] W. Wing: "*On neutral particle trapping in quasistatic electromagnetic fields.*" Progress in Quantum Electronics **8**, 181 (1984)

[192] D. M. Stamper-Kurn, H.-J. Miesner, A. P. Chikkatur, S. Inouye, J. Stenger, and W. Ketterle: "*Reversible Formation of a Bose-Einstein Condensate.*" Phys. Rev. Lett. **81**, 2194 (1998)

[193] P. W. H. Pinkse, A. Mosk, M. Weidemüller, M. W. Reynolds, T. W. Hijmans, and J. T. M. Walraven: "*Adiabatically Changing the Phase-Space Density of a Trapped Bose Gas.*" Phys. Rev. Lett. **78**, 990 (1997)

[194] Z.-Y. Ma, C. J. Foot, and S. L. Cornish: "*Optimized evaporative cooling using a dimple potential: an efficient route to Bose Einstein condensation.*" J. Phys. B **37**, 3187 (2004)

[195] T. W. Hänsch, and B. Couillaud: "*Laser frequency stabilization by polarization spectroscopy of a reflecting reference cavity.*" Opt. Comm. **35**, 441–444 (1980)

[196] Unknown authors: "*Application circuit examples of Si photodiode.*" (Unpublished, Company: Hamamatsu, 2004)

[197] C. Wieman, and T. W. Hänsch: "*Doppler-Free Laser Polarization Spectroscopy.*" Phys. Rev. Lett. **36**, 1170 (1976)

[198] W. Demtröder: "*Laserspektroskopie: Grundlagen und Techniken.*" (Springer, Berlin, 2007)

[199] P. Rehme: "*Laden eines Wellenleiters mit lasergekühlten Chromatomen.*" (PhD thesis, Stuttgart, 2006)

[200] M. Meister: "*Setup of a stable reference cavity for laser spectroscopy.*" (MA thesis, Stuttgart, 2008)

[201] E. D. Black: "*An introduction to Pound-Drever-Hall laser frequency stabilization.*" Am. J. Phys. **69**, 79 (2001)

[202] E. Black: "*Notes on the Pound-Drever-Hall technique.*" (unpublished, 2001) Note: LIGO-T980045-00-D

[203] R. W. P. Drever, J. L. Hall, F. V. Kowalski, J. Hough, G. M. Ford, A. J. Munley, and H. Ward: "*Laser phase and frequency stabilization using an optical resonator.*" App. Phys. B **31**, 97 (1983)

[204] B. Steinheil: "*Aufbau eines frequenzverdoppelten Diodenlasersystems zur Untersuchung ultrakalter Chrom-Atome.*" (MA thesis, Stuttgart, 2003)

[205] R. Grimm, M. Weidemüller, and Y. B. Ovchinnikov: "*Optical dipole traps for neutral atoms.*" arXiv:physics.atom-ph/9902072v1 (1999)

[206] Y. C. Wenas, and M. D. Hoogerland: "*A versatile all-optical Bose-Einstein condensates apparatus.*" Rev. Sci. Inst. **79**, 3101 (2008)

[207] B. Fröhlich, T. Lahaye, B. Kaltenhäuser, H. Kübler, S. Müller, T. Koch, M. Fattori, and T. Pfau: "*Two-frequency acousto-optic modulator driver to improve the beam pointing stability during intensity ramps.*" Rev. Sci. Inst. **78**, 3101 (2007)

[208] O. Morsch, and M. Oberthaler: "*Dynamics of Bose-Einstein condensates in optical lattices.*" Rev. Mod. Phys. **78**, 179 (2006)

[209] A. J. Moerdijk, B. J. Verhaar, and A. Axelsson: "*Resonances in ultracold collisions of ^{6}Li, ^{7}Li, and ^{23}Na.*" Phys. Rev. A **51**, 4852 (1995)

[210] T. Köhler, K. Góral, and P. S. Julienne: "*Production of cold molecules via magnetically tunable Feshbach resonances.*" Rev. Mod. Phys. **78**, 1311 (2006)

[211] D. M. Bauer, M. Lettner, G. Rempe, and S. Dürr: "*Controlling a magnetic Feshbach resonance with laser light.*" Nature Physics **5**, 339–342 (2009)

[212] S. Gupta, A. E. Leanhardt, A. D. Cronin, and D. E. Pritchard: "*Coherent manipulation of atoms with standing light waves.*" C. R. Acad. Sci. **2**, 479–495 (2001)

[213] H. Batelaan: "*The Kapitza-Dirac effect.*" arXiv:quant-ph/0007094v1 (2000)

[214] Y. B. Ovchinnikov, J. H. Müller, M. R. Doery, E. J. D. Vredenbregt, K. Helmerson, S. L. Rolston, and W. D. Phillips: "*Diffraction of a Released Bose-Einstein Condensate by a Pulsed Standing Light Wave.*" Phys. Rev. Lett. **83**, 284 (1999)

[215] B. Gadway, D. Pertot, R. Reimann, M. G. Cohen, and D. Schneble: "*Analysis of Kapitza-Dirac diffraction patterns beyond the Raman-Nath regime.*" Optics Express **17**, 19173 (2009)

[216] P. O. Fedichev, M. W. Reynolds, and G. V. Shlyapnikov: "*Three-Body Recombination of Ultracold Atoms to a Weakly Bound s Level.*" Phys. Rev. Lett. **77**, 2921 (1996)

[217] D. S. Petrov: "*Three-Boson Problem near a Narrow Feshbach Resonance.*" Phys. Rev. Lett. **93**, 143201 (2004)

[218] R. Ozeri, N. Katz, J. Steinhauer, and N. Davidson: "*Colloquium: Bulk Bogoliubov excitations in a Bose-Einstein condensate.*" Rev. Mod. Phys. **77**, 187 (2005)

[219] N. W. Ashcroft, and N. D. Mermin: "*Solid state physics.*" (Holt-Saunders, unknown, 1976)

[220] L. D. Landau, and E. M. Lifschitz: "*Lehrbuch der Theoretischen Physik: Statistische Physik.*" (Akademie, Berlin, 1966)

[221] D. M. Stamper-Kurn, A. P. Chikkatur, A. Görlitz, S. Inouye, S. Gupta, D. E. Pritchard, and W. Ketterle: "*Excitation of Phonons in a Bose-Einstein Condensate by Light Scattering.*" Phys. Rev. Lett. **83**, 2876 (1999)

[222] R. Nath, P. Pedri, and L. Santos: "*Phonon Instability with Respect to Soliton Formation in Two-Dimensional Dipolar Bose-Einstein Condensates.*" Phys. Rev. Lett. **102**, 50401 (2009)

[223] S. Balibar: "*Looking back at superfluid helium.*" arXiv:cond-mat/0303561v1 (2003)

[224] S. Balibar: "*Rotons, Superfluidity, and Helium Crystals.*" AIP Conf. Proc. **850**, 18 (2006)

[225] L. Landau: "*Theory of superfluidity of He II.*" J. Phys. U.S.S.R. **5**, 71–90 (1941)

[226] L. Landau: "*Theory of superfluidity of He II.*" J. Phys. U.S.S.R. **11**, 91–92 (1947)

[227] R. Feynman: "*Atomic theory of the two-fluid model of liquid helium.*" Phys. Rev. **94**, 262–277 (1954)

[228] A. P. Ivashin, and Y. M. Poluektov: "*Short-Wave Excitations in Non-Local Gross-Pitaevskii Model.*" arXiv:cond-mat.stat-mech/1004.0442v1 (2010)

[229] R. Nath, and L. Santos: "*Faraday patterns in two-dimensional dipolar Bose-Einstein condensates.*" Phys. Rev. A **81**, 33626 (2010)

[230] J. Stenger, S. Inouye, A. P. Chikkatur, D. M. Stamper-Kurn, D. E. Pritchard, and W. Ketterle: "*Bragg Spectroscopy of a Bose-Einstein Condensate.*" Phys. Rev. Lett. **82**, 4569 (1999) Note: See erratum [231].

[231] J. Stenger, S. Inouye, A. P. Chikkatur, D. M. Stamper-Kurn, D. E. Pritchard, and W. Ketterle: "*Erratum: Bragg Spectroscopy of a Bose-Einstein Condensate [230].*" Phys. Rev. Lett. **84**, 2283 (2000)

[232] P. T. Ernst, S. Götze, J. S. Krauser, K. Pyka, D.-S. Lühmann, D. Pfannkuche, and K. Sengstock: "*Probing superfluids in optical lattices by momentum-resolved Bragg spectroscopy.*" Nature Physics **6**, 56 (2009)

[233] M. Klawunn, and L. Santos: "*Hybrid multisite excitations in dipolar condensates in optical lattices.*" Phys. Rev. A **80**, 13611 (2009)

[234] D.-W. Wang, and E. Demler: "*Collective excitations and instabilities in multi-layer stacks of dipolar condensates.*" arXiv:cond-mat.other/0812.1838v1 (2008)

[235] V. M. Pérez-García, H. Michinel, J. I. Cirac, M. Lewenstein, and P. Zoller: "*Low Energy Excitations of a Bose-Einstein Condensate: A Time-Dependent Variational Analysis.*" Phys. Rev. Lett. **77**, 5320 (1996)

[236] P. A. Ruprecht, M. J. Holland, K. Burnett, and M. Edwards: "*Time-dependent solution of the nonlinear Schrödinger equation for Bose-condensed trapped neutral atoms.*" Phys. Rev. A **51**, 4704 (1995)

[237] T. Koch, T. Lahaye, J. Metz, B. Fröhlich, A. Griesmaier, and T. Pfau: "*Stabilization of a purely dipolar quantum gas against collapse.*" Nature Physics **4**, 218 (2008)

[238] P. M. Lushnikov: "*Collapse of Bose-Einstein condensates with dipole-dipole interactions.*" Phys. Rev. A **66**, 51601 (2002)

[239] S. Giovanazzi, A. Görlitz, and T. Pfau: "*Ballistic expansion of a dipolar condensate.*" J. Phys. B **5**, 208 (2003)

[240] N. G. Parker, C. Ticknor, A. M. Martin, and D. H. J. O'Dell: "*Structure formation during the collapse of a dipolar atomic Bose-Einstein condensate.*" Phys. Rev. A **79**, 13617 (2009)

[241] S. Rau, J. Main, and G. Wunner: "*Variational methods with coupled Gaussian functions for Bose-Einstein condensates with long-range interactions. I. General concept.*" Phys. Rev. A **82**, 023610 (2010)

[242] S. Rau, J. Main, H. Cartarius, P. Köberle, and G. Wunner: "*Variational methods with coupled Gaussian functions for Bose-Einstein condensates with long-range interactions. II. Applications.*" Phys. Rev. A **82**, 023611 (2010)

[243] J. L. Bohn, R. M. Wilson, and S. Ronen: "*How does a dipolar Bose-Einstein condensate collapse?*" Laser Physics **19**, 547 (2009)

[244] T. Lahaye, J. Metz, B. Fröhlich, T. Koch, M. Meister, A. Griesmaier, T. Pfau, H. Saito, Y. Kawaguchi, and M. Ueda: "*d-Wave Collapse and Explosion of a Dipolar Bose-Einstein Condensate.*" Phys. Rev. Lett. **101**, 80401 (2008) Note: See accompanying viewpoint [258].

[245] J. Metz, T. Lahaye, B. Fröhlich, A. Griesmaier, T. Pfau, H. Saito, Y. Kawaguchi, and M. Ueda: "*Coherent collapses of dipolar Bose–Einstein condensates for different trap geometries.*" New J. Phys. **11**, 055032 (2009)

[246] S. L. Cornish, S. T. Thompson, and C. E. Wieman: "*Formation of Bright Matter-Wave Solitons during the Collapse of Attractive Bose-Einstein Condensates.*" Phys. Rev. Lett. **96**, 170401 (2006)

[247] K. E. Strecker, G. B. Partridge, A. G. Truscott, and R. G. Hulet: "*Formation and propagation of matter-wave soliton trains.*" Nature **417**, 150 (2002)

[248] H. Saito, and M. Ueda: "*Mean-field analysis of collapsing and exploding Bose-Einstein condensates.*" Phys. Rev. A **65**, 33624 (2002)

[249] M. Ueda, and H. Saito: "*A Consistent Picture of a Collapsing Bose-Einstein Condensate.*" arXiv:cond-mat/0305242v1 (2003)

[250] I. Shvarchuck, C. Buggle, D. S. Petrov, M. Kemmann, W. V. Klitzing, G. V. Shlyapnikov, and J. T. Walraven: "*Hydrodynamic behavior in expanding thermal clouds of ^{87}Rb.*" Physical Review A **68**, 63603 (2003)

[251] R. Wilson: "*Private communication.*" (NIST, 2010)

[252] P. Horowitz, and W. Hill: "*The Art of Electronics.*" (Cambridge University Press, Cambridge, 1999)

[253] M. R. Matthews, B. P. Anderson, P. C. Haljan, D. S. Hall, C. E. Wieman, and E. A. Cornell: "*Vortices in a Bose-Einstein Condensate.*" Phys. Rev. Lett. **83**, 2498 (1999)

[254] C. N. Weiler, T. W. Neely, D. R. Scherer, A. S. Bradley, M. J. Davis, and B. P. Anderson: "*Spontaneous vortices in the formation of Bose-Einstein condensates.*" Nature **455**, 948 (2008)

[255] J. R. Abo-Shaeer: "*Novel Ground States Of Bose-Condensed Gases.*" (PhD thesis, MIT, 2004)

[256] M. Ueda: "*Private communication.*" (Tokyo, 2008)

[257] C. Ticknor, N. G. Parker, A. Melatos, S. L. Cornish, D. H. J. O'Dell, and A. M. Martin: "*Collapse times of dipolar Bose-Einstein condensates.*" Phys. Rev. A **78**, 61607 (2008)

[258] M. Lewenstein: "*Dancing the Bose-nova with a twirl.*" Physics **1**, 13 (2008)

[259] E. I. Butikov: "*Parametric excitation of a linear oscillator.*" Eur. J. Phys. **25**, 535 (2004)

[260] S. Balik, A. L. Win, and M. D. Havey: "*Imaging-based parametric resonance in an optical dipole-atom trap.*" Phys. Rev. A **80**, 23404 (2009)

[261] G. Magyar, and L. Mandel: "*Interference Fringes Produced by Superposition of Two Independent Maser Light Beams.*" Nature **198**, 255 (1963)

[262] R. L. Pfleegor, and L. Mandel: "*Interference of Independent Photon Beams.*" Phys. Rev. **159**, 1084 (1967)

[263] P. Anderson: "*Measurement in quantum theory and the problem of complex systems.*" (North Holland, Amsterdam, 1986)

[264] M. R. Andrews, C. G. Townsend, H.-J. Miesner, D. S. Durfee, D. M. Kurn, and W. Ketterle: "*Observation of Interference Between Two Bose Condensates.*" Science **275**, 637–641 (1997)

[265] Y. Shin, M. Saba, T. A. Pasquini, W. Ketterle, D. E. Pritchard, and A. E. Leanhardt: "*Atom Interferometry with Bose-Einstein Condensates in a Double-Well Potential.*" Phys. Rev. Lett. **92**, 50405 (2004)

[266] Y. Castin, and J. Dalibard: "*Relative phase of two Bose-Einstein condensates.*" Phys. Rev. A **55**, 4330 (1997)

[267] J. Javanainen, and S. M. Yoo: "*Quantum Phase of a Bose-Einstein Condensate with an Arbitrary Number of Atoms.*" Phys. Rev. Lett. **76**, 161 (1996)

[268] S. Ashhab: "*Interference between a large number of independent Bose-Einstein condensates.*" Phys. Rev. A **71**, 63602 (2005)

[269] E. Altman, E. Demler, and M. D. Lukin: "*Probing many-body states of ultracold atoms via noise correlations.*" Phys. Rev. A **70**, 13603 (2004)

[270] M. Greiner, O. Mandel, T. Esslinger, T. W. Hänsch, and I. Bloch: "*Quantum phase transition from a superfluid to a Mott insulator in a gas of ultracold atoms.*" Nature **415**, 39 (2002)

[271] W. Kohn: "*Analytic Properties of Bloch Waves and Wannier Functions.*" Phys. Rev. **115**, 809 (1959)

[272] R. W. Robinett: "*Self-interference of a single Bose Einstein condensate due to boundary effects.*" Physica Scripta **73**, 681 (2006)

[273] H. J. Paus: "*Physik in Experimenten und Beispielen.*" (Carl Hanser, München, 1995)

[274] Z. Hadzibabic, S. Stock, B. Battelier, V. Bretin, and J. Dalibard: "*Interference of an Array of Independent Bose-Einstein Condensates.*" Phys. Rev. Lett. **93**, 180403 (2004)

[275] F. Gerbier, S. Fölling, A. Widera, and I. Bloch: "*Visibility of a Bose-condensed gas released from an optical lattice at finite temperatures.*" arXiv:cond-mat.stat-mech/0701420v1 (2007)

[276] F. Gerbier, S. Trotzky, S. Fölling, U. Schnorrberger, J. D. Thompson, A. Widera, I. Bloch, L. Pollet, M. Troyer, B. Capogrosso-Sansone, N. V. Prokof'ev, and B. V. Svistunov: "*Expansion of a Quantum Gas Released from an Optical Lattice.*" Phys. Rev. Lett. **101**, 155303 (2008)

[277] I. Bloch, T. W. Hänsch, and T. Esslinger: "*Atom lasers and phase coherence of atomic Bose gases.*" RIKEN Review **33**, 6–9 (2001)

[278] I. F. Bloch: "*Atomlaser und Phasenkohärenz atomarer Bose-Einstein-Kondensate.*" (PhD thesis, München, 2000)

[279] I. Bloch, T. W. Hänsch, and T. Esslinger: "*Measurement of the spatial coherence of a trapped Bose gas at the phase transition.*" Nature **403**, 166 (2000)

[280] D. E. Miller, J. R. Anglin, J. R. Abo-Shaeer, K. Xu, J. K. Chin, and W. Ketterle: "*High-contrast interference in a thermal cloud of atoms.*" Phys. Rev. A **71**, 43615 (2005)

[281] T. B. Ottenstein: "*A New Objective for High Resolution Imaging of Bose-Einstein Condensates.*" (MA thesis, Heidelberg, 2006)

[282] M. Weidemueller: "*Rydberg atoms: There can be only one.*" Nature Physics **5**, 91 (2009)

[283] E. Urban, T. A. Johnson, T. Henage, L. Isenhower, D. D. Yavuz, T. G. Walker, and M. Saffman: "*Observation of Rydberg blockade between two atoms.*" Nature Physics **5**, 110 (2009)

[284] A. Gaetan, Y. Miroshnychenko, T. Wilk, A. Chotia, M. Viteau, D. Comparat, P. Pillet, A. Browaeys, and P. Grangier: "*Observation of collective excitation of two individual atoms in the Rydberg blockade regime.*" Nature Physics **5**, 115–118 (2009)

[285] P. Engels, C. Atherton, and M. A. Hoefer: "*Observation of Faraday Waves in a Bose-Einstein Condensate.*" Phys. Rev. Lett. **98**, 95301 (2007)

[286] P. Köberle: "*unknown (in preparation).*" (PhD thesis, Stuttgart, 2011)

[287] D. Budker, D. F. Kimball, and D. P. DeMille: "*Atomic physics: an exploration through problems and solutions.*" (Oxford University Press, Oxford, 2004)

[288] C. H. Townes, and A. L. Schawlow: "*Microwave spectroscopy.*" (Dover, New York, 1975)

[289] I. I. Sobelman: "*Atomic Spectra and Radiative Transitions.*" (Springer, Berlin, 1996)

[290] K. Viering: "*Spatially resolved single atom detection of neutral atoms.*" (PhD thesis, Austin, 2006)

[291] R. Heidemann: "*Rydberg Excitation of Bose-Einstein Condensates: Coherent Collective Dynamics.*" (PhD thesis, Stuttgart, 2008)

[292] R. C. Hilborn: "*Einstein coefficients, cross sections, f values, dipole moments, and all that.*" Am. J. Phys. **50**, 982–986 (1982)

[293] C. S. Adams, S. G. Cox, E. Riis, and A. S. Arnold: "*Laser cooling of calcium in a 'golden ratio' quasi-electrostatic lattice.*" J. Phys. B **36**, 1933 (2003)

[294] W. M. Frix, G. G. Karady, and B. A. Venetz: "*Comparison of calibration systems for magnetic field measurement equipment.*" IEEE Trans. Power Del. **9**, 100–8 (1994)

[295] M. Misakian: "*Equations for the Magnetic Field Produced by One or More Rectangular Loops of Wire in the Same Plane.*" J. Res. Natl. Inst. Stand. Technol. **105**, 557 (2000)

[296] M. Lighthill: "*Einführung in die Theorie der Fourier-Analysis und der Verallgemeinerten Funktionen.*" (Cambridge University Press, Cambridge, 1966)

[297] M. Abramowitz, and I. A. Stegun: "*Handbook of mathematical functions with formulas, graphs and mathematical tables.*" (Dover, New York, 1972)

[298] K. R. Overstreet, P. Zabawa, J. Tallant, A. Schwettmann, and J. P. Shaffer: "*Multiple scattering and the density distribution of a Cs MOT.*" Optics Express **13**, 9672 (2005)

[299] L. M. Smith, D. R. Keefer, and S. I. Sudharsanan: "*Abel inversion using transform techniques.*" J. Quant. Spec. Rad. Trans. **39**, 367–373 (1988)

[300] G. Corbó, and M. Testa: "*Magnetic dipoles and electric currents.*" arXiv:physics.pop-ph/0905.2324v1 (2009)

[301] J. D. Jackson: "*Klassische Elekrodynamik.*" (de Gruyter, New York, 1980)

[302] A. Pelster: "*Bose-Einstein-Kondensation.*" (scriptum, University of Duisburg-Essen, 2004)

[303] J.-M. Hou, T.-T. Zhao, and L.-J. Zhang: "*Excitations in a Dipolar Bose Einstein Condensate.*" Int. J. Theo. Phys. **47**, 1211 (2008)

[304] P. Amore: "*Asymptotic and exact series representations for the incomplete Gamma function.*" Eur. Phys. Lett. **71**, 1 (2005)

[305] J.-P. Martikainen, M. Mackie, and K.-A. Suominen: "*Comment on [69]: "Bose-Einstein condensation with magnetic dipole-dipole forces".*" Phys. Rev. A **64**, 37601 (2001)

„Schäme dich nicht, dir helfen zu lassen. Denn dir ist, wie dem Krieger beim Sturmlauf, nur vorgeschrieben, deine Pflicht zu tun. Wie nun, wenn du deines lahmen Fußes wegen nicht alleine imstande bist, die Schanze zu ersteigen, dies aber mit Hilfe eines andern dir möglich wäre?“ (Marc Aurel)

Danksagung

Abschließend möchte ich die Möglichkeit wahrnehmen, all denjenigen zu danken, die mich während der Promotion unterstützten.

An erster Stelle danke ich Tilman Pfau für seinen stetigen Einsatz, der zum Gelingen dieser Arbeit maßgeblich beitrug. Gerne ließ ich mich von Deiner Faszination für Physik anstecken und aufmuntern, wenn etwas trotz vieler Mühen nicht klappte. Deine grundpositive Einstellung, Diskussionsbereitschaft und sprudelnden Ideen waren wesentliche Motivationsfaktoren der vergangenen Jahre.

Second, I like to thank Thierry Lahaye. Working with you was a precious experience to me. Learning from your brilliant experimental skills and your mastery of work techniques, I don't want to miss the time you spend in Stuttgart.

Desweiteren bedanke ich mich bei den „Chromis“ Tobias Koch und Bernd Fröhlich für das angenehme Arbeitsklima. „Der Bock rannte“ und die vielen Tage, die wir mit der Aufnahme und Analyse der Messdaten verbrachten, vergingen wie im Flug. Wir waren ein gut eingespieltes Team, in dem jeder seine Aufgaben erledigte und das Experiment weiterbrachte. Euer Ausscheiden hinterlies Lücken, die nicht einfach zu schließen waren.

Insbesondere dafür, fürs Schließen der Lücken, möchte ich mich sehr herzlich bei Stefan Müller bedanken. Nach einer Durststrecke, in der wir versuchten dem Zerfall des Experimentes entgegen zu wirken, warst Du mein Weihnachtsgeschenk 2008. Schnell arbeitetest Du Dich in das Experiment ein und wir verbesserten kontinuierlich dessen Zustand. Es in Deinen Händen zu wissen ist beruhigend und ich wünsche Dir und unseren Weihnachtsgeschenken 2009, Julitte Billy und Emanuel Henn, nicht nur viel Spaß sondern auch baldigen Erfolg. Die Diskussionen, die ich für gewöhnlich mit „I have a question ...“ einleitete, und die fast immer in „finger-finger interactions“ veranschaulicht wurden, halfen die richtigen Fragen zu stellen. Außerdem möchte ich mich bei Euch für das intensive Korrekturlesen der Arbeit bedanken.

Axel Griesmaier, Robert Löw, Patrick Köberle, Rolf Heidemann, Ulrich Krohn, Vera Benkowski und Björn Butscher danke ich für die vielen hilfreichen Diskussionen.

Special thanks goes to Masahito Ueda and his dipolar theory group in Tokyo, Hiroki Saito and Yuki Kawaguchi. Not only did your simulations allow to understand the dipolar

collapse dynamics, but it were your comments about the vortex rings, which motivated us to probe the phase-coherence of the collapsed cloud.

Schließlich möchte ich mich für die gute Arbeitsatmosphäre bei allen Mitarbeitern des 5. Physikalischen Instituts bedanken. Außerdem bei Harald Kübler und Paul Rehme für die schnelle und kompetente Hilfe in Computerfragen, so wie bei Oliver Nagel, Beatrice Olgun-Lichtenberg, Karin Otter, Nadine Prellwitz und Sylvia Tassi für die Abnahme bürokratischer Hindernisse.